

**NUMERICAL AND ANALYTICAL MODELLING OF
OCEANIC/ATMOSPHERIC PROCESSES**

by

ANDREW JOHN WEAVER

B.Sc., University of Victoria, 1983
C.A.S.M., Cambridge University, 1984

**A THESIS SUBMITTED IN PARTIAL FULFILMENT OF
THE REQUIREMENTS FOR THE DEGREE OF
DOCTOR OF PHILOSOPHY**

in

THE FACULTY OF GRADUATE STUDIES

Department of Mathematics
Institute of Applied Mathematics
Department of Oceanography

We accept this thesis as conforming
to the required standard

THE UNIVERSITY OF BRITISH COLUMBIA

October 1987

© Andrew John Weaver, 1987

In presenting this thesis in partial fulfilment of the requirements for an advanced degree at the University of British Columbia, I agree that the Library shall make it freely available for reference and study. I further agree that permission for extensive copying of this thesis for scholarly purposes may be granted by the Head of my Department or by his or her representatives. It is understood that copying or publication of this thesis for financial gain shall not be allowed without my written permission.

Department of Mathematics

The University of British Columbia

2075 Wesbrook Place

Vancouver, Canada

Date: October 9, 1987

Abstract

Two problems in oceanic/atmospheric modelling are examined in this thesis. In the first problem the release of fresh water from a midlatitude estuary to the continental shelf is modelled numerically as a Rossby adjustment problem using a primitive equation model. As the initial salinity front is relaxed, a first baroclinic mode Kelvin wave propagates into the estuary, while along the continental shelf, the disturbance travels in the direction of coastally trapped waves but with a relatively slow propagation speed. When a submarine canyon extends offshore from the estuary, the joint effect of baroclinicity and bottom relief provides forcing for barotropic flow. The disturbance now propagates along the shelf at the first coastally trapped wave mode phase speed, and the shelf circulation is significantly more energetic and barotropic than in the case without the canyon. For both the experiments with and without a canyon an anticyclonic circulation is formed off the mouth of the estuary, generated by the surface outflow and deeper inflow over changing bottom topography. As the deeper inflow encounters shallower depth, the column of fluid is vertically compressed, thereby spinning up anticyclonically due to the conservation of potential vorticity. This feature is in qualitative agreement with the Tully eddy observed off Juan de Fuca Strait. A study of the *reverse estuary* (where the estuarine water is denser than the oceanic water) shows that this configuration has more potential energy available for conversion to kinetic energy than the normal estuary. Bass Strait may be considered as a possible *reverse estuary* source for the generation of coastally trapped waves. Model solutions are compared with field observations in the Bass Strait region and with the results of the Australian Coastal Experiment. The effects of a wider shelf and a wider estuary are examined by two more experiments. For the wider shelf, the resulting baroclinic flow is similar to that of the other runs, although the barotropic flow is weaker. The wide estuary model proves to be the most dynamic of all, with the intensified anticyclonic circulation now extending well into the estuary.

In the second problem the effect of the horizontal structure of midlatitude oceanic

heating on the stationary atmospheric response is examined by means of a continuously stratified model and a simple two level model, both in the quasigeostrophic β -plane approximation. Solutions are obtained for three non-periodic zonal heating structures (line source, segmented cosine, and segmented sine). Little difference is observed between the solutions for these two different models (continuously stratified and two level). There are two cases which emerge in obtaining analytic solutions. In case 1, for large meridional wavenumbers, there exists a large local response and a constant downstream response. In case 2, for small meridional wavenumbers, the far field response is now sinusoidal. A critical wavenumber separating these two cases is obtained. The effect of oceanic heating on the atmosphere over the Kuroshio region is examined in an attempt to explain the large correlations observed between winter Kuroshio oceanic heat flux anomalies, and the winter atmospheric surface pressure and 500 & 700 mb geopotential heights, both upstream and downstream of the heating region. In both models, the response is consistent with the observed correlations. When western North Pacific heating and eastern North Pacific cooling are introduced into the models, a large low pressure response is observed over the central North Pacific. This feature is in excellent agreement with the observed correlations. A time dependent, periodic, two level model (with and without surface friction) is also introduced in order to study the transient atmospheric response to oceanic heating. The height at which the thermodynamic equation is applied is found to be crucial in determining the response of this model. When the heating is entered into the model near to the surface, unstable modes are prevalent sooner than they would be when the heat forcing is applied at a higher level. As in the steady state models, two cases dependent on the meridional wavenumber l emerge in the analysis. For small scale meridional heating structures (large l), the response consists of an upper level high and a lower level low which propagate eastward with time. For large scale meridional heating structures (small l) the response essentially consists of a wavenumber 3–4 perturbation superimposed on the solution for large l .

Table of Contents

	page
Abstract	ii
List of Tables	viii
List of Figures	ix
Acknowledgements	xiv
Glossary	xvi
1. Introduction	1
2. The Influence of Buoyancy Flux from Estuaries on Continental Shelf Circulation	4
2.1 Introduction	4
2.2 Configurations Used in the Model	5
2.3 Relaxation in the Absence of a Canyon	9
2.4 Relaxation in the Presence of a Canyon	11
2.5 Reverse Estuaries	17
2.6 Experiments with a Wider Shelf and a Wider Estuary	17
2.7 Discussion	21
3. Bass Strait as a Reverse Estuary Source for Coastally Trapped Waves	32
3.1 Introduction	32
3.2 Description of the Model	33
3.3 Model Results	34
3.4 Comparison with Observations	45

4. Statistical Relationships between Northeast Pacific Atmospheric Surface Pressure and the Sea Surface Temperature along the British Columbia Coast	49
4.1 Introduction	49
4.2 Data	52
4.3 Analysis	53
4.4 Estimates of SST Anomalies Since 1900	56
5. Oceanic Heat Flux Anomalies over the Kuroshio Region: Statistical Relationship with Heat Flux Anomalies over the North Pacific and the Overlying Atmospheric Circulation	68
5.1 Introduction	68
5.2 Data	70
5.3 Analysis	71
5.4 Seasonal Structure of the North Pacific Oceanic Surface Heat Flux . . .	73
5.5 Oceanic Heat Flux Anomaly Correlations over the North Pacific . . .	78
5.6 Winter Correlations between Kuroshio Heat Flux Anomalies and the Overlying Atmospheric Surface Pressure, and 500 & 700 mb heights	82
6. The Steady State Response of the Atmosphere to Midlatitude Heating with Various Zonal Structures	87
6.1 Introduction	87
6.2 Description of the Model	88
6.3 Line Source Heating	90
6.4 Solutions for Various Zonal Distributions of Heating	95

6.5 Discussion	97
6.6 Application to the Kuroshio Region in Winter	107
7. A Two Level Model of the Steady State Response of the Atmosphere to Midlatitude Heating with Various Zonal Structures	113
7.1 Introduction	113
7.2 Description of the Model	113
7.3 Solution of the Equations	114
7.4 Solutions for Other Heating Structures	120
7.5 Discussion	125
7.6 Application to the Kuroshio Region	136
8. A Time Dependent Model of the Atmospheric Response to Midlatitude Heating with Various Zonal Structures	139
8.1 Introduction	139
8.2 Description of the Model	140
8.3 Solution of the Equations	142
8.4 Solutions for Other Heating Structures	145
8.5 Discussion	149
8.5.1 Description of the Parameters Used	149
8.5.2 The Model Solutions for ψ_1 and ψ_3	150
8.5.3 Stability Analysis	160
9. Conclusions	164
References	169

Appendix I – Inclusion of Rayleigh Friction in the Continuously	
Stratified Model	175
Appendix II – Inclusion of Rayleigh Friction and Newtonian Cooling	
in the Two Level Model	176

List of Tables

	page
1. Seasonal mean North Pacific pressure indices and corresponding least squares coefficients for predicting seasonal SST anomalies.	55
2. Correlation coefficients r between the seasonal mean predicted and observed SST anomalies.	56
3. Seasonal mean North Pacific pressure indices and corresponding least squares coefficients for predicting SST differences between seasons.	61
4. Correlation coefficients r between the seasonal mean predicted and observed SST changes with respect to the previous season.	61
5. Predicted mean seasonal temperature anomalies for the winter and summer seasons.	65
6. Real and imaginary parts of the zeroes of (II.3) for Model 1 (equally spaced levels).	178
7. Real and imaginary parts of the zeroes of (II.3) for Model 2 (unequally spaced levels).	178

List of Figures

	page
1. Schematic diagram of the topography used in models without a canyon.	7
2. Schematic diagram of the topography used in models with a submarine canyon. . .	7
3. East-west section of the model taken at the centre of the estuary.	8
4. Vertical velocity w at the interface between the first two levels for Experiment 1 (the fresh estuary without a canyon).	10
5. Transport streamfunction ψ for Experiment 1.	12
6. Space-time plot of transport streamfunction ψ along a north-south section 65 km offshore (for Experiment 1).	13
7. Horizontal velocity field at ten days for Experiment 1.	14
8. Transport streamfunction ψ for Experiment 2 (the fresh estuary with a canyon). .	15
9. Space-time plot of transport streamfunction ψ along a north-south section 65 km offshore (for Experiment 2).	16
10. Horizontal velocity field at ten days for Experiment 2.	18
11. Transport streamfunction ψ for Experiment 5 (the wider shelf).	20
12. Vertical velocity w at the interface between the first two levels, for Experiment 6 (the wide estuary) at $t = 10$ days.	21
13. Transport streamfunction ψ for Experiment 6.	22
14. Horizontal velocity field at ten days for Experiment 6.	23
15. Simple linear slope model showing the available potential energy per unit horizontal area as a function of $\delta\rho$ (see equation 2.11).	26
16. Total kinetic energy of the model ocean as a function of time.	28

17. Satellite image of Juan de Fuca Strait region off the west coast of British Columbia, taken on June 17, 1985 at 02:57 PST.	29
18. Map of Southeastern Australia indicating the five lines of current meter moorings in the Australian Coastal Experiment.	31
19. Schematic diagram of the model region and the dimensions used.	35
20. Topography at each u, v grid point near the mouth of Bass Strait.	36
21. The initial temperature and salinity data used at each vertical level for both the Bass Strait and Tasman Sea water masses.	37
22. Transport streamfunction ψ at 1, 5 and 10 days.	38
23. Space-time plot of transport streamfunction ψ along a north-south section 60 km offshore.	40
24. Vertical velocity w at the interface between the the first two levels at $t = 10$ days.	41
25. Horizontal velocity field at $t = 10$ days.	43
26. Space-time plot of the longshore velocity v along a north-south section 30 km offshore.	45
27. Long term mean (1947–1982) seasonal climatology of the surface pressure in the North Pacific.	50
28. Map of the western coast of British Columbia showing the two lighthouse stations at Kains Island and Langara Island.	53
29. Comparison of the time series of the observed and predicted seasonal SST anomalies from Kains Island for the period 1935–1977.	57
30. Comparison of the time series of the observed and predicted seasonal SST anomalies from Langara Island for the period 1941–1977.	59

31. Predicted SST anomalies at Kains Island for the period 1900–1934.	63
32. Predicted SST anomalies at Langara Island for the period 1900–1940.	64
33. Five year running mean from 1900–1977 of the predicted SST anomalies at Kains Island.	66
34. Five year running mean from 1900–1977 of the predicted SST anomalies at Langara Island.	67
35. Map of the North Pacific indicating the <i>Kuroshio region</i> used in determining an index representing the oceanic heat flux over the Kuroshio and its adjacent area.	71
36. Mean oceanic heat flux over the North Pacific for the period 1950–1979.	74
37. Surface heat flux anomaly maps for winter 1977 and summer 1977.	76
38. Surface heat flux anomaly maps for winter 1963 and winter 1978.	77
39. Simultaneous correlations between the oceanic heat flux anomaly over the <i>Kuroshio region</i> and the heat flux anomaly throughout the whole North Pacific. . .	79
40. Correlations between <i>Kuroshio region</i> heat flux anomalies and oceanic heating anomalies throughout the North Pacific in the following season.	81
41. Correlations between <i>Kuroshio region</i> heat flux anomalies and oceanic heating anomalies throughout the North Pacific two seasons later.	83
42. Correlations between winter oceanic heat flux anomalies over the <i>Kuroshio</i> <i>region</i> and the atmospheric surface pressure and 500 & 700 mb geopotential heights.	84
43. Contour of integration for the evaluation of I_{1R} , defined by equation (6.30) and (6.35).	94
44. Steady state perturbation streamfunction ϕ at $z = 0.0$	99

45. Perturbation streamfunction ϕ for the section along $y = 0.0$ at $z = 0.0$	101
46. Perturbation streamfunction ϕ for the section along $y = 0.0$ at $z = 0.5$	102
47. Perturbation streamfunction ϕ for heating with a meridional wavenumber $l = \frac{\pi}{2}$ along a section $y = 0.0$	104
48. Perturbation streamfunction ϕ in a vertical plane at $x = -0.01$ for line source heating.	105
49. Perturbation streamfunction ϕ for rectangular heating and segmented cosine heating at $x = -0.50$ and $y = 0.0$	106
50. Far field perturbation streamfunction ϕ in a vertical plane and as a function of height.	108
51. Perturbation streamfunction ϕ for rectangular and segmented cosine heating structures with $x_0 = 0.5$ at $x = -0.25$	110
52. Perturbation streamfunction ϕ along $y = 0.0$ at $z = 0.0$ for the western North Pacific heating and eastern North Pacific cooling model.	112
53. Schematic diagram of the two level model indicating the five pressure levels.	115
54. Contour of integration for the evaluation of (7.22).	118
55. Contour of integration for the evaluation of (7.28).	118
56. Model 1 solutions for <u>case 1</u> $l^2 > \{\gamma^2 + \delta\}^{\frac{1}{2}} - \gamma$, and the parameters of Section 7.3.	126
57. As in Fig. 56 but for Model 2.	128
58. Model 1 solutions for <u>case 2</u> $l^2 < \{\gamma^2 + \delta\}^{\frac{1}{2}} - \gamma$, and the parameters of Section 7.3.	131
59. As in Fig. 58 but for Model 2.	133
60. Contour of integration for the evaluation of (8.25).	144

61. Asymptotic ($t \rightarrow \infty$) zonal heating distributions for the segmented cosine and segmented sine heating functions, along the line $y = 0$	147
62. Hovmöller diagram of streamfunction contours for Model 1 for the segmented cosine heating distribution with $\varepsilon = 0.0 \text{ s}^{-1}$ and $l = 1.4 \times 10^{-6} \text{ m}^{-1}$	151
63. As in Fig. 62 but for Model 1 for the segmented cosine heating distribution with $\varepsilon = 2.0 \times 10^{-6} \text{ s}^{-1}$ and $l = 1.4 \times 10^{-6} \text{ m}^{-1}$	152
64. As in Fig. 62 but for Model 2 for the segmented cosine heating distribution with $\varepsilon = 2.0 \times 10^{-6} \text{ s}^{-1}$ and $l = 1.4 \times 10^{-6} \text{ m}^{-1}$	154
65. As in Fig. 62 but for Model 1 for the segmented sine heating distribution with $\varepsilon = 2.0 \times 10^{-6} \text{ s}^{-1}$ and $l = 1.4 \times 10^{-6} \text{ m}^{-1}$	155
66. As in Fig. 62 but for Model 1 for the segmented cosine heating distribution with $\varepsilon = 2.0 \times 10^{-6} \text{ s}^{-1}$ and $l = 0.8 \times 10^{-6} \text{ m}^{-1}$	157
67. As in Fig. 62 but for Model 2 for the segmented cosine heating distribution with $\varepsilon = 2.0 \times 10^{-6} \text{ s}^{-1}$ and $l = 0.8 \times 10^{-6} \text{ m}^{-1}$	158
68. As in Fig. 62 but for Model 1 for the segmented sine heating distribution with $\varepsilon = 2.0 \times 10^{-6} \text{ s}^{-1}$ and $l = 0.8 \times 10^{-6} \text{ m}^{-1}$	159
69. Stability curves for the time dependent model.	161

Acknowledgements

First and foremost I wish to thank my supervisor Dr. L. A. Mysak for his support, encouragement, motivation, inspiration and guidance during my stay at the University of British Columbia and my visit to McGill University. It was both a pleasure and a privilege to have Dr. Mysak as a supervisor and I hope to have the opportunity to collaborate with him in the years to come. I also wish to thank the rest of my committee, Drs. U. Ascher, A. Bennett, W. Hsieh, G. McBean, and B. Seymour for their helpful comments and criticisms. I am especially grateful to Drs. A. Bennett and W. Hsieh, who in the early stages of my research gave me a gentle nudge in the right direction. Over the years I have had interesting and stimulating discussions pertaining to my research with Drs. G. Boer, J. Church, J. Derome, B. DeYoung, D. Dunbar, D. Griffin, K. Hamilton, T. Kessler, P. LeBlond, C. Lin, P. McIntosh, G. Swaters and K. Thomson, for which I am grateful. The atmosphere and environment of the Department of Oceanography at the University of British Columbia provided me with surroundings which made my research both productive and interesting. I thank my fellow students and friends, especially B. TerHart, R. Dewey, R. Bermejo-Bermejo, P. Cummins, C. Reason, D. Webb for making the last few years as enriching as they have been. Finally I thank my family and Helen for their patience over the last few years.

Financial support by the Natural Sciences and Engineering Research Council of Canada (NSERC), in the form of a 1967 Science and Engineering Research Scholarship, and by Teaching Assistantships in the Department of Mathematics, are gratefully acknowledged. This research was also supported by NSERC Operating and Strategic grants and by a U.S. Office of Naval Research grant awarded to L.A. Mysak. Without this support none of this work would have been possible.

The years teach much which the days never know

Ralph Waldo Emerson, *Experience*

Glossary

Chapters 2 and 3

x, y, z	Coordinates oriented eastwards, northwards and vertically, respectively.
t	Time.
u, v, w	Velocity in the x, y, z direction, respectively.
R	Baroclinic Rossby radius.
c	Phase speed of wave fronts.
ψ	Transport streamfunction defined by (2.1).
h	Depth of the fluid.
$\frac{D}{Dt}$	Lagrangian derivative ($\frac{D}{Dt} = \frac{\partial}{\partial t} + \underline{u} \cdot \nabla$).
f	Coriolis parameter, $f = 2\Omega\sin\phi$ where, Ω is the magnitude of the earth's rotation and ϕ is the latitude.
ρ_0	Reference density used in the Boussinesq approximation.
p	Pressure.
ν	Lateral viscosity.
κ	Vertical viscosity.
ρ	Density of the fluid.
g	Acceleration due to gravity.
p_s	Surface pressure.
KE_{ssr}	Kinetic energy of the reverse estuary model.
KE_{ssf}	Kinetic energy of the fresh estuary model.
APE_r	Available potential energy of the reverse estuary model.
APE_f	Available potential energy of the fresh estuary model.
ρ_i	Initial density of the model ocean.
ρ_f	Final density of the model ocean.
V	Volume of the model ocean.
ρ_1, ρ_2	Densities used in the linear slope model.

$\delta\rho$	Density difference used in the linear slope model.
H	Depth of the estuary used in the linear slope model.

Chapter 4

γ	Index used in the summation of (4.1)
a_γ, b_γ	Coefficients used in least squares regression analysis.
n	Variable indicating a particular season.
$n - 1$	Two month period before season n .
P	Pressure in a particular season.
r	Correlation coefficient.

Chapter 5

Q_t	Net heat flux from the ocean to the atmosphere.
Q_l	Latent heat flux.
Q_s	Sensible heat flux.
Q_b	Net long wave radiative heat flux.
Q_i	Incoming solar radiative heat flux.
Q_T	Total heat flux from the ocean to the atmosphere.
Q_{b0}	Constant defined by (5.4)
C	Cloud cover in tenths.
ε	Emissivity of the sea surface.
σ	Stefan-Boltzmann constant.
T_s	Temperature of the ocean surface.
T_a	Air temperature at a height of 10m.
e	Air vapour pressure.
L	Latent Heat of vapourization.
C_e	Exchange coefficient of water vapour.
q_s, q_a	Mixing ratio of air at water level and at 10m, respectively.
V_a	Wind speed at a height of 10m.

C_s	Exchange coefficient of sensible heat.
C_p	Specific heat at constant pressure.
r	Correlation coefficient.

Chapter 6

x, y, z	Coordinates oriented eastwards, northwards and vertically, respectively.
Q	Diabatic heat forcing term.
k	Zonal wavenumber.
β	Effect of variation of Coriolis force with latitude. $\beta = \frac{2\Omega \cos \phi}{R}$, where Ω is the magnitude of the earth's rotation vector, R is the radius of the earth of the earth, and ϕ is the latitude.
U_0	Constant zonal flow of the basic state.
Ψ	Streamfunction of the basic state.
ϕ	Perturbation streamfunction.
ρ_s	Basic state density .
S	Stratification parameter.
H	Density scale height.
N_s	Brunt-Väisälä frequency of the basic state.
f_0	Coriolis parameter.
D	Scale for vertical coordinate.
L	Scale for horizontal coordinates.
U	Scale for horizontal velocities.
Q_1, Q_2	Prescribed heating functions.
Q_3, Q_4	Prescribed heating functions.
Q_0	Magnitude of diabatic heating.
p	Delta function heating constant, $\delta(x - p)$.
l	Meridional wavenumber of heat forcing.
α	Exponential trapping of heat forcing.

x_0	Width of zonal heating distributions.
ξ	Fourier transform variable.
q^2	Defined by $q^2 = \frac{\beta}{U_0} - l^2 - \frac{1}{4H^2S}$.
a	Defined by (6.19).
χ	Defined by (6.20).
r_0	Rayleigh friction coefficient.
c, η	Defined by (6.26).
b	Defined by (6.29).
C_R, C_A	Defined by Fig. 43.
C_B, C_b	Defined by Fig. 43.
$C_{R'}, C_{A'}$	Defined by Fig. 43.
$C_{B'}, C_{b'}$	Defined by Fig. 43.
λ	Defined by (6.33).
t	Integration variable.
\hat{q}	Defined by (6.43).
T_*	Temperature of the isothermal atmosphere.
g	Acceleration due to gravity.
Q_*	Imposed heating amplitude.
C_p	Specific heat at constant pressure.
R	Gas constant.

Chapters 7 and 8

x, y	Coordinates oriented eastwards and northwards respectively.
\bar{U}	Zonal wind.
p	Pressure.
ψ	Geostrophic streamfunction.
$\bar{\sigma}$	Static stability parameter.
C_p, R	As in Chapter 6.

β, f_0	As in Chapter 6.
ω	Vertical motion field.
q'	Imposed diabatic heating.
\bar{T}	Temperature field.
p_0, p_1	Pressure levels for two level model.
p_2, p_3	Pressure levels for two level model.
p_4	Pressure level for two level model.
ψ_1, ψ_3	Geostrophic streamfunction at the upper and lower level, respectively.
U_1, U_3	Zonal wind at the upper and lower level, respectively.
ω_2	Vertical motion field at level 2.
ψ_2, U_2	Geostrophic streamfunction and zonal wind at level 2.
Δp_1	Spacing between p_2 and p_0 .
Δp_2	Spacing between p_3 and p_1 .
Δp_3	Spacing between p_4 and p_2 .
Q_0, ξ	As in Chapter 6.
p, x_0	As in Chapter 6.
α_1, α_3	Defined by (7.13).
λ^{-1}	Deformation radius defined by (7.14).
γ, δ	Defined by (7.16) and (7.17), respectively.
r_0	Rayleigh friction and Newtonian cooling coefficient.
ξ_1, ξ_3	Defined by (7.19) and (7.20), respectively.
η_1, η_3	Defined by $\eta_1 = -i\xi_1$ and $\eta_3 = -i\xi_3$.
χ	Defined by (7.24).
q'_C, q'_S	Imposed segmented cosine and sine heating structures, respectively.
c	Phase speed (Chapter 7).
c_x	Phase speed in x direction.
c_{x1}, c_{x2}	Phase speeds in x direction.

K	Defined by (7.51).
U_m, U_T	Defined by (7.51).
k, l	Zonal and meridional wavenumber, respectively.
$\bar{\delta}$	Defined by (7.50).
t_1, t_2	Times for Rossby mode propagation around the globe.
t_d	Dissipative damping time scale.
t	Time.
τ	Imposed heating growth constant.
\bar{k}	Summation index.
c	Circumference of the earth (Chapter 8).
ε	Ekman friction coefficient.
f_1, f_3	Defined by (8.13).
ν	Laplace transform variable.
ν_1, ν_3	Defined by (8.18).
B, C	Defined by (8.19) and (8.20), respectively.
C_R	Contour of integration defined by Fig. 60.
d	Parameter used in defining the inverse Laplace transform.
χ	Defined by (8.32).
$a_{\bar{k}}$	Fourier series coefficients.

1. Introduction

Over the past few years there has been a flurry of research activity on estuarine outflow plumes. The goal of this research was to answer the question (addressed by Csanady, 1978; Beardsley and Hart, 1978; Beardsley and Winant, 1979) "How large is the influence of estuarine buoyancy flux on the continental shelf circulation—is it a local effect or does it dominate the shelf circulation over a broad region?". In Chapter 1 this question is examined in detail using, for the first time, a numerical general circulation model.

Two interesting applications arise from the analysis. A mechanism for eddy generation is obtained whereby oceanic water flowing into the estuary (below outflowing, less dense estuarine water) encounters shallowing depth and hence spins up anticyclonically through the conservation of potential vorticity. The model results are compared with observations of the well documented Tully eddy, which is observed at the entrance to Juan de Fuca Strait during the summer months (Tully, 1942; Freeland and Denman, 1982). The impact on the fishing industry of the upwelling associated with this eddy is currently the subject of the multidisciplinary *La Perouse Project* (Ware and Thomson, 1987).

The second application of the model is to the Australian Coastal Experiment (ACE) conducted from September 1983 to March 1984 (Freeland *et al.*, 1986; Church *et al.*, 1986a,b). In this experiment coastally trapped waves were detected along the coast of New South Wales. There is, however, a great debate going on in the scientific community as to where lies the source for these waves, and as to what is the forcing mechanism.

In Chapter 3 the topography and stratification of the Bass Strait region are used in the general circulation model of Chapter 2 in order to examine this latter application more closely. A forcing mechanism for the generation of the coastally trapped waves observed in ACE is proposed in this chapter. Dense Bass Strait water flowing down the continental shelf transfers energy into coastally trapped waves through the joint effect of baroclinicity and relief (JEBAR).

The interrelationship between the sea surface temperature (SST) in the North Pacific

Ocean and the overlying atmospheric circulation has been the subject of much controversy in recent years. High correlations have been observed between the SST and the atmospheric sea level pressure (SLP) and 700 mb height (Namais, 1959; Davis, 1976; Davis, 1978), although the question of cause and effect is still the subject of debate. In Chapter 4 we approach the problem from an Oceanographer's viewpoint; that is, we demonstrate that the SST's along the coast of British Columbia are most likely controlled by the regional atmospheric wind, and we see how the relationship between SLP and SST varies with season. This work is an extension of the work of Emery and Hamilton (1985), which is briefly reviewed in Section 4.1.

Throughout the rest of this thesis (Chapters 5–8) we examine the problem of large-scale air/sea interactions from a Meteorologist's perspective. In particular, we examine the effect of oceanic heat flux anomalies (comprised of latent, sensible and back radiative terms) on the overlying atmospheric circulation. We use the oceanic heat flux since it gives a more accurate way of representing the oceanic thermal influence on the atmosphere than the SST. The oceanic heat flux data used in this thesis is described in Chapter 5.

The annual and interannual variability of the total heat transfer from the ocean to the atmosphere over the entire North Pacific was examined by Zhao and McBean (1986), while Zhao and McBean (1987a) examined the principal patterns (empirical orthogonal functions—EOFs) of this variability. In addition, Zhao and McBean (1987b) constructed an index representing the oceanic heat flux over the Kuroshio region, and correlated this with atmospheric SLP and 700 mb height over the northern hemisphere. On the basis of these correlations they postulated that the oceanic heat forcing had a significant effect on the atmospheric circulation. In Chapter 5 the essential features of their analysis are presented, which provides motivation for the models of Chapters 6, 7 and 8.

The steady state response of the atmosphere to midlatitude heating with various zonal structures is investigated analytically in Chapter 6 using a linear, continuously stratified quasigeostrophic model. The results are then compared to the data analysis of Chapter 5.

To examine the effects of vertical shear on these steady state solutions, we consider a two level model in Chapter 7. Finally, in Chapter 8 we examine the transient atmospheric response to oceanic heat forcing and remove the assumption of an unbounded zonal domain ($-\infty < x < \infty$) used in the previous two chapters. This is accomplished by using a zonally periodic, time dependent version of the two level model in Chapter 7, with surface friction included in the lower level vorticity equation.

A more extensive introduction to each problem studied in this thesis is given in the first section of each chapter, and the conclusions are presented in Chapter 9.

2. The Influence of Buoyancy Flux from Estuaries on Continental Shelf Circulation

2.1 Introduction

The mainline of theoretical continental shelf circulation research has been along wind-forced coastally trapped wave models (see e.g., the reviews of Mysak, 1980, and Allen, 1980). In these studies, the continental shelf is usually assumed uniform in the alongshore direction. In reality, the coastline is often interrupted by estuaries. The influence of buoyancy flux from the estuarine outflow on the continental shelf circulation is not well understood.

The term *coastally trapped wave*, mentioned above, refers to a class of wave motions at subinertial frequencies which always propagate such that their phase travels with shallow water to the right (left) in the northern (southern) hemisphere (Brink, 1987). They are hybrid waves, with properties characteristic of both Kelvin waves (waves that may exist in a stratified ocean with constant depth and have exponentially decaying offshore dependence with zero offshore flow—the offshore trapping scale is determined by the deformation radius, Gill, 1982) and barotropic shelf waves (coastally trapped waves which may exist in a homogeneous ocean with offshore topographic variation, Mysak, 1980).

Two approaches have been used in the modelling of estuarine outflow onto the continental shelf. Csanady (1978), Beardsley and Hart (1978) and Beardsley and Winant (1979), have modelled the estuarine influence on the shelf circulation by sources or sinks of volume or vorticity along the coastline. Using barotropic or two-layer models, these studies of limited vertical structure concentrated on the steady-state horizontal shelf circulation induced by the sources or sinks on the coastal boundary, with the motion inside the estuary ignored. In contrast, Ou (1984), Wang (1984) and Van Heijst (1985), studied steady shelf-slope fronts with two-dimensional models in the xz -plane, where x and z are the offshore and vertical coordinates. By using a three-dimensional numerical model in this chapter, we not only combine the two aforementioned types of models, but are also able to study

the transient motions.

Fresh water runoff often increases suddenly over a week or less (e.g., in association with ice melting in late spring). This situation is modelled here by the Rossby adjustment problem in the absence of external forcing (Gill, 1976, 1982, and Hsieh and Gill, 1984), where at time $t = 0$, a vertical dam at the mouth of the estuary is rapidly removed, and the fresh estuarine water is allowed to interact with the denser oceanic water. This “dam break” technique gives a good sense of the time development of the response from an initial rest state.

Many estuaries, e.g., Juan de Fuca Strait off the coast of British Columbia, have submarine canyons extending offshore from the mouth of the estuary. We examine the effects of this canyon topography on the adjustment process.

In some areas, strong evaporation causes the estuarine water to be more saline than the oceanic water (eg., in Bass Strait in Australia). The adjustment process for this *reverse estuary* (or *inverse estuary*) is compared with the normal estuary.

The outline of this chapter is as follows: Section 2.2 describes the numerical model used. The adjustment of fresh estuarine outflow (in the absence of a canyon) is studied in Section 2.3 (experiment 1), and in the presence of a canyon in Section 2.4 (experiment 2). The *reverse estuary* is examined in Section 2.5 (experiments 3 and 4). Two sensitivity studies are made in Section 2.6, with a wider shelf (experiment 5) and a wider estuary (experiment 6). Section 2.7 discusses some of the basic dynamics and energetics of the adjustment process, as well as some applications to the Tully eddy off Juan de Fuca Strait (Tully, 1942, Freeland and Denman, 1982), and the Australian Coastal Experiment (Freeland *et al.*, 1986), where the Bass Strait is considered as a possible *reverse estuary* generating coastally trapped waves.

2.2 Configurations Used in the Numerical Model

The geometry of the estuary and shelf used in the first and third experiments is depicted in Fig. 1, with the initial salinity front indicated. Figure 2 illustrates the geometry used

in the second and fourth experiments, where a submarine canyon extends offshore from the mouth of the estuary. The steep-sloping continental shelf used in all four of these runs is typical of the west coast of the North American continent. In Fig. 3, the cross shelf topography and the initial vertical distributions of temperature and salinity, typical of Northeast Pacific summertime conditions, are shown (Halpern and Holbrook, 1972 p.330, Holbrook and Halpern, 1974 p.286, Emery and Dewar, 1982 p.273 and p.276).

In the fifth experiment we examined the effects of a wider shelf. The topography profile used is similar to that of Figs. 1 and 3, with the offshore width of each level approximately doubled. The influence of the estuary width on the continental shelf circulation was examined by means of a sixth experiment, with a 130 km wide estuary. The shelf topography used was identical to that of the first experiment (Figs. 1, 3).

The geostrophic adjustment process was investigated using the Cox (1984) version of the GFDL Bryan-Cox primitive equation ocean circulation model, with five vertical levels. In this model the prediction of currents is carried out using a finite-differenced, spherical coordinate form of the Navier-Stokes equations with three basic assumptions: 1)—The hydrostatic assumption is made, in which local acceleration and other terms of equal order are eliminated from the equation for vertical motion. 2)—The Boussinesq approximation is adopted, in which density differences are neglected except in the buoyancy term. 3)—A turbulent mixing hypothesis is used, in which stresses exerted by scales of motion too small to be resolved by the grid are represented as enhanced molecular mixing. To eliminate high speed external gravity waves (which would otherwise seriously limit the length of the time step of the numerical integration) the "rigid lid" approximation is used at the surface (ie., $w = 0$ at $z = 0$, where w is the vertical velocity). On the solid boundaries a no-slip boundary condition is used and the normal derivative of tracer elements (temperature, salinity) is set to zero. For a detailed description of the model see Bryan (1969), Cox (1984), Cox and Bryan (1984), Cox (1985).

Variable grid spacing was used to focus on the region near the mouth of the inlet where

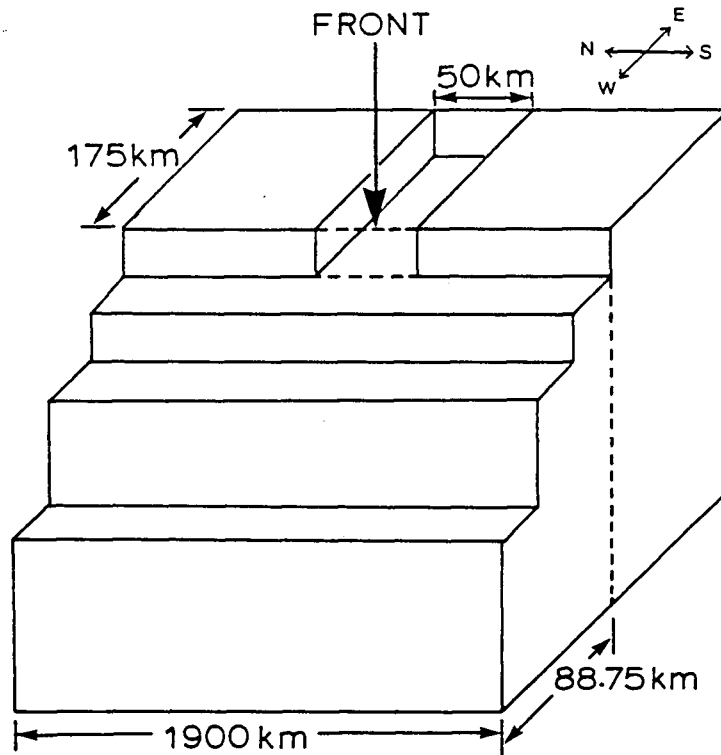


Figure 1 . Schematic diagram of the topography used in models without a canyon. The solid boundaries, 950 km north and south of the centre of the estuary and 300 km offshore, are not shown.

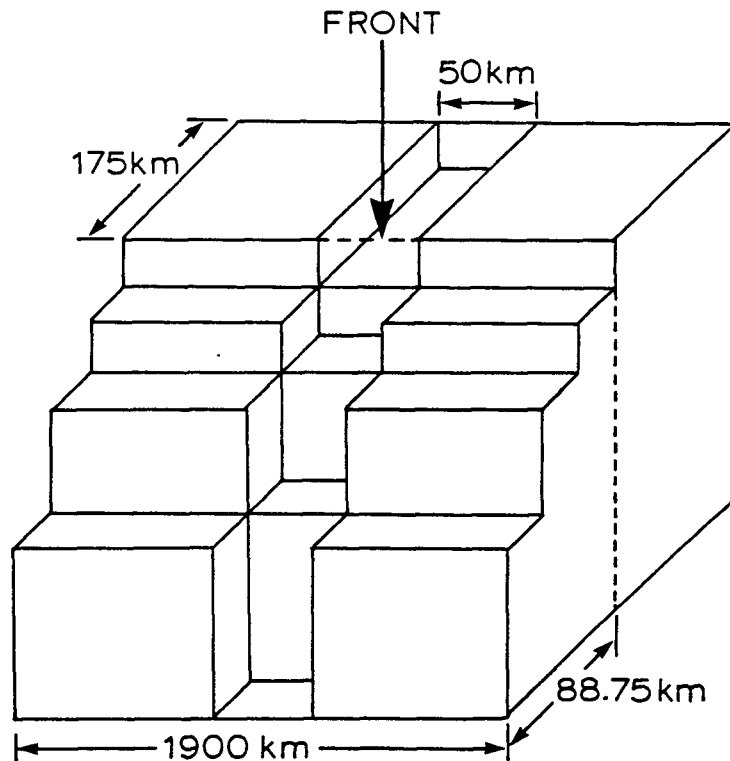


Figure 2 . Schematic diagram of the topography used in models with a submarine canyon. The solid boundaries, 950 km north and south of the centre of the estuary and 300 km offshore, are not shown.

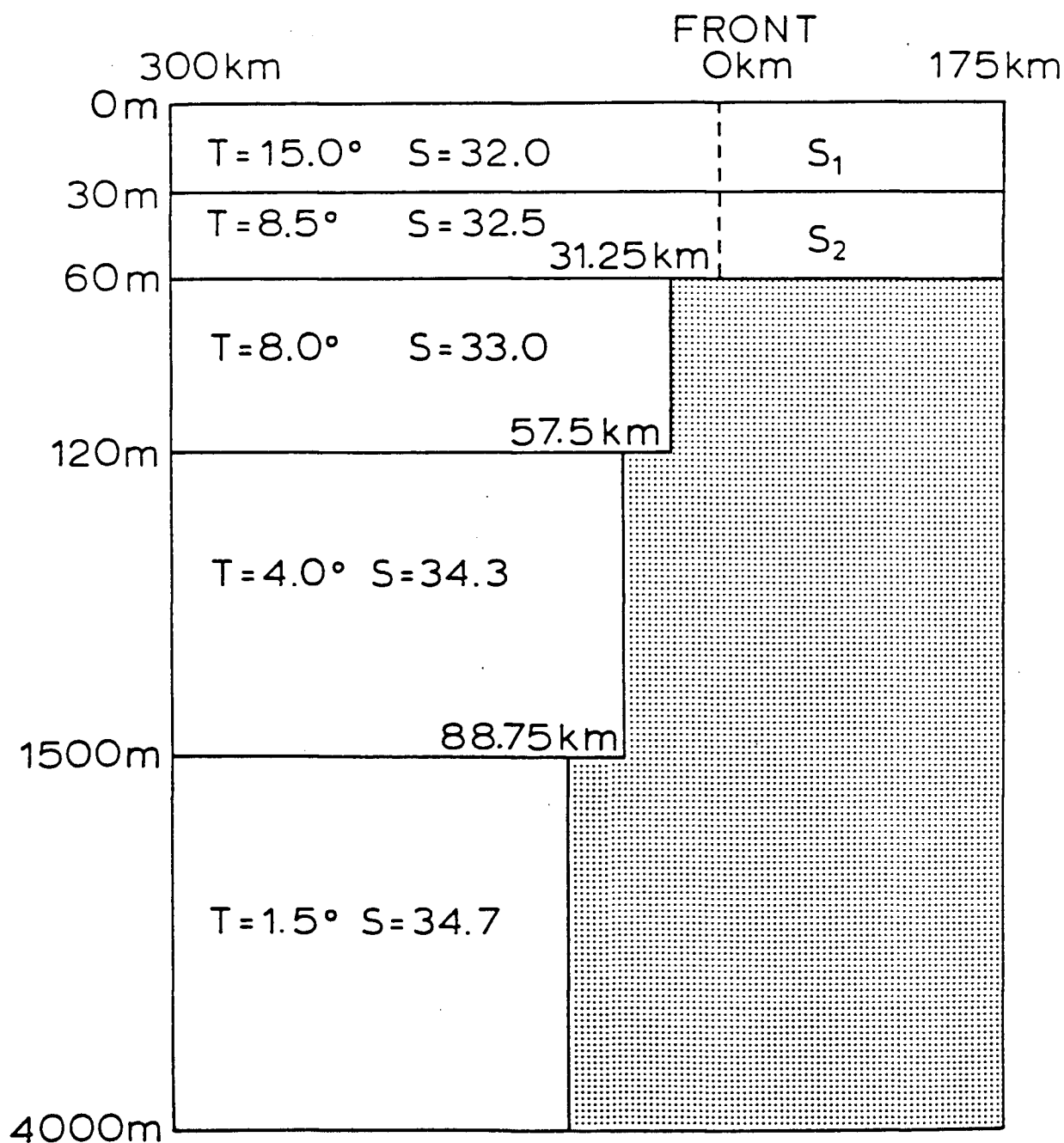


Figure 3 . East-west section of the model taken at the centre of the estuary. The initial temperature and salinity data used and the shelf topography are indicated. The initial temperature distribution was horizontally uniform, but there was a discontinuity of the salinity across the front. For the fresh estuary model $S_1 = 30.0$, $S_2 = 30.5$. For the *reverse estuary* model $S_1 = 34.0$, $S_2 = 34.5$.

a 10 km by 10 km grid was incorporated. The grid spacing in the north-south direction was increased monotonically to a maximum of 100 km at the northern and southern solid boundaries, 950 km from the centre of the inlet at 45°N . In the east-west direction the grid size was increased to a maximum of 30 km at the western solid boundary, 300 km offshore, and to 20 km at the eastern inlet boundary. All six experiments were relaxed without external forcing for ten days with a time step of fifteen minutes. The lateral eddy viscosity and diffusivity were set at $1.0 \times 10^3 \text{ m}^2\text{s}^{-1}$ and $4.0 \times 10^2 \text{ m}^2\text{s}^{-1}$, respectively, while the vertical viscosity and diffusivity were both set at $1.0 \times 10^{-4} \text{ m}^2\text{s}^{-1}$. Sensitivity tests were done with viscosities and diffusivities an order of magnitude greater and less than the aforementioned. The results presented here proved to be relatively insensitive to the viscosities and diffusivities. Unrealistically large viscosities, however, caused damping of the results as expected.

In the following analysis the first experiment is used as a control for comparison with the other five experiments.

2.3 Relaxation in the Absence of a Canyon

The first experiment (with no canyon) was the relaxation of the initial density front at the mouth of a fresh estuary in the absence of external forcing. The vertical velocity field at 30 m depth at days 1 and 10 is plotted in Fig. 4. The initial adjustment process generated a first mode baroclinic (ie., internal) Kelvin wave front, with a baroclinic Rossby radius $R \sim 30 \text{ km}$, which propagated eastward along the southern wall of the estuary at a phase speed $c \sim 12 \text{ km/day}$. The offshore grid-spacing of 10 km used in the model is about twice the analytical two-layer model Rossby radius ($\sim 5 \text{ km}$). This, combined with lateral viscosity used in the numerical model, produces a baroclinic Kelvin wave with much larger Rossby radius ($R \sim 30 \text{ km}$) and slower phase speed than the theoretical results ($R \sim 5 \text{ km}$ and $c \sim 43 \text{ km/day}$) (for a detailed description of this numerical effect see Hsieh *et al.*, 1983). Along the continental shelf, coastally trapped wavelike disturbances are seen propagating northward in Fig. 4.

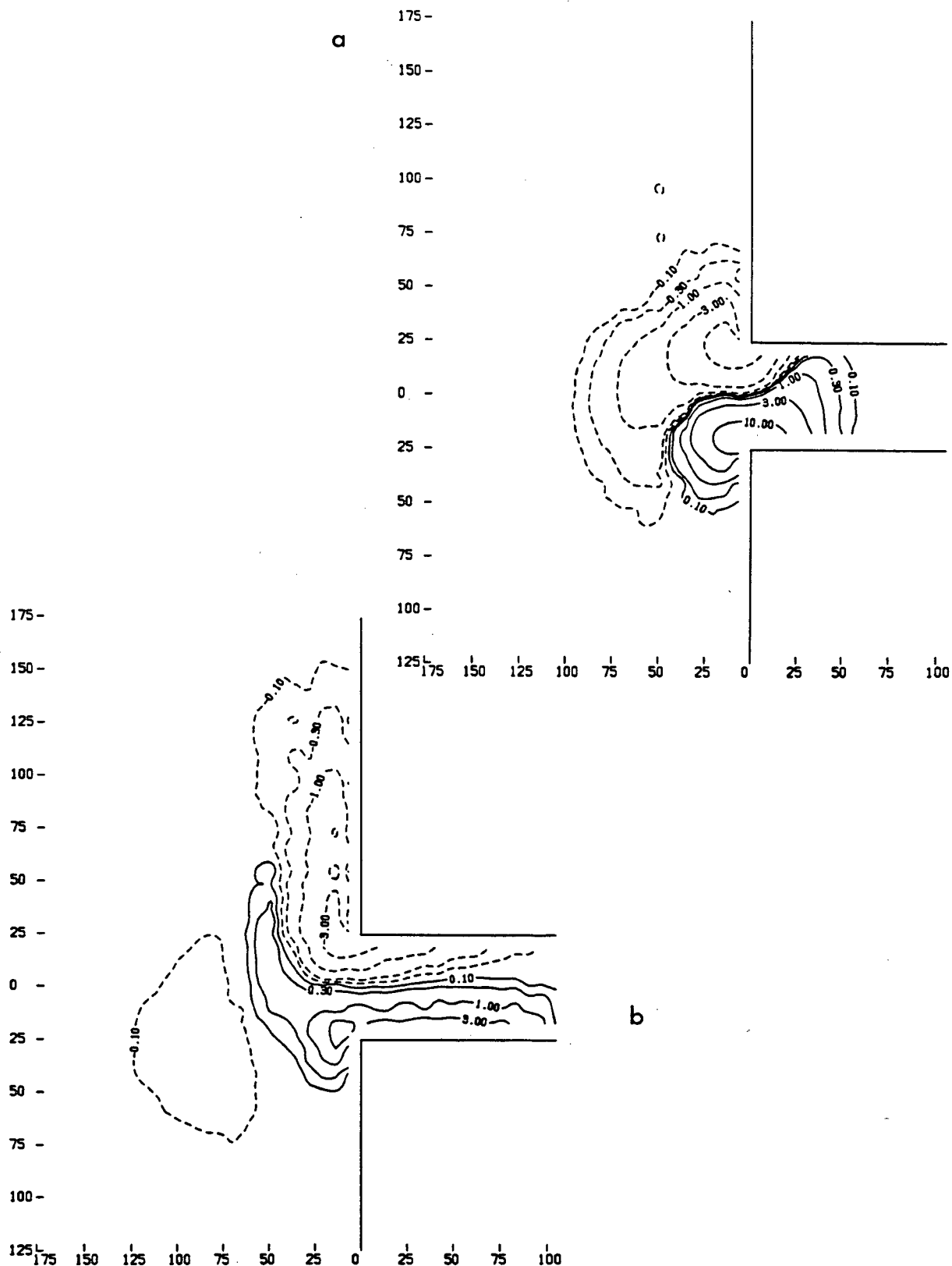


Figure 4 . Vertical velocity w (10^{-3} cm/s), at the interface between the first two levels ($z = 30$ m), for Experiment 1 (the fresh estuary without a canyon), (a) $t = 1$ day, (b) $t = 10$ days. The vertical and horizontal axes are in km.

The transport streamfunction ψ is defined by

$$\psi_y = - \int_{-h}^0 u dz, \quad \psi_x = \int_{-h}^0 v dz, \quad (2.1)$$

where h is the depth and u and v , the eastward and northward velocity components respectively. Figure 5 shows the ψ field at days 1 and 10, while Fig. 6, a space-time contour plot, reveals the temporal variations of ψ along a north-south section located 65 km offshore. Soon after the start of the relaxation, oscillations of period 17 hours are seen propagating northward at around 450 km/day (Fig. 6), as an alternating series of cyclonic and anticyclonic cells (Fig. 5a). Overall, the northward propagation of the disturbances is rather slow and weak. After day 2, an anticyclonic circulation develops near the mouth of the estuary (Fig. 6), intensifying and extending offshore with time (Fig. 5b).

Figure 7 focuses on the horizontal velocity field in the vicinity of the salinity front. In the upper layer (Fig. 7a) the less saline estuarine water flowed out of the inlet and progressed northward along the coast, whereas in the lower layer, the denser ocean water flowed in (Fig 7b). Comparing the velocity fields in Figs. 7a and 7b, we find that in the northern shelf region, the flow established after the passage of the coastally trapped wave is quasi-barotropic, while the Kelvin wave inside the inlet produces a baroclinic flow. The anticyclonic circulation, mentioned above, appears in Fig. 7b trapped against the shelf break 55 km offshore. This is consistent with the conservation of potential vorticity, where a column of water in the lower layer, flowing eastward into the inlet, vertically contracts over the shallowing topography, and spins up in an anticyclonic sense.

2.4 Relaxation in the Presence of a Canyon

To examine the effects of topography on the relaxation process more closely, a canyon was introduced into the model. The resulting baroclinic flow field in the estuary was similar to that of Section 2.3 in that a baroclinic Kelvin wave was generated, propagating eastward with a phase speed $c \sim 12$ km/day. North of the estuary the presence of the

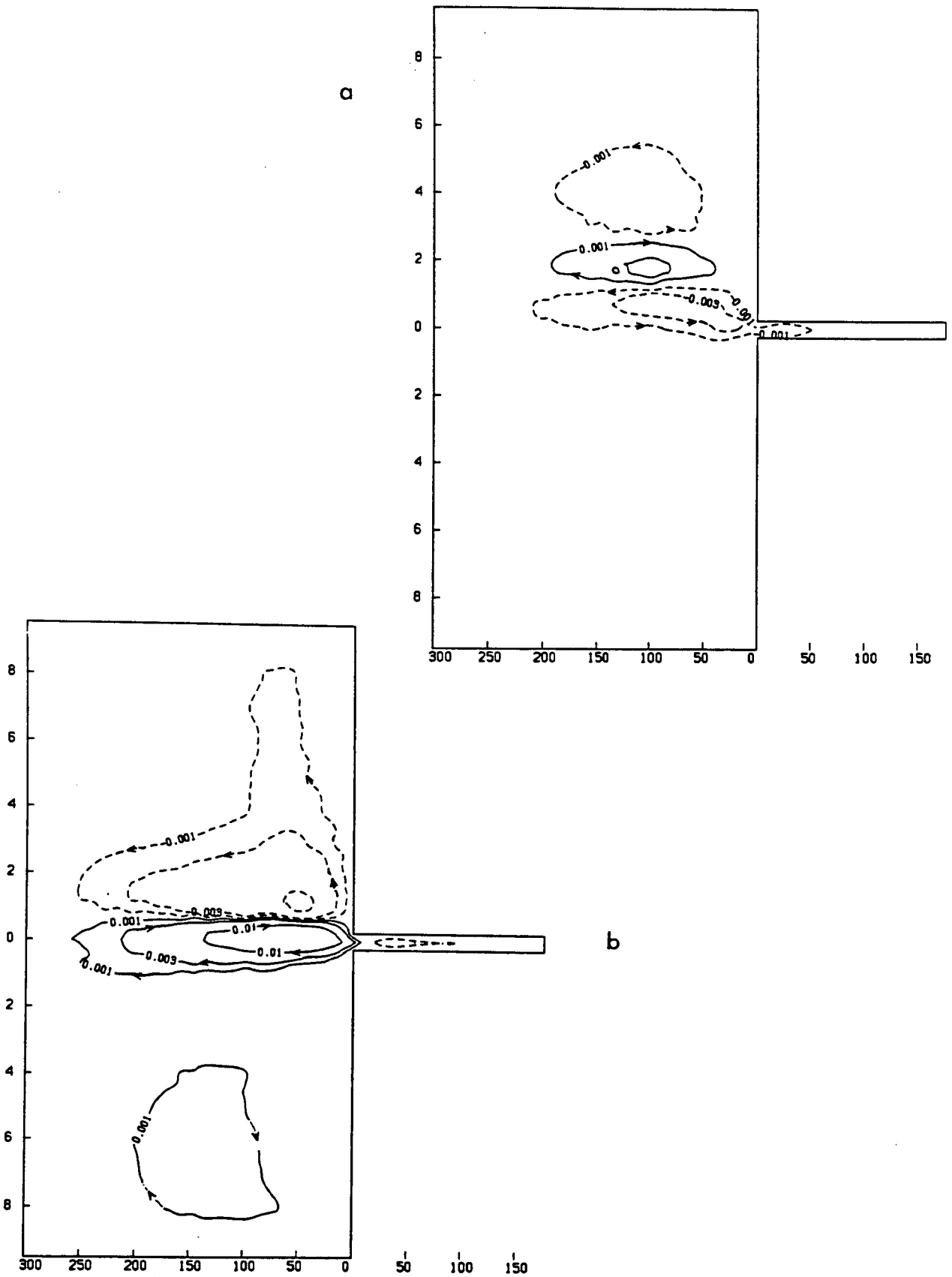


Figure 5 . Transport streamfunction ψ ($10^6 \text{ m}^3 \text{ s}^{-1}$) at, (a) $t = 1$ day, (b) $t = 10$ days, for Experiment 1. The vertical axis is in 10^2 km and the horizontal axis is in km.

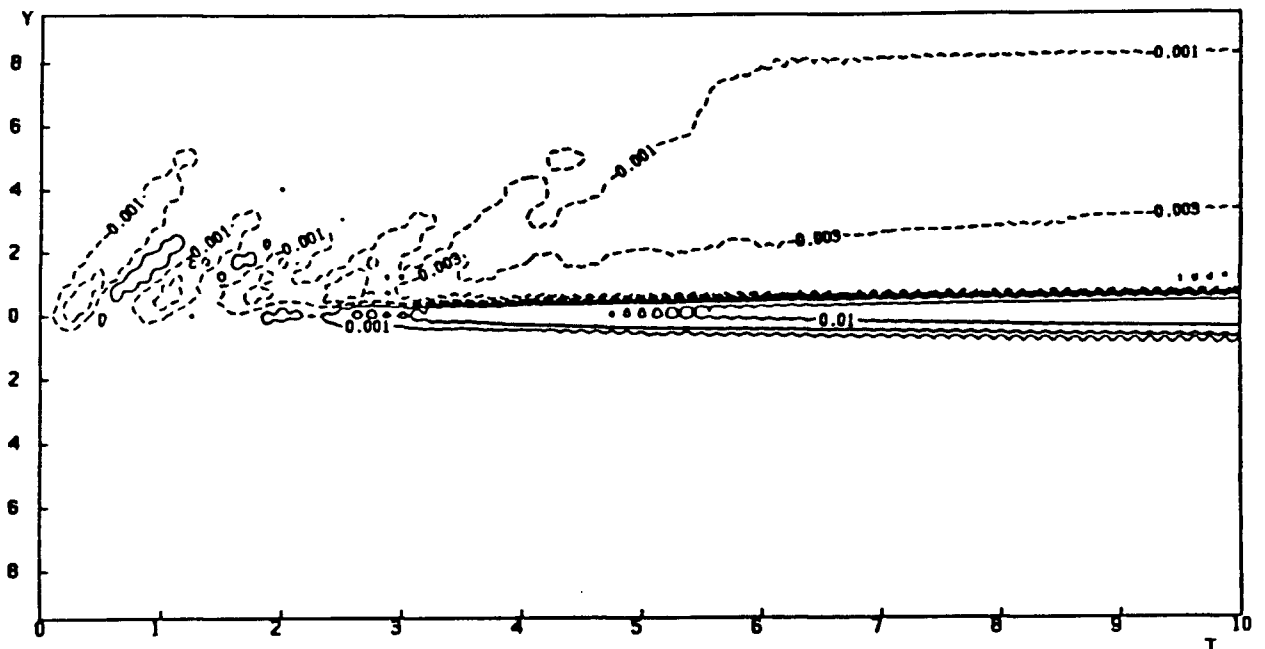


Figure 6 . Space-time plot of transport streamfunction ψ ($10^6 \text{m}^3 \text{s}^{-1}$), along a north-south section 65 km offshore, for Experiment 1. The top of the graph is the northern boundary. The vertical axis is in 10^2 km and the horizontal axis is in days.

coastally trapped waves was also evident.

Comparing Figs. 8a, b with Figs. 5a, b, we find that in the presence of the canyon a much stronger barotropic circulation has developed within one day (Fig. 8a). A cyclonic flow was generated throughout the whole northern region of the model and an intense anticyclonic circulation was trapped in the mouth of the estuary. Contrary to Section 2.3, the inlet-trapped anticyclonic circulation did not spread extensively offshore (Fig. 8b).

In Fig. 9, a streamfunction space-time plot across the same north-south section as in Fig. 6, the first coastally trapped wave mode is manifested in the 0.001 and 0.003 contours, which show northward propagation with $c \sim 600$ km/day. Figure 9 suggests the dominance of the first mode in the presence of the canyon, a situation not found in the absence of a

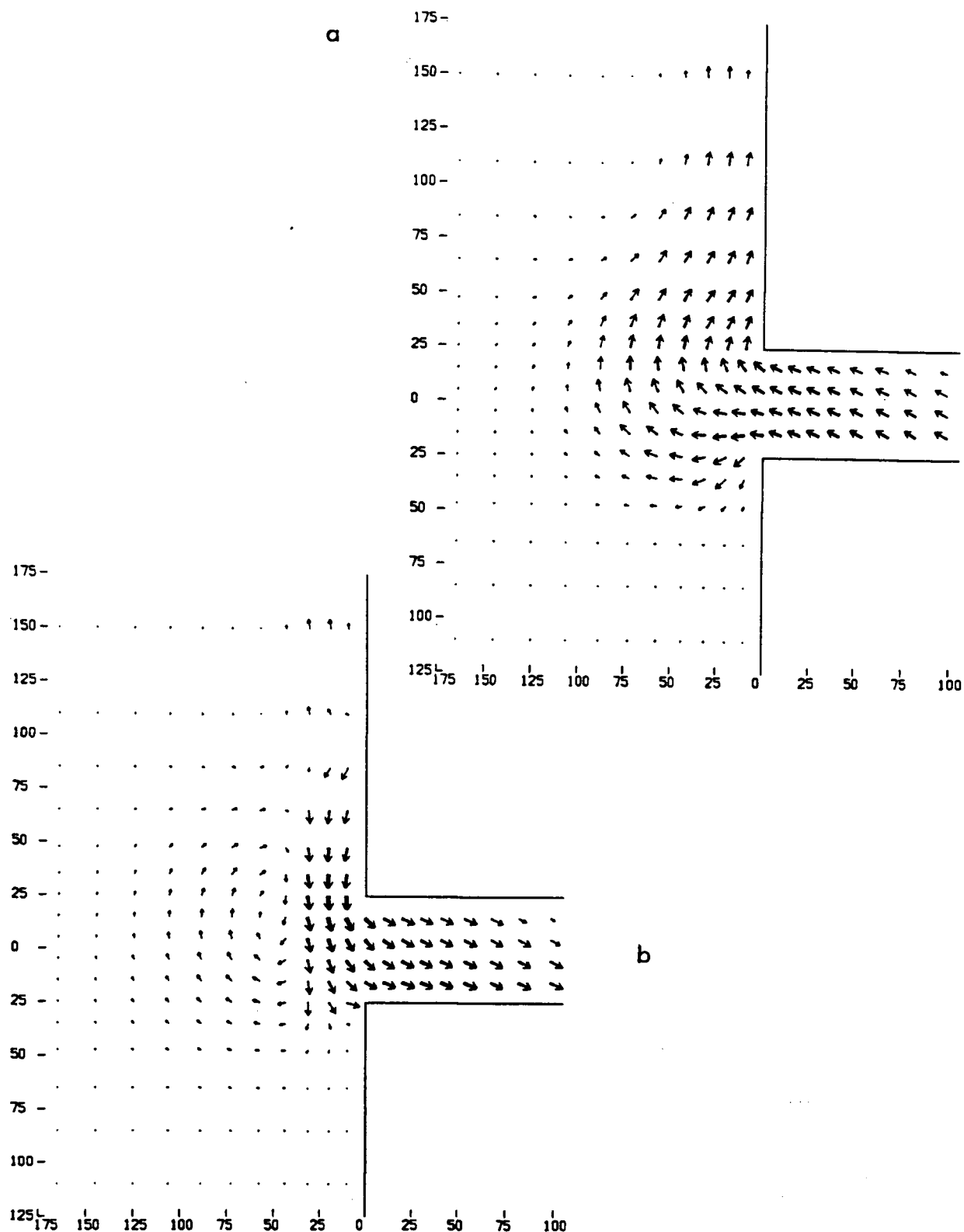


Figure 7 . Horizontal velocity field at ten days for Experiment 1, (a) upper level ($z = 15$ m), (b) second level ($z = 45$ m). The magnitude of the velocity is proportional to the thickness and length of the vector (ie., once the vector has a magnitude of 1 cm/s it gets wider). Both the vertical and horizontal axes are in km.

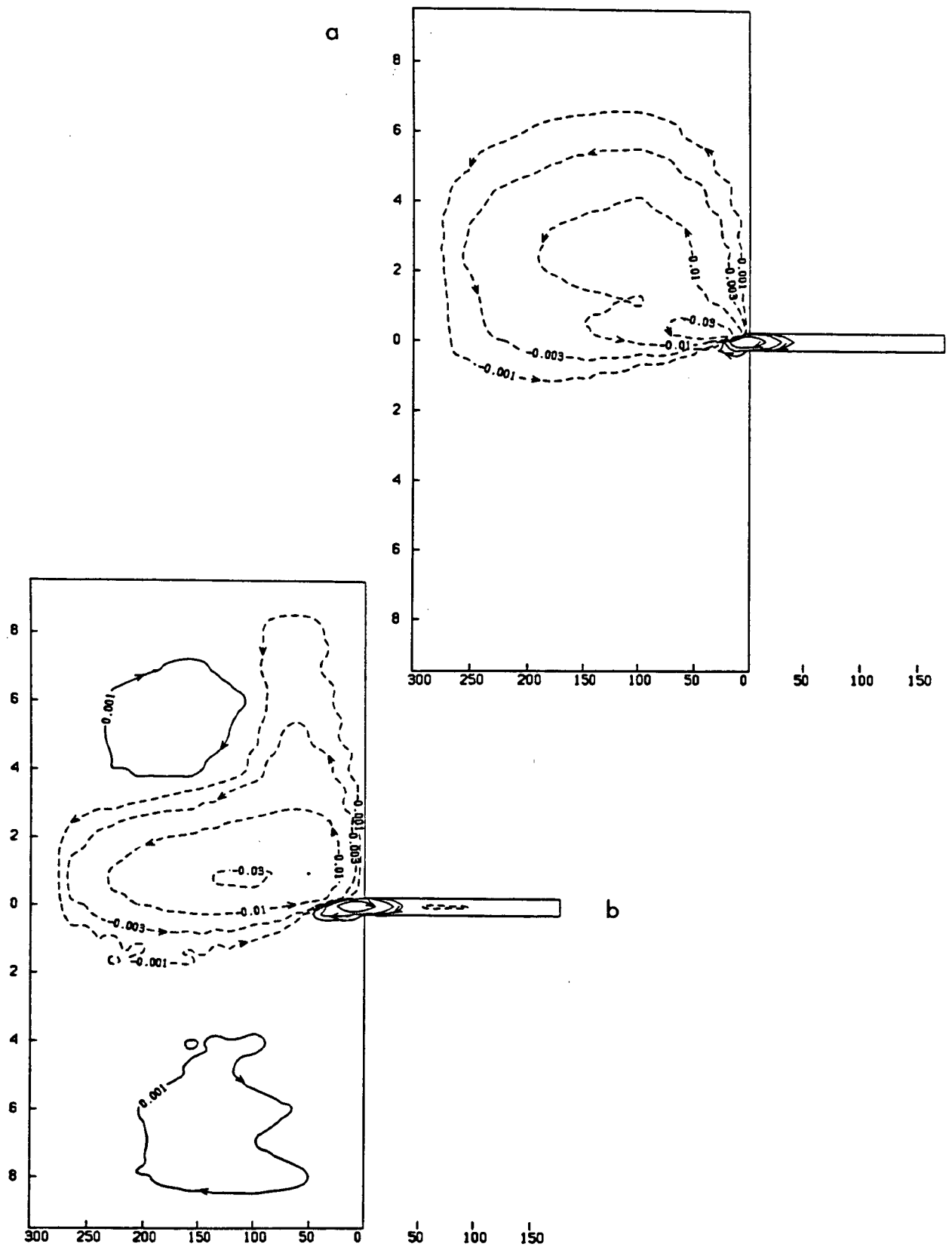


Figure 8 . Transport streamfunction ψ ($10^6 \text{ m}^3 \text{ s}^{-1}$) at, (a) $t = 1$ day, (b) $t = 10$ days, for Experiment 2 (the fresh estuary with a canyon). The vertical axis is in 10^2 km and the horizontal axis is in km.

of potential vorticity provides a mechanism for the circulation's existence and location—with the canyon, the most rapid compression of the inflowing lower column of water occurs much closer to the mouth of the inlet, hence the new location of the anticyclonic circulation. Figs. 10a,b also show that the canyon had little effect on the generation and propagation of the first mode baroclinic Kelvin wave into the estuary (cf. Figs. 7a,b).

2.5 Reverse Estuaries

For the *reverse estuary*, the first and second experiments were repeated (experiments 3 and 4) with the estuarine water more saline than the oceanic water at corresponding depth (Fig.3). The general circulation was similar to that depicted in Figs. 4–10, although more available potential energy was converted into kinetic energy (Section 2.6) and the direction of the flow was basically reversed.

In experiments 3 and 4 a first mode baroclinic Kelvin wave was again generated at the mouth of the inlet and was observed to propagate into the estuary with $c \sim 12$ km/day. In the presence of a canyon the first coastally trapped mode appeared dominant in the northern velocity field, whereas with no canyon present the first mode was not dominant.

The eddy trapped at the shelf break (Fig. 7b) was also present in the *reverse estuary* experiments except its direction was reversed. Similarly, when a canyon was added, the cyclonic eddy was trapped near the mouth of the inlet as in Fig. 10b, but with the direction reversed. Both the above observations are once more consistent with the conservation of potential vorticity—in the *reverse estuary*, a column of deeper water flows out of the inlet, vertically stretches over the deepening topography, with a corresponding cyclonic spinup.

2.6 Experiments with a Wider Shelf and a Wider Estuary

In the fifth experiment we examined the effects of a wider shelf (with no canyon). The baroclinic flow field remained largely unchanged, although it extended further offshore in the current field. There was less energy transferred into barotropic motion as is evident in Figs. 11a,b (cf., Figs. 5b, 6). Near inertial oscillations of period 17 hours propagated northward soon after the start of the relaxation process (Fig. 11b) as in Fig. 6, but now

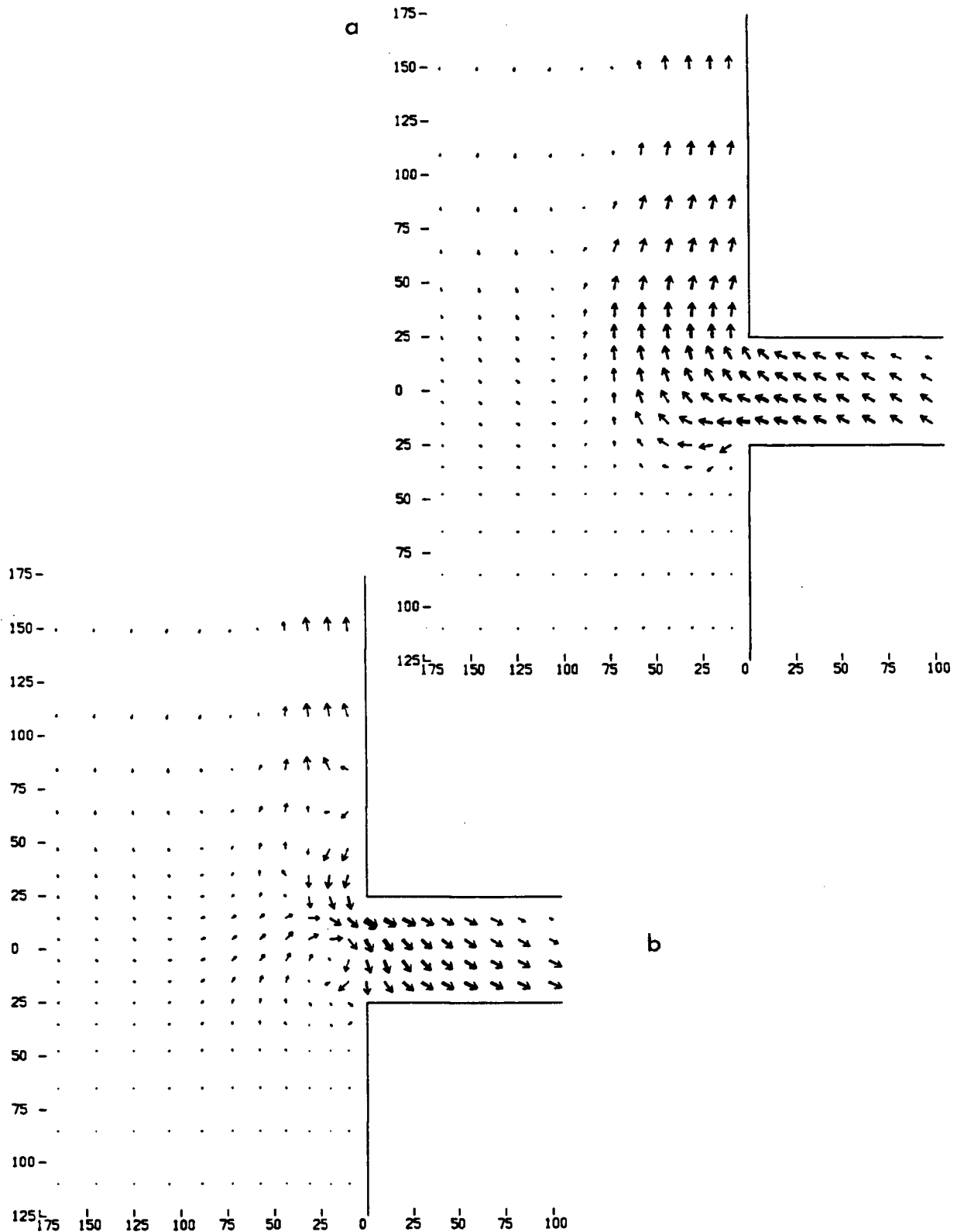


Figure 10 . Horizontal velocity field at ten days for Experiment 2, (a) upper level, (b) second level. The magnitude of the velocity is proportional to the thickness and length of the vector (ie., once the vector has a magnitude of 1 cm/s it gets wider). Both the vertical and horizontal axes are in km.

with a faster phase speed and greater offshore extent, as expected for coastally trapped waves on a wider shelf (Mysak, 1980). A large anticyclonic circulation was once more trapped at the shelf break 88.75 km offshore (as opposed to 57.5 km).

The model response is much more sensitive to a change in the width of the estuary. Experiment 6 was run with an estuary 130 km wide (as opposed to 50 km). The resulting motion was more energetic than the narrow estuary case, since the wider estuary had a larger initial reservoir of fresh water and hence more available potential energy.

In the case with the narrow estuary, the Kelvin wave completely dominated the baroclinic motion inside the estuary (Fig. 4b). In the wide estuary, there are alternating patches of upwelling and downwelling across the channel (Fig. 12), suggesting the excitation of Poincaré modes in addition to the Kelvin mode. From the dispersion relation of Poincaré waves (LeBlond and Mysak, 1978, p. 271), we know that for narrow channels, Poincaré modes are spatially evanescent—they decay down channel from their point of origin. Even for a wide channel, the Poincaré modes form part of the transient response, since at low enough frequency, the Poincaré waves are temporally decaying. The baroclinic field associated with the coastally trapped waves appears little affected by the change in the width of the estuary (Fig. 12, cf. Fig. 4b).

The barotropic motion was much more energetic for the wide estuary model than for the narrow estuary model. Figure 13a illustrates the streamfunction ψ at ten days. The large anticyclonic circulation which now extends well into the estuary itself is much stronger than that in Fig. 5b. The alternating cyclonic-anticyclonic cell pattern observed in Fig. 5a was also present in the wide estuary case, although the circulation was stronger and had greater northward extent, as seen in Fig. 13b, a space-time plot across the same section as Fig. 6.

The velocity field at ten days is depicted in Figs. 14a,b for the wide estuary case. The large anticyclonic circulation in the lower layer (Fig. 14b) is once more evident at the shelf break (cf., Fig. 7b). Inside the estuary there exists an anticyclonic eddy in the upper layer

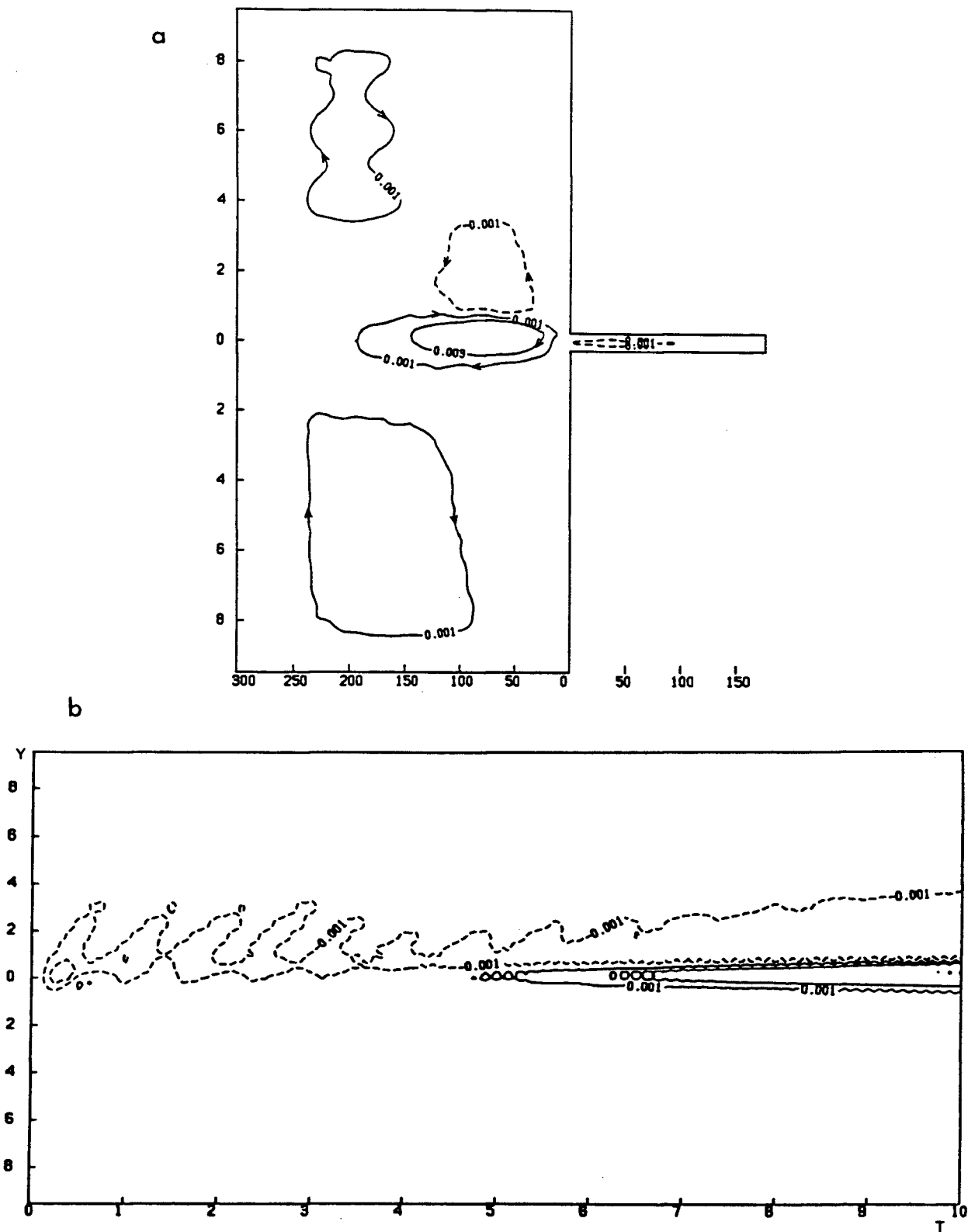


Figure 11 . Transport streamfunction ψ ($10^6 \text{ m}^3 \text{ s}^{-1}$) for Experiment 5 (the wider shelf). (a) $t = 10$ days. The vertical axis is in 10^2 km and the horizontal axis is in km. (b) Space-time plot along a north-south section 65 km offshore. The top of the graph is the northern boundary. The vertical axis is in 10^2 km and the horizontal axis is in days.

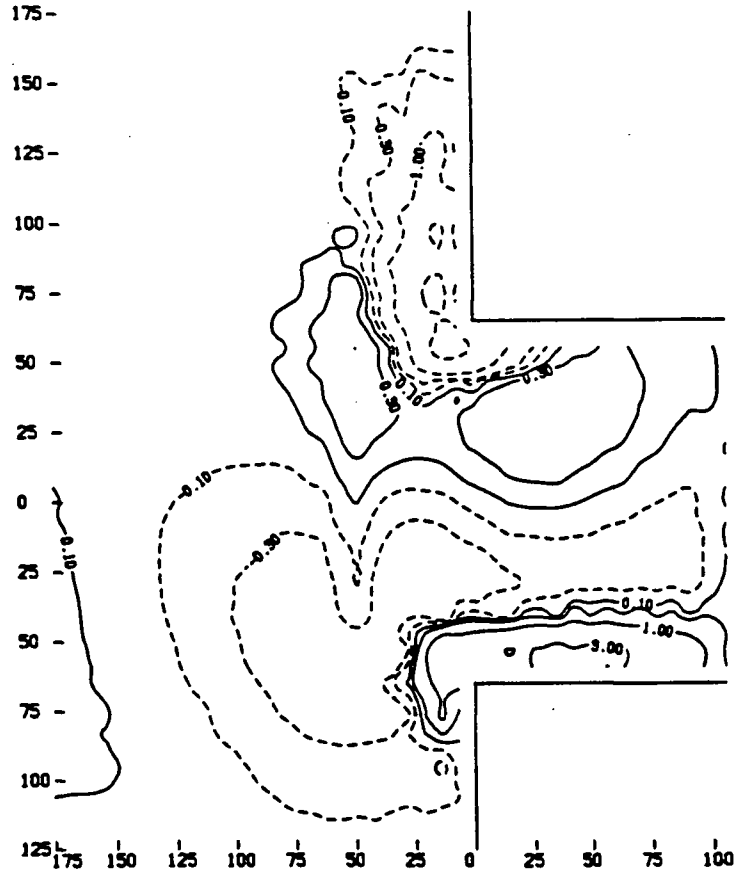


Figure 12 . Vertical velocity w (10^{-3} cm/s), at the interface between the first two levels ($z = 30$ m), for Experiment 6 (the wide estuary) at $t = 10$ days. The vertical and horizontal axes are in km.

(Fig. 14a) which was not apparent in the narrow estuary case (Fig. 7a), where the Kelvin wave dominated the estuarine circulation.

2.7 Discussion

We now consider how barotropic circulation is generated from the initial density front. Here for simplicity the governing momentum equations are used in Cartesian form as opposed to the spherical form used in the numerical model (Cox, 1984).

$$\frac{Du}{Dt} - fv = -\frac{1}{\rho_0}p_x + \nu(u_{xx} + u_{yy}) + \kappa u_{zz}, \quad (2.2)$$

$$\frac{Dv}{Dt} + fu = -\frac{1}{\rho_0}p_y + \nu(v_{xx} + v_{yy}) + \kappa v_{zz}, \quad (2.3)$$

$$p_z = -\rho g, \quad (2.4)$$

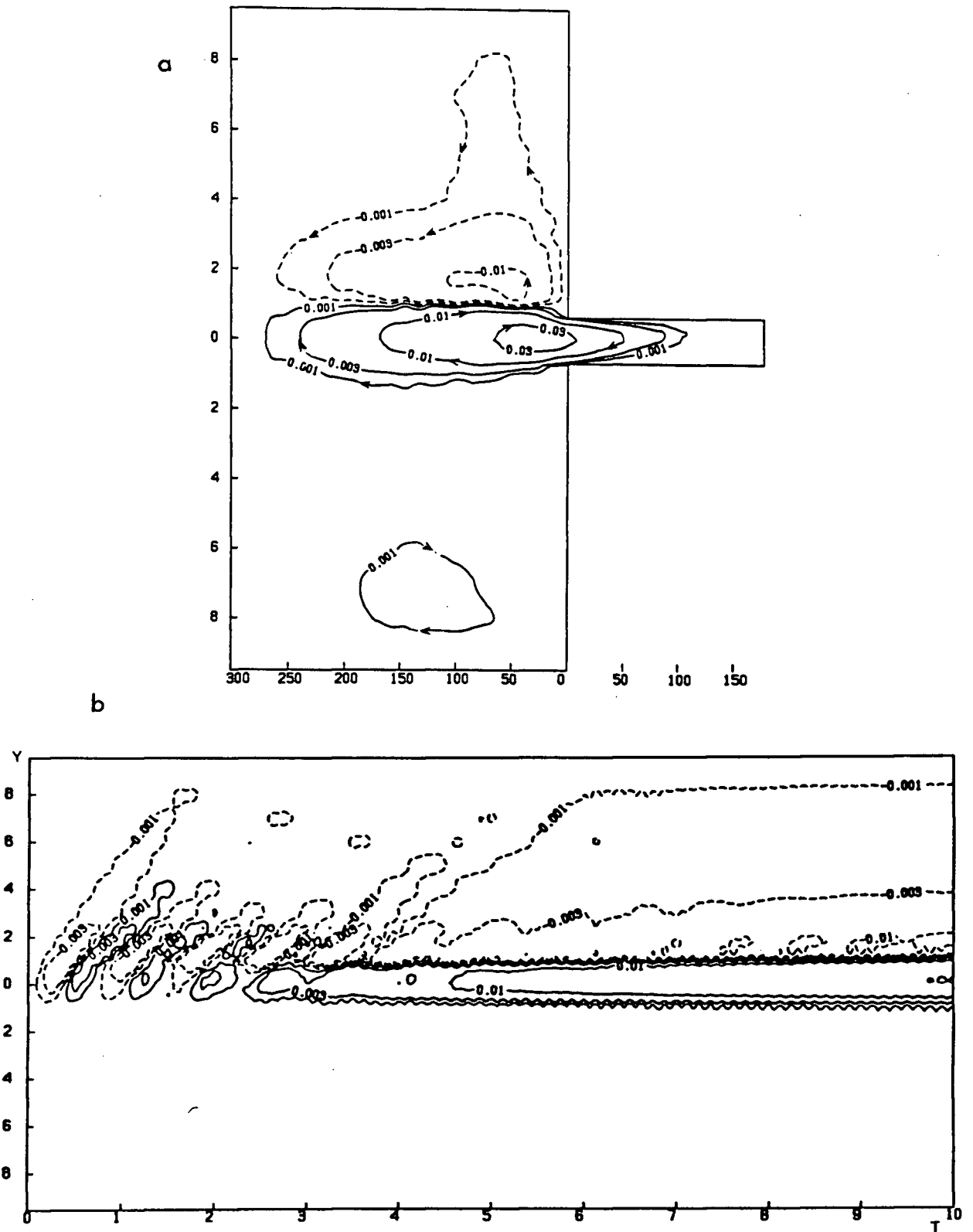


Figure 13 . Transport streamfunction ψ ($10^6 \text{ m}^3 \text{ s}^{-1}$) for Experiment 6. (a) $t = 10$ days. The vertical axis is in 10^2 km and the horizontal axis is in km. (b) Space-time plot along a north-south section 65 km offshore. The top of the graph is the northern boundary. The vertical axis is in 10^2 km and the horizontal axis is in days.

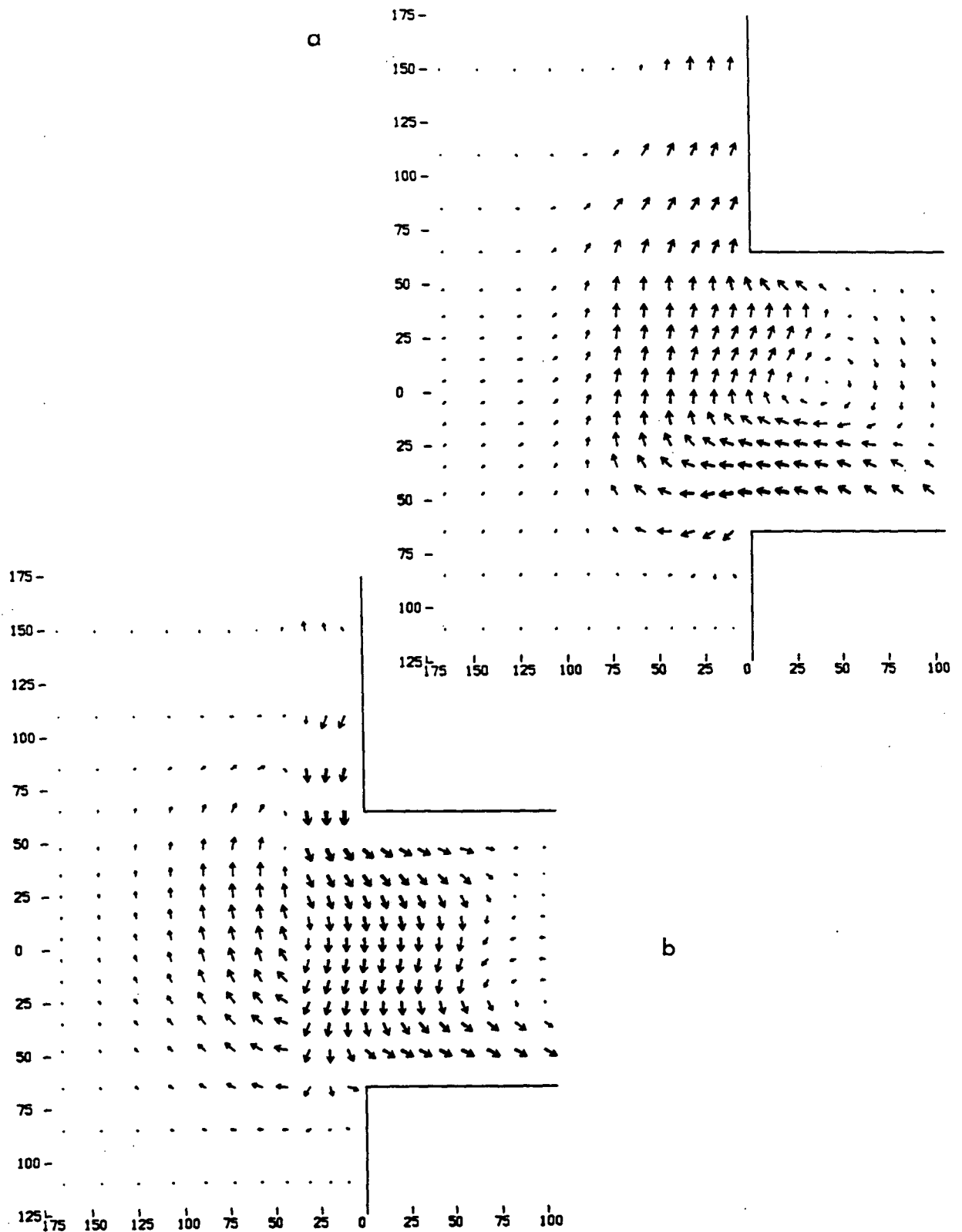


Figure 14 . Horizontal velocity field at ten days for Experiment 6, (a) upper level ($z = 15$ m), (b) second level ($z = 45$ m). The magnitude of the velocity is proportional to the thickness and length of the vector (ie., once the vector has a magnitude of 1 cm/s it gets wider).

where x is oriented eastward and y northward. The constants ν and κ are the lateral and vertical viscosities respectively. Depth averaging the linearized, inviscid versions of (2.2) and (2.3), substituting in (2.1) and taking the curl, we obtain,

$$\begin{aligned} \left(\frac{1}{h} \psi_{yt} \right)_y + \left(\frac{1}{h} \psi_{xt} \right)_x + \left(\frac{f}{h} \psi_x \right)_y - \left(\frac{f}{h} \psi_y \right)_x \\ = \left[\frac{g}{\rho_0 h} \int_{-h}^0 \int_z^0 \rho_x dz' dz \right]_y - \left[\frac{g}{\rho_0 h} \int_{-h}^0 \int_z^0 \rho_y dz' dz \right]_x, \end{aligned} \quad (2.5)$$

where (2.4) has been written as,

$$p(z) = p_s + \int_z^0 g \rho dz', \quad (2.6)$$

with p_s the rigid lid surface pressure. Equation (2.5) is an equation for barotropic motion, with the forcing term on the right hand side arising from the joint effect of baroclinicity and relief (JEBAR). For our application f is constant and *initially* $\rho = \rho(x, z)$, so that at the initial moment (2.5) reduces to,

$$\begin{aligned} \{\psi_{yyt} + \psi_{xxt}\} - \frac{1}{h} \{h_y \psi_y + h_x \psi_x\}_t - \frac{f}{h} \{h_y \psi_x - h_x \psi_y\} \\ = \frac{gh_y}{\rho_0} \left\{ \frac{-1}{h} \int_{-h}^0 \int_z^0 \rho_x dz' dz + \int_{-h}^0 \rho_x dz \right\}. \end{aligned} \quad (2.7)$$

In the models without the canyon, $h = h(x)$, the forcing term vanishes from (2.7), hence only weak barotropic flow is observed. With the canyon, h_y is nonzero, and the JEBAR term produces a much stronger barotropic circulation, with the emission of coastally trapped wave fronts as in Hsieh and Gill (1984).

The *reverse estuary* experiments produced more energetic flows than the fresh estuary experiments, despite having initial salinity fronts of equal strength. This can be accounted for by the difference in the available potential energy in the two cases. In the *reverse estuary* models, dense water from the estuary flowed down the shelf to a considerable depth, whereas the rearrangement of water masses in the fresh estuary cases was restricted to the top two levels, hence a more limited conversion of potential to kinetic energy. The

ratio between the steady state (assuming no viscosity) total kinetic energy of the reverse and fresh estuary models was estimated using

$$KE_{ssr}/KE_{ssf} = APE_r/APE_f, \quad (2.8)$$

where APE_r and APE_f are the available potential energies of the *reverse* and fresh estuary models, respectively. The available potential energies were calculated using a simple slab model. The water masses of fixed density were assumed to move without mixing from the initial configuration to the final state where the slabs of water masses laid on top of each other, with the denser ones below. We let

$$APE = \int_V (\rho_i - \rho_f)gzdV, \quad (2.9)$$

where ρ_i and ρ_f are the initial and final densities and V is volume of the model ocean. This somewhat simple calculation yielded,

$$APE_r/APE_f \sim 2, \quad (2.10)$$

i.e., the *reverse estuary* had nearly twice the available potential energy of the fresh estuary.

For idealized situations, the APE for fresh and reverse estuaries can be calculated analytically. Consider the initial configuration of Fig. 15a, where the available potential energy per unit horizontal area, for given $\delta\rho$, was calculated using equation (2.9). Once more, water masses of fixed density were assumed to move without mixing from the initial state (Fig. 15a) to the final state. This calculation gave

$$APE = \frac{gH^2}{16} \begin{cases} (\rho_1 - \rho_2) - 2\delta\rho, & \text{if } \rho_1 + \delta\rho \leq \rho_1, \rho_2 + \delta\rho \leq \rho_1; \\ -\delta\rho, & \text{if } \rho_1 + \delta\rho \leq \rho_1 \leq \rho_2 + \delta\rho \leq \rho_2; \\ \frac{17}{6}\delta\rho, & \text{if } \rho_1 \leq \rho_1 + \delta\rho \leq \rho_2 \leq \rho_2 + \delta\rho; \\ 2(\rho_1 - \rho_2) - \frac{29}{6}\delta\rho, & \text{if } \rho_1 + \delta\rho \geq \rho_2, \rho_2 + \delta\rho \geq \rho_2. \end{cases} \quad (2.11)$$

The available potential energy per unit area (2.11), plotted as a function of $\delta\rho$ in Fig. 15b, shows that the reverse estuary ($\delta\rho > 0$) has much greater available potential

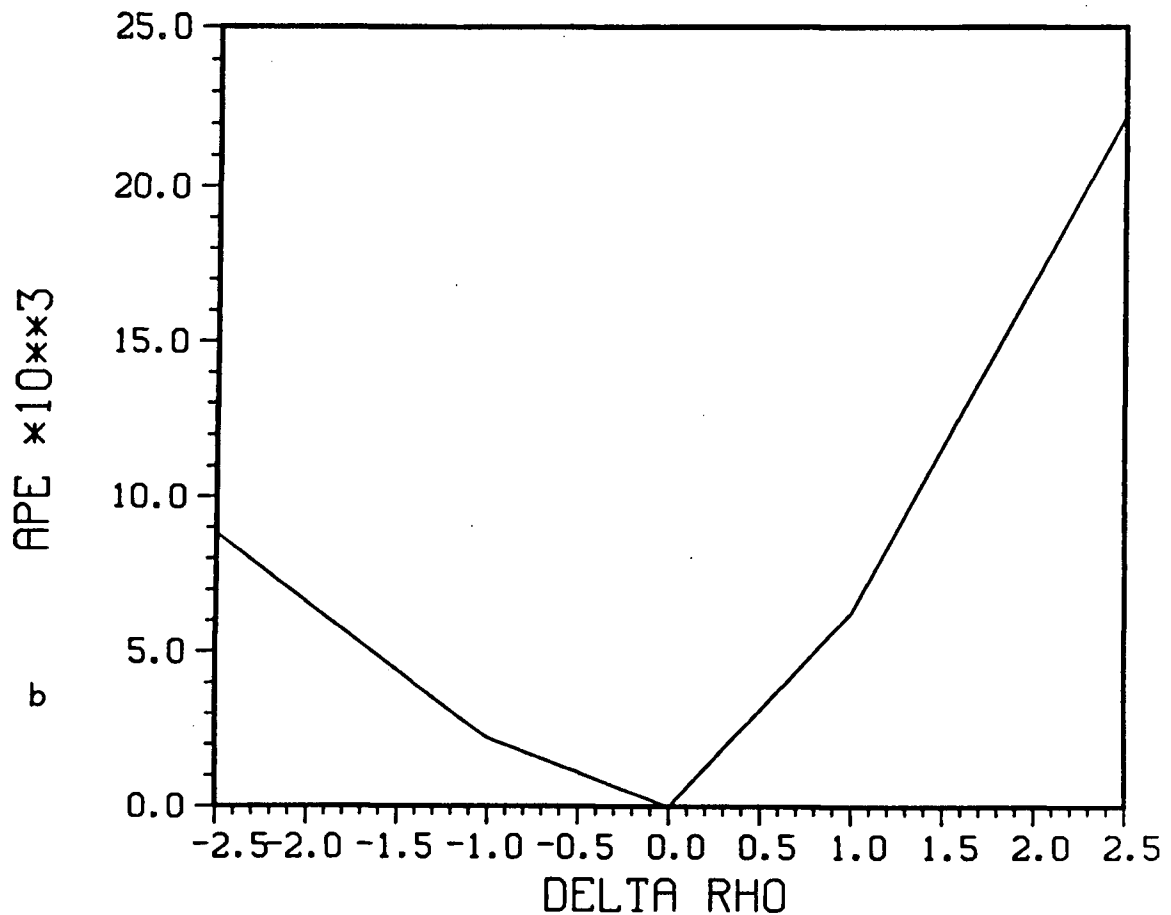
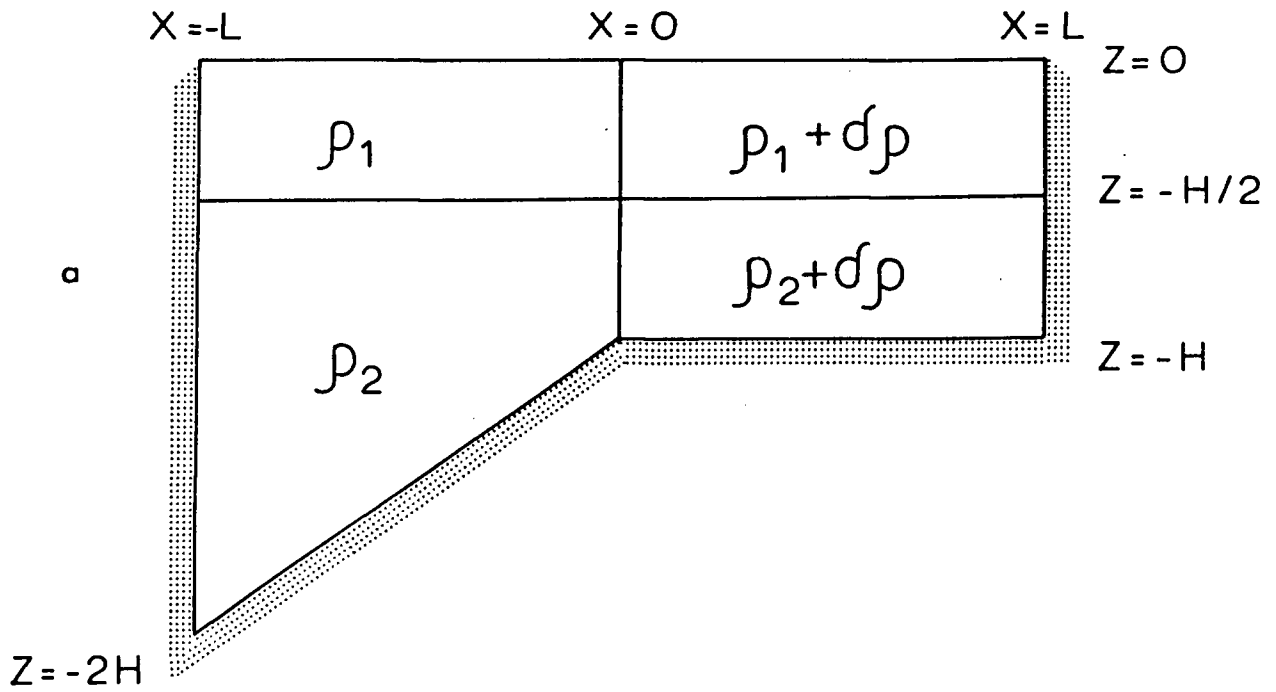


Figure 15 . (a) Simple linear slope model with $\rho_1 = 1024.0 \text{ kg m}^{-3}$, $\rho_2 = 1025.0 \text{ kg m}^{-3}$, $-2.5 \text{ kg m}^{-3} \leq \delta\rho \leq 2.5 \text{ kg m}^{-3}$ and $H = 60 \text{ m}$. (b) Available potential energy per unit horizontal area in Joules m^{-2} as a function of $\delta\rho$ (see equation 2.11).

energy than the corresponding fresh estuary ($\delta\rho < 0$) of equivalent density difference ($|\delta\rho|$). Hence, the reverse estuary cases were more energetic than the fresh estuary cases.

Figure 16 illustrates the time progression of the total kinetic energy of the model ocean for all six experiments. The initially prevalent inertial oscillations gradually diminish with time in all but the wide estuary experiment. Both experiments with the canyon have more kinetic energy than the corresponding experiments without the canyon. The *reverse estuary* with the canyon was by far the most energetic case. The dense fluid from the estuary, instead of flowing across the shelf, dropped directly into the canyon, thereby releasing considerable potential energy. The wide estuary run proved to be more energetic than the narrow estuary run due to the larger reservoir of fresh water and hence the more available potential energy. Even after ten days, inertial oscillations are prevalent in the wide estuary solution (Fig. 16).

Shelf-trapped eddies are commonly observed off the coast of British Columbia, the best documented of which is the Tully eddy (Tully, 1942; Freeland and Denman, 1982). This eddy is observed at the entrance to Juan de Fuca Strait during the summer months when runoff from the Fraser river is high, often doubling in magnitude over the period of a week in association with ice and snow melting (Tully, 1942, Fig. 2). Figure 17 shows the approximate location of this eddy in relation to the mouth of Juan de Fuca Strait.

The previous dynamic height observations found that the upper layer of the eddy moved cyclonically relative to the lower layer. Recent current meter observations during the summer of 1985 (P.C. McIntosh, personal communication, 1985) showed cyclonic circulation near the surface and a small anticyclonic circulation below. The observation that the deeper flow is anticyclonic relative to the surface flow is consistent with the mechanism proposed in this chapter, namely the inflowing lower layer compresses vertically, with an anticyclonic spinup. The cyclonic circulation at the surface is not predicted by the model. Freeland and Denman (1982) postulated that this cyclonic circulation spins up during the "spring transition", a period when the shelf edge currents reverse in direction. In winter

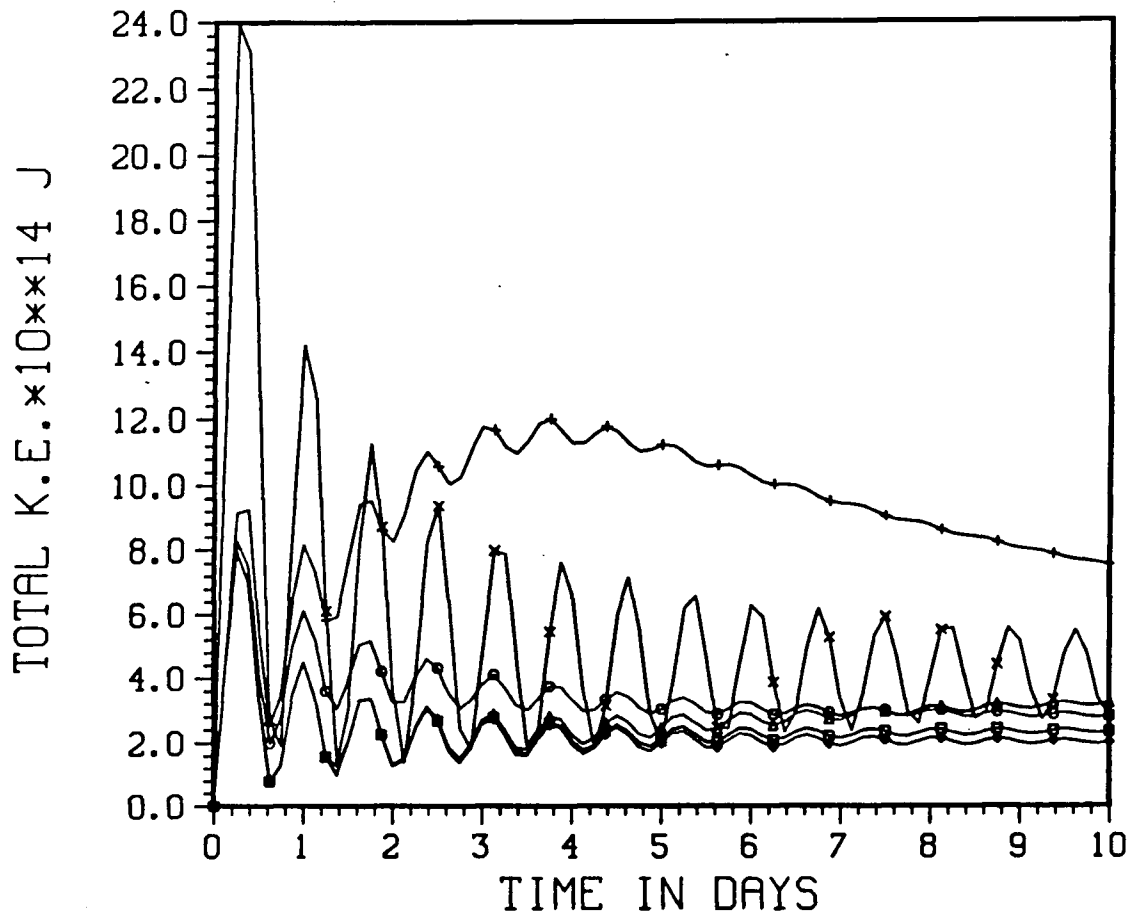


Figure 16 . Total kinetic energy (Joules) of the model ocean as a function of time: \square —Fresh estuary with no canyon. \circ —Fresh estuary with the canyon. \triangle —*Reverse estuary* with no canyon. $+$ —*Reverse estuary* with the canyon. \times —Wide fresh estuary with no canyon. \diamond —Fresh estuary with no canyon and a wide shelf.

the shelf edge currents flow northwards and in summer they flow southwards.

In the four fresh estuary experiments a strong anticyclonic circulation was found to be trapped at the shelf break. In the reverse estuary experiments this circulation was cyclonic. Since the variation in the width of the shelf and the estuary, and the inclusion of a canyon had no effect on its existence and since this type of circulation has indeed been observed in nature (eg., the Tully eddy discussed above), we conclude that the circulation is not a

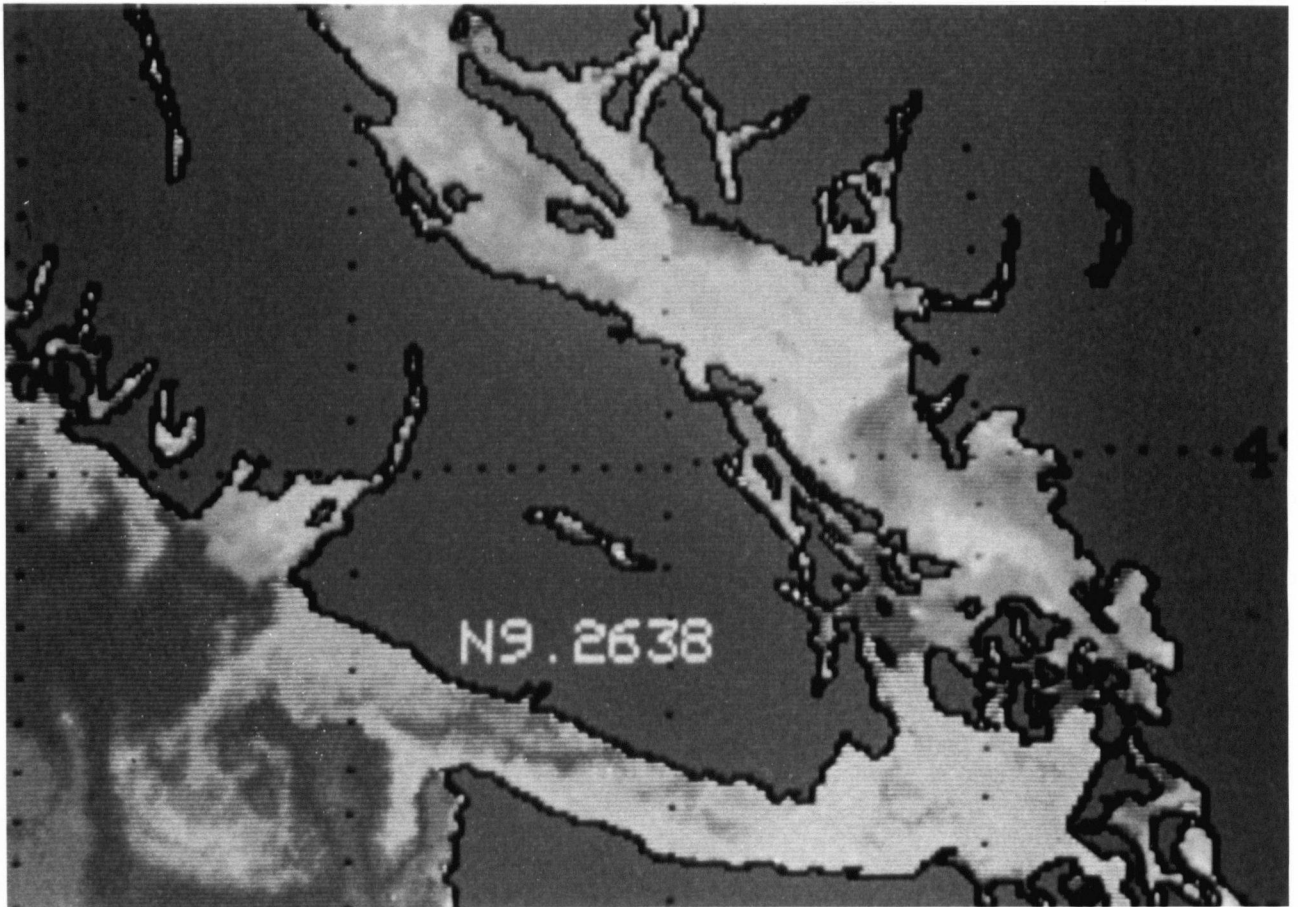


Figure 17 . Infrared satellite image of Juan de Fuca Strait region off the west coast of British Columbia, taken on June 17, 1985 at 02:57 PST (courtesy of A. Thomas, UBC Satellite Oceanography Lab). The Tully eddy is visible in the lower left corner of the diagram where the water is colder (whiter in the figure) than its surroundings.

numerical effect. The conservation of potential vorticity provides the physical mechanism for the existence of the circulation. For the fresh estuary, a column of incoming dense water widens as it vertically compresses, so that the initial fluid motion is away from the center of the column. The Coriolis force then acts on the flow and turns it to the right. Thus the column spins up anticyclonically. For the reverse estuary, a column of outgoing dense water contracts as it vertically expands, so that the initial fluid motion is towards

the center of the column. Thus the column spins up cyclonically. In all the experiments described in this chapter the circulation was trapped at the shelf break. The shelf break occurred at the mouth of the estuary for the experiments with a canyon. Physically we would expect the circulation to be trapped at this location since the incoming (outgoing) columns of fluid would compress (expand) there.

The results from the Australian Coastal Experiment (ACE), conducted from September 1983 to March 1984, indicate the presence of coastally trapped waves (CTWs) along the eastern coast of New South Wales (Freeland *et al.*, 1986). The experiment was designed to test the hypothesis of Clarke and Thompson (1984) that CTWs would be forced by the local wind stress. ACE turned out to reject this hypothesis since there was no CTW signal observed at Line 0 (Fig. 18) and since the northward propagation of CTWs from Line 1 to 2 was not modified by the winds.

Throughout the year, the water in Bass Strait is 1–3 °C colder than the surface waters of the Tasman Sea to the east, and in the southern hemisphere winter it is also 0.5–2.0 ppt more saline (Godfrey *et al.* 1980, Tomczak, 1985). Thus a *reverse estuary* configuration is set up. There are no large-scale topographic features (eg., canyons) in its vicinity. Dense Bass Strait water cascading down the continental shelf gives a possible mechanism for the generation of the CTWs which propagate along the coast of New South Wales. Using realistic topography, Weaver (1987a) numerically simulated the flow of dense Bass Strait water onto the continental shelf. Though CTWs were generated, the magnitude of the alongshore velocities appeared to be somewhat lower than those observed in ACE. The results of Weaver (1987a) will be discussed further in Chapter 3.

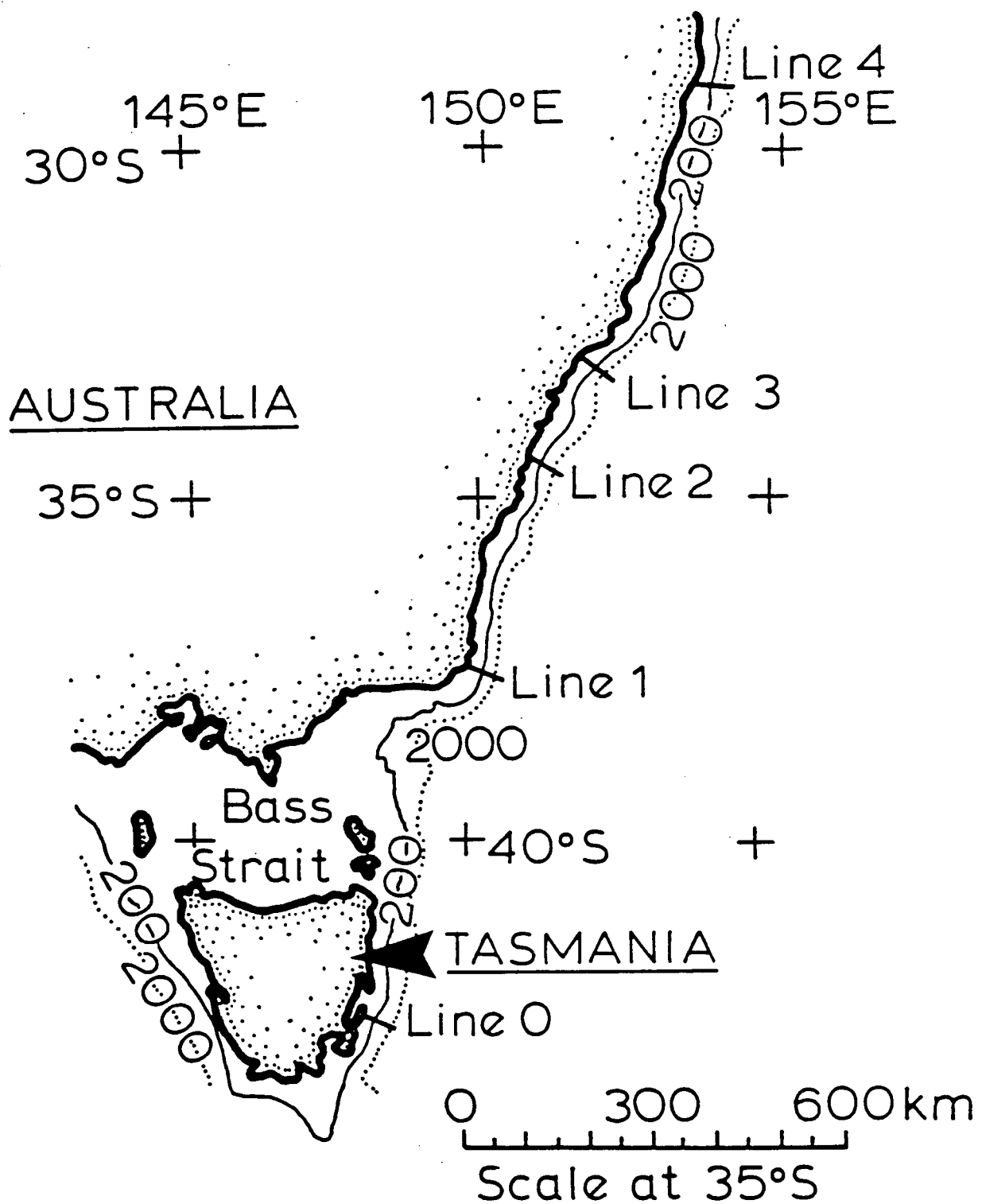


Figure 18 . Map of Southeastern Australia indicating the five lines of current meter moorings used in the Australian Coastal Experiment (redrawn from Freeland *et al.*, 1985).

3. Bass Strait as a Reverse Estuary Source for Coastally Trapped Waves

3.1 Introduction

Bass Strait is about 250 km wide and has an average depth of 60 m. Throughout the year, the water in Bass Strait is 1–3 °C colder than the surface waters of the Tasman Sea to the east, and in the southern hemisphere winter it is also 0.5–2.0 ppt more saline (Godfrey *et al.*, 1980, Tomczak, 1985, Gibbs *et al.*, 1986). Hence, a *reverse estuary* configuration is set up. It is well known that in the southern hemisphere winter the dense Bass Strait water flows down the eastern continental shelf to as deep as 400 m below the surface (Boland, 1971, Tomczak, 1985), producing a narrow northward flow along the shelf edge. Godfrey *et al.* (1980) called this the Bass Strait winter cascade.

Weaver and Hsieh (1987) modelled the *reverse estuary* as a particular example of a coastal buoyancy source. They found that coastally trapped waves (CTWs) were generated, when the dense water was allowed to flow onto a continental shelf. They alluded to the possible application to the Australian Coastal Experiment (ACE). Buchwald and Kachoyan (1987) also examined the generation of coastally trapped waves by coastal flux using a barotropic model with an exponentially decaying shelf profile. They found that second and third modes tended to dominate the northward travelling waves when data for the Bass Strait region were used. This result was consistent with the observations of ACE (discussed below). A further consequence of their solution was the presence of a barotropic jet flowing into the Tasman Sea.

The results from ACE, conducted from September 1983 to March 1984, indicate the presence of coastally trapped waves along the eastern coast of New South Wales (Freeland *et al.*, 1986, Church *et al.*, 1986a,b). Based on the work of Clarke and Thompson (1984), Freeland *et al.* (1986) expected to observe coastally trapped waves forced by the local wind stress. On this assumption they further expected to see little or no signal at Line 1 (Fig. 18) but at more northerly lines, the northward propagation of alongshore currents at

(350–450) km/day (the phase speed of a first mode wave).

The experiment turned out to reject the above hypothesis. A large coastally trapped wave signal was observed at Line 1 and Freeland *et al.* (1986) wrote, “The significant result from these calculations is the clear indication that the CTW signal appears to propagate from Line 1 to 2 with little modification by the winds.”. There was, however, no CTW signal observed at Hobart (Line 0), (Fig. 18). From a modal decomposition of the energy flux through a vertical section across Line 1, Freeland *et al.* (1986) found the first three coastally trapped wave modes contributed, 30.5%, 49.0% and 20.5% respectively, to the total energy flux.

To examine how the *reverse estuary* and the subsequent flow of dense water down the continental shelf can force coastally trapped waves, the Rossby adjustment problem is considered (Gill, 1982). At time $t = 0$, a vertical dam separating dense Bass Strait water and fresher Tasman Sea water is removed, and the two water masses are allowed to interact without external forcing. The Rossby adjustment problem therefore gives a good sense of the time development of the response from an initial rest state.

The outline of this chapter is as follows: Section 3.2 describes the model used. In Section 3.3 the results of the model are presented and in Section 3.4 these results are compared to field observations and to ACE.

3.2 Description of the Model

The geostrophic adjustment process was investigated using the Cox (1984) version of the GFDL Bryan-Cox primitive equation model, with five vertical levels as in Chapter 2. Variable grid spacing was used to focus on the region near the eastern mouth of Bass Strait where a 12.5 km by 15 km grid was incorporated. The grid spacing in the north-south direction was increased monotonically to a maximum of 100 km at the northern solid boundary, and to 75 km at the southern solid boundary. In the east-west direction the grid size was increased to a maximum of 50 km at the eastern and western solid boundaries. A no-slip boundary condition was used on all the solid boundaries. The initial configuration,

with dense Bass Strait water separated from the less dense Tasman Sea water, was relaxed without external forcing for ten days with a time step of 15 min. The lateral eddy viscosity and diffusivity were set at $1.0 \times 10^3 \text{ m}^2\text{s}^{-1}$ and $4.0 \times 10^2 \text{ m}^2\text{s}^{-1}$, respectively, while the vertical viscosity and diffusivity were both set at $1.0 \times 10^{-4} \text{ m}^2\text{s}^{-1}$.

Figure 19 illustrates the horizontal geometry of the model region. The southern boundaries of Bass Strait and the Tasman Sea are at 41° S and 43.5° S , respectively. The topography at each u , v grid point is depicted in Fig. 20, with the integers corresponding to the number of vertical levels at each grid point. The depth of each level is given in Fig. 21.

Initial temperature and salinity data, typical of southern hemisphere winter conditions, were taken from Edwards (1979) and Tomczak (1985) for the upper three layers, and from Levitus (1982) for the lower two layers. The data were chosen to represent winter conditions since the Bass Strait/Tasman Sea front is most pronounced in this season (Tomczak, 1985, Gibbs *et al.*, 1986), and thus the adjustment process is most dynamic at this time. These data are illustrated in Fig. 21 for both the Bass Strait and the Tasman Sea regions. The vertical dam which initially separated the Bass Strait and Tasman Sea water is indicated in Fig. 20.

3.3 Model Results

The transport streamfunction ψ is defined by

$$\psi_y = - \int_{-h}^0 u dz, \quad \psi_x = \int_{-h}^0 v dz, \quad (3.1)$$

where h is the depth and u and v , the eastward and northward velocity components respectively as in (2.1). Fig. 22 shows the ψ field at days 1, 5, and 10, while Fig. 23, a space-time contour plot, reveals the temporal variations of ψ along a north-south section located 60 km off the model coast of New South Wales (125 km off the coast of Tasmania).

The presence of coastally trapped waves propagating northward along the model coast of New South Wales is evident in Figs. 22, 23. The first coastally trapped wave mode is manifested in the 0.001, 0.003, and 0.01 contours of Fig. 23, which show northward

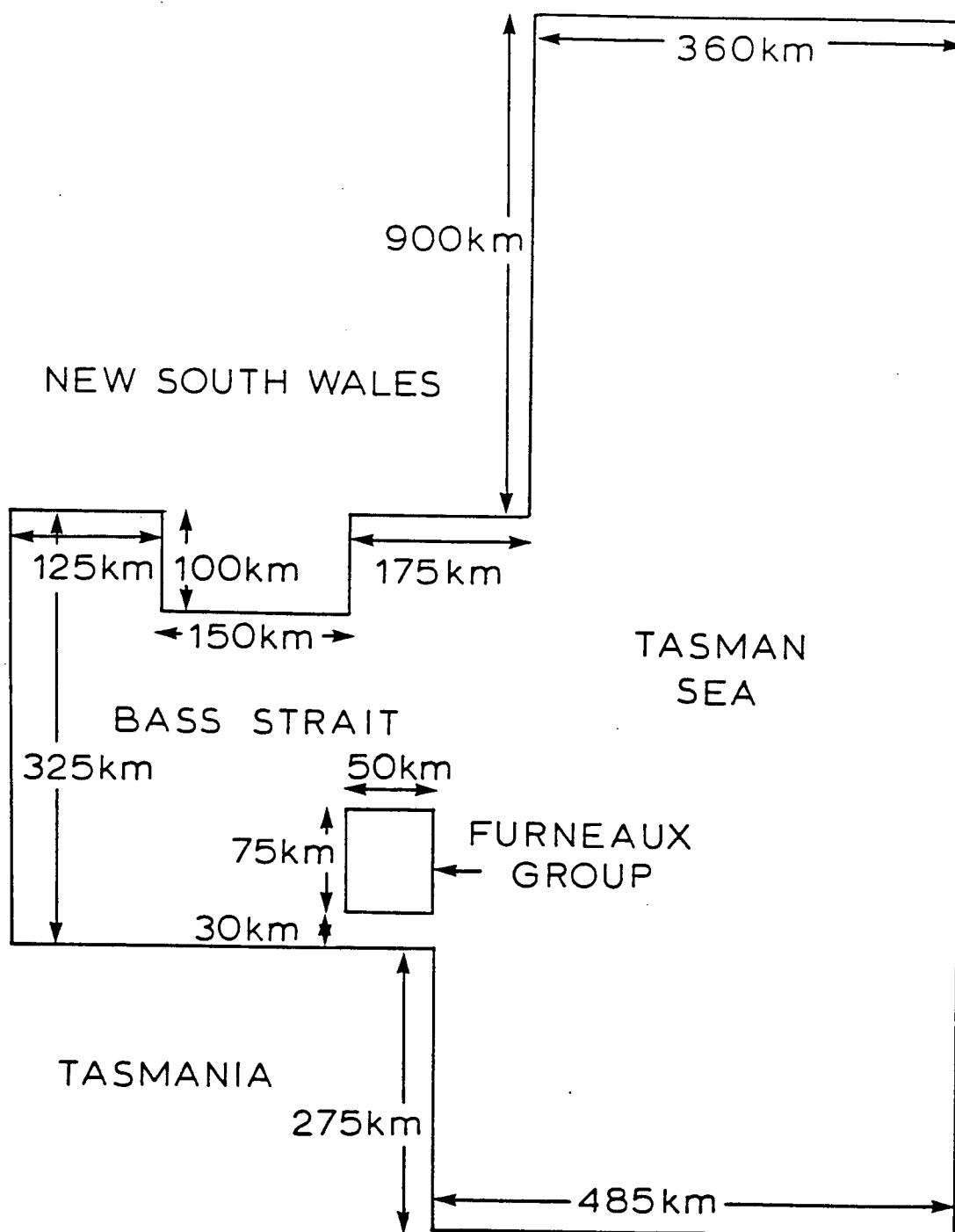


Figure 19 . Schematic diagram of the model region and the dimensions used.

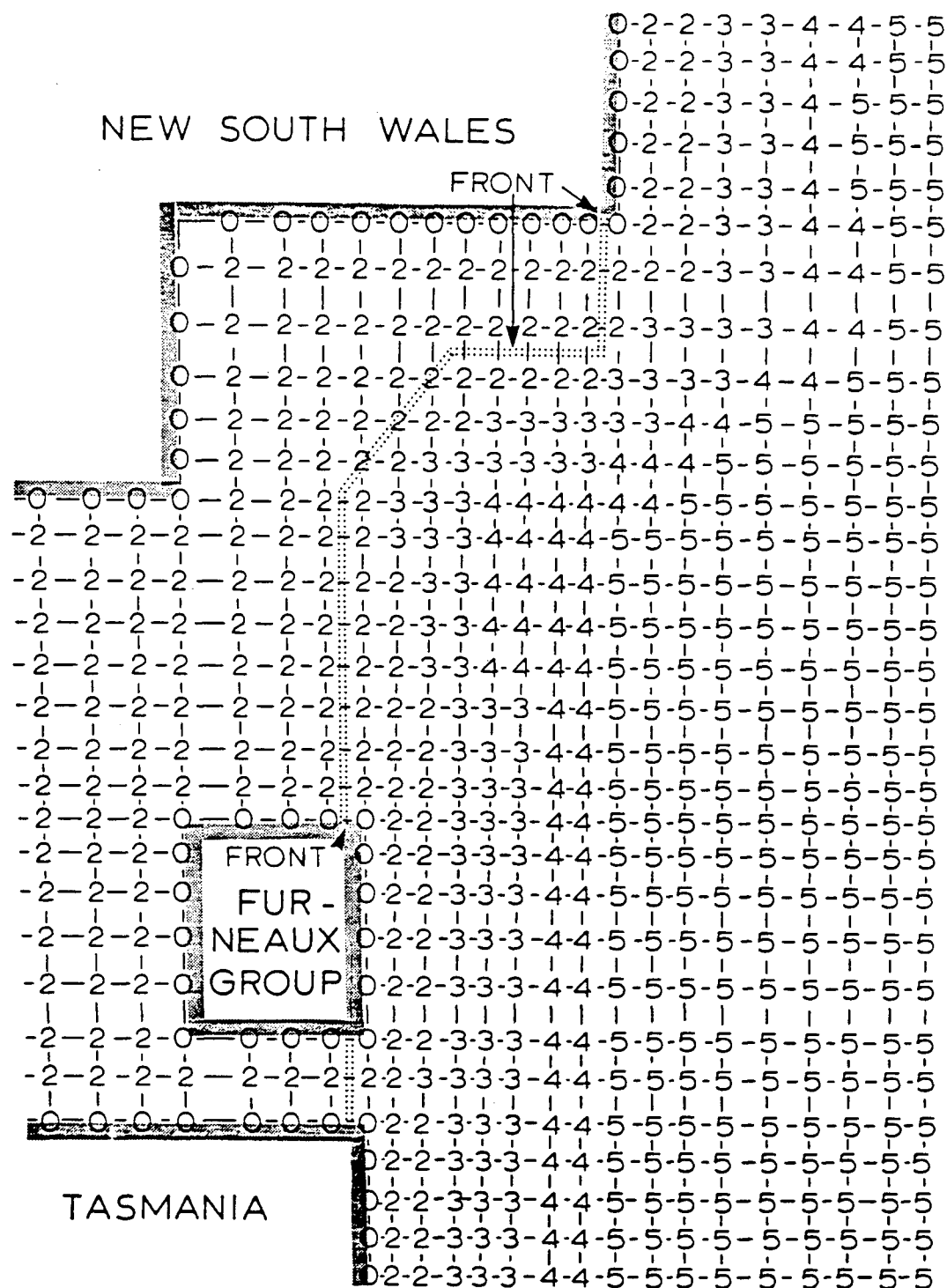


Figure 20 . Topography at each u,v grid point near the mouth of Bass Strait. The integers correspond to the number of vertical levels used at each particular grid point (see Fig. 21 for the depth of each level). In Bass Strait two vertical levels (60 m) were used at all grid points. The shelf slope remained uniform up to the northern and southern boundaries and five vertical levels were used in the deep ocean region up to the eastern boundary. The initial density front is indicated by a double dotted line.

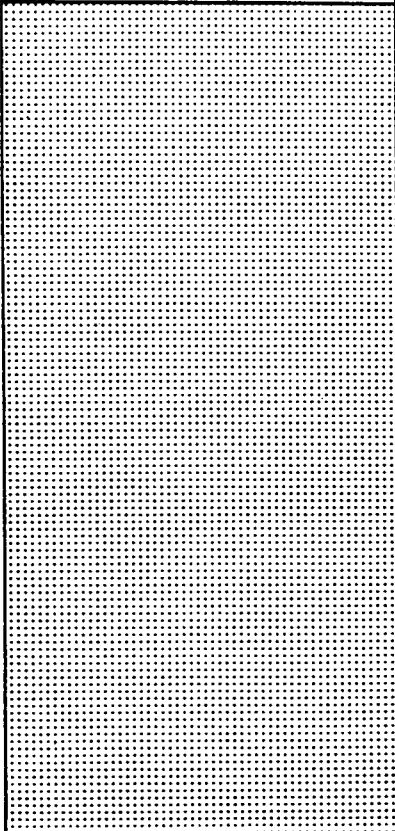
BASS STRAIT	TASMAN SEA	
T=13.0° S=35.6‰	T=16.0° S=35.0‰	0 m
T=12.0° S=35.8‰	T=15.0° S=35.0‰	30m
	T=11.0° S=35.4‰	60m
	T= 6.5° S=34.6‰	120m
	T= 2.2° S=34.7‰	1500m
		4000m

Figure 21 . The initial temperature and salinity data used at each vertical level for both the Bass Strait and Tasman Sea water masses. The depth of each level is also given.

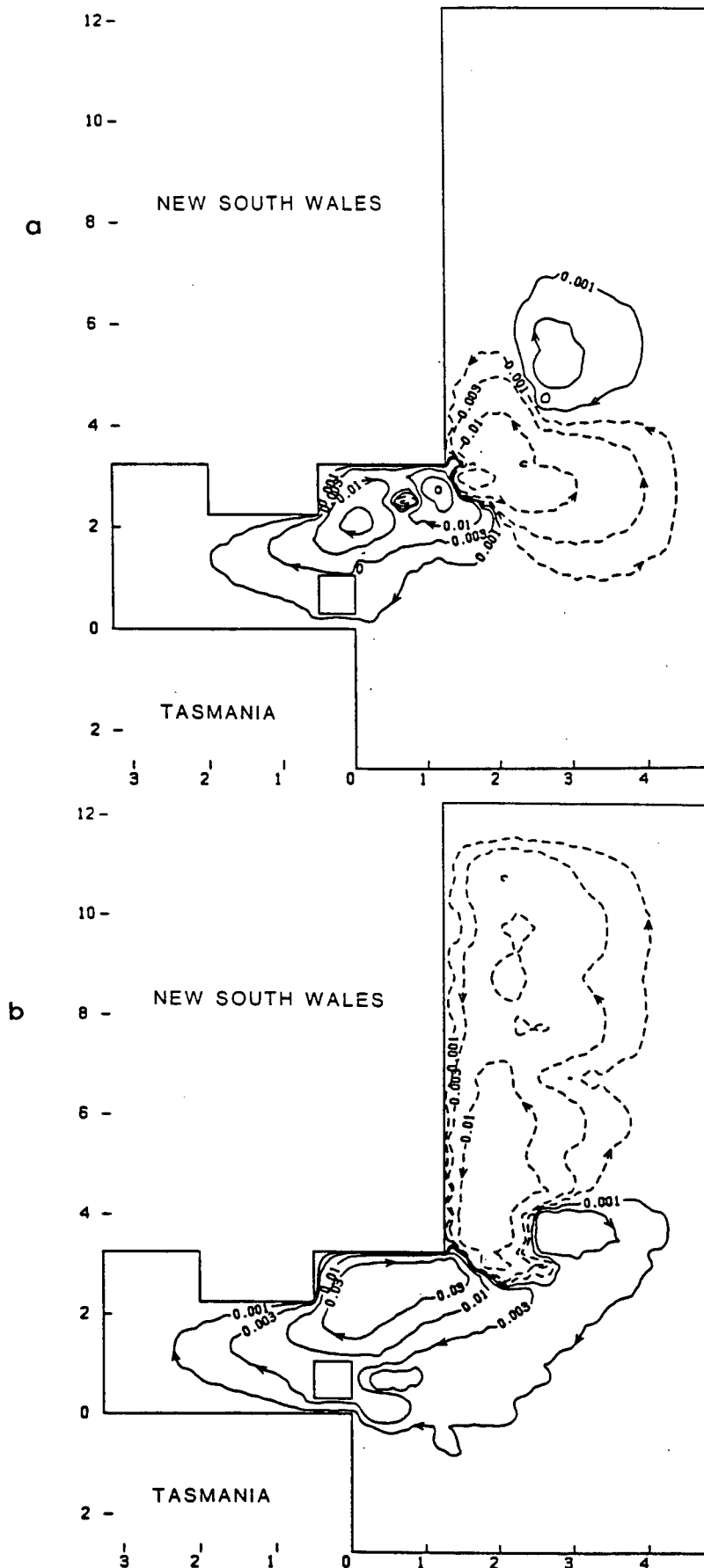


Figure 22 . Transport streamfunction ψ ($10^6 \text{ m}^3 \text{ s}^{-1}$) at, (a) $t = 1$ day, (b) $t = 5$ days, (c) $t = 10$ days. The vertical and horizontal axes are in 10^2 km .

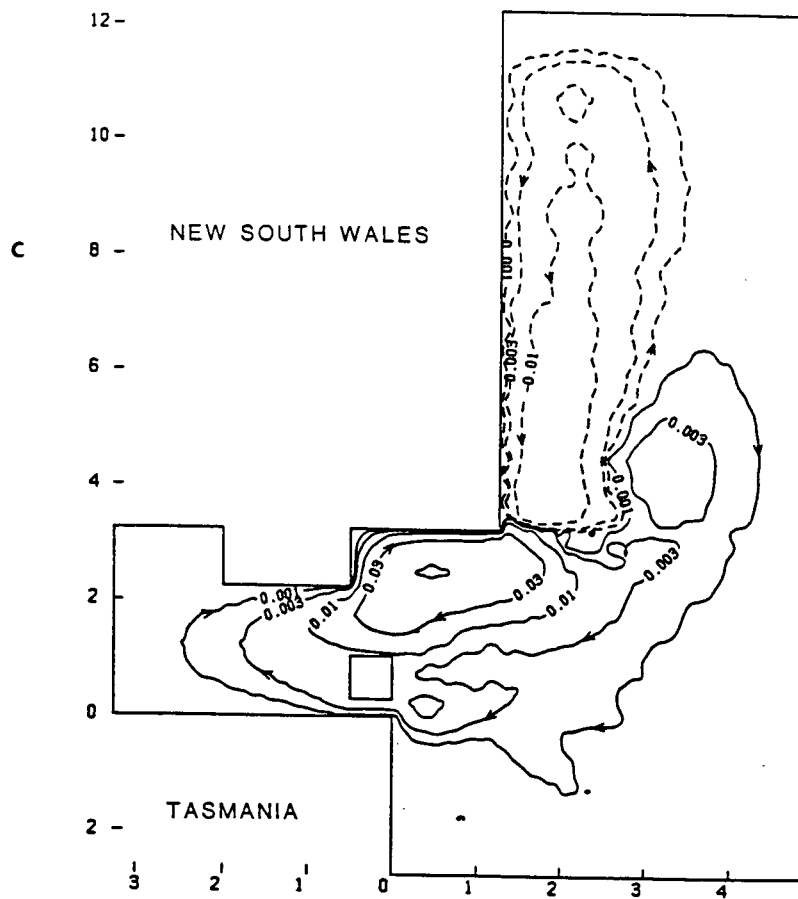


Figure 22 cont.

propagation with $c \sim 700$ km/day. It is of interest to note that at the northeastern entrance to Bass Strait a large cyclonic circulation develops (Fig. 22a). This strong barotropic circulation intensifies and broadens with time (Figs. 22b,c).

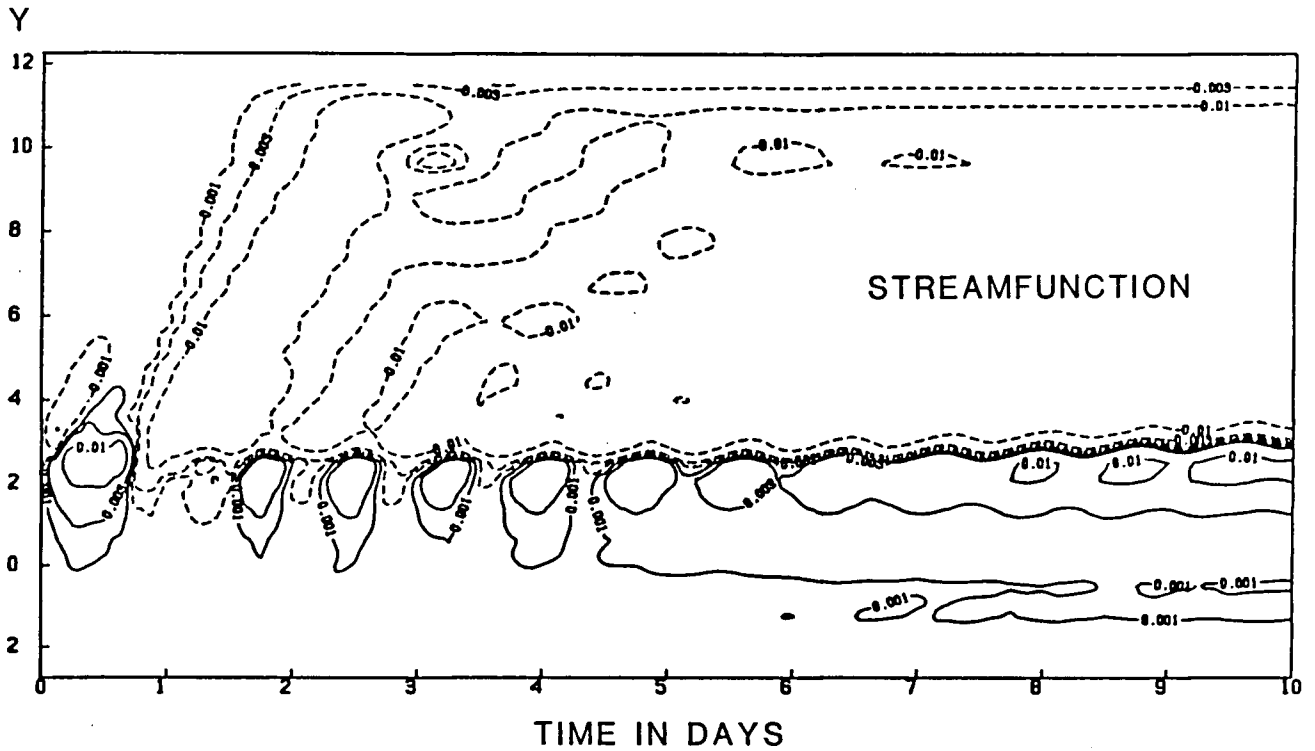


Figure 23 . Space-time plot of transport streamfunction ψ ($10^6 \text{ m}^3\text{s}^{-1}$), along a north-south section 60 km offshore. The top of the graph is the northern boundary and the vertical axis is in 10^2 km.

Weaver and Hsieh (1987) found that for a midlatitude estuary with uniform offshore slope (ie., $h = h(x)$), a barotropic circulation developed near the mouth of the estuary intensifying and extending offshore with time. This feature is also observed in our model. Due to the width of Bass Strait and since $h = h(x, y)$, it is not as apparent as in the aforementioned work. The presence of the solid wall on the eastern boundary of the Tasman Sea in our model (see Fig. 19) has the effect of bending this circulation northwards (Fig. 22c, cf., Fig. 22a,b). The model of Buchwald and Kachoyan (1987) predicted a barotropic jet

flowing into the Tasman Sea, which is consistent with the above discussion, although their jet extended out to infinity as their domain was unbounded.

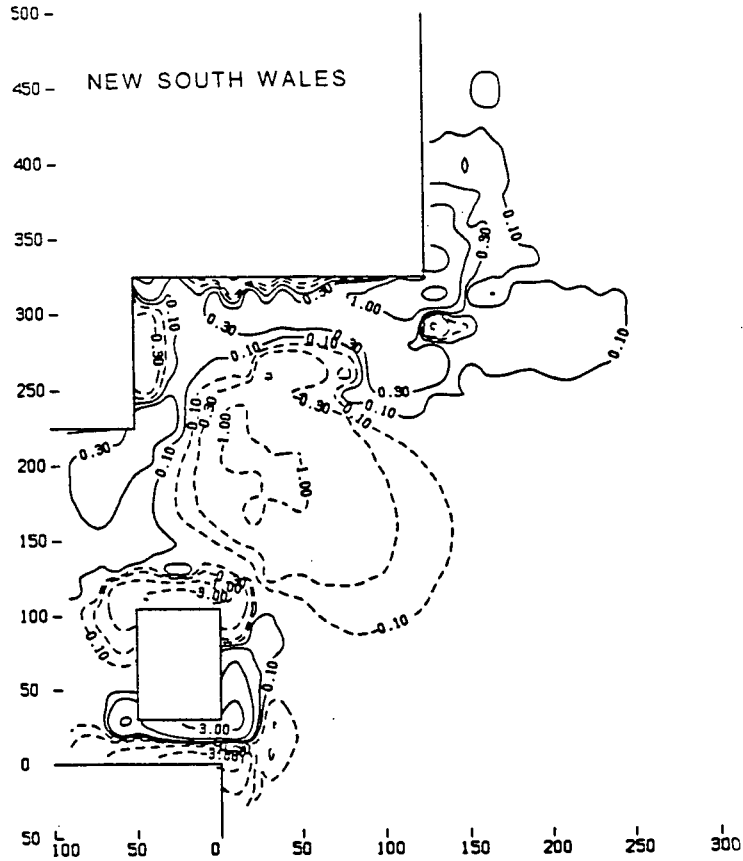


Figure 24 . Vertical velocity w (10^{-3} cm/s; positive values correspond to upwelling) at the interface between the first two levels ($z = 30$ m) at $t = 10$ days. The vertical and horizontal axes are in km.

In Section 2.7 we derived a wave equation for barotropic motion, with the forcing term on the right hand side arising from the JEBAR (see equation 2.5). As in Section 2.7 f is assumed constant so that (2.5) may be written as

$$\begin{aligned} \{\psi_{yyt} + \psi_{xxt}\} - \frac{1}{h} \{h_y \psi_y + h_x \psi_x\}_t - \frac{f}{h} \{h_y \psi_x - h_x \psi_y\} \\ = \left[\frac{g}{\rho_0 h} \int_{-h}^0 \int_z^0 \rho_x dz' dz \right]_y - \left[\frac{g}{\rho_0 h} \int_{-h}^0 \int_z^0 \rho_y dz' dz \right]_x. \end{aligned} \quad (3.2)$$

In the southern region of Bass Strait $h = h(x)$ and initially $\rho = \rho(x, z)$ (Fig. 20), so that the forcing term in (3.2) vanishes. In the northern region of Bass Strait, however,

$h = h(x, y)$ and $\rho = \rho(x, y, z)$ (Fig. 20) so the JEBAR term produces a strong barotropic circulation, with the emission of coastally trapped wave fronts as in Hsieh and Gill (1984) and Weaver and Hsieh (1987). Thus, it appears that the coastally trapped waves observed in Figs. 22, 23 propagating northward along the east coast of New South Wales, are generated by dense Bass Strait water flowing over changing bottom topography, at the northeastern entrance to Bass Strait.

The vertical velocity field at 30 m depth is illustrated in Fig. 24 at $t = 10$ days. Along the south and east coasts of New South Wales and along the east coast of the Furneaux Island Group, coastally trapped wavelike disturbances are evident. Two first mode baroclinic Kelvin waves were generated by the adjustment process and are seen to propagate along the northern coasts of Tasmania and the Furneaux Group. At the northeastern entrance to Bass Strait intense downwelling is observed. This is associated with dense Bass Strait water flowing down the continental shelf under the less dense Tasman Sea water.

The net velocity field is depicted in Figs. 25a-c. The quasi-barotropic flow established after the passage of the coastally trapped waves is visible in the upper layer (Fig. 25a), and second layer (Fig. 25b), along the south and east coasts of New South Wales. The baroclinic motion associated with the passage of the two Kelvin wave fronts along the northern coasts of Tasmania and the Furneaux Island Group, is evident in these figures, as is the baroclinic flow in the neighbourhood of the initial density front (Fig. 20). The intense cyclonic circulation seen in Fig. 22, at the northeastern entrance to Bass Strait, is also visible in Figs. 25a-c. This is consistent with the conservation of potential vorticity, where a column of dense Bass Strait water flowing eastward into the Tasman Sea, vertically expands over deepening topography and spins up in a cyclonic sense. A weaker cyclonic circulation is also observed at the southern entrance to Bass Strait (between Tasmania and the Furneaux Group), trapped against the shelf break. Both these cyclonic eddies and their generation are similar to those observed and discussed by Weaver and Hsieh (1987)

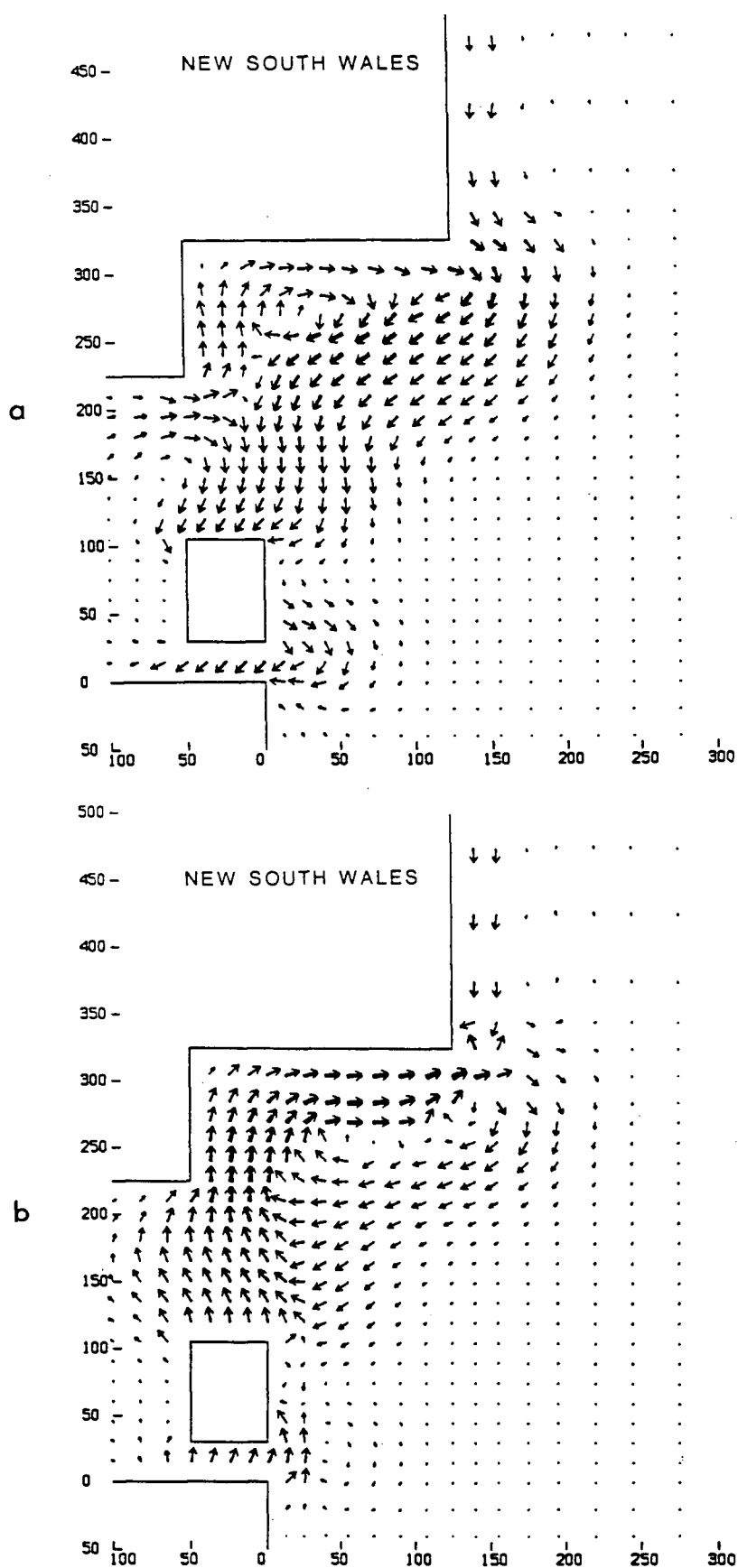


Figure 25 . Horizontal velocity field at $t = 10$ days, (a) upper level ($z = 15$ m), (b) second level ($z = 45$ m), (c) third level ($z = 90$ m). The magnitude of the velocity is proportional to the thickness and length of the vector (ie., once the vector has a magnitude of 1 cm/s it gets wider).

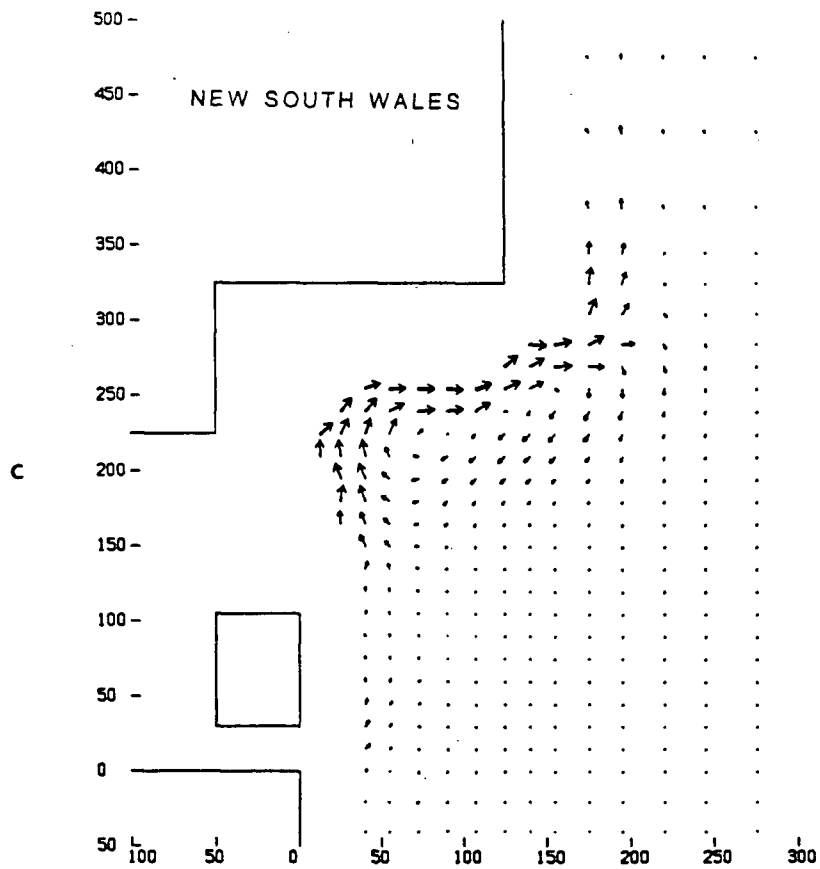


Figure 25 cont.

and described in Chapter 2. The flow field in the third layer ($z = 90$ m) indicates the presence of a narrow northward flow along the slope (Fig. 25c), which is most intense in the neighbourhood of the initial front.

Figure 26 illustrates the time progression of the alongshore velocity v (cm/sec) along a section 30 km off the east coast of New South Wales. The northward propagation of coastally trapped waves (0.1 cm/s and 0.3 cm/s contours) is once more evident in Fig. 26.

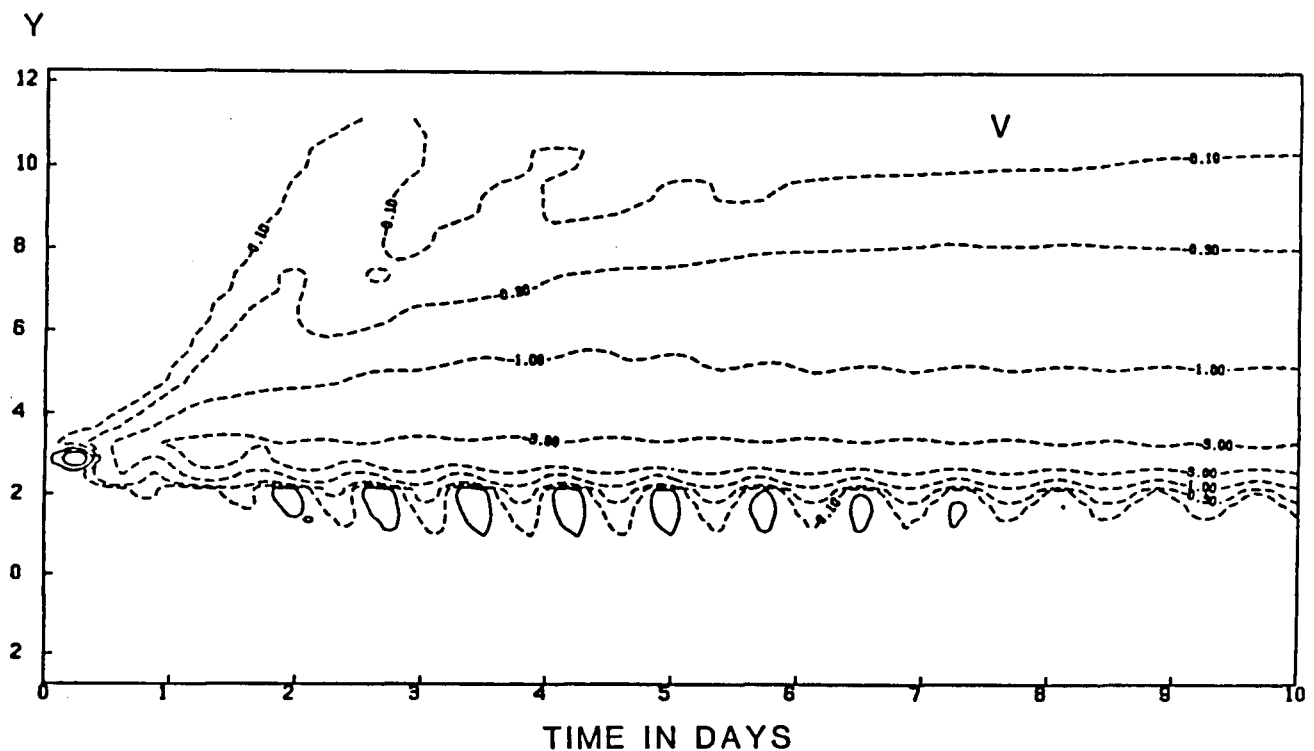


Figure 26 . Space-time plot of the longshore velocity v (cm/s), along a north-south section 30 km offshore. The top of the graph is the northern boundary and the vertical axis is in 10^2 km.

3.4 Comparison with Observations

As mentioned in Section 3.2 the data used in the model corresponded to winter conditions in the Bass Strait region, since the response is most dynamic in this season. The

model results are in good agreement with the observations of the winter cascade described in Godfrey *et al.* (1980), Tomczak (1985) and Gibbs *et al.* (1986), in that the dense Bass Strait water flows into the Tasman Sea and flows along the slope as a narrow northward stream (Fig. 25c). In addition, the adjustment process generates coastally trapped wave fronts which propagate along the New South Wales coast.

The Rossby adjustment problem yields coastally trapped waves as a transient phenomenon. If one argues that the Bass Strait/Tasman Sea front is intermittently off balance, so that repeated adjustment occurs, then continuous coastally trapped wave activity would occur. This idea is similar to that of Buchwald and Kachoyan (1987), who considered Bass Strait as an oscillating coastal source.

The results of the Australian Coastal Experiment, conducted from September 1983 to March 1984, indicated the presence of coastally trapped waves (CTWs) along the east coast of New South Wales. Freeland *et al.* (1986) observed that the energy at Lines 2 and 3 (Fig. 18) largely arose from the northward propagation of free waves from Line 1, where the CTW energy was already large. They rejected the hypothesis of Clarke and Thompson (1984) that the CTWs would be generated by local wind stress forcing with little energy at Line 1. On the basis of energy arguments they further showed that wind forcing over Bass Strait could possibly generate the observed CTWs. They rejected the idea that CTWs, generated in the Great Australian Bight, travelled around Tasmania and up the coast, since there was virtually no signal at Line 0 (Fig. 18). Finally, they considered the possibility that the wind stress over the ocean east of Bass Strait could generate the observed CTWs. Although they found insufficient available energy in their calculations, they concluded that the wind stress over the ocean east of Bass Strait was a possible source for the CTWs. This conclusion they based on high correlations (0.68) between "predicted" and observed currents at inshore sites.

In the summer the front between Bass Strait and the Tasman Sea is not as pronounced as in the winter. The work of Gibbs *et al.* (1986) does show a distinct difference in tem-

perature between Bass Strait water and the surface waters of the Tasman Sea in January 1980 (their Fig. 3). There appears to be no published data available during the period that ACE was conducted. The results of this chapter are, however, consistent with the observations of ACE. In particular, the observation that there was no signal at Line 0 and a large signal at Line 1 is consistent with the results of the model (Fig. 22). Similarly, CTW energy at more northward locations would largely arise from the northward propagation of free waves from Line 1 (Fig. 23).

Due to the large viscosities and finite grid spacing in the model, it is difficult to make a comparison with observed and predicted phase speeds. Similarly, a modal decomposition of the alongshore velocities at northerly cross-sections is difficult. The propagation speed of the quasibarotropic first mode is seen to be about 700 km/day (Fig. 23), compared to the observed phase speeds of about 450 km/day (Freeland *et al.*, 1986). The shelf topography used in the model was chosen to typify the New South Wales coast. The shelf width has a profound effect on the phase speed of the first coastally trapped wave mode. A slightly narrower shelf would decrease the phase speed of the first mode (Weaver and Hsieh, 1987; see also Section 2.6) and hence may account for the discrepancy between observed and predicted phase speeds. The initial temperature and salinity data would have comparatively little effect on this phase speed although it would affect the phase speeds of the higher modes. It is, however, impossible to compute the phase speeds of the higher modes in Fig. 23.

Velocity fluctuations observed in ACE were as high as 40 cm/s. The contamination of the “eddy mode” of Church *et al.* (1986a) accounted for 35% of the observed variance in the alongshore currents on the shelf and slope at Line 1 (Fig. 1), 60% at Line 2, and 76% at Line 3. In the results of this numerical model, alongshore velocities of up to 3 cm/sec (rather smaller than those observed in ACE even after the removal of the “eddy mode”), propagated northward (Fig. 26). The shelf width also has a profound effect on the energy in the first quasibarotropic mode. Narrowing the shelf width would have the

effect of increasing the energy in the first CTW mode (Weaver and Hsieh, 1987) and hence would yield velocities with larger magnitudes than those of Fig. 26. Once again, the large viscosities required for numerical stability and the finite grid spacing would also yield results with lower than expected velocities (Hsieh *et al.*, 1984).

Future work is being planned to investigate the source and mechanism for the generation of the coastally trapped waves observed in ACE. A complete understanding of this phenomenon can only be obtained if wind forcing over the Bass Strait region is incorporated into the model. It is hoped that a combination of the wind driven model of A. Clarke (personal communication at the IUGG conference, Vancouver, B.C., August 1987), the oscillating coastal buoyancy source model of Buchwald and Kachoyan (1987) and the JEBAR model of this thesis, will provide a unified forcing mechanism for the generation of the coastally trapped waves observed in ACE.

4. Statistical Relationships between Northeast Pacific Atmospheric Surface Pressure and the Sea Surface Temperature along the British Columbia Coast

4.1 Introduction

There has been a long history of investigation of the interrelationships between sea surface temperature (SST) in the North Pacific Ocean and the overlying atmospheric circulation. Early workers established that there is a clear correlation between seasonal mean SST and atmospheric sea level pressure (SLP) patterns (eg., Namias, 1959). There has been some controversy concerning the question of whether this empirical relationship results primarily from atmospheric influence on ocean circulation or from oceanic influence on the circulation of the atmosphere. On the basis of both numerical modelling studies (eg., Huang, 1978) and sophisticated statistical analyses (Davis, 1976) it is now believed that atmospheric forcing largely determines the North Pacific SST pattern.

Emery and Hamilton (1985) recently examined the connection between the winter SST in the Northeast Pacific and the coincident atmospheric surface circulation on a year by year basis. Fig. 27a shows the long term mean (1947-82) climatology of the winter (December through February) surface pressure in the North Pacific. The atmospheric circulation in this figure is dominated by the Aleutian Low. Emery and Hamilton (1985) noted that the winter SLP pattern in individual winters differed principally in the strength of this Aleutian Low. They constructed an index of the intensity of the low by taking the pressure difference between the two points (170°W , 50°N and 120°W , 40°N) marked on Figs. 27a-d. The winter mean value of this particular pressure index was found to correlate quite well with the winter mean SST anomalies at stations along the British Columbia outer coast. Winters with anomalously strong (weak) Aleutian Lows were found to have anomalously warm (cold) coastal SSTs as greater (less) warm water was advected northward from more southern waters. The correlation between the time series of winter mean index and the SSTs at individual stations averaged out to around 0.7.

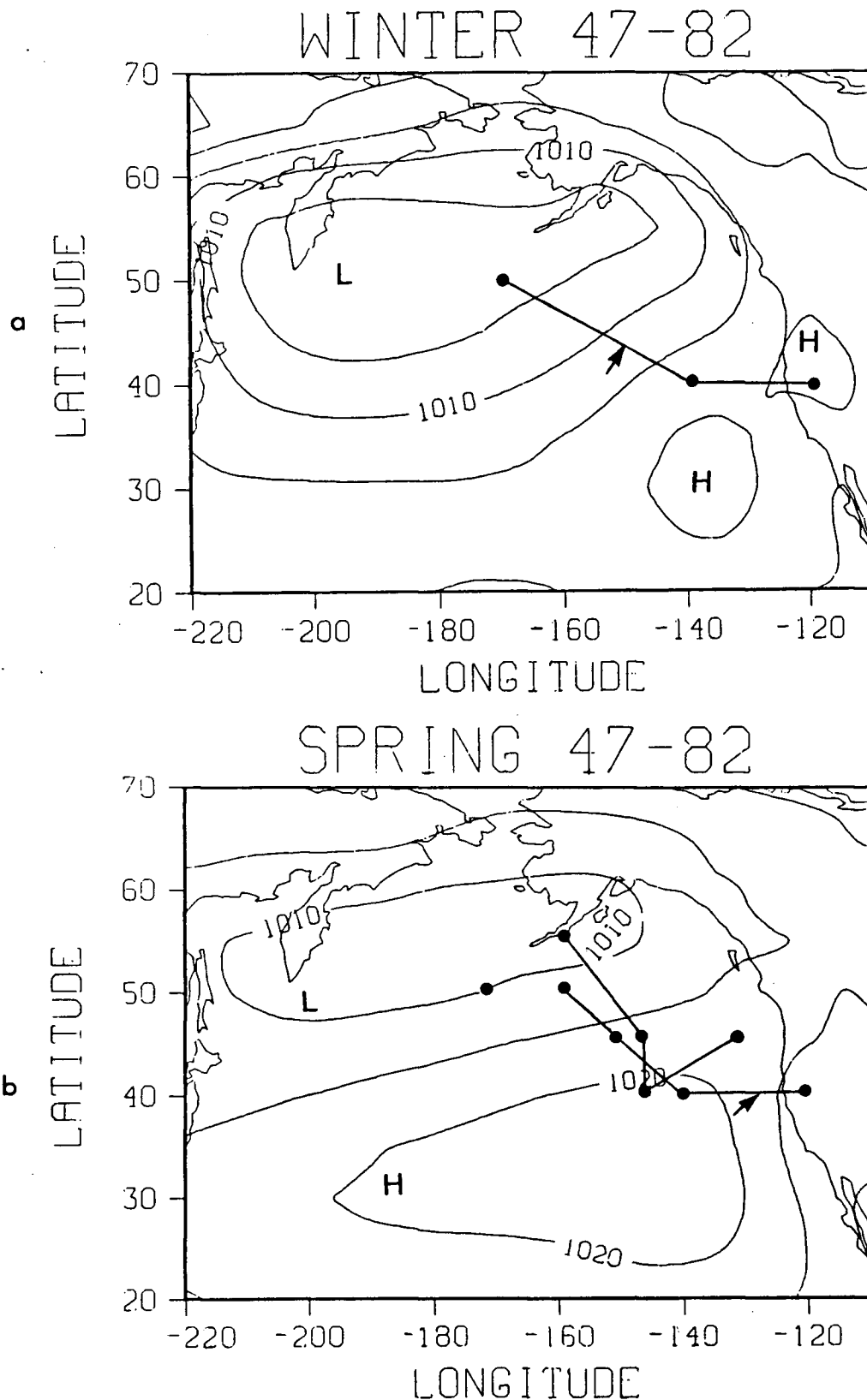


Figure 27 . Long term mean (1947-1982) climatology of the a)—winter (December, January, February); b)—spring (March, April, May); c)—summer (June, July, August); Autumn (September, October, November) surface pressure in the North Pacific (from Hamilton, 1984). The points at 170°W, 50°N, and 120°W, 40°N were used by Emery and Hamilton (1985). The arrow indicates the points used in predicting the temperature change between the indicated season and the previous season (Table 3). Contours are labelled in millibars and the contour interval is 5 mb.

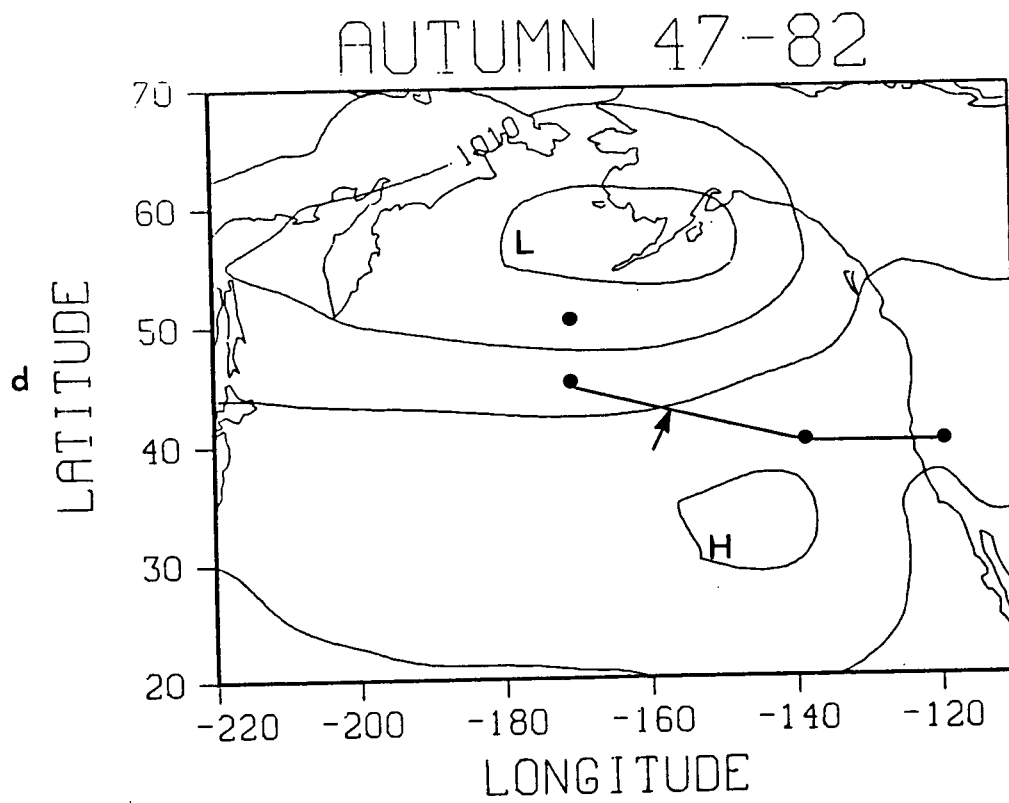
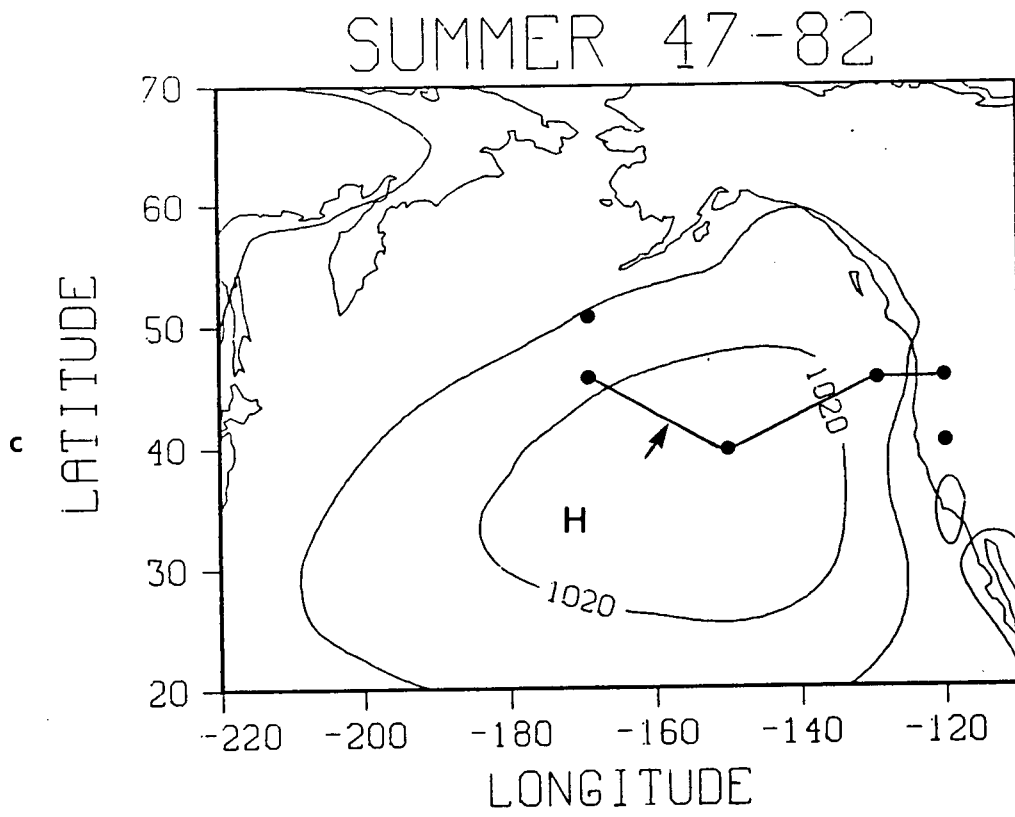


Figure 27 cont.

Weaver and Hamilton (1985) generalized the earlier work of Emery and Hamilton (1985) through the construction of atmospheric circulation indices that involved pressure data from several points in the Gulf of Alaska (see Figs. 27a-d). These indices were designed to correlate as well as possible with the time series of coastal SSTs. This exercise was undertaken in order to demonstrate the strong control of coastal SST by the regional atmospheric wind forcing, and to see how the relationship between SLP and SST changes with season. In addition, the results of their analysis are useful in that they can be used to estimate the seasonal mean SST from a knowledge of the SLP field. This feature is of considerable interest since SLP analyses for the Northeast Pacific region are available back to 1899, while SSTs along the outer coast have been measured only since 1934. Estimates of the pre-1934 SST may be of value for studies of the environmental effects on the commercial fisheries of British Columbia (eg., Mysak *et al.*, 1982, 1986 Hamilton, 1985, Mysak, 1986).

The work of Weaver and Hamilton (1985) and Weaver (1987) will be presented in this chapter. The data used in this study are described in Section 4.2 below. Section 4.3 discusses the pressure indices that were constructed and the correlation between the time series of the indices and the observed SST at different stations. Section 4.4 considers the extension of the SST time series back to the turn of the century using the relations determined between SST and the pressure indices.

4.2 Data

Observations of SST have been taken at several lighthouse stations along the British Columbia coast. In this study monthly mean SST data were employed from Langara Island in northern British Columbia and from the more southerly station on Kains Island (see Fig. 28). The monthly means were available for the period 1935–1977 at Kains Island and for 1941–1977 at Langara Island. According to Emery and Hamilton (1985), the seasonal SST anomalies along the British Columbia coast are generally representative of those in the region at least 500 km offshore.

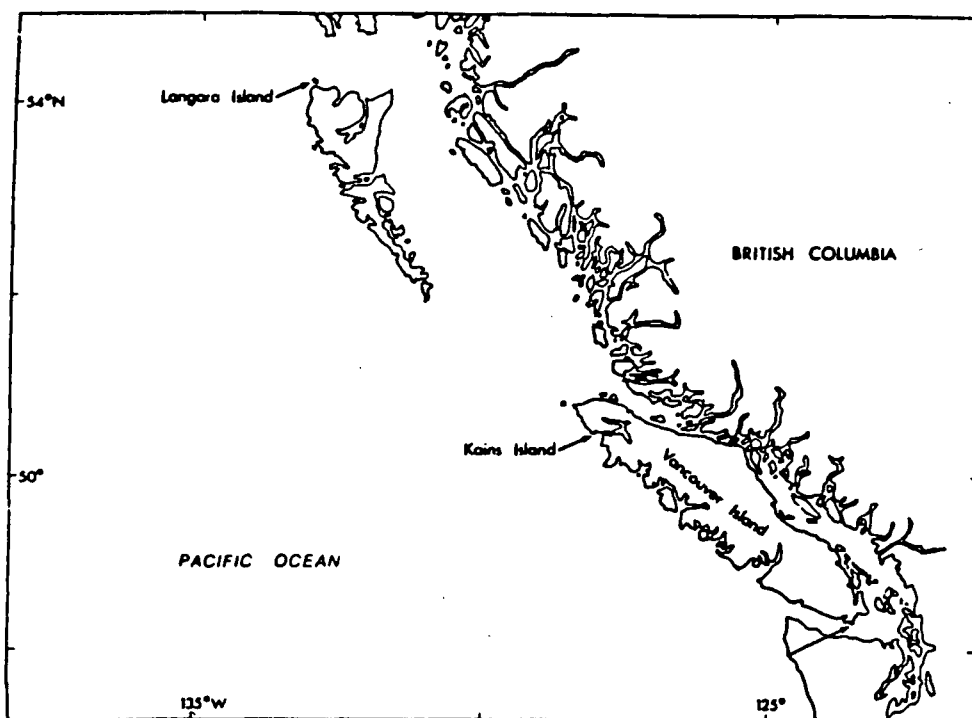


Figure 28 . Map of the western coast of British Columbia showing the two lighthouse stations at Kains Island and Langara Island.

Monthly mean SLP analyses for the region north of 15°N for the period 1899–1982 were obtained from the Data Support Section at NCAR. This data set was originally constructed at NCAR from various sources throughout the period considered (Jenne, 1975). Trenberth and Paolino (1980) reworked some of this data to eliminate spurious trends and to fill in some of the missing observations. The analyses are on a 5° by 5° latitude-longitude grid. Data were available for each month except September 1935 and December 1944 (in the analysis to be described below the SLP anomalies for these months were simply taken from adjacent months).

4.3 Analysis

The pressure indices were arrived at through least squares fits of linear combinations of grid point pressure values to the station SST time series. That is, choices were made

of a_γ and b_γ so that the following expression produced the best fit to the observed time series of SST anomalies in season n :

$$\text{Predicted SST}(n) = \sum_{\gamma} a_{\gamma} P_{\gamma}(n) + \sum_{\gamma} b_{\gamma} P_{\gamma}(n-1), \quad (4.1)$$

where the season n represents a two month period of the year (i.e., *winter* is January and February, *spring* is April and May, *summer* is July and August, and *autumn* is October and November), $n-1$ labels the two month period immediately before season n , $P_{\gamma}(n)$ is the mean pressure at the gridpoint γ over the season n . The sums in expression (4.1) were taken over three or four grid points. In a particular season, the pressure at each grid point is not independent of the pressure at other grid points (i.e., they are part of the same large-scale circulation pattern). Thus the choice of the a_γ and b_γ coefficients was constrained by the requirement that the sum of the a_γ 's and of the b_γ 's be zero. Therefore, in cases where three (four) grid points were used in the construction of the index, there are four (six) independent parameters in the linear regression (4.1).

The regression of the SST time series for each season was repeated using various combinations of grid points in expression (4.1), with the aim of finding the locations allowing the best fit to the SST data. This trial and error analysis was done using SLP data at three grid points; if an adequate fit to the temperature data could not be obtained then SLP data at four grid points were employed. The indices yielding the best fit to the observed SST data were not obtained in a completely random manner. These indices (described in Tables 1 and 3) have been plotted in Figs. 27a–d (the climatological mean SLP maps constructed for each season using the SLP data during the period December 1946 to November 1982) and connected by a solid line. Since the isobars of Figs. 27a–d tend to be perpendicular to the lines connecting the grid points, the indices give an indication of the magnitude of the flow across the lines. For example, in the winter of major North Pacific warming events, when the Aleutian low is often very intense, we get an indication of the magnitude of warm water transport (along the isobars) from the south (see Section 4.4).

Table 1 gives the optimum choices of the grid points and of the a_γ and b_γ coefficients needed for pressure indices that predict the seasonal SST anomalies. These parameters are given for both Kains Island and Langara Island. The coefficients are quoted in units of $^\circ\text{C mb}^{-1}$.

Table 1

Seasonal mean North Pacific pressure indices and corresponding least squares coefficients for each reference point (see Figs. 27a–d).

Season	Position	Kains Island a_γ	Kains Island b_γ	Langara Island a_γ	Langara Island b_γ
winter	170°W 50°N	−0.0561	−0.0096	−0.0785	−0.0048
	140°W 40°N	−0.0413	−0.0950	−0.0334	−0.0777
	120°W 40°N	0.0973	0.1046	0.1118	0.0825
spring	160°W 50°N	−0.0667	−0.0852	−0.0699	−0.1051
	150°W 45°N	0.1845	0.1383	0.1993	0.1529
	140°W 40°N	−0.1844	−0.1621	−0.1965	−0.1554
	120°W 40°N	0.0666	0.1089	0.0671	0.1075
summer	170°W 45°N	0.0728	0.0373	0.0402	0.0629
	150°W 40°N	−0.1031	−0.0174	−0.1477	−0.0842
	130°W 45°N	−0.3752	−0.1676	0.0270	−0.1372
	120°W 45°N	0.4055	0.1476	0.0806	0.1586
autumn	170°W 45°N	−0.0356	−0.0073	−0.0547	−0.0540
	140°W 40°N	−0.1007	−0.1311	−0.0751	0.0122
	120°W 40°N	0.1364	0.1384	0.1298	0.0418

Table 2 shows the correlation coefficients computed between the actual time series of seasonal SST anomalies and those predicted by (4.1) with optimal indices in Table 1. It is apparent that very high correlations can be obtained in both winter and autumn using only three grid points to define the SLP index. The correlations in spring and summer are weaker, despite the use of four grid points in the index (see Table 1). Figures 29 and 30 show comparisons of the time series of the observed and predicted seasonal SST anomalies for Kains Island and Langara Island, respectively. In these figures the predicted SST anomalies are shown by the small circles, the observations are represented by the other curve. In order to avoid clutter, the predicted values in Figs. 29 and 30 have all been

displaced downward by one degree.

Table 2

Correlation coefficients r between the seasonal mean predicted SST anomalies, obtained from the pressure indices defined in Table 1, and the observed seasonal mean temperature anomalies. Correlation coefficients were calculated at Kains Island for the period 1935 to 1977 and at Langara Island for the period 1941 to 1977.

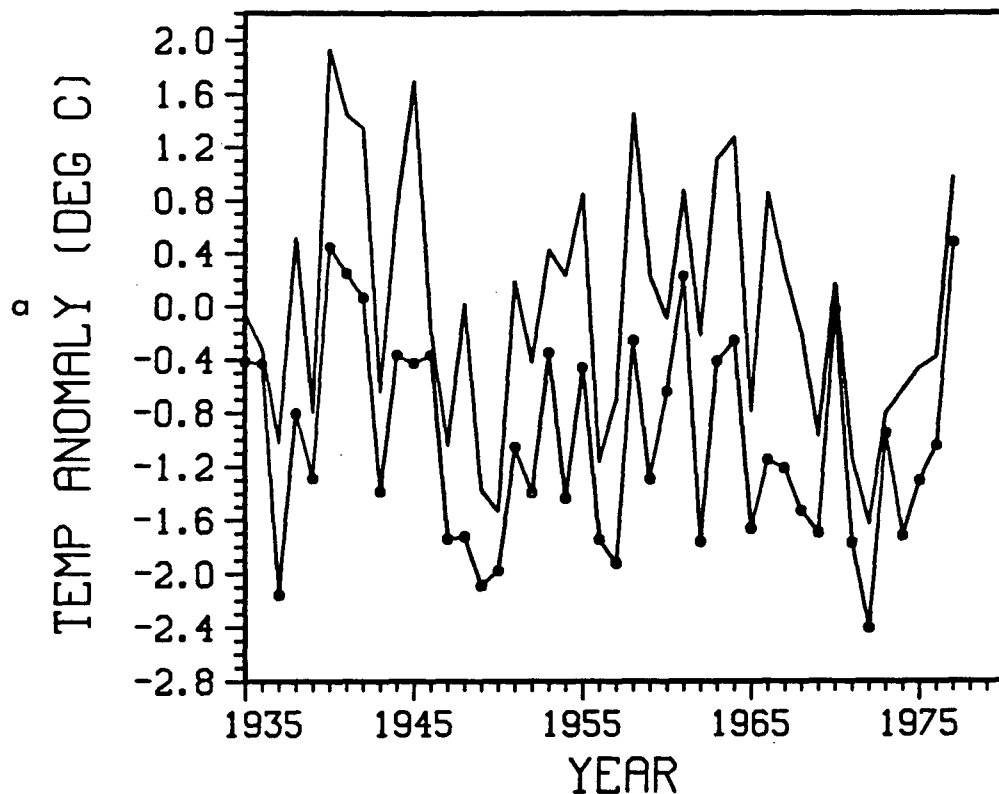
Season	Kains Island r	Langara Island r
winter	0.832	0.888
spring	0.616	0.636
summer	0.696	0.716
autumn	0.773	0.737

The analysis discussed above was also applied to find pressure indices that correlate well with SST differences between seasons. Thus the time series of differences between January-February (*winter*) average SST and the October-November (*autumn*) average SST was fit with a linear combination of grid point SLP values for January-February (involving the a_γ coefficients in expression, 4.1) and for November-December (the b_γ coefficients). A similar analysis was carried out for the SST differences between spring and winter, between summer and spring, and between autumn and summer. The indices that were finally obtained are described by the parameters listed in Table 3, while the correlation coefficients between the observed and predicted SST differences are given in Table 4. All the correlation coefficients in Table 4 are less than the corresponding coefficients in Table 2 with the exception of Spring–Winter.

4.4 Estimates of SST Anomalies Since 1900

It is straightforward to employ the indices discussed above to construct estimates of coastal SST anomalies in the years before direct observations are available. Table 5 gives the estimates for the winter and summer SST anomalies at Kains Island for the period 1900–1934, and at Langara Island during 1900–1940. The time series of these SST

KAINS ISLAND JAN/FEB TEMP



KAINS ISLAND APR/MAY TEMP

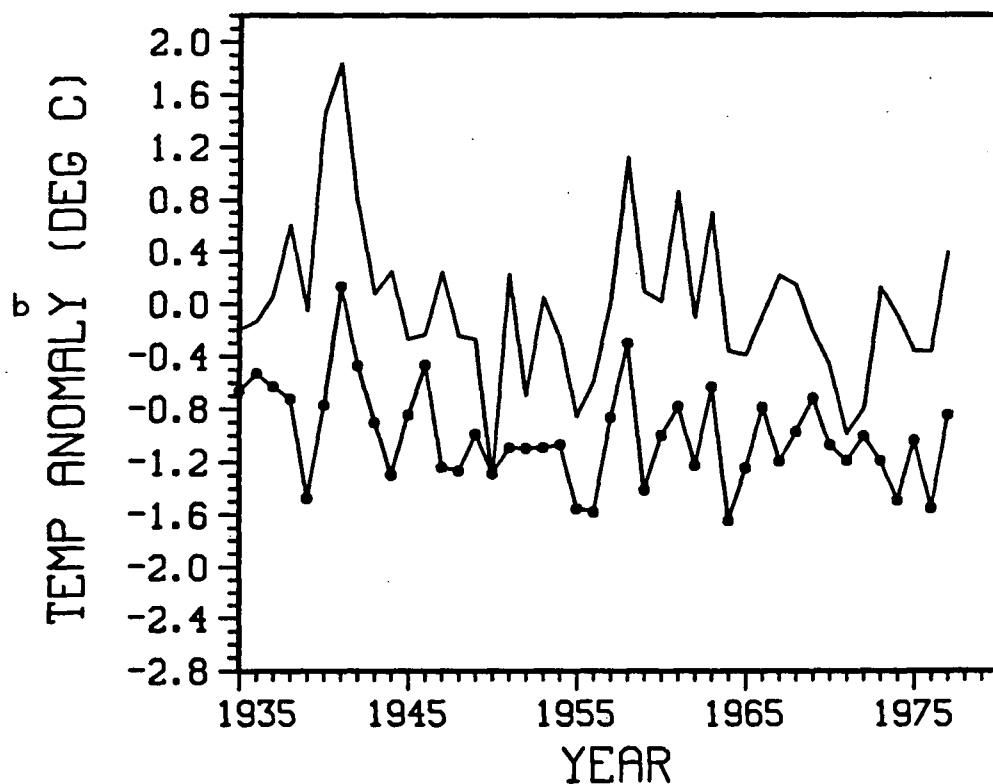
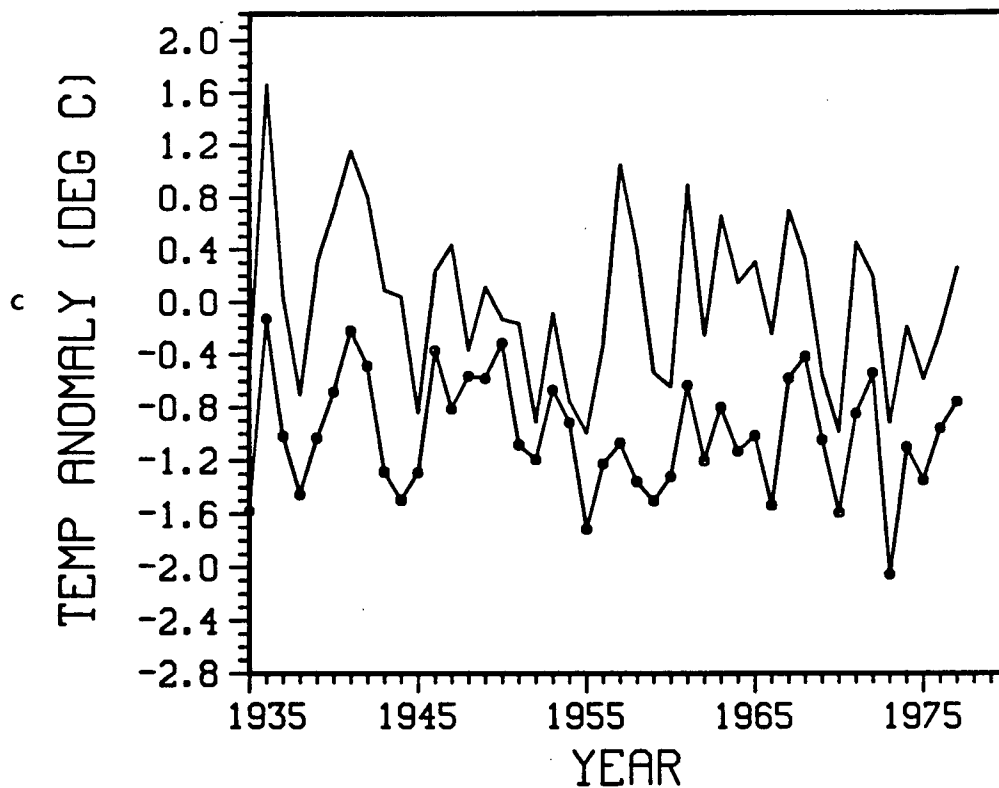


Figure 29 . Comparison of the time series of the observed (no dots) and predicted (dotted) seasonal SST anomalies from Kains Island for the period 1935-1977. a)—winter; b)—spring; c)—summer; d)—autumn. The predicted time series has been displaced downward by 1°C.

KAINS ISLAND JUL/AUG TEMP



KAINS ISLAND OCT/NOV TEMP

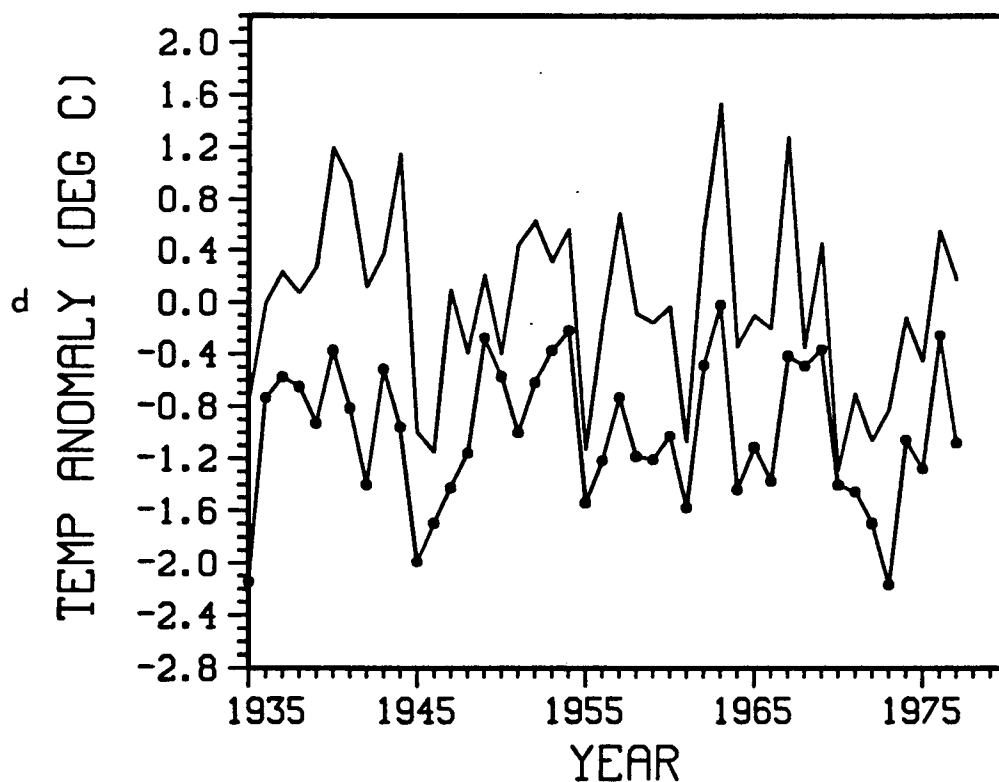
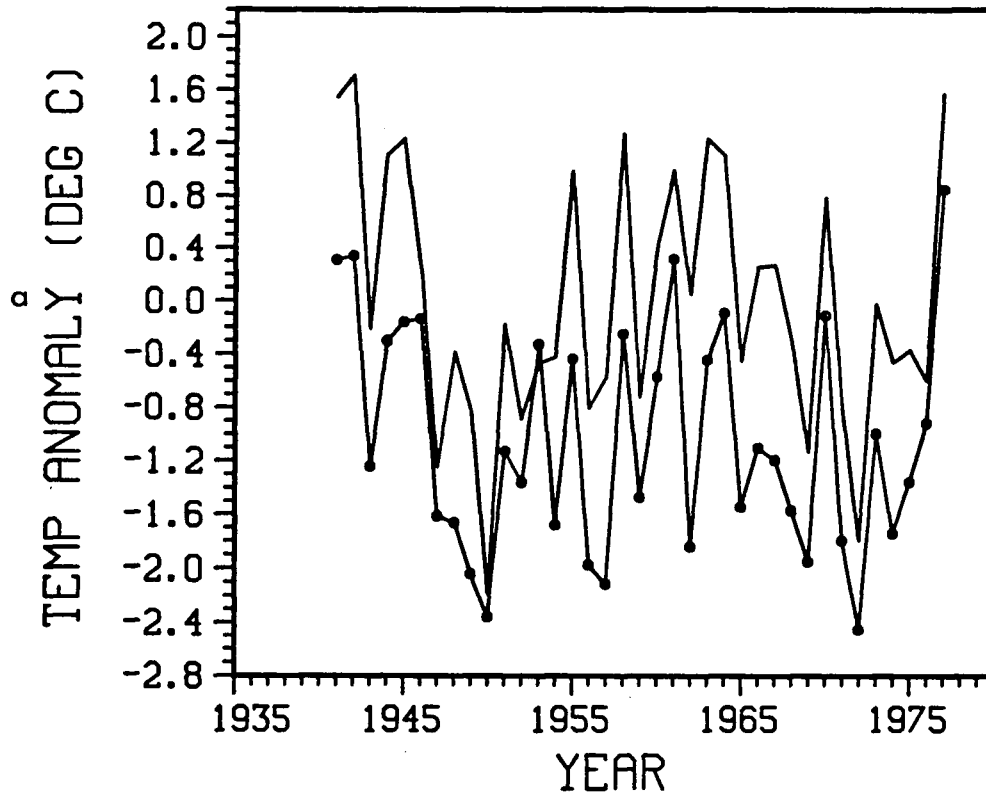


Figure 29 cont.

LANGARA ISLE JAN/FEB TEMP



LANGARA ISLE APR/MAY TEMP

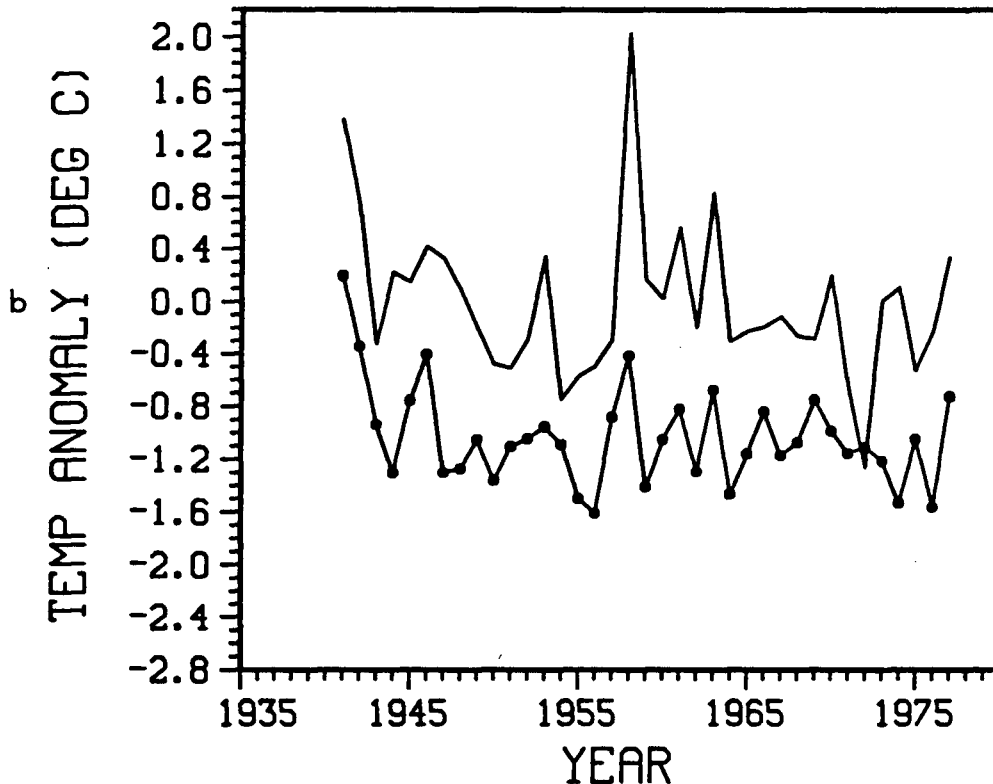
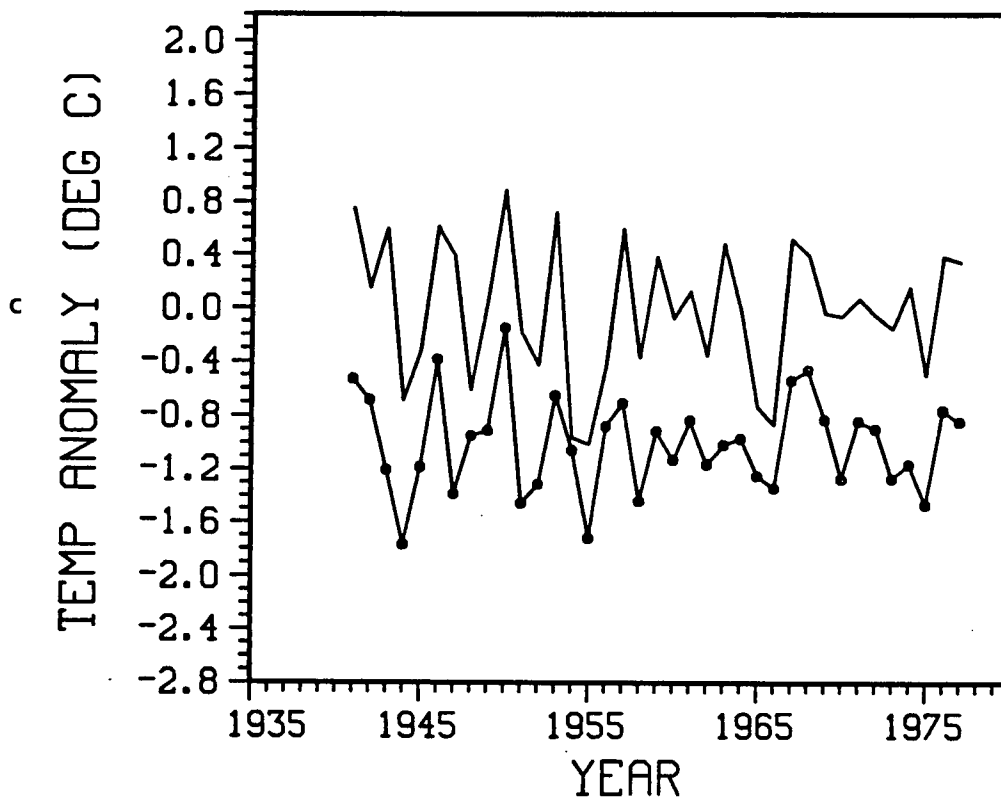


Figure 30 . Comparison of the time series of the observed (no dots) and predicted (dotted) seasonal SST anomalies from Langara Island for the period 1941–1977. a)—winter; b)—spring; c)—summer; d)—autumn. The predicted time series has been displaced downward by 1°C.

LANGARA ISLE JUL/AUG TEMP



LANGARA ISLE OCT/NOV TEMP

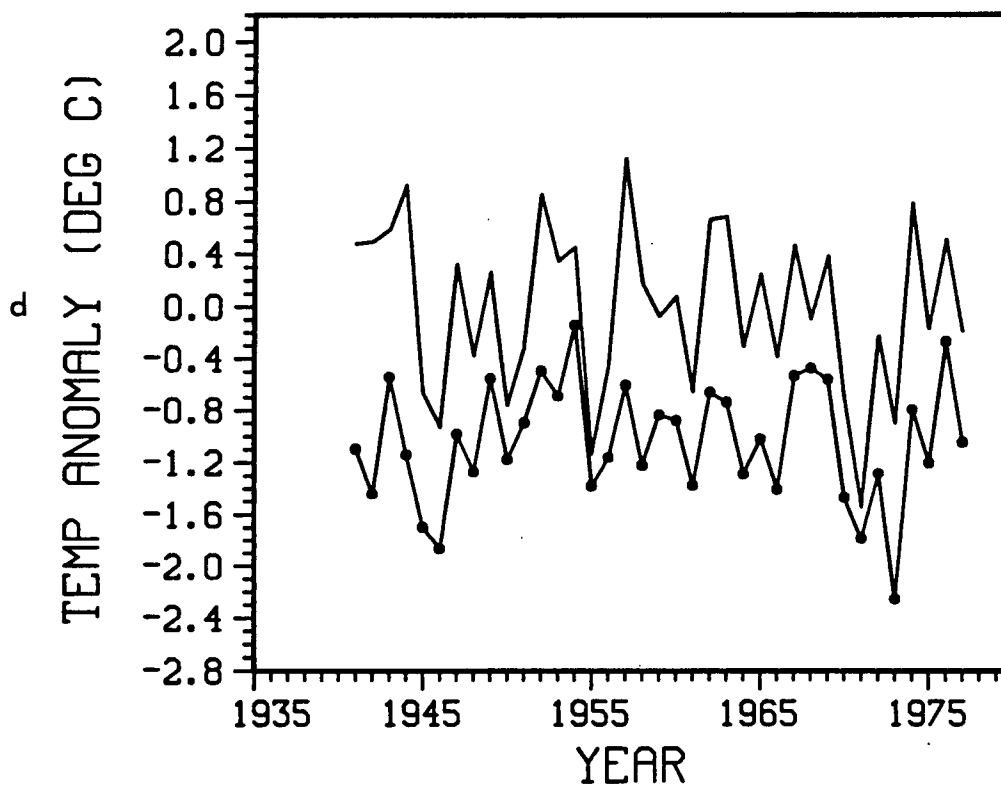


Figure 30 cont.

Table 3

Seasonal mean North Pacific pressure indices and corresponding least squares coefficients for each reference point (see Figs. 27a–d).

Season	Position	Kains Island a_{γ}	Kains Island b_{γ}	Langara Island a_{γ}	Langara Island b_{γ}
winter– autumn	170°W 50°N	–0.0632	–0.0040	–0.0806	0.0087
	140°W 40°N	–0.0621	–0.0561	–0.0423	–0.1215
	120°W 40°N	0.1253	0.0602	0.1229	0.1128
spring– winter	160°W 55°N	–0.0165	–0.0645	0.0002	0.0786
	145°W 45°N	–0.0878	0.0000	–0.0254	–0.1460
	145°W 40°N	–0.0307	–0.0493	–0.1306	0.0532
	130°W 45°N	0.1350	–0.0153	0.1559	0.0142
summer– spring	170°W 45°N	0.1420	0.0527	0.1637	0.0626
	150°W 40°N	–0.1801	–0.0530	–0.1935	–0.1893
	130°W 45°N	–0.2640	0.0290	–0.1730	0.2784
	120°W 45°N	0.3020	–0.0287	0.2028	–0.1517
autumn– summer	170°W 45°N	–0.0179	0.0564	–0.0410	–0.0278
	140°W 40°N	–0.1241	–0.0886	–0.1194	0.1395
	120°W 40°N	0.1419	0.0322	0.1603	–0.1117

Table 4

Correlation coefficients r between the seasonal mean predicted SST changes, obtained from the pressure indices defined in Table 3, and the observed seasonal mean temperature changes with respect to the previous season. Correlation coefficients were calculated at Kains Island for the period 1935 to 1977 and at Langara Island for the period 1941 to 1977.

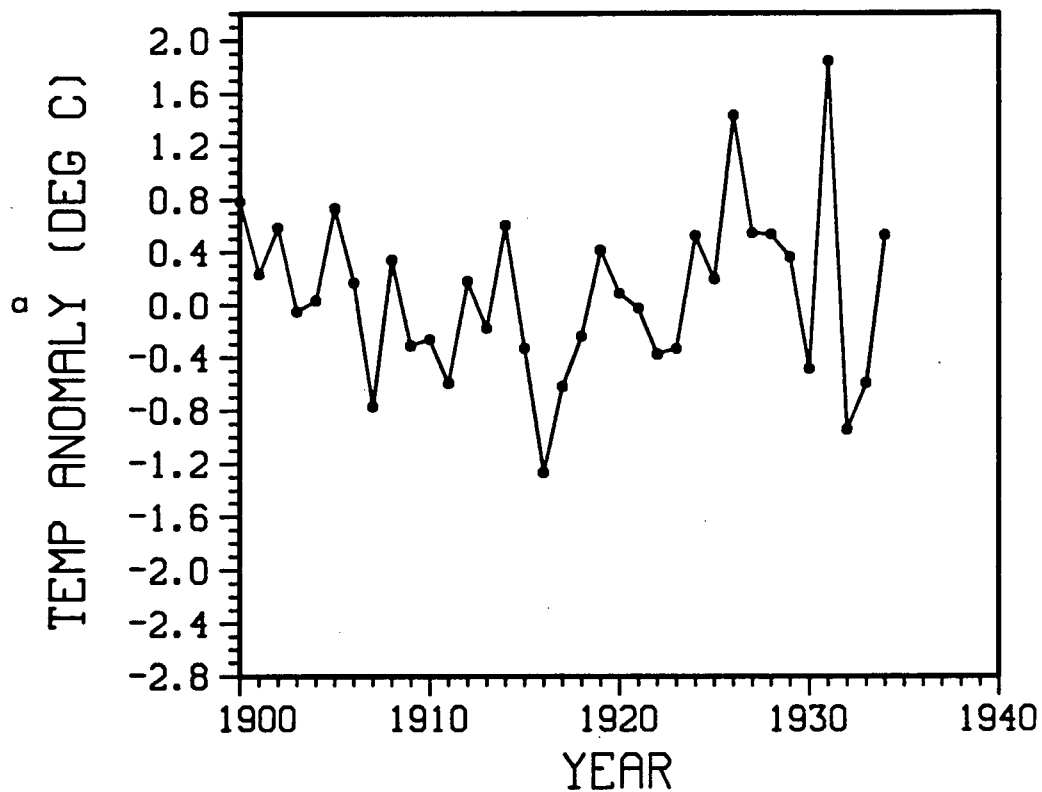
Season	Kains Island r	Langara Island r
winter–autumn	0.738	0.809
spring–winter	0.634	0.698
summer–spring	0.657	0.712
autumn–summer	0.596	0.638

estimates are shown in Figs. 31 and 32. As mentioned in Section 4.1 these data may be of importance in the study of environmental effects on the commercial fisheries of British Columbia. Mysak (1986) postulates that the return sockeye salmon migration routes back to the Fraser River spawning grounds may be influenced by North Pacific warming events, often associated with El Niño. For example strong El Niño events occurred in 1899–1900,

1925–1926 and 1940–1941 (Quinn *et al.*, 1978). The SST data of Table 5 and Figs. 31 and 32 indicate the presence of North Pacific warming events associated with these El Niños. Similarly, Table 5 and Figs. 31 and 32 indicate the presence of a warming event in 1931 independent of an ENSO event. These warming events may in turn influence the percentage of Sockeye salmon returning to the Fraser river through the Johnstone Strait at the northern end of Vancouver Island (Fig. 28) rather than through Juan de Fuca Strait (at the southern end of Vancouver Island). Research is currently underway at the University of British Columbia to study this “Johnstone Strait diversion” under the project name—Meteorological and Oceanographic Influences on Sockeye Tracks (MOIST). For a review of project MOIST see Mysak *et al.*, (1986).

The number of SLP observations available in the Northeast Pacific region increased enormously during this century. Thus it is possible that some kinds of systematic errors in the SLP analyses may affect the present predictions of SST anomalies in the early years. In particular, one might reasonably expect that in the absence of much data there would be a tendency to underestimate pressure contrasts (and hence underestimate the strength of the Aleutian Low). If such errors did affect the SLP analyses, this would be reflected in a tendency of the present calculations to underestimate the coastal SST in the early years. Figures 33 and 34 show the five year running means of the predicted SST anomalies in winter and summer at both stations over the entire 1900-1977 period. There are some systematic long term trends evident in these figures, particularly for the winter SST. It is comforting, however, that the general behaviour of the predicted SST shows no obvious difference between the early and later parts of the period. In particular there is no tendency for predicted cold SSTs in the earliest part of the record.

KAINS ISLAND JAN/FEB TEMP



KAINS ISLAND JUL/AUG TEMP

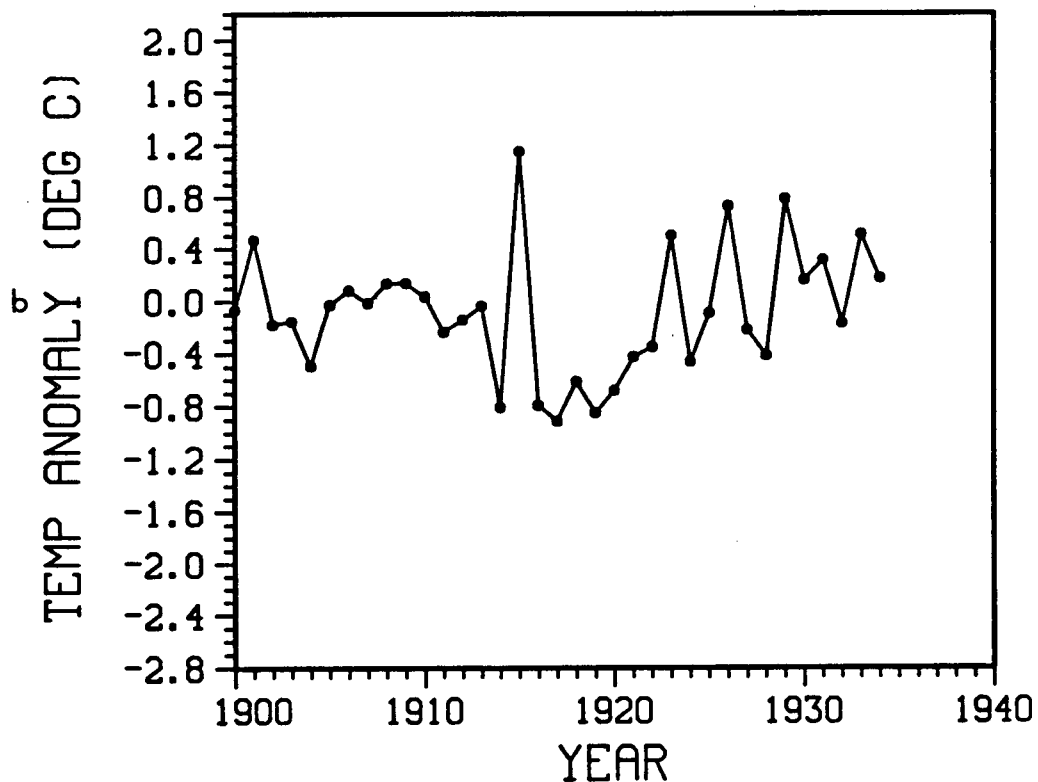
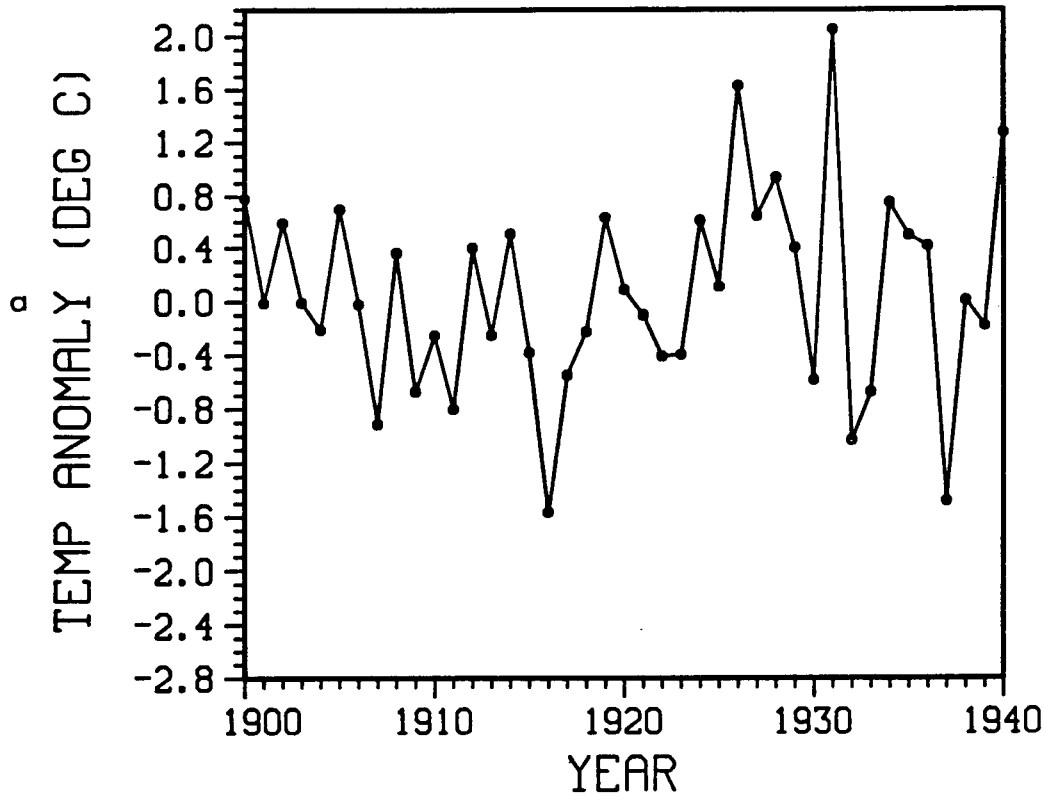


Figure 31 . Predicted SST anomalies at Kains Island for the period 1900-1934. a)—winter; b)—summer. The data are given in Table 5.

LANGARA ISLE JAN/FEB TEMP



LANGARA ISLE JUL/AUG TEMP

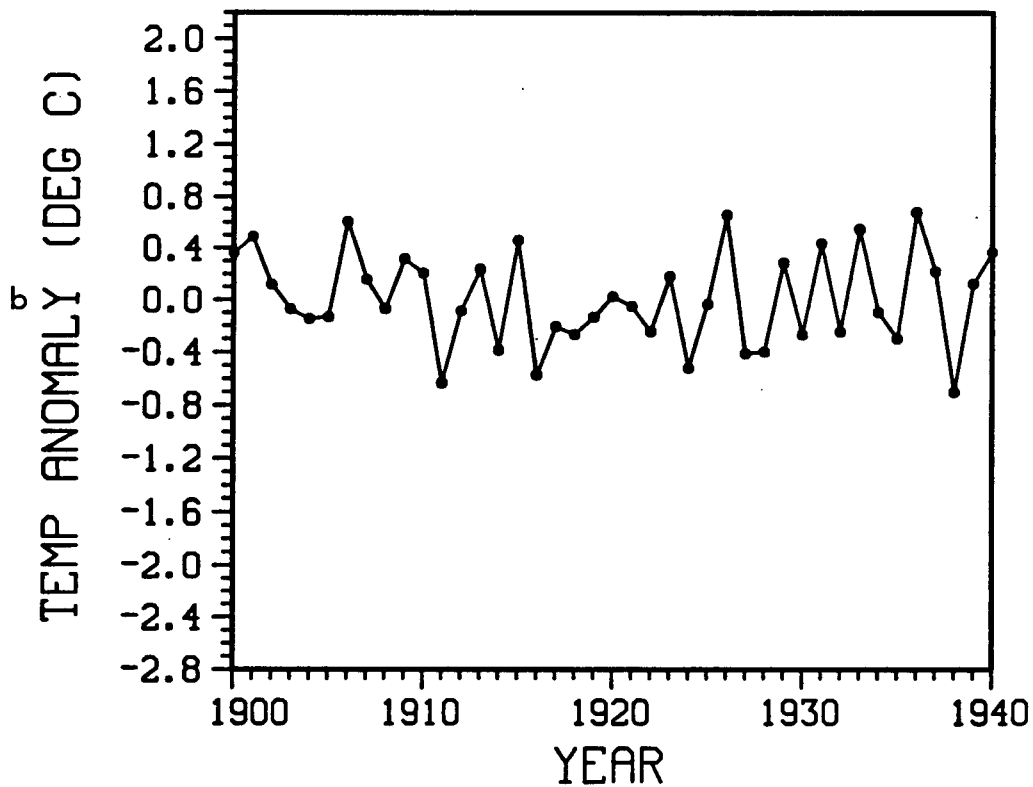


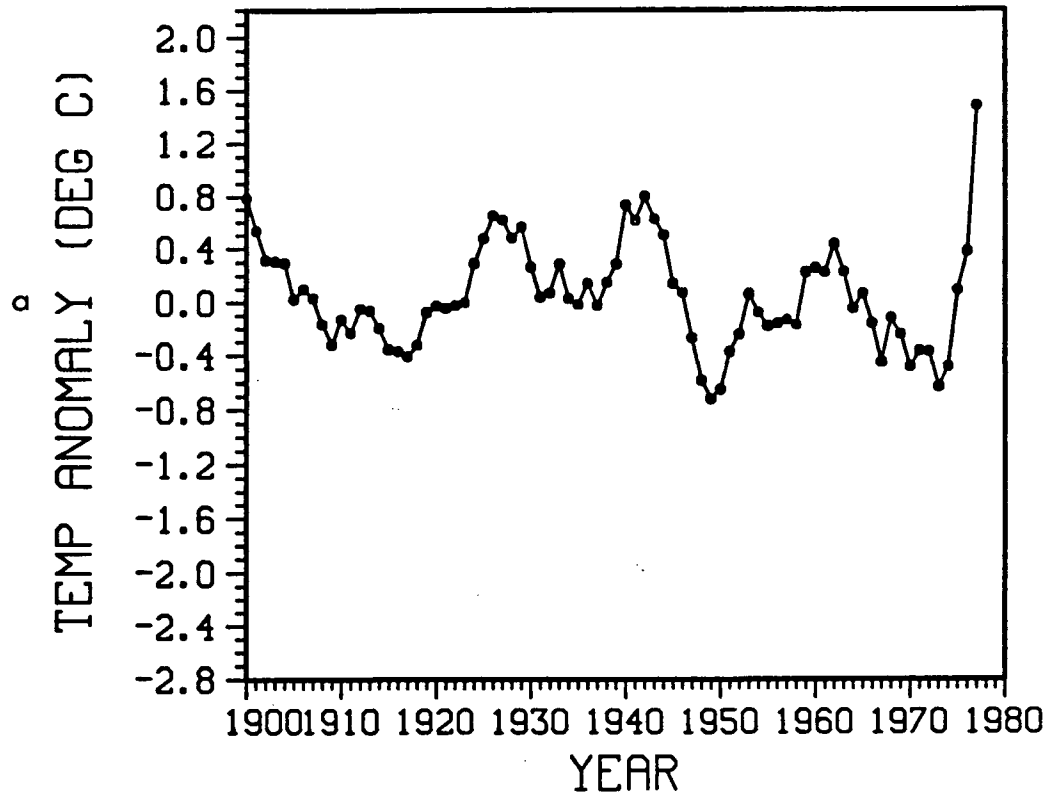
Figure 32 . Predicted SST anomalies at Langara Island for the period 1900-1940. a)—winter; b)—summer. The data are given in Table 5.

Table 5

Predicted mean seasonal temperature anomalies for the winter and summer seasons. The mean seasonal pressure indices are as given in Table 1. Kains Island temperatures were predicted for the period 1900–1934 and Langara Island temperatures for the period 1900–1940. The temperature anomalies are given in °C.

Year	Kains Island winter	Kains Island summer	Langara Island winter	Langara Island summer
1900	0.788	−0.065	0.780	0.361
1901	0.234	0.468	−0.008	0.492
1902	0.589	−0.176	0.592	0.121
1903	−0.048	−0.153	−0.006	−0.071
1904	0.036	−0.489	−0.209	−0.147
1905	0.738	−0.026	0.700	−0.133
1906	0.174	0.084	−0.021	0.606
1907	−0.770	−0.010	−0.913	0.161
1908	0.343	0.137	0.363	−0.068
1909	−0.309	0.142	−0.673	0.316
1910	−0.262	0.039	−0.254	0.207
1911	−0.591	−0.232	−0.801	−0.632
1912	0.182	−0.139	0.402	−0.088
1913	−0.174	−0.034	−0.249	0.237
1914	0.608	−0.802	0.509	−0.384
1915	−0.329	1.153	−0.379	0.463
1916	−1.264	−0.788	−1.562	−0.568
1917	−0.616	−0.908	−0.549	−0.205
1918	−0.237	−0.609	−0.221	−0.266
1919	0.418	−0.844	0.636	−0.134
1920	0.091	−0.676	0.091	0.025
1921	−0.021	−0.422	−0.098	−0.050
1922	−0.373	−0.346	−0.406	−0.243
1923	−0.331	0.506	−0.393	0.183
1924	0.530	−0.457	0.616	−0.518
1925	0.202	−0.085	0.116	−0.035
1926	1.432	0.736	1.630	0.658
1927	0.552	−0.216	0.651	−0.408
1928	0.543	−0.410	0.941	−0.396
1929	0.368	0.792	0.408	0.285
1930	−0.480	0.167	−0.585	−0.264
1931	1.844	0.319	2.054	0.437
1932	−0.938	−0.164	−1.027	−0.243
1933	−0.590	0.515	−0.675	0.549
1934	0.535	0.180	0.753	−0.095
1935	—	—	0.503	−0.295
1936	—	—	0.419	0.679
1937	—	—	−1.478	0.221
1938	—	—	0.011	−0.699
1939	—	—	−0.177	0.125
1940	—	—	1.275	0.368

KAINS ISLAND JAN/FEB TEMP



KAINS ISLAND JUL/AUG TEMP

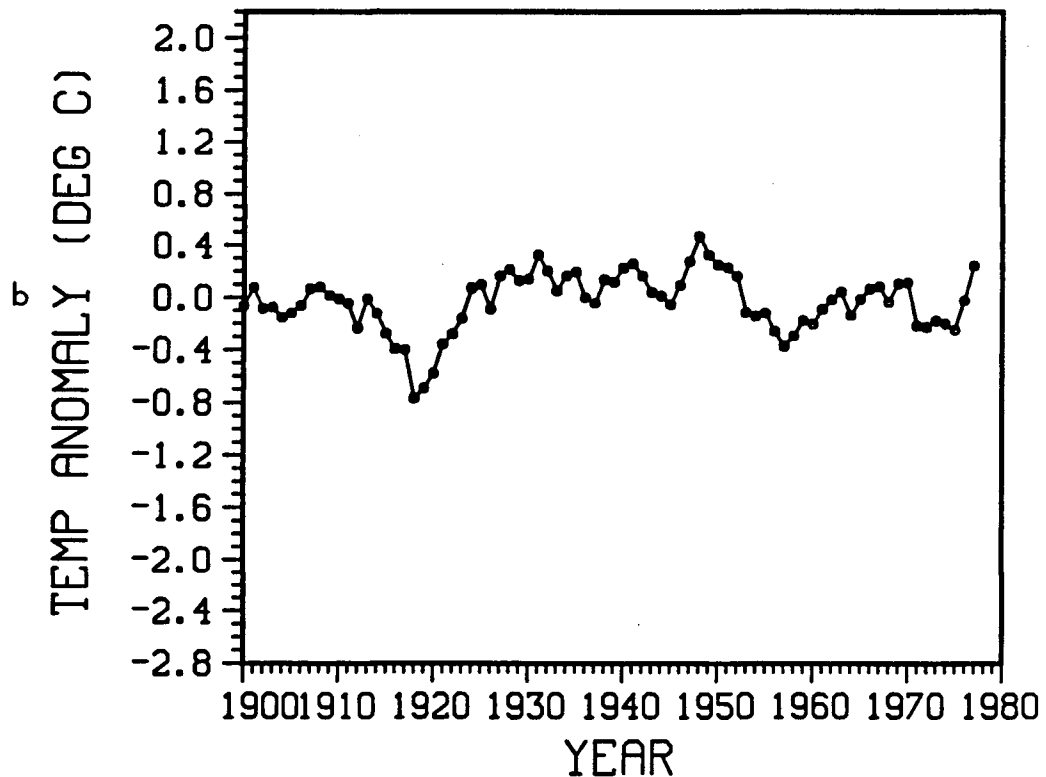
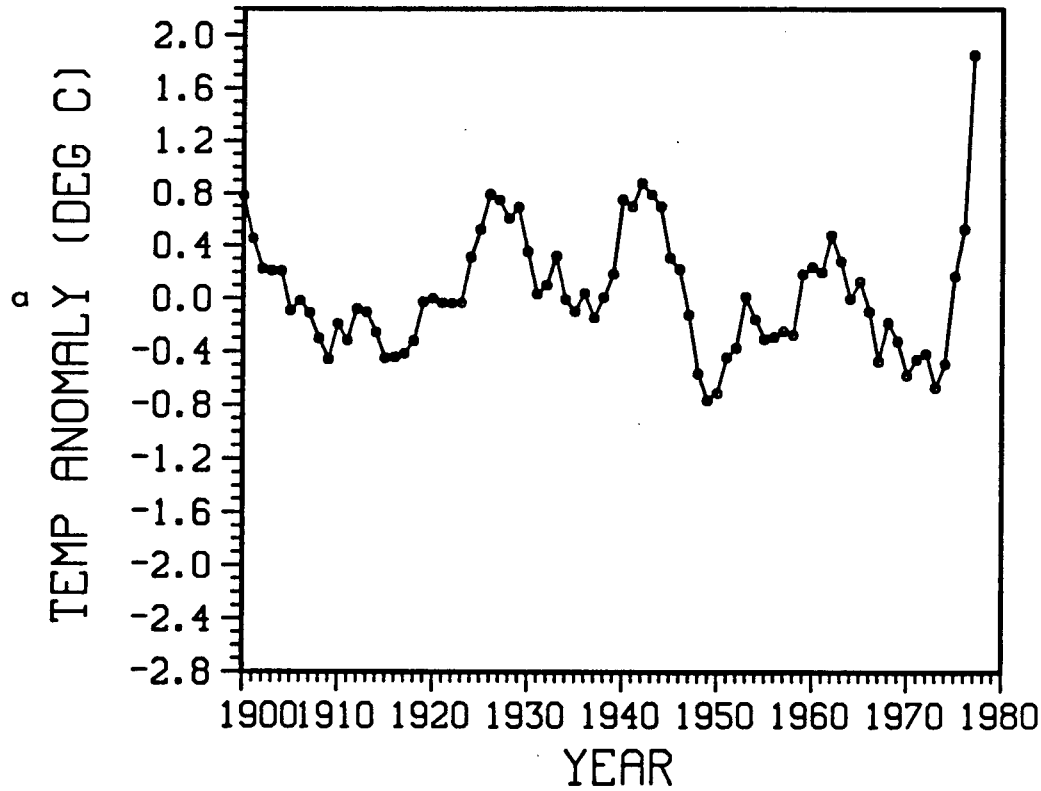


Figure 33 . Five year running mean from 1900–1977 of the predicted SST anomalies at Kains Island in a)—winter; b)—summer.

LANGARA ISLE JAN/FEB TEMP



LANGARA ISLE JUL/AUG TEMP

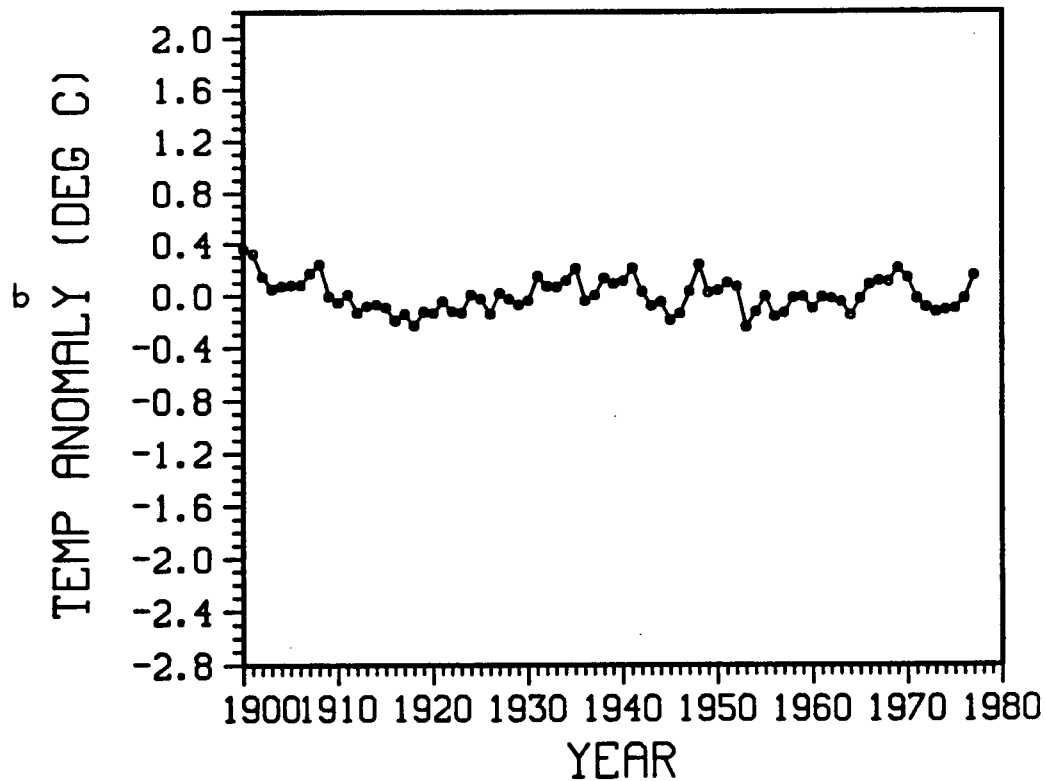


Figure 34 . Five year running mean from 1900–1977 of the predicted SST anomalies at Langara Island in a)—winter; b)—summer.

5. Oceanic Heat Flux Anomalies over the Kuroshio Region: Statistical Relationship with Heat Flux Anomalies over the North Pacific and the Overlying Atmospheric Circulation

5.1 Introduction

In recent years many investigators have attempted to explain the observed correlations between sea surface temperature (SST) in the North Pacific Ocean, and the overlying atmospheric circulation in the troposphere (see Frankignoul, 1985a for a review). Since the pioneering works of Namias (1959) and Uda (1962), where this correlation was established, research has been carried out to resolve the question of cause and effect. Davis (1976), on the basis of lag-correlations between monthly SST anomalies and sea level pressure, concluded that the atmosphere was indeed driving the ocean, although, in a later paper using seasonal statistics, Davis (1978) showed that autumn and winter sea level pressure anomalies could be reasonably predicted from summer and autumn SST anomalies respectively. However, numerical atmospheric general circulation model (AGCM) investigations (e.g., Huang, 1978) have shown that the atmosphere is relatively insensitive to midlatitude SST anomalies unless they are unreasonably large (Chervin *et al.*, 1980). The linear analysis of Webster (1981, 1982) attempted to resolve this apparent paradox. He argued that a significant atmospheric response to midlatitude SST anomalies could only arise when the basic flow was small (i.e., during summer).

Since the surface heat flux is a more accurate way of representing the oceanic thermal influence on the atmosphere than the SST used by the above authors, researchers have begun to investigate the relationship between the oceanic heat flux Q and the overlying atmospheric circulation. Q is comprised of the latent, sensible and backward radiative heat fluxes. Zhao and McBean (1987b) have recently examined the possible relationship between monthly mean surface heat flux anomalies and the overlying atmospheric circulation patterns. They found that surface heat flux anomalies over the Kuroshio region are significantly correlated with downstream atmospheric conditions in following months. As

a continuation of their study, Weaver and Mysak (1986b) reworked their analysis using seasonal statistics. Once again, large correlations were observed between Kuroshio heat flux anomalies and atmospheric conditions downstream. The most striking correlations were observed between winter Kuroshio heat flux anomalies and the winter 500 & 700 mb geopotential heights and surface pressure over the North Pacific, eastern Asia and Canada.

The annual and interannual variability of the total heat transfer from the ocean to the atmosphere over the entire North Pacific was examined by Zhao and McBean (1986), while Zhao and McBean (1987a) examined the principal patterns (empirical orthogonal functions; EOFs) of this variability. In winter they found that the first EOF consisted of a bipolar pattern, with anomalous heating (cooling) over the western North Pacific and anomalous cooling (heating) over the eastern North Pacific of nearly equal magnitude (see for example Fig. 37a). They found that this first principal component accounted for about 21% of the total variance. In summer the first “positive-dominant” EOF consisted of nearly the same sign anomaly over the whole North Pacific (see for example Fig. 37b). This principal pattern accounted for 32% of the total summer variance. Both these EOFs are apparent in the seasonal oceanic heat flux anomaly charts of Weaver and Mysak (1986a).

In this chapter the essential features of Weaver and Mysak (1986a,b) and Zhao and McBean (1986, 1987a,b) will be summarized, and in Chapters 6, 7 and 8 these observations will be compared to the results of several analytical models. Section 5.2 describes the heat flux and atmospheric data used in this study, while in Section 5.3, the analysis involved in determining the heat flux data is presented. In Section 5.4 the seasonal structure of the oceanic surface heat flux over the whole North Pacific is examined. The relationship between the oceanic heat flux over the Kuroshio region and the oceanic heat flux over the whole North Pacific is discussed in Section 5.5. Finally, in Section 5.6 the winter relationship between Kuroshio heating anomalies and the overlying atmospheric circulation is explored.

5.2 Data

The monthly mean heat flux data over the North Pacific Ocean (20°N to 55°N, 110°W to 120°E) were obtained from G. McBean and Y. Zhao, Institute of Ocean Sciences, B.C. These data consisted of the sum of latent, sensible and back radiative fluxes averaged over $5^\circ \times 5^\circ$ grids for the period 1950–1979, and were originally obtained from the N.E. Clark data set at Scripps Institute of Oceanography. The heat flux data, described in Barnett (1981) and Talley (1984), have a fair weather bias as they were obtained from ships of opportunity.

The mean annual cycle was removed from the data, and a three month running mean (low-pass filter) was performed on the resulting anomaly fields in order to concentrate on seasonal statistics (Zhao and McBean, 1987a). Systematic errors which occur in the data are thus removed through this process. Since the number of observations in each grid is large (Zhao and McBean, 1987a), random errors in the data are probably small. Four characteristic seasons are considered: *Winter* (December, January, February), *Spring* (March, April, May), *Summer* (June, July, August), *Autumn* (September, October, November). In the following plots *Winter* is labelled by the year in which it ends (i.e., *Winter* 1951 is December 1950 through February 1951).

The *Kuroshio region* has been defined by the area 25–30°N, 130–150°E and 30–35°N, 130–160°E (Fig. 35), as in Zhao and McBean (1986c). An index, representing the oceanic heat flux over the Kuroshio and its adjacent area, was obtained by averaging the heat flux data over the *Kuroshio region* defined above. In the following analysis we use the heat flux data over the *Kuroshio region* since this is one of the most dynamically active regions in the North Pacific. The warm northward flowing Kuroshio western boundary current and the colder southward flowing Oyashio current meet in this region, separate from the coast and flow eastward. The seasonal ocean to atmosphere heat flux over this region is also larger and more variable than over other areas of the North Pacific (Figs. 36, 37, 38) and hence would have a larger influence on the overlying atmosphere.

KUROSHIO REGION

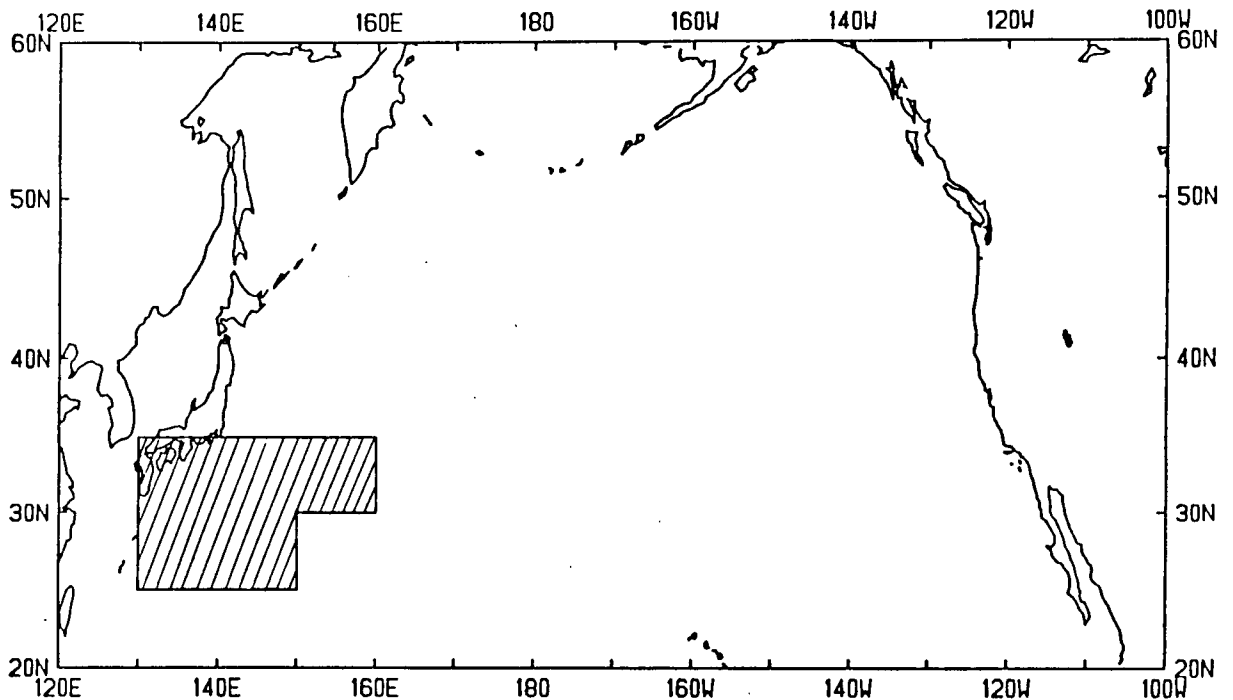


Figure 35 . Map of the North Pacific indicating the *Kuroshio region* (shown as hatched) used in determining an index representing the oceanic heat flux over the Kuroshio and its adjacent area.

Monthly surface pressure analyses over the northern hemisphere from 20°N to 80°N for the period 1950–1979 were obtained from the Data Support Section at NCAR. There were several missing observations in the region 0°E to 40°E in the earlier data. These were not used in the following correlation analysis. The 500 (700) mb geopotential height data for the region north of 15°N from 1956 (1963)–1979 were also obtained from G. McBean and Y. Zhao. These were originally part of the NCAR data set. Once again, in order to concentrate on seasonal statistics, the pressure and geopotential height data were averaged over the four characteristic seasons described above.

5.3 Analysis

The energy exchange at the ocean surface is represented by the equation (Budyko,

1963),

$$Q_t = (Q_l + Q_s + Q_b) - Q_i, \quad (5.1)$$

where $Q_t > 0$ (< 0) is the net heat loss (gain) of the ocean; Q_l is the latent heat flux; Q_s is the sensible heat flux; Q_b is the net longwave radiative flux and Q_i the solar radiation absorbed by the ocean.

In this study the focus is on the heat flux from the ocean to the atmosphere, denoted by, Q_T , where

$$Q_T = Q_l + Q_s + Q_b. \quad (5.2)$$

A review of the empirical calculation of the individual components of (5.2) is given in an appendix (written by N.E. Clark) to Barnett (1981); the results are summarized here.

The net longwave radiation term Q_b is empirically given by

$$Q_b = Q_{b0}(1 - 0.8C), \quad (5.3)$$

$$Q_{b0} = \varepsilon\sigma T_s^4(0.39 - 0.05e^{1/2}) + 4\varepsilon\sigma T_s^3(T_s - T_a), \quad (5.4)$$

where ε is the emissivity of the sea surface; σ is the Stefan-Boltzmann constant; T_s is the sea surface temperature and T_a is the air temperature at a height of 10 m ($^{\circ}\text{K}$); e is the air vapour pressure (mb); and C is the cloud cover in tenths. The latent heat flux Q_l is calculated from,

$$Q_l = LC_e(q_s - q_a)V_a, \quad (5.5)$$

where L is the latent heat of vapourization; C_e is the exchange coefficient of water vapour; q_s and q_a are the mixing ratios of air at water level and at a height of 10 m respectively; V_a is the wind speed at a height of 10 m. Finally the sensible heat flux Q_s is obtained from,

$$Q_s = \rho C_p C_s(T_s - T_a)V_a, \quad (5.6)$$

where ρ is the density of air; C_p is the specific heat of air at constant pressure; C_s is the exchange coefficient of sensible heat.

Values for the exchange coefficients C_e and C_s were taken by N.E. Clark from a table in Bunker (1975). These values were then adjusted as described in Barnett (1981).

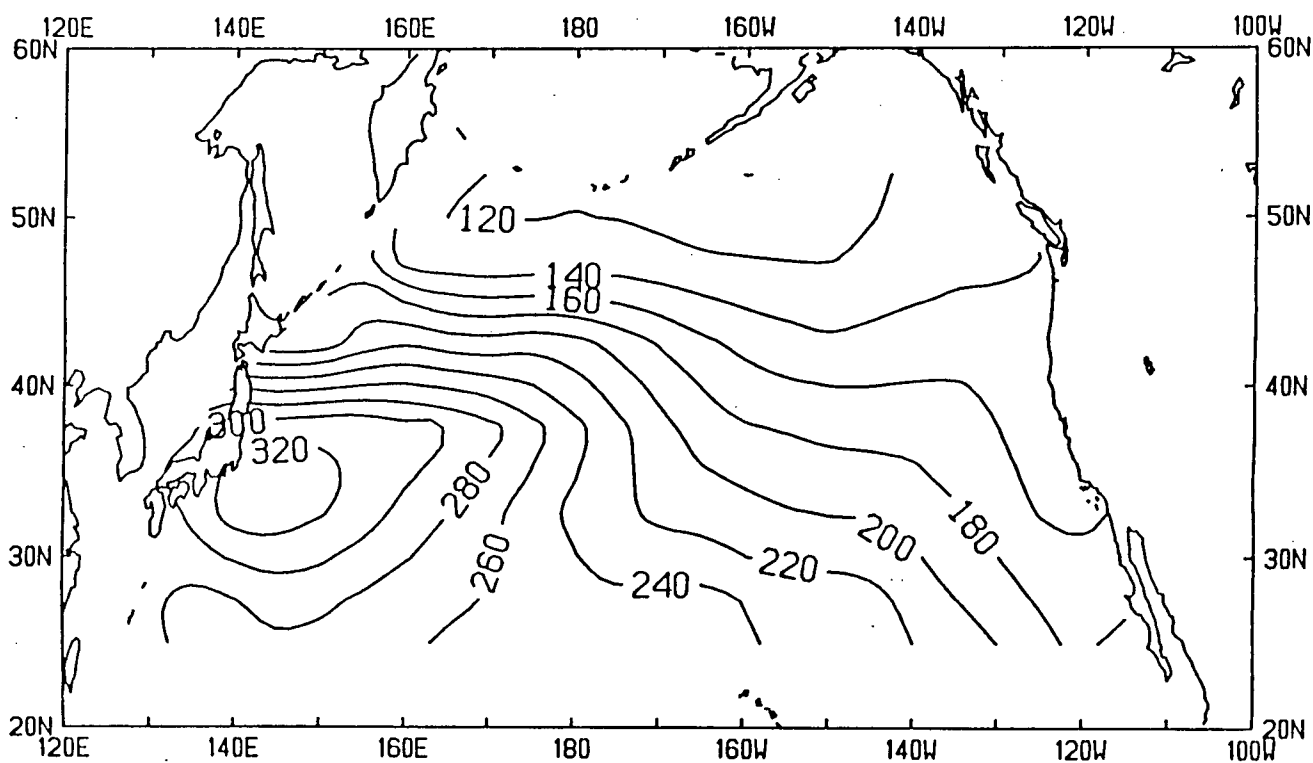
5.4 Seasonal Structure of the North Pacific Oceanic Surface Heat Flux

The mean oceanic heat flux for each season, based on the data for the period 1950–1979, is depicted in Fig 36. Two distinct regimes exist. In the summer (Fig. 36c) the marine heat flux west of 140°W exhibits a zonal structure, decreasing northward in magnitude corresponding to decreasing sea surface temperature. In the winter (Fig. 36a) an intense heating over the *Kuroshio region* is observed and the heating at a particular location is generally much stronger. This is due to a much greater ocean-atmosphere temperature difference $T_s - T_a$, and generally larger wind velocities V_a , in the winter months. These two larger quantities therefore induce larger contributions from the latent and sensible heat terms in (5.2). Spring (Fig. 36b) and autumn (Fig. 36d) appear as transition periods between the winter and summer conditions.

Figure 37 illustrates the structures of the first EOF of variability for winter 1977 (Fig. 37a) and for summer 1977 (Fig. 37b). As mentioned in Section 5.1 the first EOF in winter consists of a bipolar pattern with anomalous heating (cooling) over the western North Pacific and anomalous cooling (heating) over the eastern North Pacific of nearly the same magnitude (Zhao and McBean 1987a). In summer the first EOF has nearly the same sign anomaly over the entire North Pacific.

The horizontal distribution of oceanic heat flux anomalies over the *Kuroshio region* varies greatly from year to year (Zhao and McBean 1986, Weaver and Mysak 1986a). This is illustrated in Figs. 38a,b for winter, where anomalies between ten and thirty percent of the seasonal long term mean are observed in the proximity of and eastward of the *Kuroshio region* (defined above). In the following chapters, the atmospheric response to heating with various distributions will be examined. Rectangular and segmented cosines heating structures will be introduced to model heating over a broad expanse (Fig. 38a), whereas a line source heat forcing will be used as a model for localized heating (Fig. 38b).

a MEAN HEAT FLUX, WINTER



b MEAN HEAT FLUX, SPRING

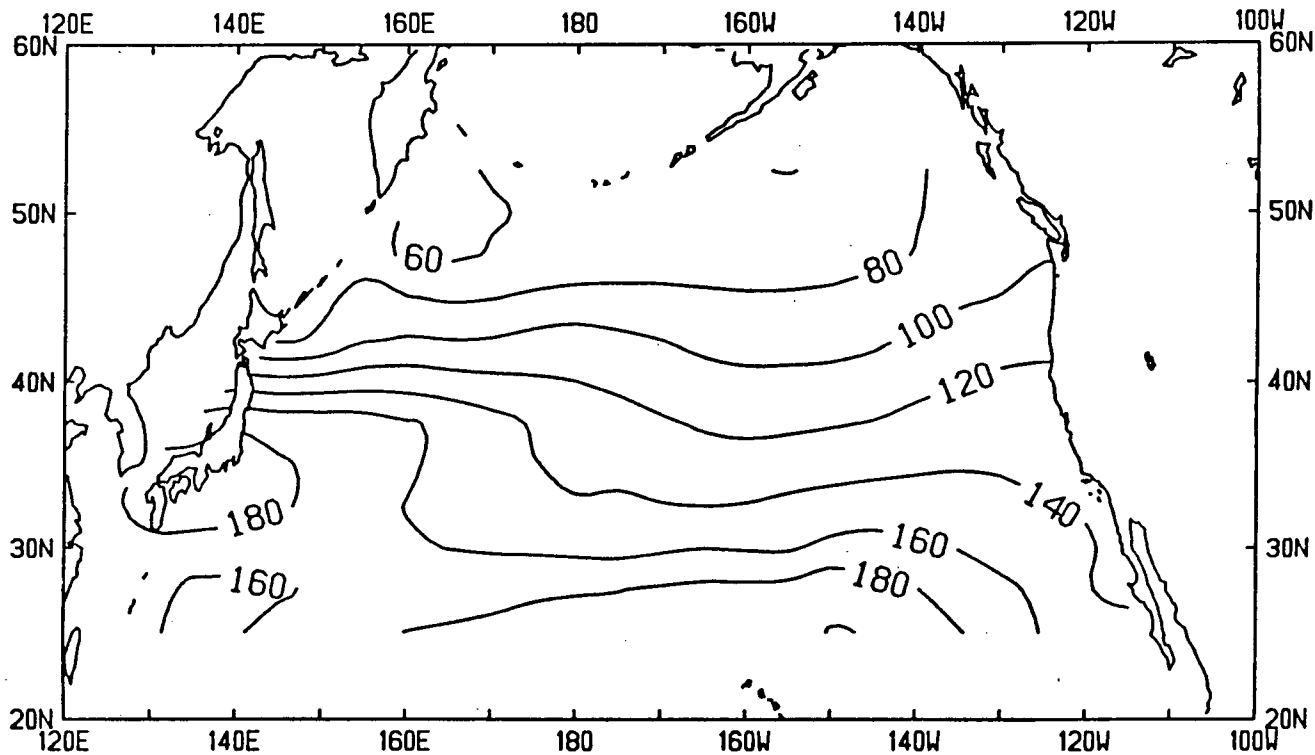
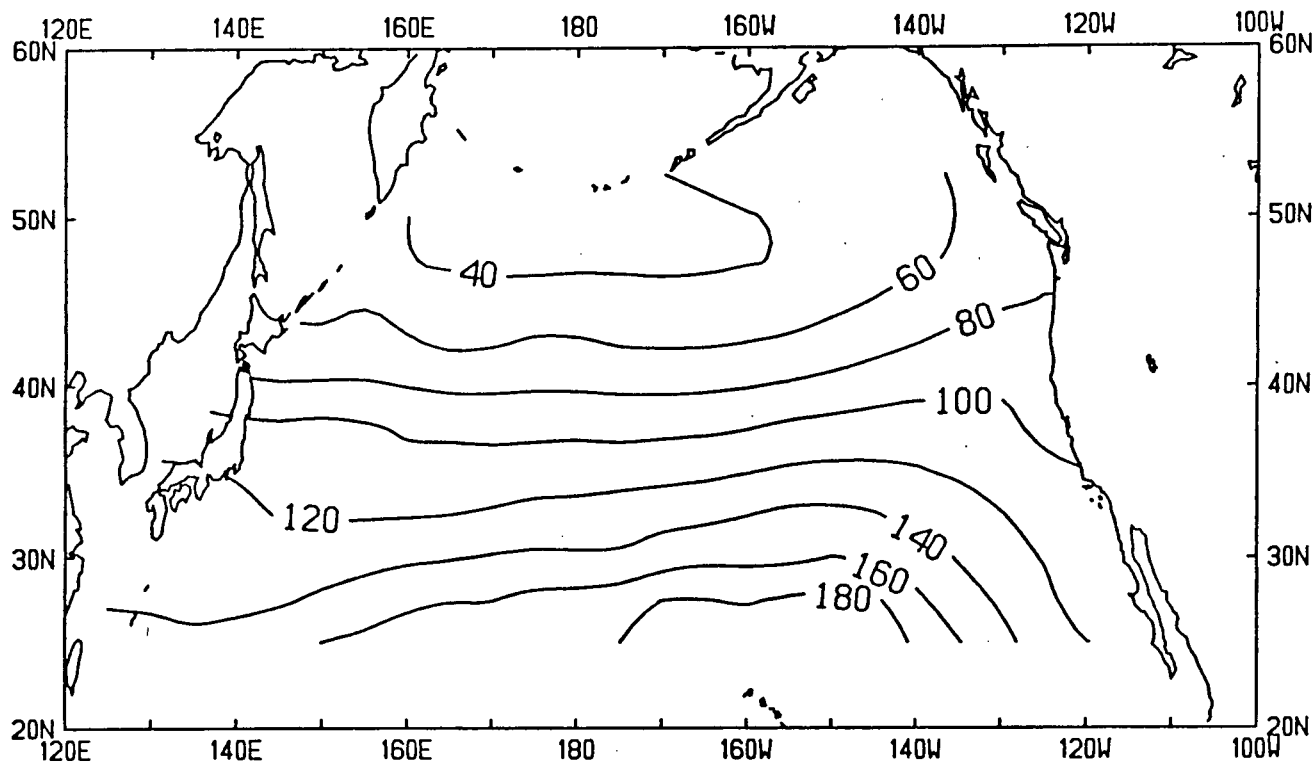


Figure 36 . Mean oceanic heat flux (latent, sensible, back radiative—see 5.2) over the North Pacific for the period 1950–1979. a)—winter; b)—spring; c)—summer; d)—autumn. The contour are in Wm^{-2} .

c MEAN HEAT FLUX, SUMMER



d MEAN HEAT FLUX, AUTUMN

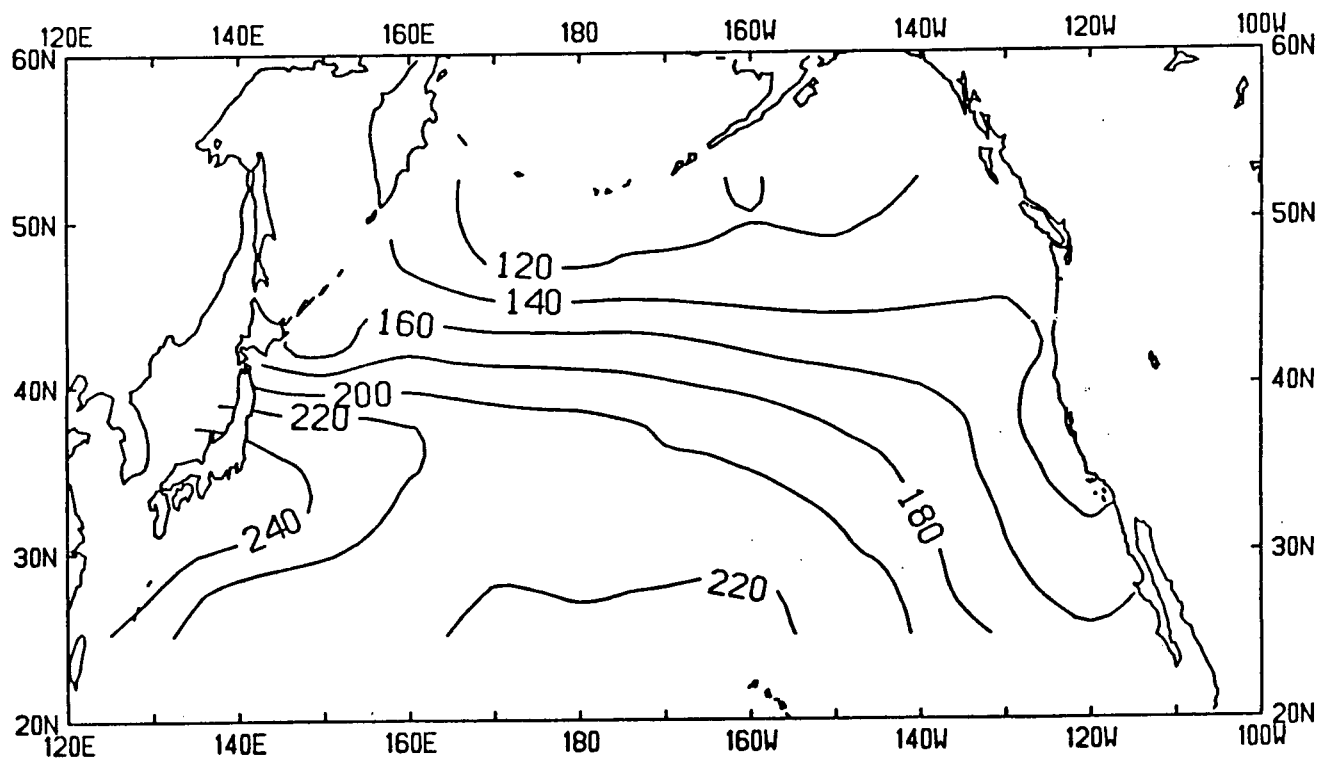
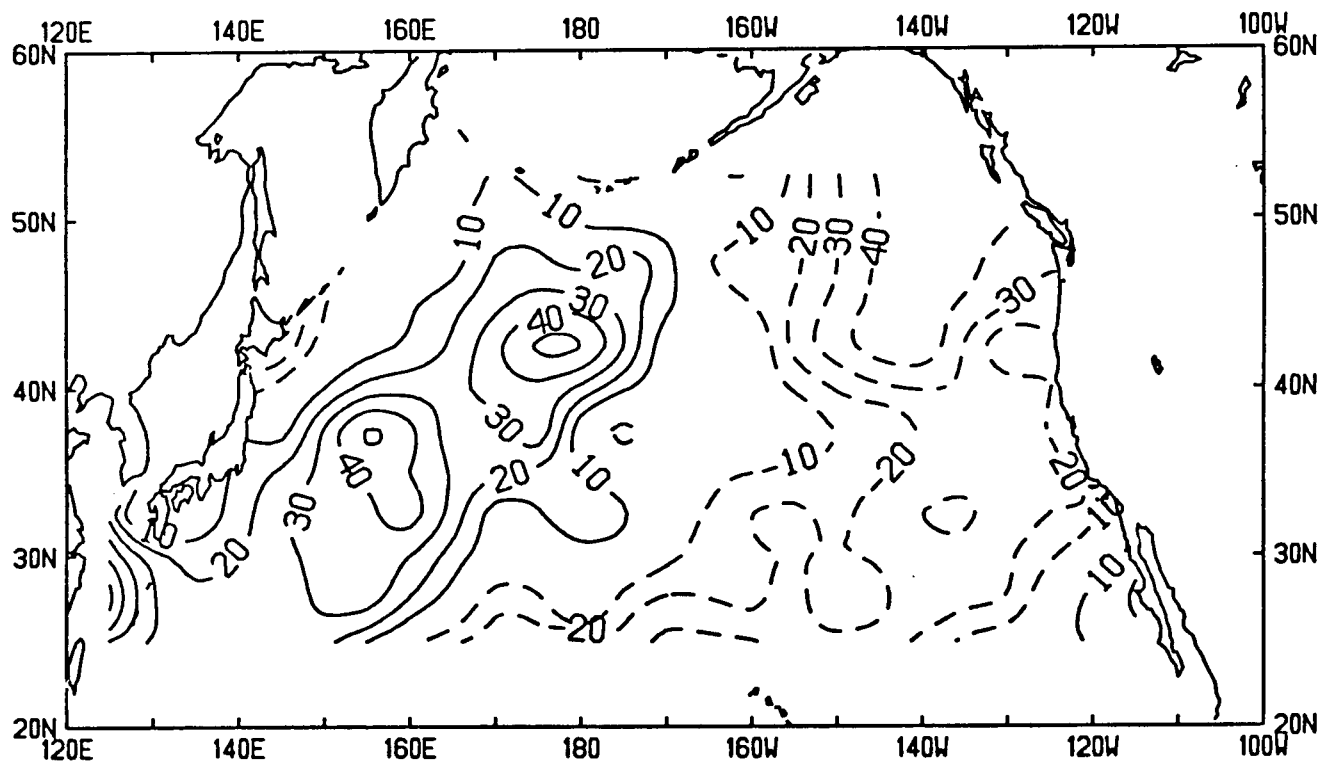


Figure 36 cont.

a HEAT FLUX ANOMALY, WINTER 1977



b HEAT FLUX ANOMALY, SUMMER 1977

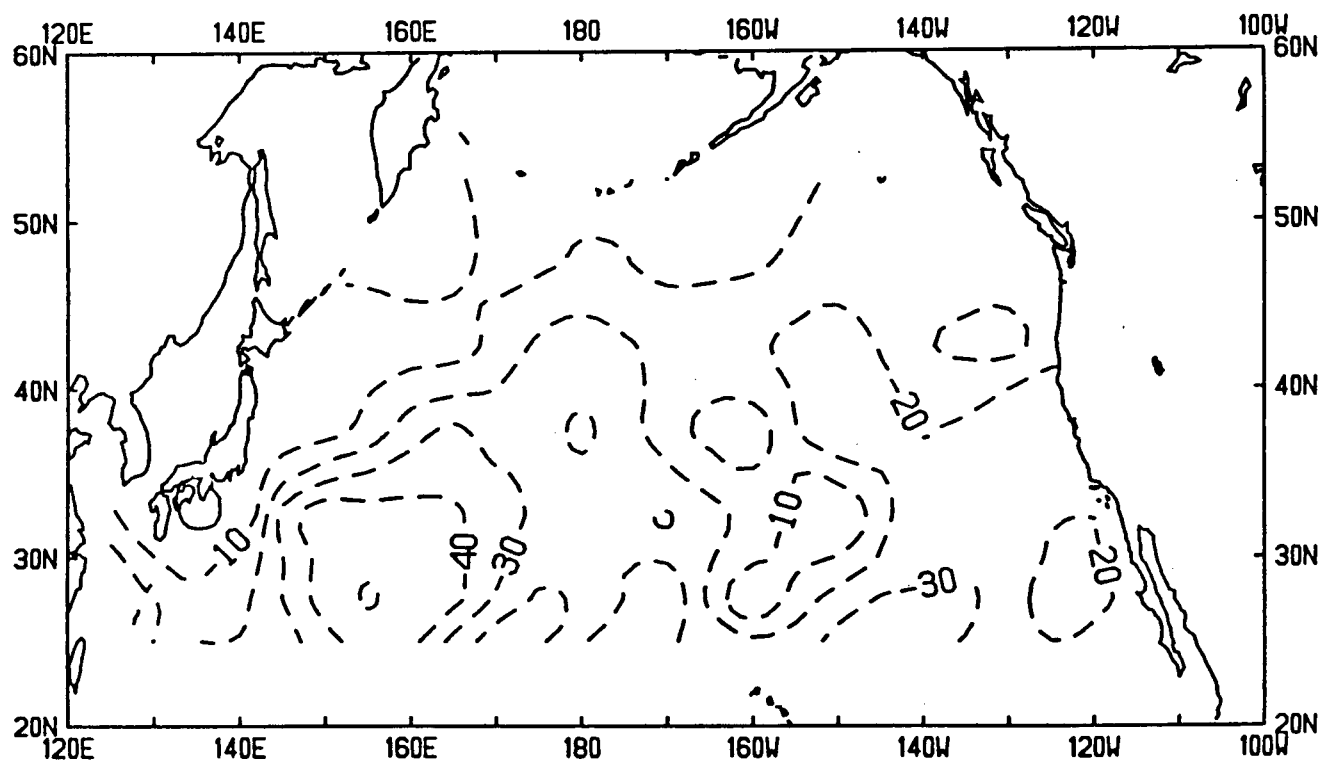
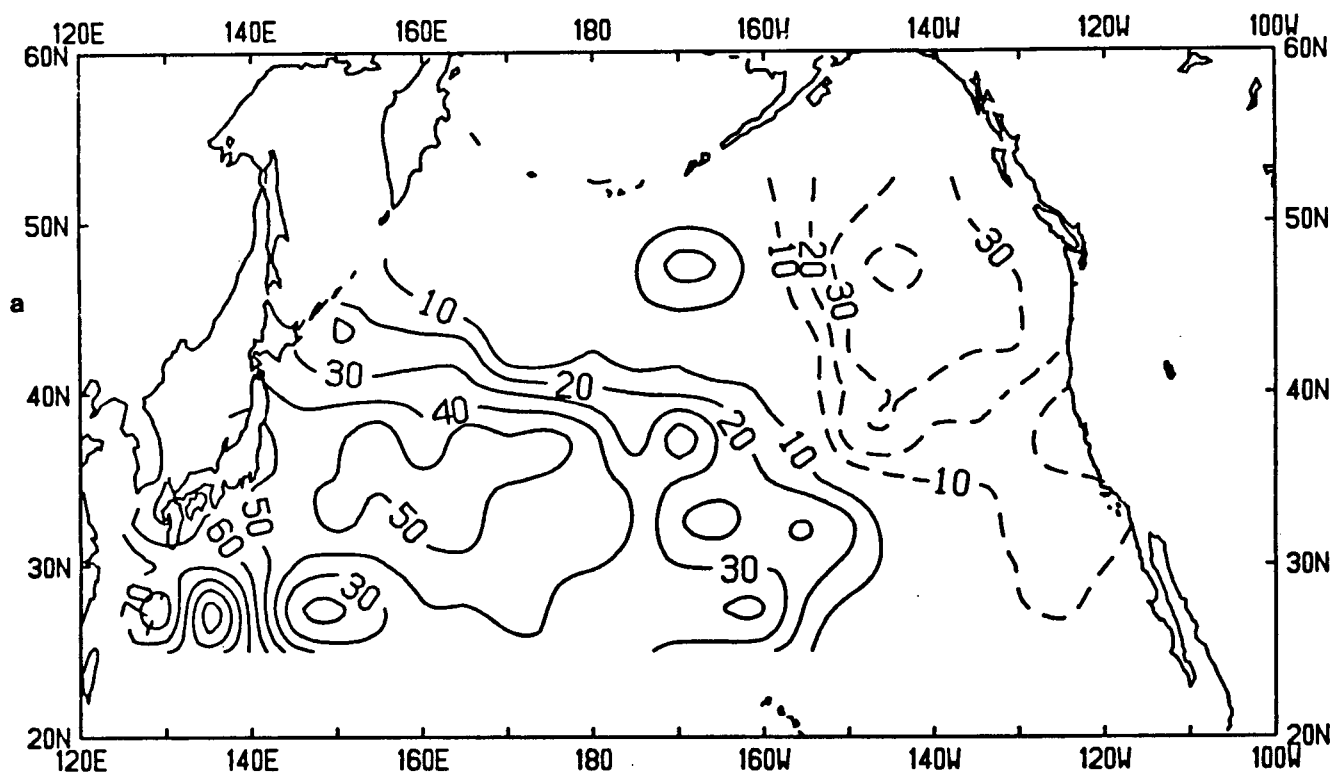


Figure 37 . Surface heat flux anomaly for: a)—winter 1977; b)—summer 1977. The structures of the first EOFs of Zhao McBean (1987a) as described in the text are visible in these maps. All contours are in Wm^{-2} .

HEAT FLUX ANOMALY, WINTER 1963



HEAT FLUX ANOMALY, WINTER 1978

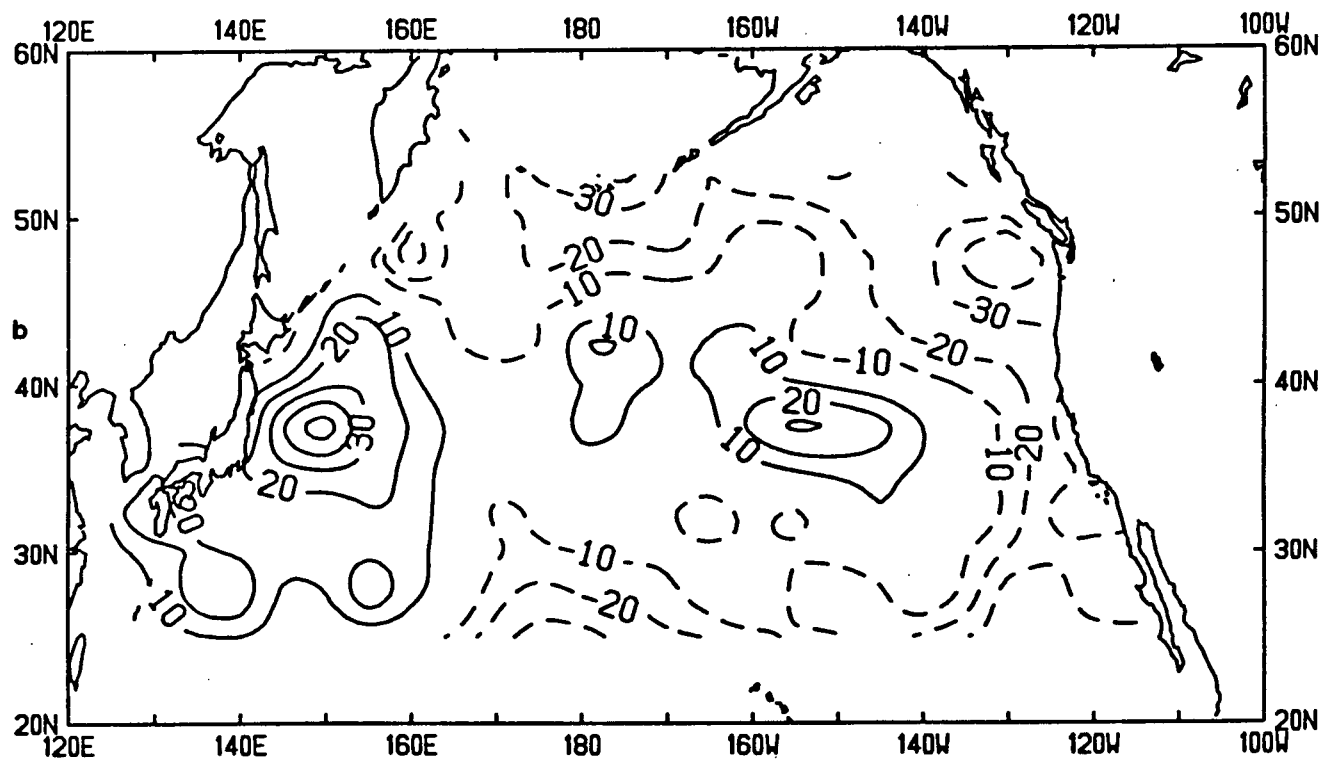


Figure 38 . Surface heat flux anomaly maps for: a)—winter 1963; b)—winter 1978. The contours are in Wm^{-2} .

5.5 Oceanic Heat Flux Anomaly Correlations over the North Pacific

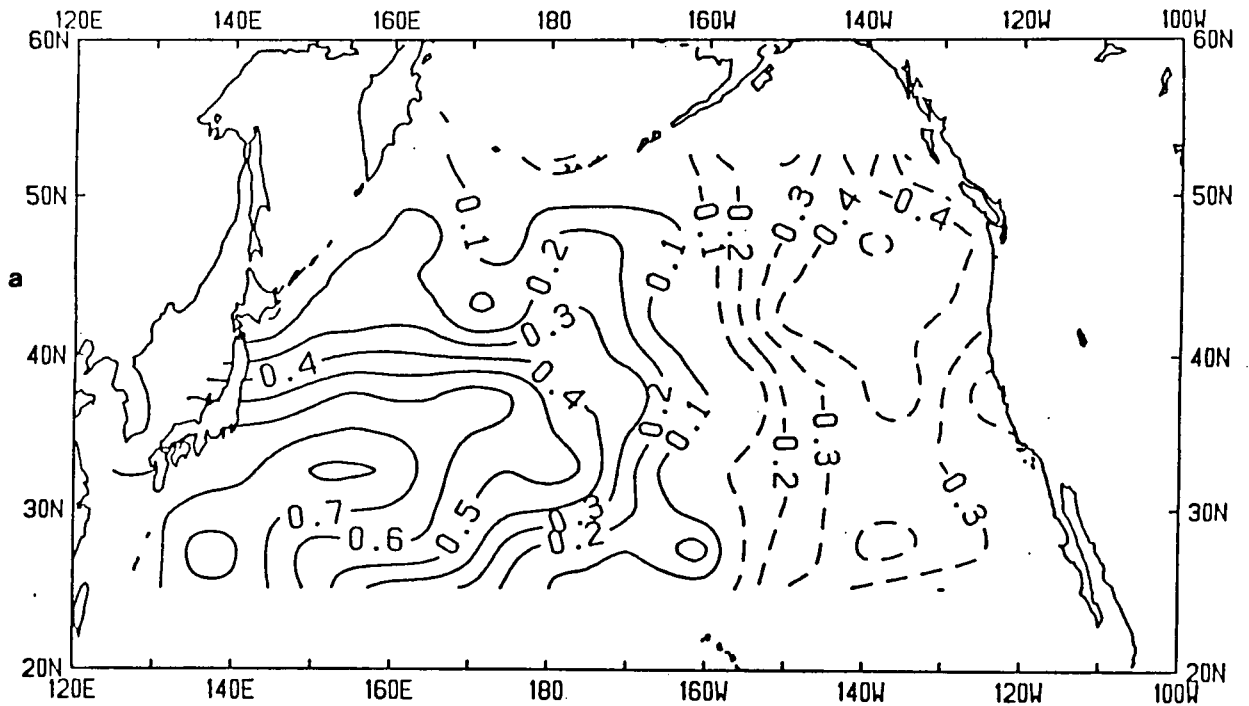
Thirty years of heat flux data were used to correlate the oceanic heat flux anomaly over the *Kuroshio region* (see Fig. 35) with the heat flux anomalies throughout the North Pacific, with lags of 0–2 seasons. In the plots referred to in this section, a correlation coefficient of $r = 0.36$ corresponds to a 0.05 confidence level, whereas a correlation coefficient of $r = 0.46$ corresponds to a 0.01 confidence level. Figures 39a–d illustrate these correlations with a zero month lag. The winter pattern shows a strong positive correlation between heat flux anomalies over the *Kuroshio region* and those over most of the Northwest Pacific. A strong negative correlation with the Northeast Pacific is also apparent. These features were observed by Zhao and McBean (1987b) and are clearly visible in the heat flux anomaly maps of Weaver and Mysak (1986a). They correspond to the first EOF of the winter oceanic heat flux anomaly pattern over the North Pacific (Zhao and McBean, 1987a).

The summer pattern shows a large correlation between heating anomalies over the *Kuroshio region* and those over most of the North Pacific as expected from the structure of the first summer EOF. Spring and autumn, although similar to summer, with weaker correlations, appear as transition seasons.

The correlations between the heat flux anomaly over the *Kuroshio region* in summer and autumn, and the heat flux anomalies over the whole North Pacific in the following season, are contoured in Fig. 40. Heat flux anomalies in the summer are significantly correlated with anomalies in autumn of the same year, over a large area of the North Pacific (Fig. 40a). The maximum correlations occur just eastward of the *Kuroshio region*. Similarly, autumn *Kuroshio* heat flux anomalies are significantly correlated with winter anomalies slightly further eastward (Fig. 40b). Winter heating anomalies over the *Kuroshio region* showed no significant correlation with spring heat flux anomalies over the North Pacific except in a small region south of the *Kuroshio region*.

Figures 41a,b illustrate similar correlations with a two season lag. The only large correlation is between summer *Kuroshio region* heat flux anomalies and winter heat flux

WINTER



SPRING

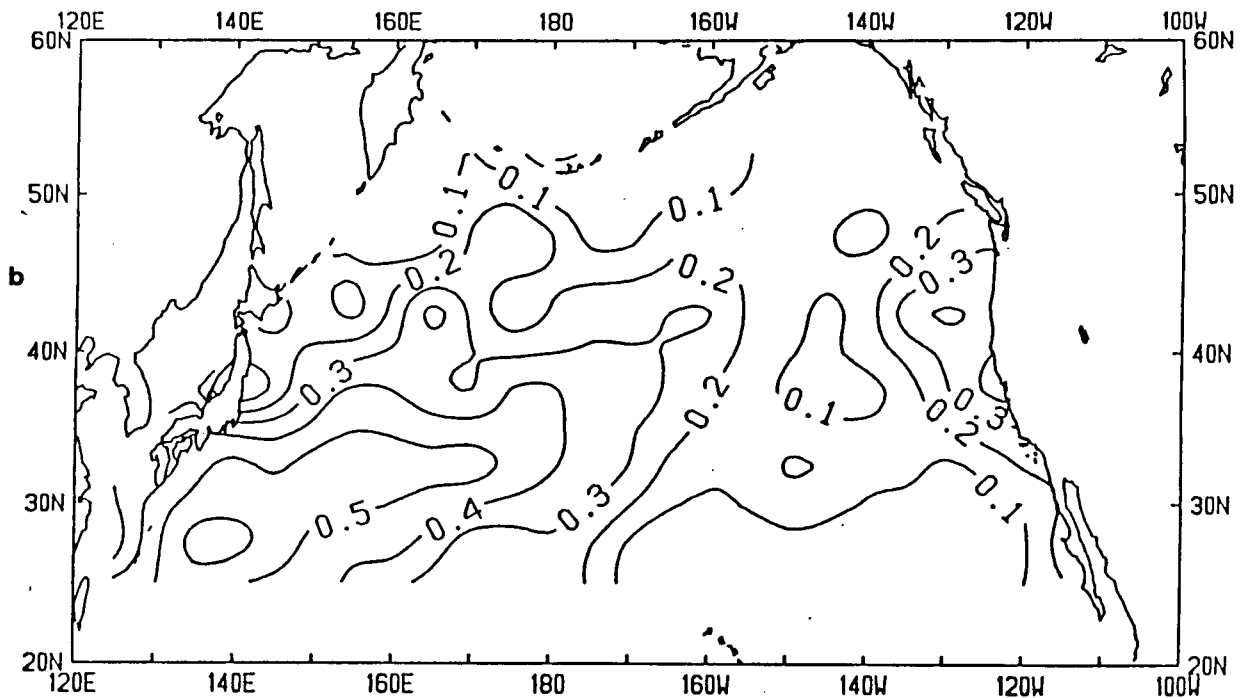
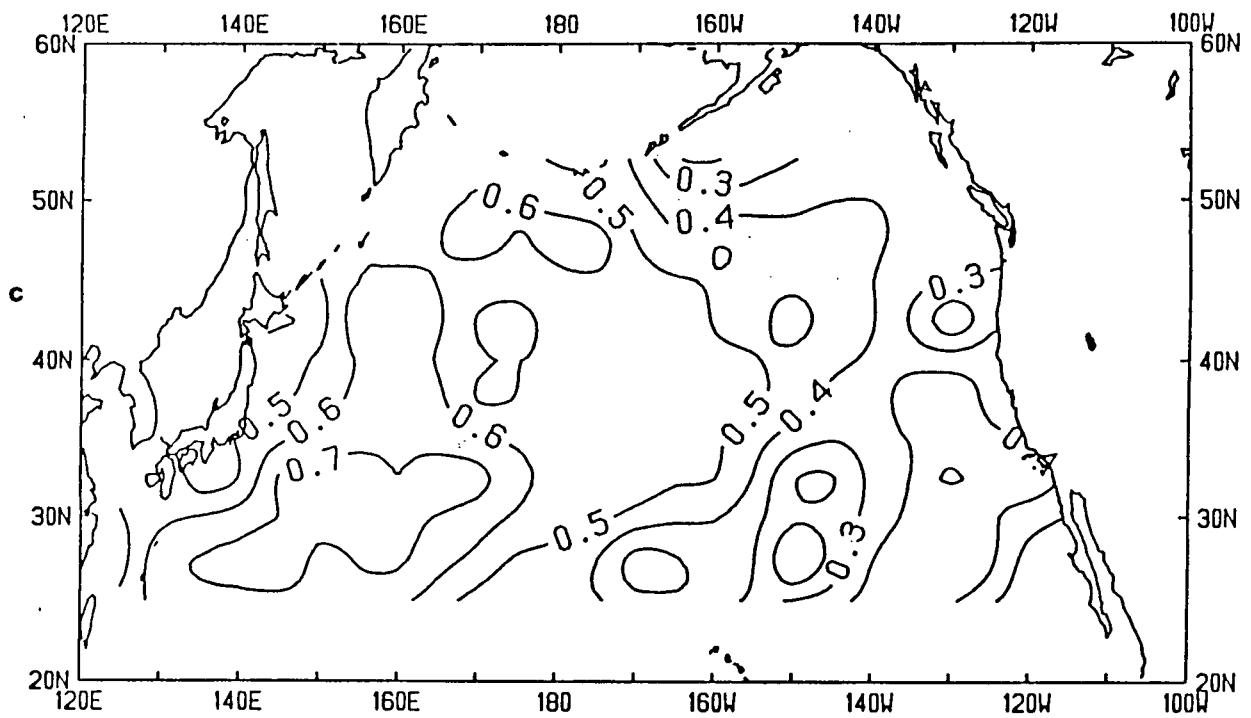


Figure 39 . Simultaneous correlations between the oceanic heat flux anomaly over the *Kuroshio* region and the heat flux anomaly throughout the whole North Pacific. a)—winter; b)—spring; c)—summer; d)—autumn.

SUMMER



AUTUMN

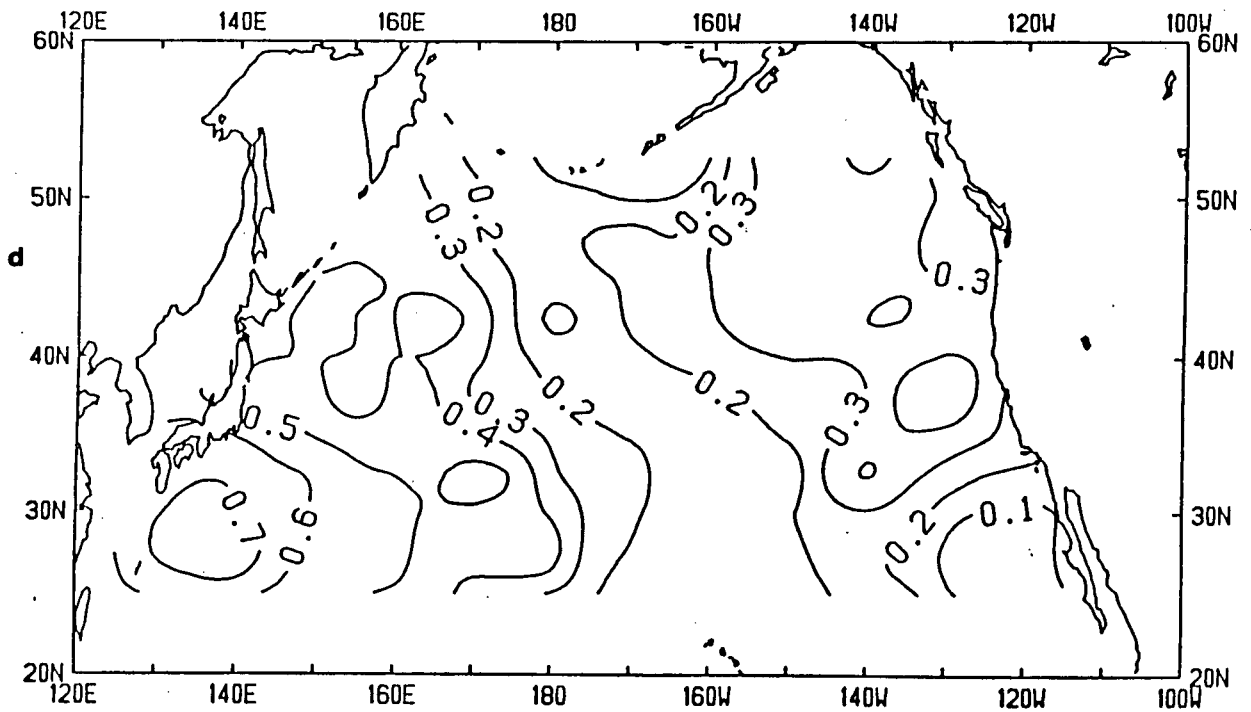
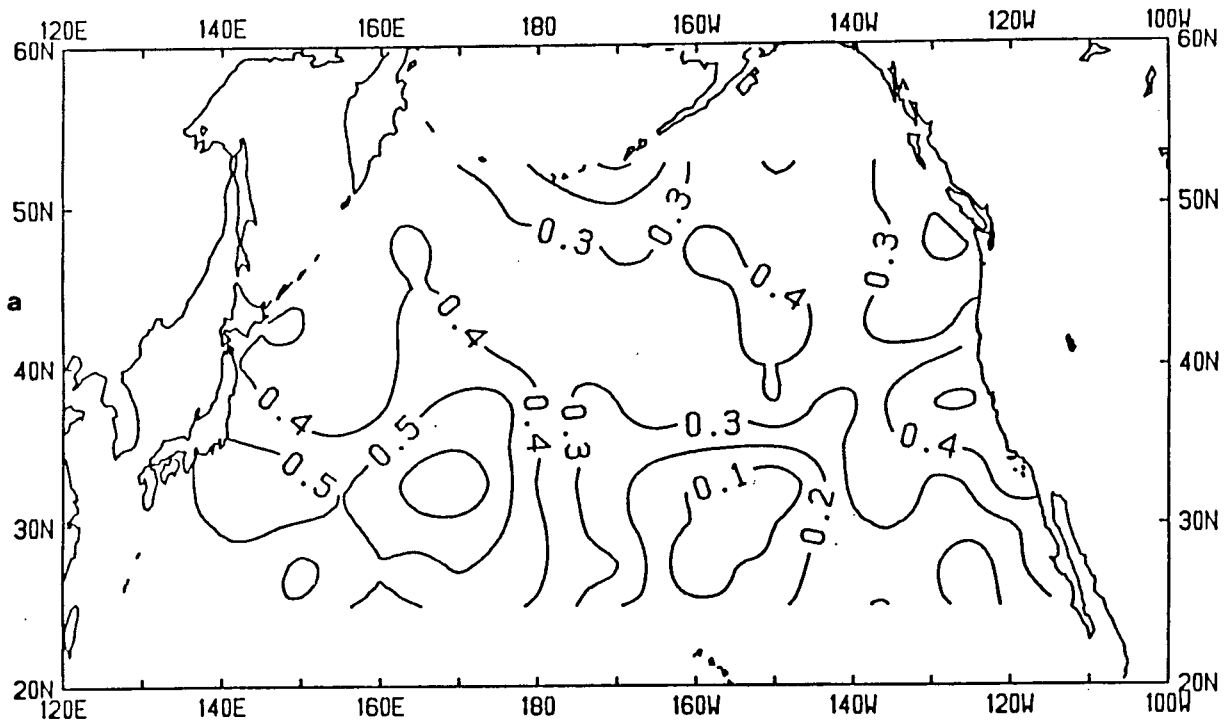


Figure 39 cont.

SUMMER-AUTUMN



AUTUMN-WINTER

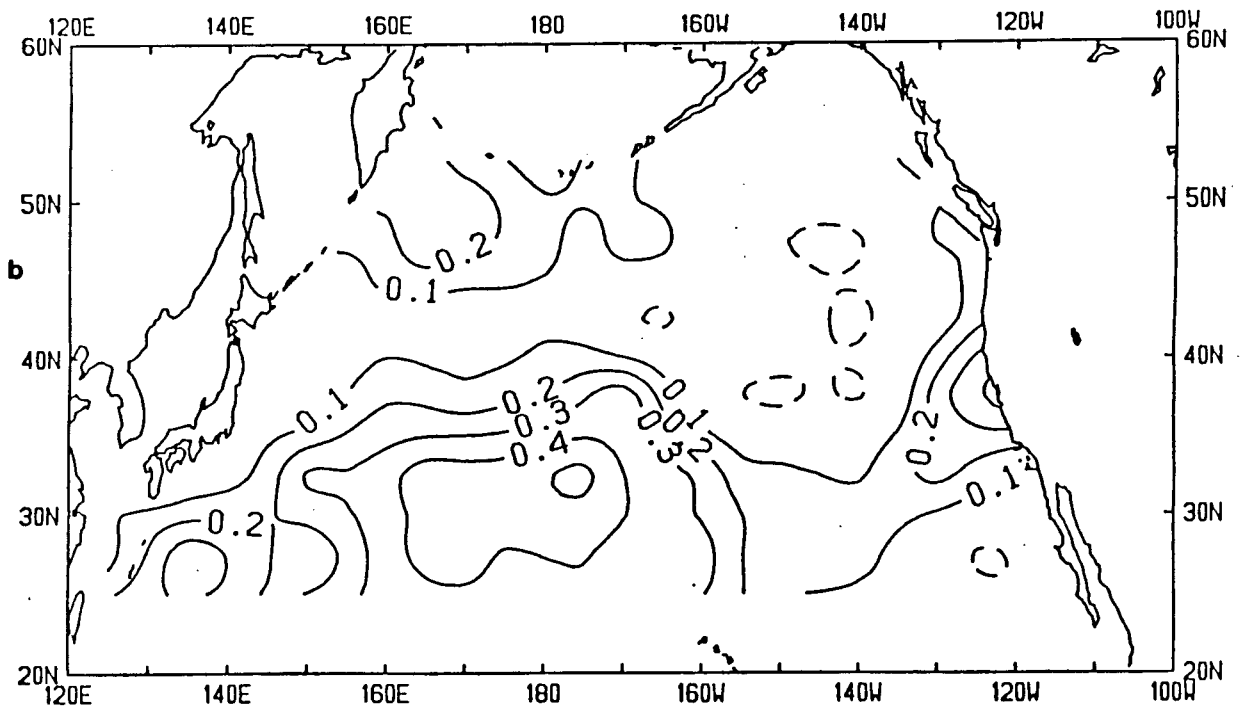


Figure 40 . Correlations between *Kuroshio region* heat flux anomalies in a)—summer; b)—autumn; and oceanic heating anomalies throughout the North Pacific in the following season.

anomalies further eastward (Fig. 41a). Once more Kuroshio winter heating anomalies are only significantly correlated with North Pacific anomalies in the small area south of the *Kuroshio region* (Fig. 41b).

The above results suggest that large heat flux anomalies over the *Kuroshio region* in the summer may persist until winter, moving eastward with time. This is in agreement with the discussion of Frankignoul (1985a, p. 359). Winter anomalies may also persist, but only in the area immediately south of the *Kuroshio region* (Fig. 41a).

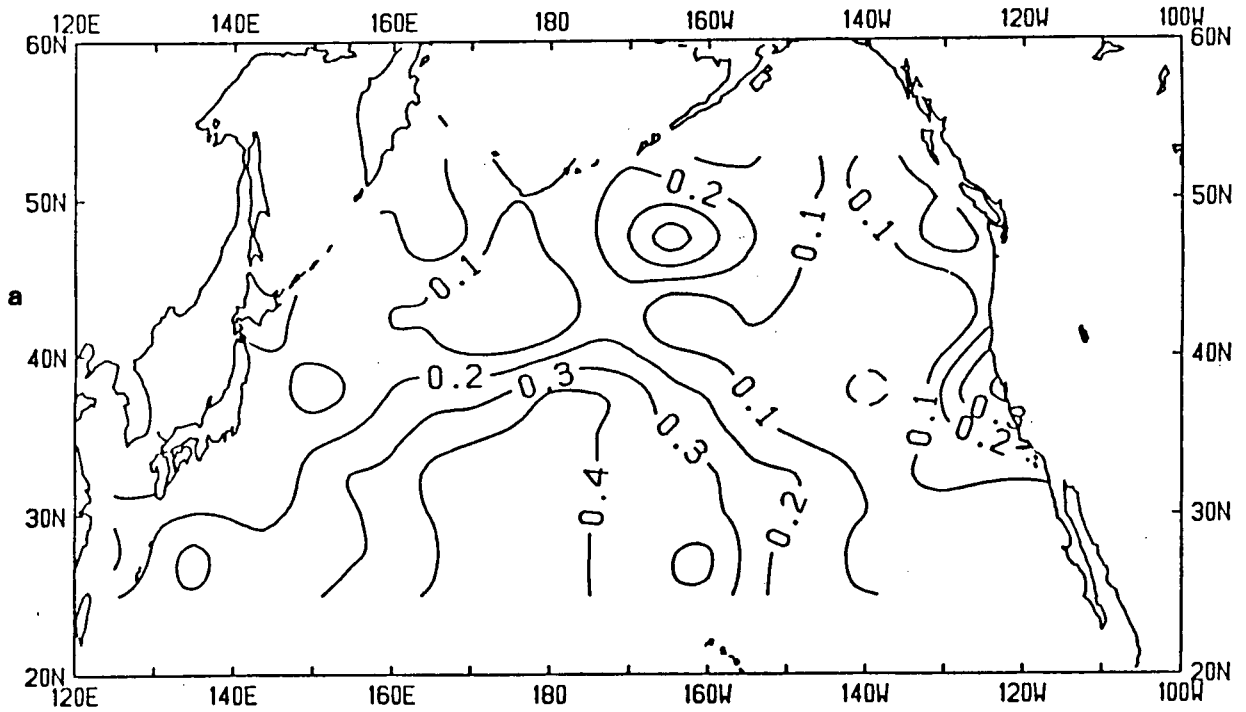
5.6 Winter Correlations between Kuroshio Heat Flux Anomalies and the Overlying Atmospheric Surface Pressure, and 500 & 700 mb heights

The magnitude of the oceanic heat flux over the Kuroshio and its adjacent area varies greatly from year to year (Zhao and McBean, 1986, 1987a,b, Weaver and Mysak, 1986a,b). The largest variance occurs in the winter season when anomalies up to 30% of the long term mean are observed. On the basis of a simultaneous monthly correlation analysis, Zhao and McBean (1987b) proposed that these heat flux anomalies have a profound effect on the overlying atmospheric circulation. They averaged the oceanic heat flux data over the *Kuroshio region* (Fig. 35) and correlated this with the atmospheric surface pressure and 700 mb geopotential height, over the northern hemisphere. Figures 42a–c illustrate results analogous to those of Zhao and McBean using seasonal statistics as opposed to monthly mean data.

The oceanic heat flux in winter has been averaged over the *Kuroshio region* and correlated with the winter surface pressure (Fig. 42a) and 700 & 500 mb geopotential heights (Figs. 42b,c, respectively), over the northern hemisphere. Since the surface pressure data was available for the period 1950–1979, the 700 mb data for the period 1963–1979, and the 500 mb data for the period 1956–1979, the correlation coefficients $r = 0.36$, $r = 0.47$, $r = 0.40$ correspond to the 0.05 confidence level in Figs. 42a,b,c, respectively.

There are three distinct regions of significant correlation: a)—Over eastern Asia, Kuroshio heat flux anomalies are significantly correlated with the surface pressure and the

SUMMER-WINTER



WINTER-SUMMER

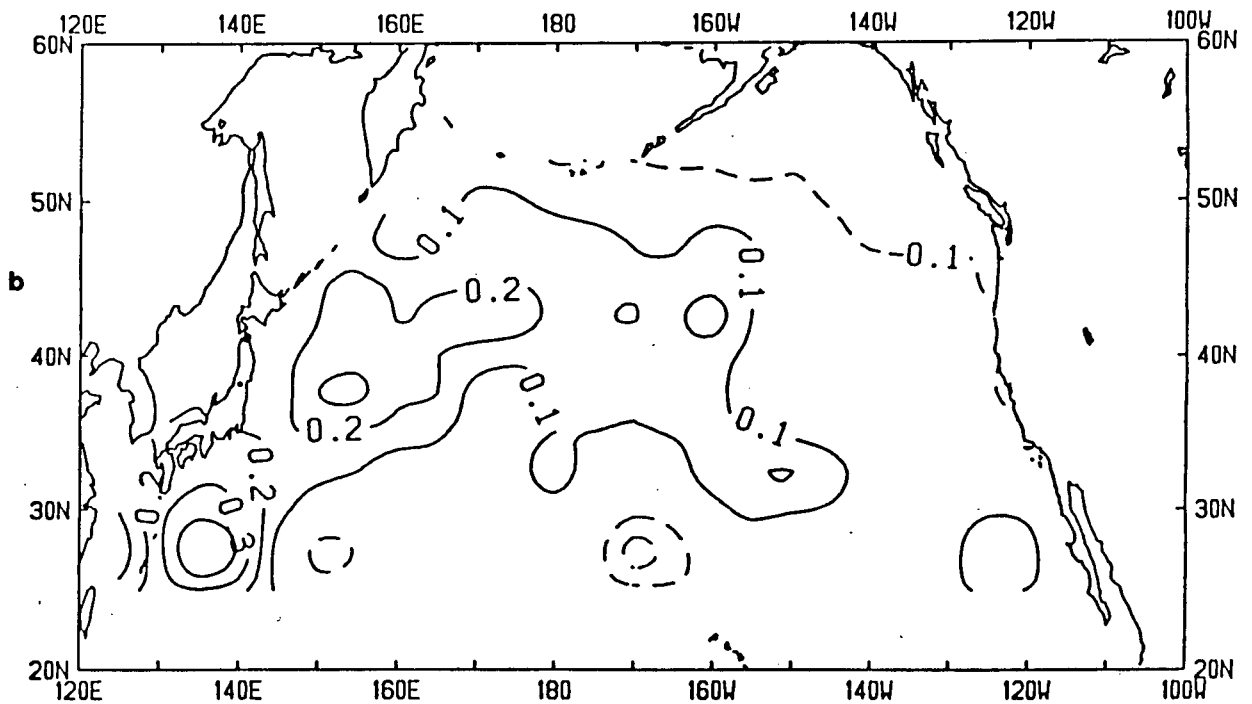


Figure 41 . Correlations between *Kuroshio* region heat flux anomalies in a)—summer; b)—winter; and oceanic heating anomalies throughout the North Pacific two seasons later.

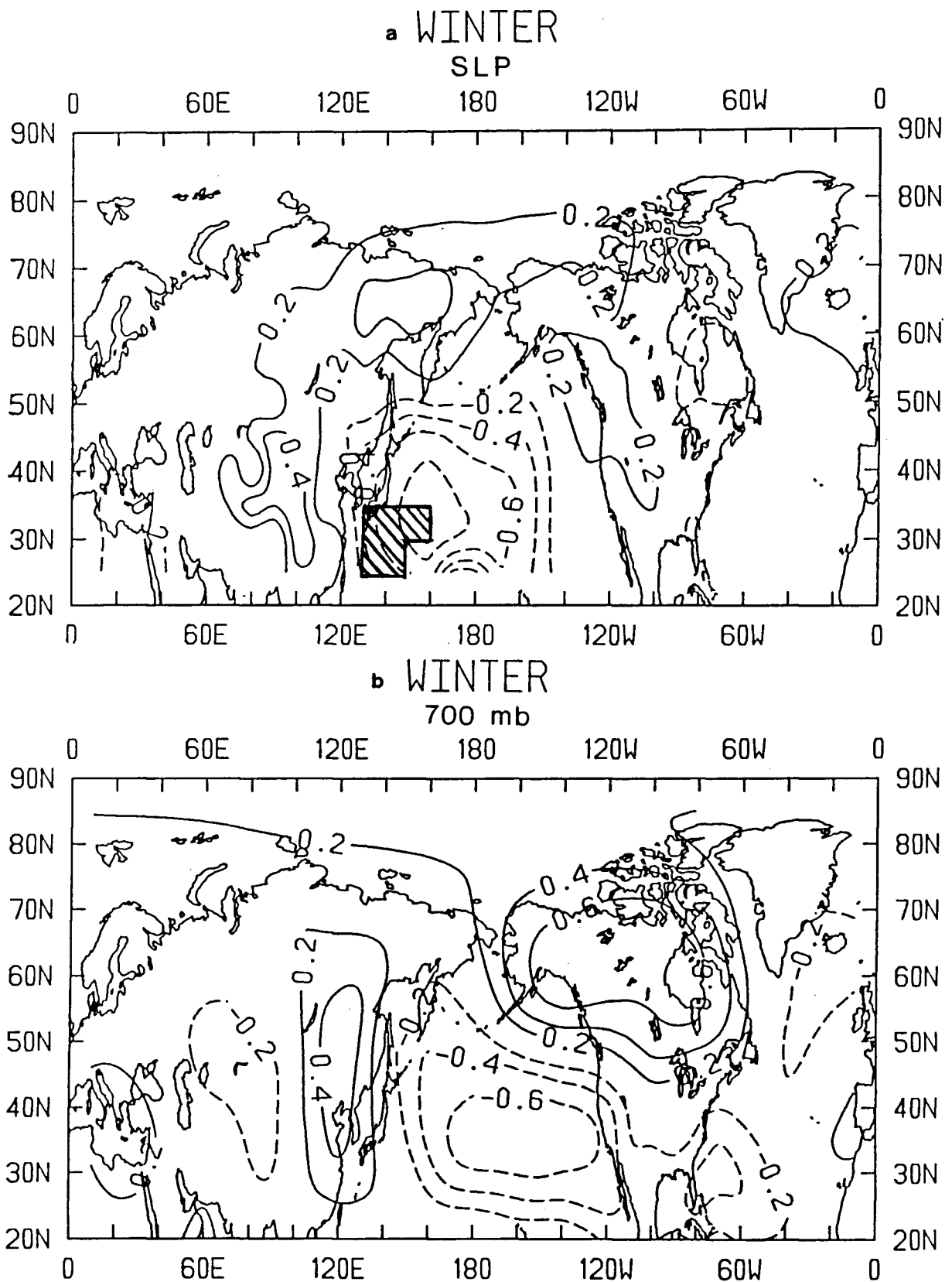


Figure 42 . Correlations between winter oceanic heat flux anomalies over the *Kuroshio* region (the hatched area in the western Pacific) and a)— surface pressure; b)— 700 mb geopotential height; c)— 500 mb geopotential height. A correlation coefficient of $r = 0.36, r = 0.47, r = 0.40$, corresponds to the 0.05 confidence level in a), b), and c), respectively.

c WINTER
500 mb

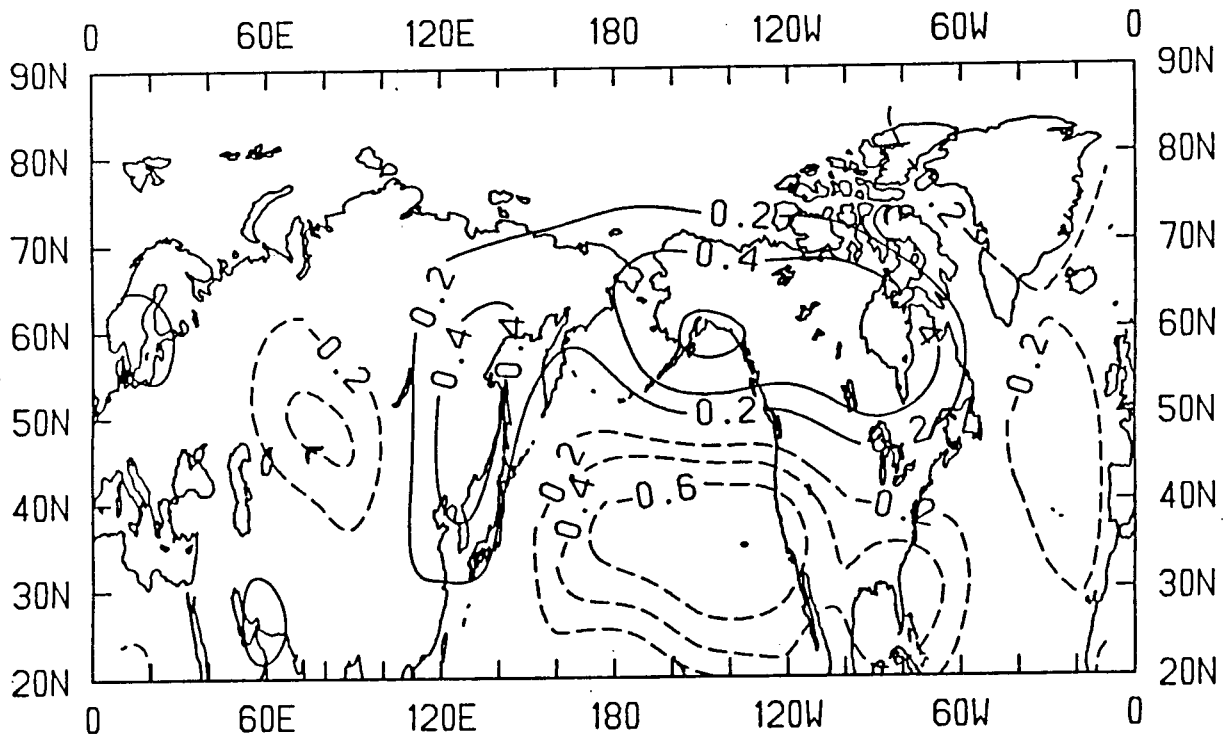


Figure 42 cont.

500 & 700 mb geopotential height data; b)— Over the central North Pacific there exists an extremely strong negative correlation, especially with the surface pressure data (Fig. 42a); c)— Over northern Canada there is another region of significant positive correlation, but only at the 700 and 500 mb heights (Figs. 42b,c, cf., Figs. 42a). One factor which may contribute to these large correlations is that the analysis used in determining the heat flux data (see Section 5.3) uses the atmospheric winds and temperature as parameters (see equations 5.3–5.6).

Zhao and McBean (1987b) argued that the higher the pressure over eastern Asia, the colder and dryer the air is over Siberia and the higher the wind velocities are over the *Kuroshio region*. Hence, the heat flux over the Kuroshio region would be larger. The resulting heat flux anomaly, they further argued, would create lower than normal pressures over the Kuroshio region. Since the influence of the Kuroshio region extends further eastward than the hatched area of Fig. 35 (Zhao and McBean 1986), they concluded that the lower than normal pressures would extend further eastward and hence cause the Aleutian low to shift southwestward during winter. In the following chapters this hypothesis will be examined using several quasigeostrophic linear models. It should be noted that the ridge/trough structure of the correlation plots (Figs. 42b,c) is often observed in teleconnection patterns associated with ENSO events, eg., Horel and Wallace, 1981; Emery and Hamilton, 1985; Mysak, 1986).

6. The Steady State Response of the Atmosphere to Midlatitude Heating with Various Zonal Structures

6.1 Introduction

Most linear wave theories of large-scale thermally-driven atmospheric motions have assumed a forcing $Q \propto \cos kx$ in order to model the differential heating associated with land and sea thermal contrasts (e.g., Frankignoul 1985a, who uses a two level β -plane channel model; Pedlosky 1979, who employs a continuously stratified β -plane model). One purpose of this chapter is to introduce more realistic zonal structures of the oceanic diabatic heating anomalies and hence to determine the effects of these distributions on the atmospheric stationary wave response. A second purpose of this chapter is to employ one particular zonal heating structure in order to find a simple explanation of the winter correlations of Zhao and McBean (1987b) and Weaver and Mysak (1986b) described in Section 5.6.

Weaver, Mysak and Bennett (1987a,b), hereafter called WMB, examined the effects of localized heating on the steady state atmospheric response using a continuously stratified quasigeostrophic model, linearized about a constant zonal flow U_0 . They found that for parameters applicable to North Pacific wintertime conditions, there was a strong local response and a constant far field response. The work of WMB will be briefly presented in this chapter.

In Chapter 7 we will compare the results of the model described in Section 6.2, with those from a two level model. The two level model results will then be compared with those from the steady state linear wave models of Egger (1977) (two level, hemispheric model with friction) and Hoskins and Karoly (1981) (five level primitive equation model) and with the GCM studies of Chervin *et al.* (1976, 1980), Kutzbach *et al.* (1977) and Frankignoul (1985b).

The outline of this chapter is as follows. In Section 6.2 the model and the assumed heating distributions are introduced. In Section 6.3 a line source zonal heating structure is

examined. The solution obtained from this line source heating is used as a Green's function in Section 6.4 to obtain solutions for rectangular and segmented cosine distributions. In Section 6.5 the solutions obtained in Sections 6.3 and 6.4 are analysed and compared with the solution obtained for a zonally periodic heat forcing. Finally, in Section 6.6 we examine the effect of sine forcing over one wavelength in order to model the atmospheric response to forcing with the structure of the first winter EOF of Zhao and McBean (1987a) (described in Chapter 5).

6.2 Description of the model

The model we use is the steady state non-dimensional, quasigeostrophic potential vorticity equation, linearized about a basic state with constant zonal flow U_0 . Let Ψ_S be the stream function of the basic state; thus

$$\Psi_S = -U_0 y. \quad (6.1)$$

We look for perturbations ϕ of the basic state (6.1) which are forced by an atmospheric heating anomaly, $Q = Q(x, y, z)$. Thus the total streamfunction is given by

$$\Psi = -U_0 y + \phi(x, y, z), \quad (6.2)$$

and the governing equation for ϕ is (Pedlosky, 1979 p.364)

$$U_0 \frac{\partial}{\partial x} \left\{ \frac{\partial^2 \phi}{\partial x^2} + \frac{\partial^2 \phi}{\partial y^2} + \frac{1}{\rho_s} \frac{\partial}{\partial z} \left\{ \frac{\rho_s}{S} \frac{\partial \phi}{\partial z} \right\} \right\} + \beta \frac{\partial \phi}{\partial x} = \frac{1}{\rho_s} \frac{\partial}{\partial z} \left\{ \frac{\rho_s Q}{S} \right\}, \quad 0 \leq z < \infty. \quad (6.3)$$

The horizontal coordinates have been scaled by $L = 10^3$ km, the vertical coordinate by $D = 10$ km, and the perturbation streamfunction by UL , where $U = 10 \text{ ms}^{-1}$ (as in Pedlosky, 1979). $\rho_s(z)$ is the non-dimensional basic state density; $S = N_s^2 D^2 / f_0^2 L^2$, is the non-dimensional stratification parameter, where N_s is the Brunt-Väisälä frequency of the basic state and f_0 is the Coriolis parameter. We assume that N_s is constant, so that S and the nondimensional density scale height $H = -\{\frac{1}{\rho_s} \frac{\partial \rho_s}{\partial z}\}^{-1}$ are constants. The appropriate boundary conditions for (6.3) will be given in Section 6.3.

Four types of zonal heating distributions will be considered here:

$$a) \quad Q_1 = Q_0 \cos ly e^{-\alpha z} \delta(x - p), \quad (6.4)$$

$$b) \quad Q_2 = \frac{Q_0}{2x_0} \cos ly e^{-\alpha z} \Pi\left(\frac{x}{2x_0}\right), \quad (6.5)$$

$$c) \quad Q_3 = \frac{\pi Q_0}{4x_0} \cos ly e^{-\alpha z} \Pi\left(\frac{x}{2x_0}\right) \cos\left(\frac{\pi x}{2x_0}\right), \quad (6.6)$$

$$d) \quad Q_4 = Q_0 \cos ly e^{-\alpha z} \cos kx, \quad (6.7)$$

where

$$\int_{-\infty}^{\infty} Q_1(x, y, z) dx = \int_{-\infty}^{\infty} Q_2(x, y, z) dx = \int_{-\infty}^{\infty} Q_3(x, y, z) dx. \quad (6.8)$$

Here $\delta(x - p)$ is the Dirac delta function and $\Pi(\frac{x}{2x_0})$ is the rectangular function, viz.,

$$\Pi\left(\frac{x}{2x_0}\right) = \begin{cases} 0, & \text{if } x > x_0; \\ 1, & \text{if } -x_0 < x < x_0; \\ 0, & \text{if } x < -x_0. \end{cases} \quad (6.9)$$

All four heating distributions assume a vertical structure $\propto e^{-\alpha z}$ for mathematical simplicity. Although this approximation is somewhat crude, it does agree well with the data of Masuda (1983) over most oceanic regions in winter (where the latent heat is often released locally), especially over the *Kuroshio region* defined in Section 5.2.

We now provide motivation for our choice of the zonal structures (6.4)–(6.7). In Chapter 5 we noted that the horizontal distribution of oceanic heat flux anomalies varies greatly from year to year. This is particularly well illustrated in Figs. 38a, b for winter (December, January, February), where anomalies between ten and thirty percent of the seasonal long term mean are observed in the proximity of and eastward of the *Kuroshio region*. The rectangular heating source is therefore introduced to model heating over a broad expanse (Fig. 38a), whereas the line source heat forcing is used as a model for localized heating (Fig. 38b). A segmented cosine heating structure is introduced to examine the effect of forcing with a half wavelength cosine function of wavenumber $k = \frac{\pi}{2x_0}$ which can then be compared with the response to the frequently used $Q \propto \cos kx$ forcing (Pedlosky, 1979).

6.3 Line Source Heating

We begin by determining the motion due to a line source heating given by equation (6.4). Substitute (6.4) into (6.3), let $\phi(x, y, z) = \bar{\phi}(x, z)\cos ly$, and define the Fourier transform

$$\hat{\phi}(\xi, z) = \frac{1}{\sqrt{2\pi}} \int_{-\infty}^{\infty} \bar{\phi}(x, z) e^{-i\xi x} dx. \quad (6.10)$$

We then find that $\hat{\phi}(\xi, z)$ satisfies,

$$\hat{\phi}_{zz} - \frac{1}{H} \hat{\phi}_z + S \left\{ \frac{\beta}{U_0} - l^2 - \xi^2 \right\} \hat{\phi} = - \frac{Q_0(1 + \alpha H) e^{-ip\xi} e^{-\alpha z}}{i\xi \sqrt{2\pi} U_0 H}. \quad (6.11)$$

The solution to (6.11) can be written as

$$\hat{\phi}(\xi, z) = e^{z/2H} \{ A(\xi) e^{im(\xi)z} + B(\xi) e^{-im(\xi)z} \} + C(\xi) e^{-\alpha z}, \quad (6.12)$$

where

$$C(\xi) = \frac{-\alpha Q_0(1 + (\alpha H)^{-1}) e^{-ip\xi}}{i\xi \sqrt{2\pi} U_0 \left\{ \alpha^2 \left(1 + (\alpha H)^{-1} \right) + S \left(\frac{\beta}{U_0} - l^2 - \xi^2 \right) \right\}}, \quad (6.13)$$

$$m(\xi) = \left\{ S \left(\frac{\beta}{U_0} - l^2 - \xi^2 \right) - \frac{1}{4H^2} \right\}^{\frac{1}{2}} \equiv \{ S(q^2 - \xi^2) \}^{\frac{1}{2}}, \quad (6.14)$$

and $A(\xi)$, $B(\xi)$ are to be determined from boundary conditions at $z = 0$ and at $z \rightarrow \infty$. Since the heating is assumed to have $e^{-\alpha z}$ vertical structure, the separable, forced solution of (6.11) simply has $e^{-\alpha z}$ vertical dependence. The free wave solution has vertical structure independent of α , while the dependence of $A(\xi)$ and $B(\xi)$ on α arises from the application of the boundary conditions discussed below. The assumption of an unbounded domain ($-\infty < x < \infty$) needed to define the Fourier transform (6.10) will be justified in Chapter 7 by using friction arguments, and in Chapter 8 by comparing the results of this chapter with those from a time dependent zonally periodic model.

We take the inverse Fourier transform of (6.12) to get,

$$\bar{\phi}(x, z) = \frac{1}{\sqrt{2\pi}} \int_{-\infty}^{\infty} e^{i\xi x} \{ \{ A(\xi) e^{im(\xi)z} + B(\xi) e^{-im(\xi)z} \} e^{z/2H} + C(\xi) e^{-\alpha z} \} d\xi, \quad (6.15)$$

where if $\xi^2 > \frac{\beta}{U_0} - l^2 - \frac{1}{4H^2S}$ we replace $im(\xi)$ by $-\bar{q}(\xi)$ with $\bar{q}(\xi)$ defined by the positive square root,

$$\bar{q}(\xi) = \left\{ S(\xi^2 + l^2 - \frac{\beta}{U_0}) + \frac{1}{4H^2} \right\}^{\frac{1}{2}}. \quad (6.16)$$

The boundary condition at $z = 0$ is obtained by assuming the vertical velocity w is zero at the surface, so that changes in the potential temperature at $z = 0$ are solely due to surface heating. For all the heating distributions (6.4)–(6.7), this boundary condition may be written as (Pedlosky, 1979 p.364)

$$U_0 \frac{\partial^2 \phi}{\partial x \partial z} = Q_j(x, y, 0) \quad (j = 1, 2, 3, 4). \quad (6.17)$$

Upon taking the Fourier transform of (6.17) with $\phi = \bar{\phi} \cos ly$ and the heating (6.4), we obtain

$$\hat{\phi}_z = \frac{Q_0 e^{-ip\xi}}{i\xi \sqrt{2\pi} U_0} \quad \text{at } z = 0. \quad (6.18)$$

There are two cases which need to be considered in order to apply the boundary condition at $z \rightarrow \infty$.

case 1: $\xi^2 > \frac{\beta}{U_0} - l^2 - \frac{1}{4H^2S}$.

Since $\rho_s |\hat{\phi}|^2$ must remain finite as $z \rightarrow \infty$, we take $B(\xi) = 0$.

case 2: $\xi^2 < \frac{\beta}{U_0} - l^2 - \frac{1}{4H^2S}$.

Here we use a radiation condition which requires that the energy flux at $z \rightarrow \infty$ be directed outwards (Pedlosky, 1979 p.367). Hence for $\xi > 0$ we take $B(\xi) = 0$ and for $\xi < 0$ we take $A(\xi) = 0$.

Let us now evaluate $\int_{-\infty}^{\infty} C(\xi) e^{i\xi x} d\xi$. Define

$$a^2 = \frac{\alpha^2}{S} (1 + (\alpha H)^{-1}) + \frac{\beta}{U_0} - l^2, \quad (6.19)$$

$$\chi = \frac{\alpha Q_0 (1 + (\alpha H)^{-1})}{\sqrt{2\pi} U_0 S}, \quad (6.20)$$

so that

$$C(\xi) = \frac{\chi e^{-ip\xi}}{i\xi(\xi - a)(\xi + a)}. \quad (6.21)$$

For typical values of α , H , S , β , U_0 and l , $a^2 > 0$ and hence $a > 0$ (see section 6.5). We can in fact always ensure that $a^2 > 0$ by requiring that the heating be sufficiently trapped at the surface (i.e., take sufficiently large α). When Rayleigh friction is included in the problem (see Appendix I), the poles of $C(\xi)$ at $\xi = 0, \pm a$ move into the upper half plane. For $x > p$ we close the contour of integration for the inverse Fourier transform in the upper half plane and thus pick up the contributions from the residues at all three poles. We also apply Jordan's Lemma to the semicircular contour, and let $r_0 \rightarrow 0$, where r_0 is the Rayleigh friction coefficient (see Appendix I). Similarly, for $x < p$ we close the contour in the lower half plane and get no pole contributions. The result is

$$\int_{-\infty}^{\infty} C(\xi) e^{i\xi x} d\xi = \frac{2\pi\chi}{a^2} \{ \cos a(x-p) - 1 \} H(x-p), \quad (6.22)$$

where $H(x-p)$ is the Heaviside step function defined by,

$$H(x-p) = \begin{cases} 1, & \text{if } x > p; \\ 0, & \text{if } x < p. \end{cases} \quad (6.23)$$

We can now evaluate (6.15). With $\phi(x, y, z) = \bar{\phi}(x, z) \cos ly$ and using the aforementioned boundary conditions at $z = 0$ and $z \rightarrow \infty$, we find that

$$\phi(x, y, z) = \frac{\cos ly}{\sqrt{2\pi}} \left\{ e^{z/2H} I_1 + \frac{2\pi\chi e^{-\alpha z}}{a^2} \{ \cos a(x-p) - 1 \} H(x-p) \right\}, \quad (6.24)$$

where the two possible forms for I_1 are given in (6.25) and (6.27). If we let $q^2 \equiv \frac{\beta}{U_0} - l^2 - \frac{1}{4H^2S}$ and if $q^2 < 0$, the solution is purely exponentially decaying in z and

$$I_1 = -\frac{\eta}{i} \int_{-\infty}^{\infty} \frac{\{ \bar{q}(\xi) + c \} e^{i\xi(x-p)} e^{-\bar{q}(\xi)z}}{\xi(\xi-a)(\xi+a)} d\xi, \quad (6.25)$$

where \bar{q} is defined by (6.16) and

$$c = \frac{1}{2H}, \quad \eta = \frac{Q_0}{\sqrt{2\pi}U_0S}. \quad (6.26)$$

If $q^2 > 0$, the solution consists of a response sinusoidal in z and a response decaying in z .

I_1 can be expressed in the form

$$I_1 = -2\eta \int_0^q \frac{\{c \sin(\xi(x-p) + m(\xi)z) - m(\xi) \cos(\xi(x-p) + m(\xi)z)\}}{\xi(\xi-a)(\xi+a)} d\xi \\ - 2\eta \int_q^\infty \frac{\{\bar{q}(\xi) + c\} \sin \xi(x-p) e^{-\bar{q}(\xi)z}}{\xi(\xi-a)(\xi+a)} d\xi. \quad (6.27)$$

Let us a priori assume that the solution is exponentially decaying with height everywhere (i.e., $q^2 < 0$). This will be justified for our parameters in Section 6.5 below. The function

$$\bar{q}(\xi) = S^{\frac{1}{2}} \{\xi^2 + b^2\}^{\frac{1}{2}}, \quad (6.28)$$

with

$$b^2 \equiv l^2 + \frac{1}{4H^2S} - \frac{\beta}{U_0} > 0, \quad (6.29)$$

has branch points at $\xi = \pm ib$ and hence we introduce branch cuts along the imaginary axis from $\xi = \pm ib$ to $\pm i\infty$ (see Fig. 43). We evaluate the integral I_1 , given by (6.25), using the solid contour shown in Fig. 43 for $x > p$, the dashed contour for $x < p$. By Cauchy's theorem,

$$I_{1R} + \int_{C_R} + \int_{C_A} + \int_{C_B} + \int_{C_b} = 2\pi i \sum \text{Res in UHP, for } x > p, \quad (6.30)$$

where

$$I_{1R} = -\frac{\eta}{i} \int_{-R}^R \frac{\{S^{\frac{1}{2}}(\xi^2 + b^2)^{\frac{1}{2}} + c\} e^{i\xi(x-p)} e^{-S^{\frac{1}{2}}(\xi^2 + b^2)^{\frac{1}{2}}z}}{\xi(\xi-a)(\xi+a)} d\xi. \quad (6.31)$$

By Jordan's lemma $\lim_{R \rightarrow \infty} \int_{C_R} = 0$; also it is easy to show that $\lim_{r \rightarrow 0} \int_{C_b} = 0$ with C_b defined by $ib + re^{i\theta}$, $(\frac{\pi}{2} \geq \theta \geq -\frac{3\pi}{2})$. The contribution from the three poles at $\xi = 0, \pm a$ in the right hand side of (6.30) is

$$2\pi i \sum \text{Res in UHP} = -\frac{2\pi\eta}{a^2} \{(\lambda + c)e^{-\lambda z} \cos a(x-p) - (S^{\frac{1}{2}}b + c)e^{-S^{1/2}bz}\}, \quad (6.32)$$

where

$$\lambda = S^{\frac{1}{2}}(a^2 + b^2)^{\frac{1}{2}}. \quad (6.33)$$

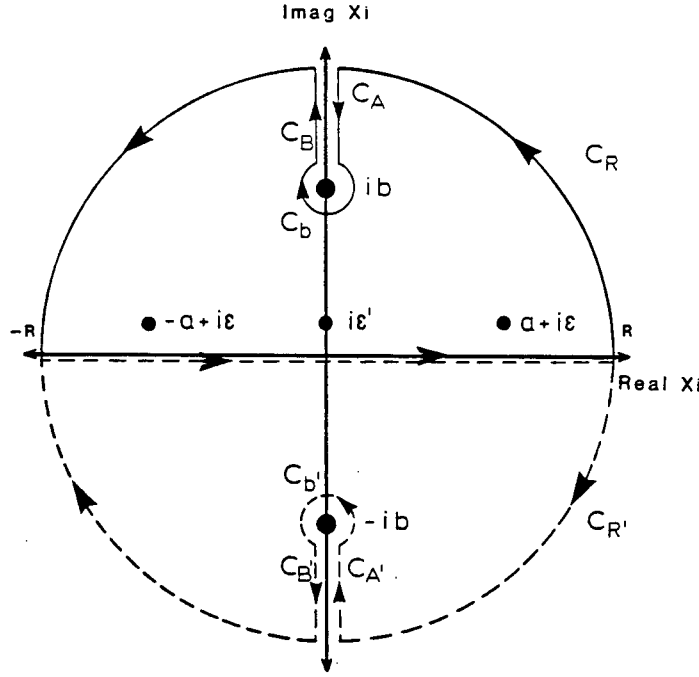


Figure 43 . Contour of integration for the evaluation of I_{1R} , defined by equation (6.31). The solid line is for $x > p$, the dashed line is for $x < p$. ϵ and ϵ' are the first order perturbations into the upper half plane of the poles at $\xi = \pm a$ and $\xi = 0$, respectively, when Rayleigh friction is included in the problem.

In \int_{C_A} , we let $\xi = it$ and take the positive value for the root of (6.28). Similarly, in \int_{C_B} we let $\xi = it$ and take the negative root of (28). Adding the contributions from \int_{C_A} and \int_{C_B} we get, for $x > p$,

$$\int_{C_A} + \int_{C_B} = 2\eta \int_b^\infty \frac{e^{-(x-p)t}}{t(t^2 + a^2)} \left\{ c \sin(S^{\frac{1}{2}}(t^2 - b^2)^{\frac{1}{2}} z) - S^{\frac{1}{2}}(t^2 - b^2)^{\frac{1}{2}} \cos(S^{\frac{1}{2}}(t^2 - b^2)^{\frac{1}{2}} z) \right\} dt. \quad (6.34)$$

For $x < p$, the application of Cauchy's theorem using the dashed contour in Fig. 43 gives

$$I_{1R} + \int_{C_R'} + \int_{C_A'} + \int_{C_B'} + \int_{C_b'} = 0. \quad (6.35)$$

Once again there is no contribution from the contour around the branch point at $\xi = -ib$,

and $\lim_{R \rightarrow \infty} \int_{C'_R} = 0$ by Jordan's lemma. The summation of $\int_{C'_A}$ and $\int_{C'_B}$ yields,

$$\int_{C'_A} + \int_{C'_B} = 2\eta \int_b^{\infty} \frac{e^{(x-p)t}}{t(t^2 + a^2)} \left\{ c \sin(S^{\frac{1}{2}}(t^2 - b^2)^{\frac{1}{2}} z) - S^{\frac{1}{2}}(t^2 - b^2)^{\frac{1}{2}} \cos(S^{\frac{1}{2}}(t^2 - b^2)^{\frac{1}{2}} z) \right\} dt. \quad (6.36)$$

Here we have put $\xi = -it$ and have taken the positive and negative roots of (6.28) in $\int_{C'_A}$ and $\int_{C'_B}$, respectively.

The solution for $\phi(x, y, z)$ is obtained by substituting (6.34) and (6.32) into (6.30), (6.36) into (6.35) and then substituting I_1 into (6.24). The result is

$$\begin{aligned} \phi(x, y, z) = & \frac{2\cos ly}{\sqrt{2\pi}} \left\{ \frac{\pi H(x-p)}{a^2} \left\{ \cos a(x-p) \left\{ \chi e^{-\alpha z} - \eta(c+\lambda) e^{(c-\lambda)z} \right\} \right. \right. \\ & \left. \left. + \eta(S^{\frac{1}{2}}b + c) e^{(c-S^{\frac{1}{2}}b)z} - \chi e^{-\alpha z} \right\} \right. \\ & \left. + \eta e^{cz} \int_b^{\infty} \frac{e^{-|x-p|t}}{t(t^2 + a^2)} \left\{ -c \sin(S^{\frac{1}{2}}(t^2 - b^2)^{\frac{1}{2}} z) + S^{\frac{1}{2}}(t^2 - b^2)^{\frac{1}{2}} \cos(S^{\frac{1}{2}}(t^2 - b^2)^{\frac{1}{2}} z) \right\} dt \right\}. \quad (6.37) \end{aligned}$$

Now from (6.19), (6.20), (6.26), (6.29), and (6.33) we find that $c - \lambda = -\alpha$ and $\eta(c + \lambda) = \chi$ so that (6.37) reduces to

$$\begin{aligned} \phi(x, y, z) = & \frac{2\cos ly}{\sqrt{2\pi}} \left\{ \frac{\pi H(x-p)}{a^2} \left\{ \eta(S^{\frac{1}{2}}b + c) e^{(c-S^{\frac{1}{2}}b)z} - \chi e^{-\alpha z} \right\} \right. \\ & \left. + \eta e^{cz} \int_b^{\infty} \frac{e^{-|x-p|t}}{t(t^2 + a^2)} \left\{ -c \sin(S^{\frac{1}{2}}(t^2 - b^2)^{\frac{1}{2}} z) + S^{\frac{1}{2}}(t^2 - b^2)^{\frac{1}{2}} \cos(S^{\frac{1}{2}}(t^2 - b^2)^{\frac{1}{2}} z) \right\} dt \right\}. \quad (6.38) \end{aligned}$$

The steady state response therefore consists of a locally trapped component exponentially decaying in x away from the source (which arises from the integration along the branch cuts) and an x -independent component for $x > p$ (which is the contribution from the pole at $\xi = 0$). For $x < p$, only the exponentially decaying integral component is allowed. Further analysis of equation (6.38) will be given in Sections 6.4 and 6.5.

6.4 Solutions for Various Zonal Distributions of Heating

In this section we obtain the atmospheric response to the zonal heating distributions (6.5), (6.6) and (6.7). We assume in all cases that $q^2 < 0$ (see 6.14) so that the atmospheric

response is exponentially decaying in height. To find the response to the rectangular (R) and segmented cosine (C) distributions, the line source heating solution (6.38) is used as a Green's function. Hence

$$\phi_{R,C}(x, y, z) = \int_{-\infty}^{\infty} f_{R,C}(p) G(x, y, z; p) dp, \quad (6.39)$$

where $f_R(p) = \frac{1}{2x_0} \Pi(\frac{p}{2x_0})$, $f_C(p) = \frac{\pi}{4x_0} \Pi(\frac{p}{2x_0}) \cos(\frac{\pi p}{2x_0})$ and $G(x, y, z; p)$ is the solution (6.38) of the line source heating problem.

Consider first the rectangular heating distribution (6.5). Upon substituting $f_R(p)$ and $G(x, y, z; p)$ into (6.39) and evaluating the integral, we obtain

$$\begin{aligned} \phi(x, y, z) = & \frac{2\eta \cos y e^{cz}}{\sqrt{2\pi} x_0} \int_b^{\infty} \frac{\{-c \sin(S^{\frac{1}{2}}(t^2 - b^2)^{\frac{1}{2}} z) + S^{\frac{1}{2}}(t^2 - b^2)^{\frac{1}{2}} \cos(S^{\frac{1}{2}}(t^2 - b^2)^{\frac{1}{2}} z)\}}{t^2(t^2 + a^2)} \\ & \times \left\{ \begin{array}{ll} e^{-|x|t} \sinh x_0 t, & \text{if } |x| \geq x_0; \\ \{1 - e^{-x_0 t} \cosh xt\}, & \text{if } |x| \leq x_0; \end{array} \right\} dt \\ & + \frac{\sqrt{2\pi} \cos y}{a^2} \left\{ \eta(S^{\frac{1}{2}} b + c) e^{(c - S^{\frac{1}{2}} b)z} - \chi e^{-\alpha z} \right\} \begin{cases} 0, & \text{if } x \leq -x_0; \\ \frac{(x + x_0)}{2x_0}, & \text{if } |x| \leq x_0; \\ 1, & \text{if } x \geq x_0. \end{cases} \end{aligned} \quad (6.40)$$

The solution for the segmented cosine distribution (equation 6.6) can be evaluated in a similar way. The result is

$$\begin{aligned} \phi(x, y, z) = & \frac{2\eta \cos y e^{cz}}{\sqrt{2\pi}} \int_b^{\infty} \frac{\{-c \sin(S^{\frac{1}{2}}(t^2 - b^2)^{\frac{1}{2}} z) + S^{\frac{1}{2}}(t^2 - b^2)^{\frac{1}{2}} \cos(S^{\frac{1}{2}}(t^2 - b^2)^{\frac{1}{2}} z)\}}{t(t^2 + a^2)(1 + \frac{4x_0^2 t^2}{\pi^2})} \\ & \times \left\{ \begin{array}{ll} e^{-|x|t} \cosh x_0 t, & \text{if } |x| \geq x_0; \\ e^{-x_0 t} \cosh xt + \frac{2x_0 t}{\pi} \cos(\frac{\pi x}{2x_0}), & \text{if } |x| \leq x_0; \end{array} \right\} dt \\ & + \frac{\sqrt{2\pi} \cos y}{a^2} \left\{ \eta(S^{\frac{1}{2}} b + c) e^{(c - S^{\frac{1}{2}} b)z} - \chi e^{-\alpha z} \right\} \begin{cases} 0, & \text{if } x \leq -x_0; \\ \frac{1}{2} \{1 + \sin(\frac{\pi x}{2x_0})\}, & \text{if } |x| \leq x_0; \\ 1, & \text{if } x \geq x_0. \end{cases} \end{aligned} \quad (6.41)$$

Equations (6.38), (6.40) and (6.41) show that the heating constant α has no effect on the horizontal structure of the solutions. The vertical structure of the response depends

trivially on α since b is independent of α (see 6.29). As α is increased the magnitude of the response decreases and becomes more surface trapped.

Finally, consider the zonally periodic heating (equation 6.7). The solution for heating of this form was obtained by Pedlosky (1979 p. 368). In the notation of this thesis,

$$\phi(x, y, z) = \frac{\sqrt{2\pi} \cos ly \sin kx}{k(k^2 - a^2)} \left\{ \chi e^{-\alpha z} - \eta(c + \hat{q})e^{(c-\hat{q})z} \right\}, \quad (6.42)$$

where,

$$\hat{q} = \left\{ S(k^2 + l^2 - \frac{\beta}{U_0}) + \frac{1}{4H^2} \right\}^{\frac{1}{2}}. \quad (6.43)$$

The solutions (6.40) and (6.41) are continuous $\forall x$ and tend to the solution (6.38), for the line source heating, in the limit as $x_0 \rightarrow 0$. Both the solutions (6.40) and (6.41) reveal a local response, with magnitude dependent on the the size of b (defined by 6.29). Decreasing b (i.e., decreasing the meridional wavenumber, l), has the effect of increasing the magnitude of the local response.

Resonance does not occur in Pedlosky's solution (6.42) at $k = a$ (contrary to his claim; Pedlosky, 1979 p. 369) since both the numerator and denominator vanish. A simple application of l'Hôpital's rule gives

$$\lim_{k \rightarrow a} \phi(x, y, z) = \frac{\sqrt{2\pi} S \sin ax}{2a\lambda} \cos ly e^{-\alpha z} (\chi z - \eta). \quad (6.44)$$

6.5 Discussion

We now obtain typical values for the nondimensional parameters introduced in the previous analysis. In terms of dimensional variables (Pedlosky 1979),

$$\beta = \frac{\beta_0 L^2}{U}, \quad S = \frac{N_s^2 D^2}{f_0^2 L^2}, \quad H = \frac{RT_*}{gD}, \quad Q_0 = \frac{Q_* gD}{C_p T_* f_0 U^2}, \quad (6.45)$$

where L , D and U were defined in Section 6.2, T_* is the temperature of the assumed isothermal atmosphere, R is the gas constant, C_p is the specific heat at constant pressure and Q_* is the imposed heating amplitude. Take $g = 10 \text{ ms}^{-2}$, $T_* = 260 \text{ K}$, $C_p = 1005 \text{ J kg}^{-1} \text{ K}^{-1}$,

$R = 300 \text{ Jkg}^{-1}\text{K}^{-1}$, $N_s = 1 \times 10^{-2}\text{s}^{-1}$, $Q_s = 0.022 \text{ m}^2\text{s}^{-3}$ and $\beta_0 = 1.9 \times 10^{-11}\text{m}^{-1}\text{s}^{-1}$, $f_0 = 8.4 \times 10^{-5}\text{s}^{-1}$ for a β -plane centered at 35°N . Hence (6.45) gives,

$$\beta = 1.9, \quad S = 1.4, \quad H = 0.78, \quad Q_0 = 1.0. \quad (6.46)$$

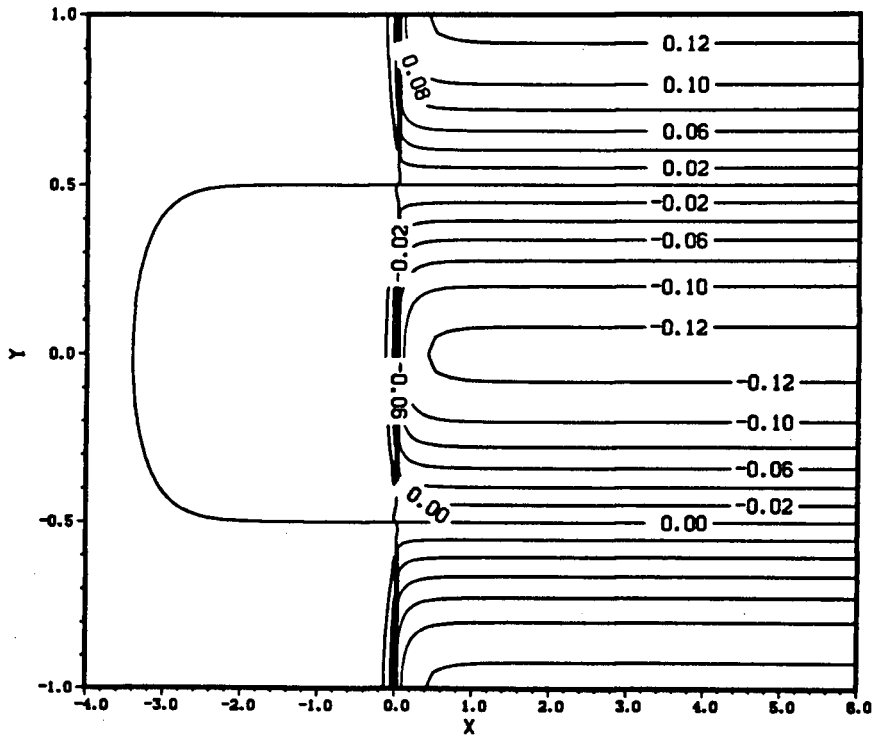
The constant zonal flow in the basic state is taken as $U_0 = 1.0$ in non-dimensional units, and the trapping scale of the imposed heating perturbation is taken as $\alpha = 4.0$, so that in dimensional variables the heating has an e-folding height of 2.5 km. If a larger α were used (ie., the heating was trapped nearer to the ocean surface), the horizontal structure of the solutions to be discussed below would be the same. The magnitudes would decrease as discussed in the last section and the response would be more surface trapped. The dependence of the solutions on α can readily be seen from (6.38), (6.40) and (6.41). For convenience we take $l = \pi$ where l is the meridional wavenumber of the heat forcing. Finally, the half-width of the rectangular and segmented cosine zonal heat distributions and the wavenumber of the periodic zonal distribution, are taken as $x_0 = 2.0$ and $k = 2.0$, respectively.

With the aforementioned parameters it is possible to evaluate the constants a , b and q which appear in the derivation of (6.38), (6.40), (6.41) and (6.42). From (6.19) and (6.29) we get $a = 2.7$ and $b = 2.9$, respectively, so that $q^2 = -b^2 < 0$. Thus the assumption $q^2 < 0$ made in Section 6.3 is indeed justified.

The solutions to (6.38), (6.40), (6.41) and (6.42) have been plotted in the x - y plane at $z = 0.0$ (Figs. 44a-d) for the parameters described above. The perturbation streamfunction ϕ has also been plotted for the section along $y = 0.0$ at $z = 0.0$ (Figs. 45a,b) and at $z = 0.5$ (Figs. 46a,b). Here we have taken $p = 0$ in (6.38) for convenience.

The line source heating solution at $z = 0.0$ (Figs. 44a, 45a) reveals a large local response near $x = 0.0$. At $z = 0.5$ (Fig. 46a), the local response diminishes in magnitude and the entire solution has changed sign. Comparing this to the rectangular and segmented cosine solutions at corresponding height (Figs. 45a, 46a), we see that the large local response has diminished in magnitude. For the rectangular and segmented cosine solutions, the

a DELTA HEATING $Z=0.0$



b RECTANGULAR HEATING $Z=0.0$

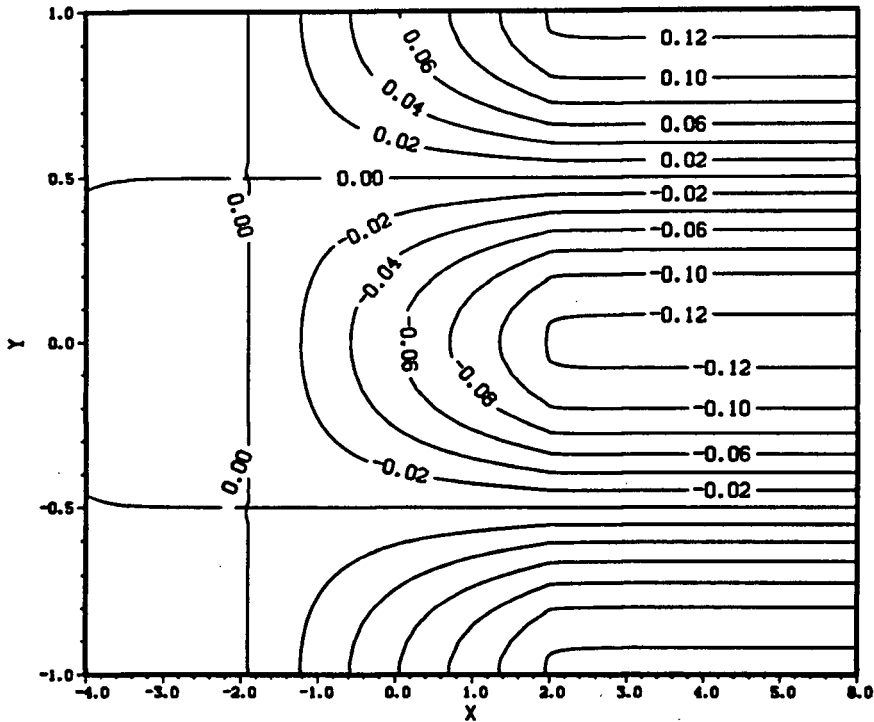
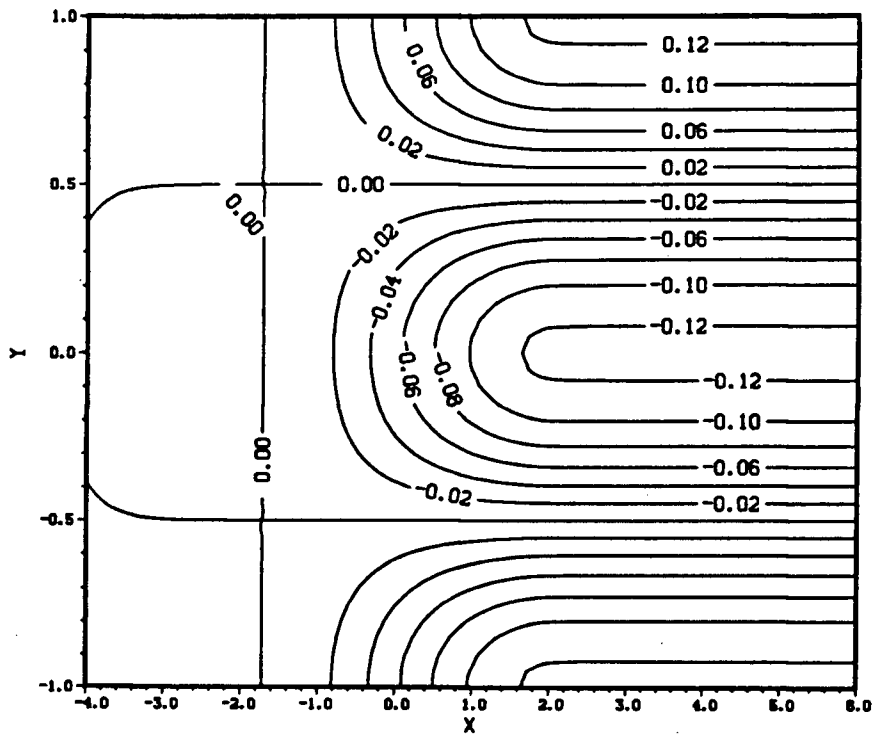


Figure 44 . Steady state perturbation streamfunction ϕ at $z = 0.0$; a)— Line source heating (equation 6.38); b)— Rectangular heating (equation 6.40); c)— Segmented cosine heating (equation 6.41); d)— Zonally periodic heating (equation 6.42).

c SEGMENTED COSINE HEATING $Z=0.0$



d WAVENUMBER K HEATING $Z=0.0$

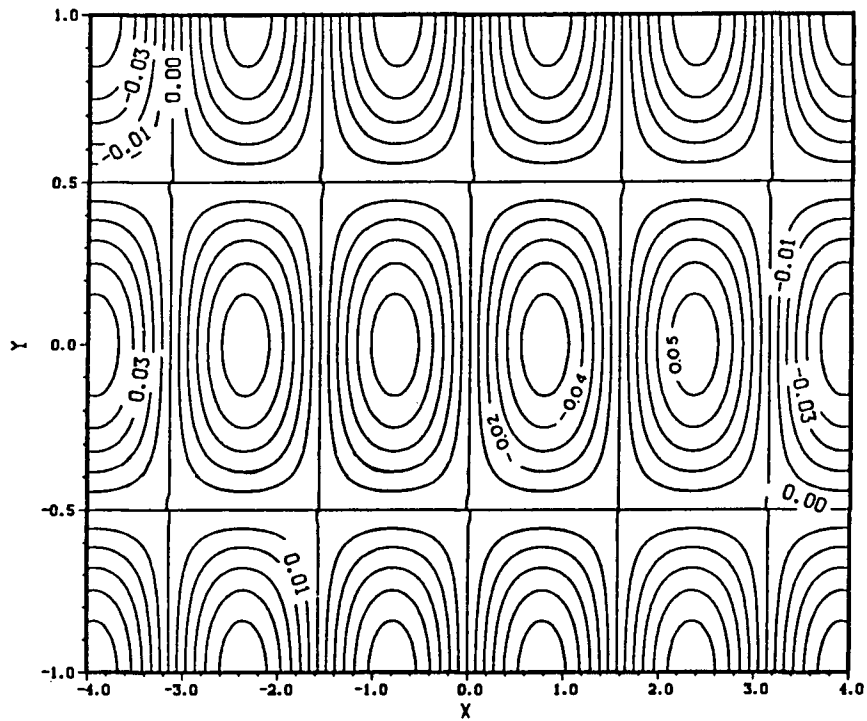
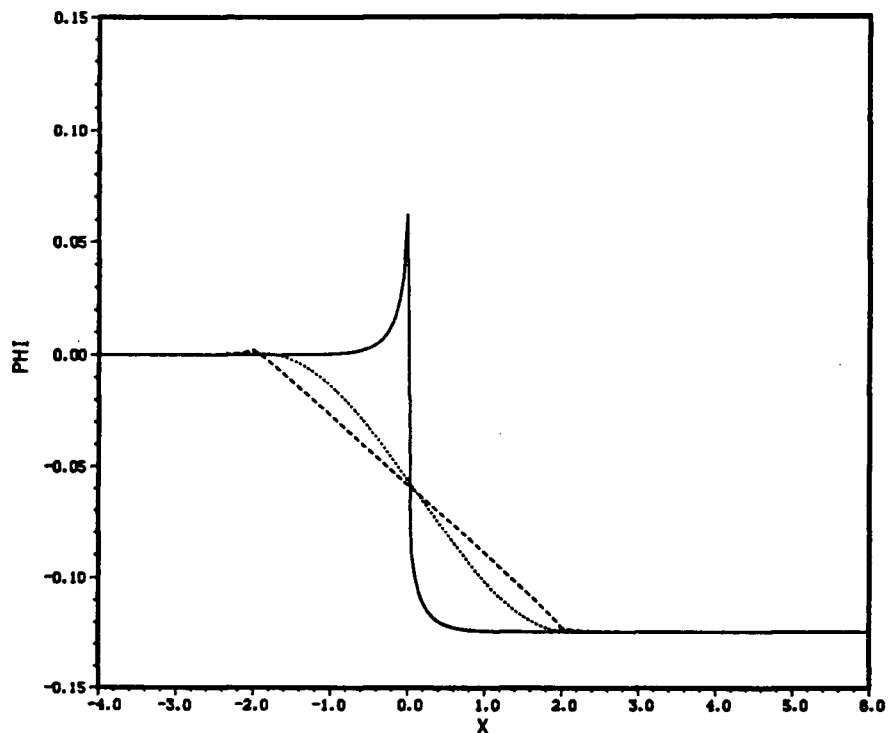


Figure 44 cont.

a STREAMFUNCTION Ψ -0, Z -0.0



b WAVENUMBER K HEATING Ψ -0, Z -0.0

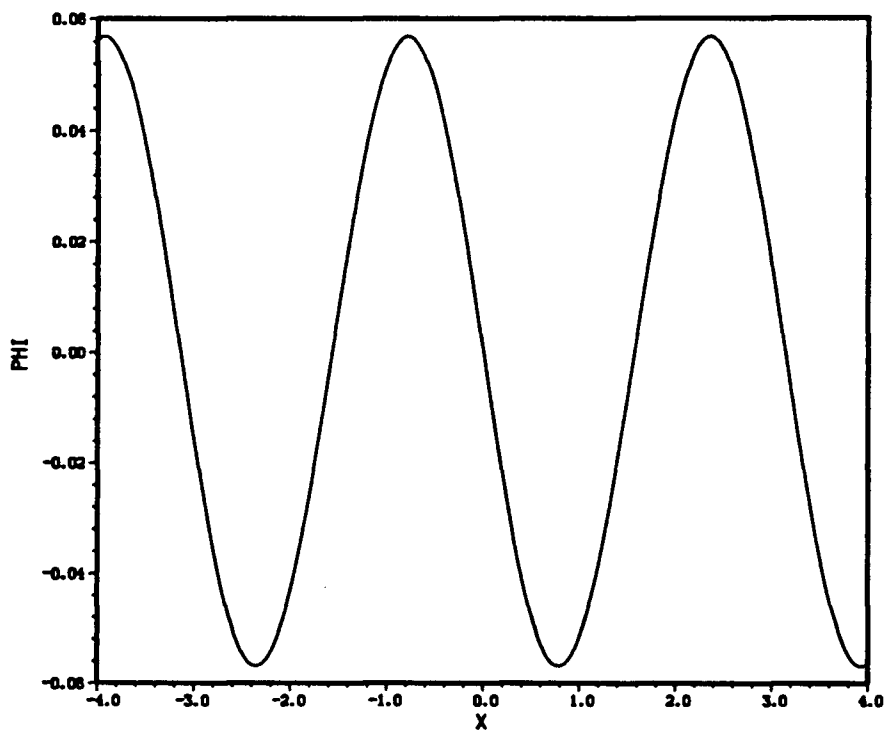


Figure 45 . Perturbation streamfunction ϕ for the section along $y = 0.0$ at $z = 0.0$; a)— Line source heating (solid line); Rectangular heating (dashed line); Segmented cosine heating (dotted line); b)— Zonally periodic heating.

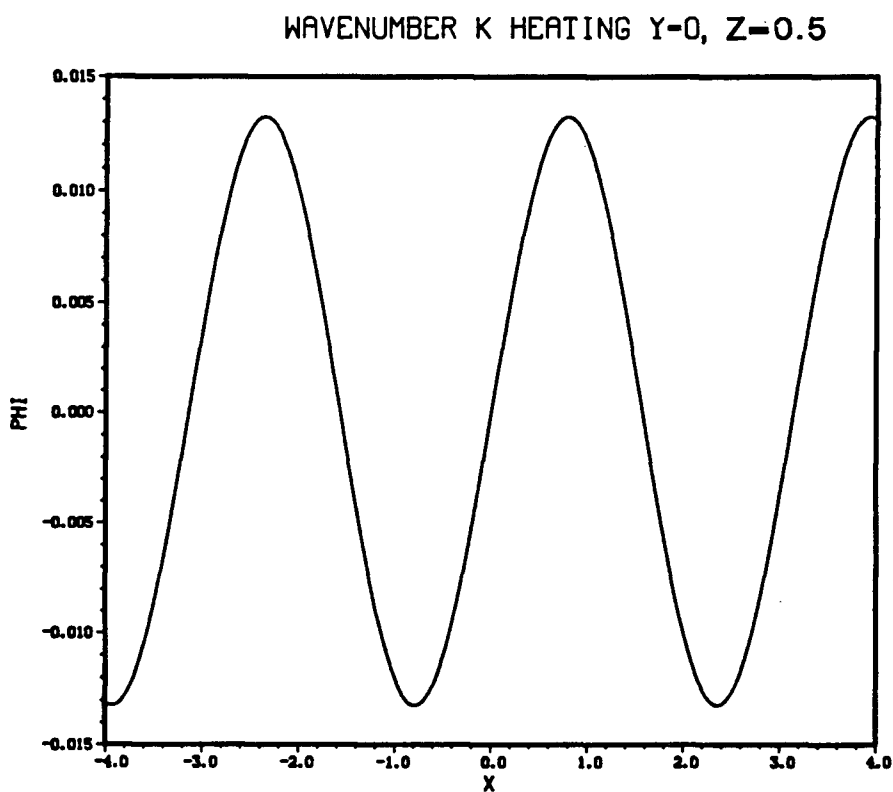
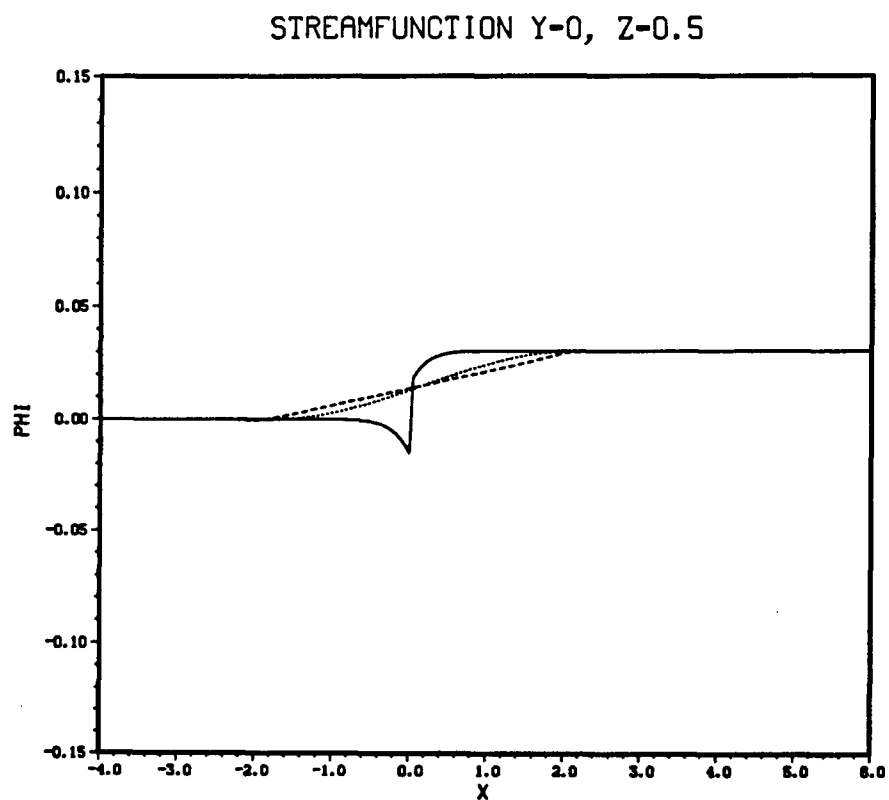


Figure 46 . Perturbation streamfunction ϕ for the section along $y = 0.0$ at $z = 0.5$; a)— Line source heating (solid line); Rectangular heating (dashed line); Segmented cosine heating (dotted line); b)— Zonally periodic heating.

local response appears as a gradual transition from the region $x < -x_0$ to the far field response $x > x_0$. It is of interest to note that due to the nature of the heating structure, the segmented cosine solution is smoother than the rectangular (Figs. 45a, 46a).

The periodic heating plots were included for sake of completeness (Figs. 44d, 45b, 46b). Due to the nature of the heating, one does not expect to find a localized response or the null response for $x < 0$. The response is purely periodic with an exponential height profile, a result obvious from (6.42).

As mentioned in Section 6.4, the magnitude of the local response is strongly dependent on the meridional wave number through the parameter b . Figures 47a,b illustrate this phenomenon for a meridional wave number $l = \frac{\pi}{2}$. The effect of decreasing l (and hence b) is to increase the magnitude of the local response (cf., Figs. 45–46 with $l = \pi$). For reference with Chapters 7 and 8 we note that both $l = \pi$ and $l = \frac{\pi}{2}$ fall into case 1. Both case 1 and another case, case 2, will be defined in Chapter 7.

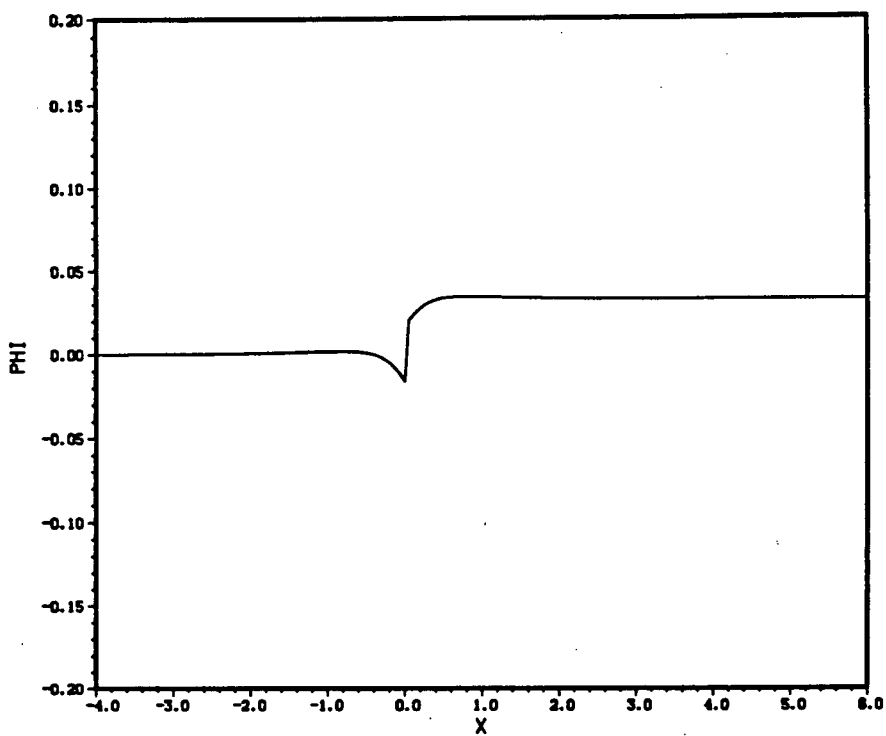
In all the plots for heating of the form (6.4), (6.5), (6.6), the far field response is constant (negative for $z = 0.0$ and positive for $z = 0.5$). This constant is non-zero since from equation (6.8) the net integrated heat input is non-zero, i.e.,

$$\int_{-\infty}^{\infty} Q_i(x, y, z) dx = Q_0 \cos l y e^{-\alpha z} \quad (i = 1, 2, 3). \quad (6.47)$$

In the solution considered in the next section the net integrated heat input will be zero and hence the far field response will be zero.

Finally, we devote our attention to the vertical structure of the solutions. Figures 48a,b illustrate the solution for the line source heating at $x = -0.01$, in the region of the local response. Most of the response is trapped in the lower 2 km and the solution slowly decays to zero as $z \rightarrow \infty$, after passing through a minimum at about $z = 0.5$. Figure 49 shows the rectangular and segmented cosine solutions with height at $x = -0.50$. Since we are in the region $-x_0 < x < x_0$, an interval which does not exist in the line source solution, there is a sign change between Fig. 48b and Fig. 49. If instead we had taken $x < -x_0$, Fig. 48b

a DELTA HEATING Y=0, Z=0.5



b DELTA HEATING Y=0, Z=0.0

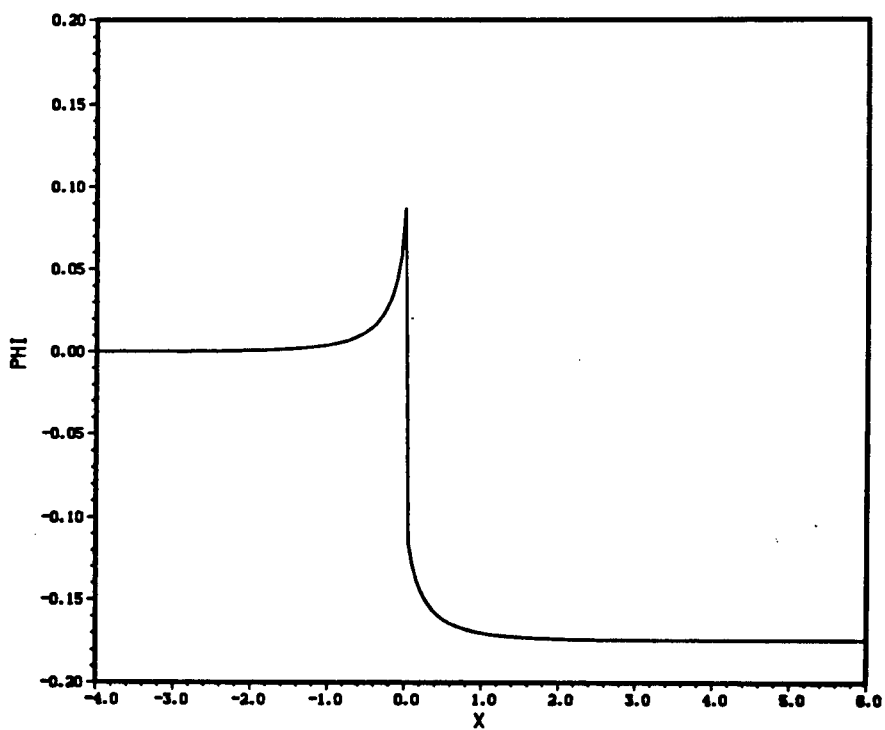


Figure 47 . Perturbation streamfunction ϕ for heating with a meridional wavenumber $l = \frac{\pi}{2}$ (as compared to $l = \pi$ in Figs. 45-46) along a section $y = 0.0$. a)— $z = 0.0$; b)— $z = 0.5$.

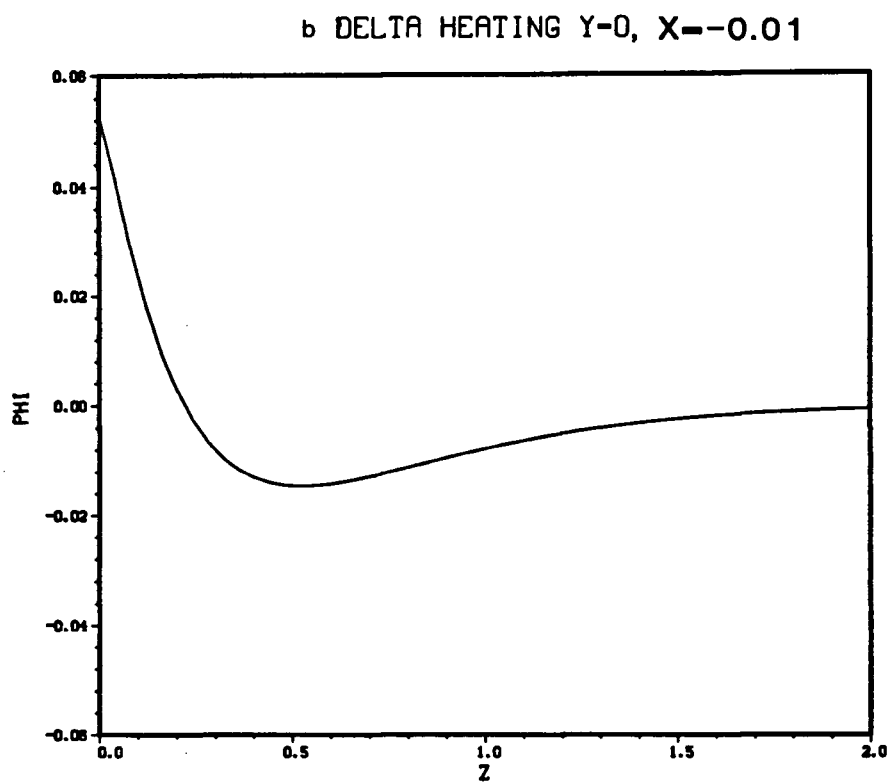
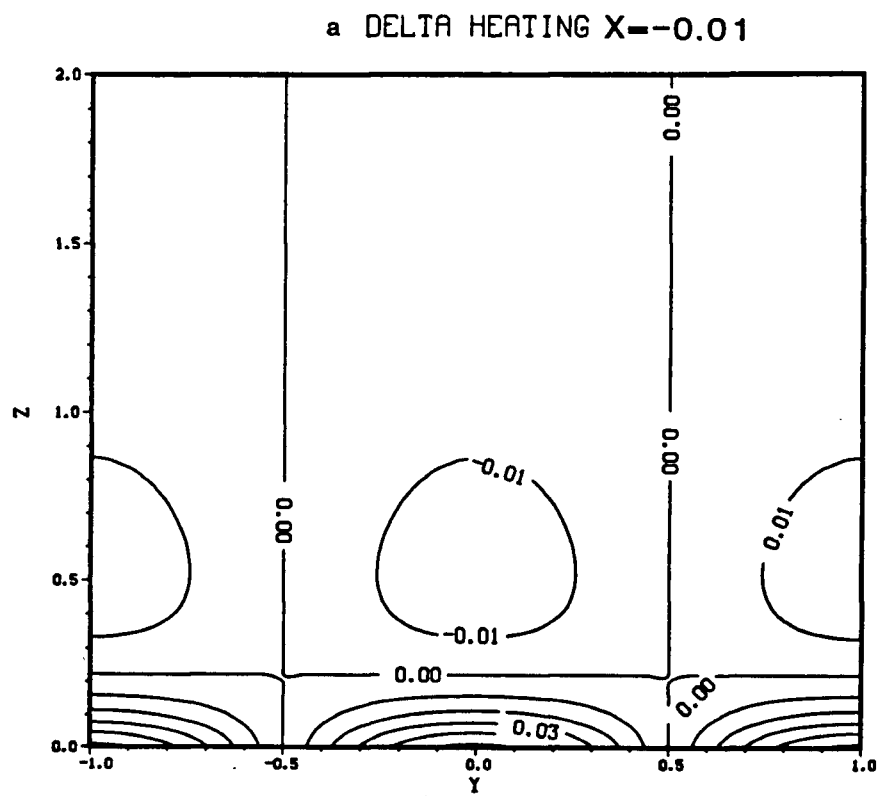


Figure 48 . Perturbation streamfunction ϕ in a vertical plane at $x = -0.01$ for line source heating. a)— $\phi(0, y, z)$; b)— $\phi(0, 0, z)$.

and Fig. 49 would have been similar. Most of the variability is once more trapped in the lower 2 km, decaying exponentially to zero as $z \rightarrow \infty$, after passing through a maximum at $z \sim 0.4$. The rectangular heating response is stronger than the segmented cosine response near the surface (Fig. 49). This result is also evident in Figs. 45a, 46a, although in the region $-x_0 < x < x_0$, with x greater than about zero, the exact opposite result is observed.

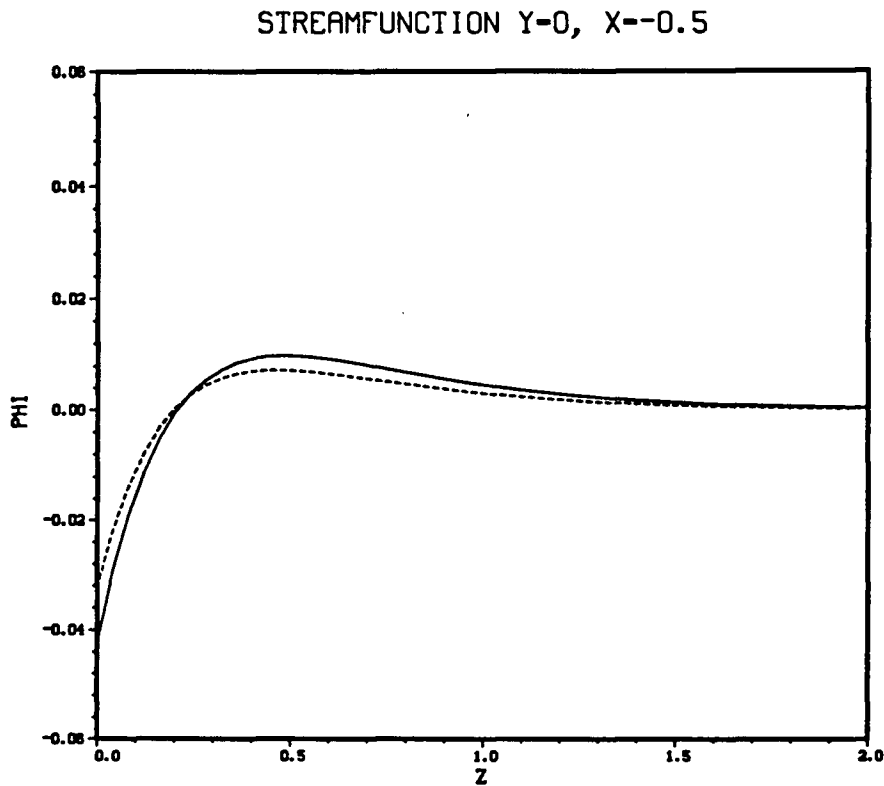


Figure 49 . Perturbation streamfunction ϕ for rectangular heating (solid line) and segmented cosine heating (dashed line) at $x = -0.50$ and $y = 0.0$.

Figures 50a-d depict the far field vertical response at $x = 4.0$ for the segmented cosine solution. Since the segmented cosine solution is similar in vertical structure to the line source and rectangular solutions, plots for the latter are not included. The structure of the response is similar to that for the corresponding solution at $x = -0.5$ (Fig. 49), although the magnitudes are greater in Figs. 50a,b, a result also apparent in Figs. 45a, 46a. The

periodic heating plots at $x = \frac{\pi}{4}$ have also been included in Figs. 50c,d. Very little difference is observed between these figures and those for the segmented cosine heating (Figs. 50a,b). Most of the response is again trapped in the lower 2 km, decaying to zero as $z \rightarrow \infty$, after passing through a maximum at $z \sim 0.4$.

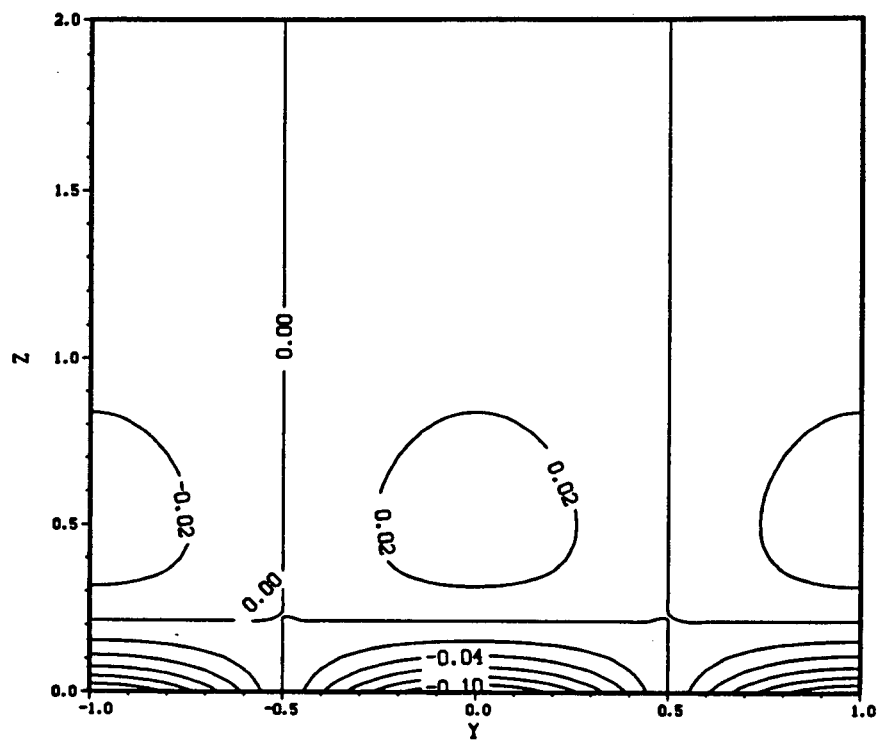
The sinusoidal contribution to the vertical structure from the integrals in (6.40) and (6.41) has not to this point been apparent, as we have considered heating spread over a rather broad expanse ($x_0 = 2.0$). Confining the region of heating (i.e., taking a smaller x_0) has a profound effect on the vertical structure. This is portrayed in Figs. 51a–b for $x_0 = 0.5$ at $x = -0.25$ for the segmented cosine heating distribution. The response now consists of two cells and a surface trapped layer (cf., Fig. 49). The large negative response that was trapped at the surface (Fig. 49) is now compressed into the lower 0.5 km, and has weakened in magnitude (Fig. 51a). A weak positive cell, with a maximum at about $z = .12$, lies above this, and above the positive cell, a weak negative cell with a minimum at about $z = 0.8$, is observed. These features are more clearly visible in the section across $y = 0.0$ (Fig. 51b).

As x_0 is decreased further, the positive cell moves down to the surface, thereby eliminating the negative surface trapped response in Figs. 51a,b., and the magnitudes increase. This process continues until $x_0 = 0.0$, when the line source heating solution is retrieved (Figs. 48a,b).

6.6 Application to the Kuroshio Region in Winter

In order to investigate the possible effect of the Kuroshio heating anomalies on the downstream atmospheric conditions, and hence to theoretically test the hypothesis of Zhao and McBean (1987b) (given at the end of Section 5.6), we consider the solution for segmented cosine heating of the form (6.6). Here we assume that the oceanic heat flux anomalies manifest themselves as diabatic heating anomalies with an exponentially decaying height profile. The results for $x_0 = 2.0$ (heating over a region of 43° zonal extent, centred at 141.5° E, 35° N) and the parameters discussed earlier, have been plotted in

a SEGMENTED COSINE HEATING $X=4.0$



b SEGMENTED COSINE HEATING $Y=0, X=4.0$

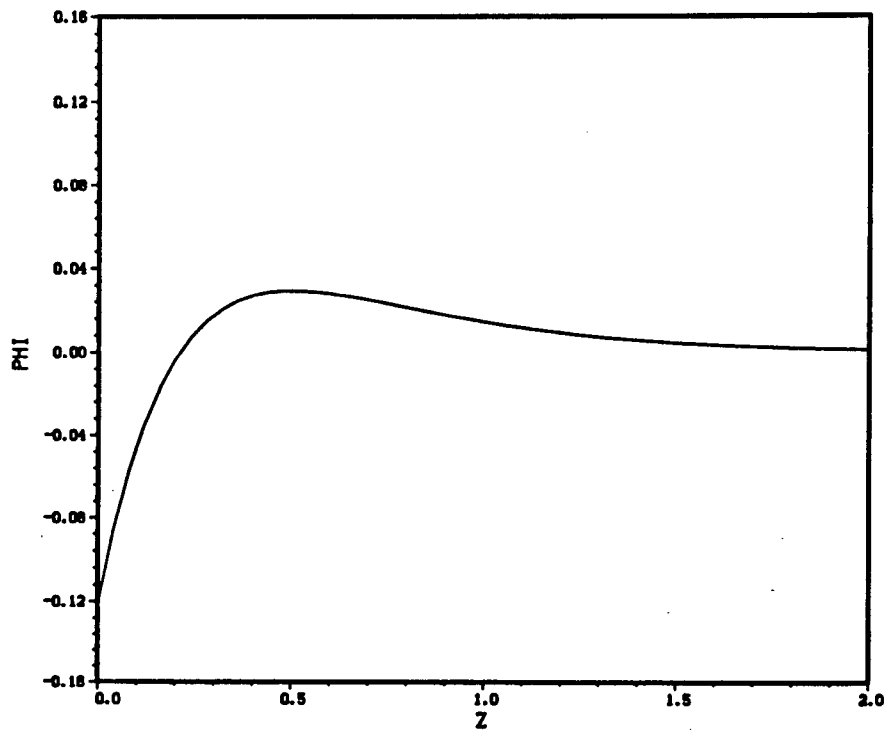
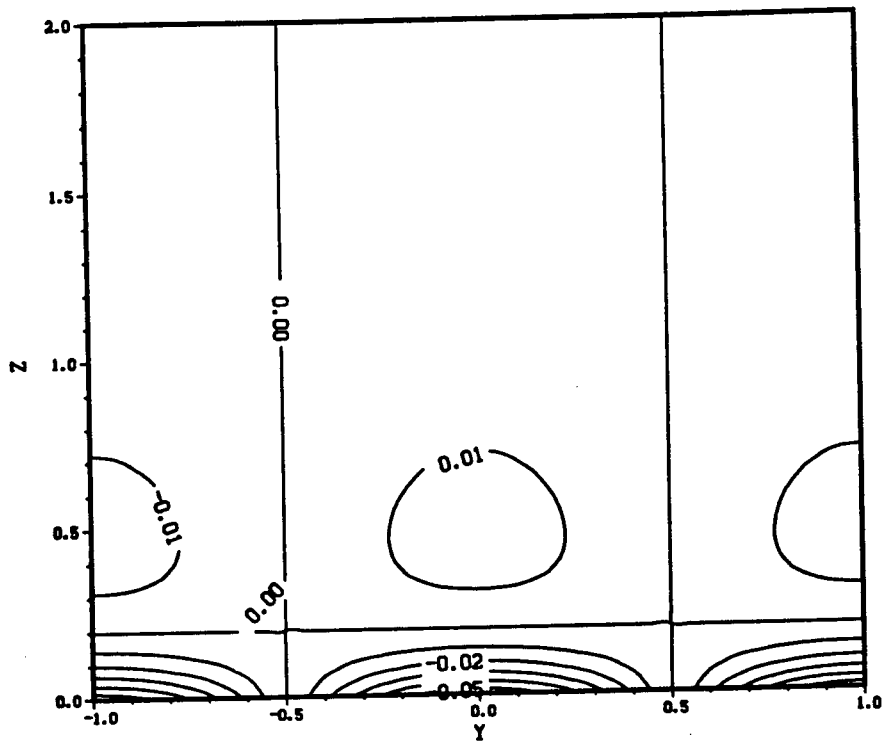


Figure 50 . Perturbation streamfunction ϕ a) — in a vertical plane at $x = 4.0$, for the segmented cosine heating; b) — as a function of height at $y = 0.0$, $x = 4.0$, for the segmented cosine heating; c) — in a vertical plane at $x = \frac{\pi}{4}$, for the periodic heating; d) — as a function of height at $y = 0.0$, $x = \frac{\pi}{4}$, for the periodic heating.

c WAVENUMBER K HEATING $X=\pi/4$



d WAVENUMBER K HEATING $Y=0, X=\pi/4$

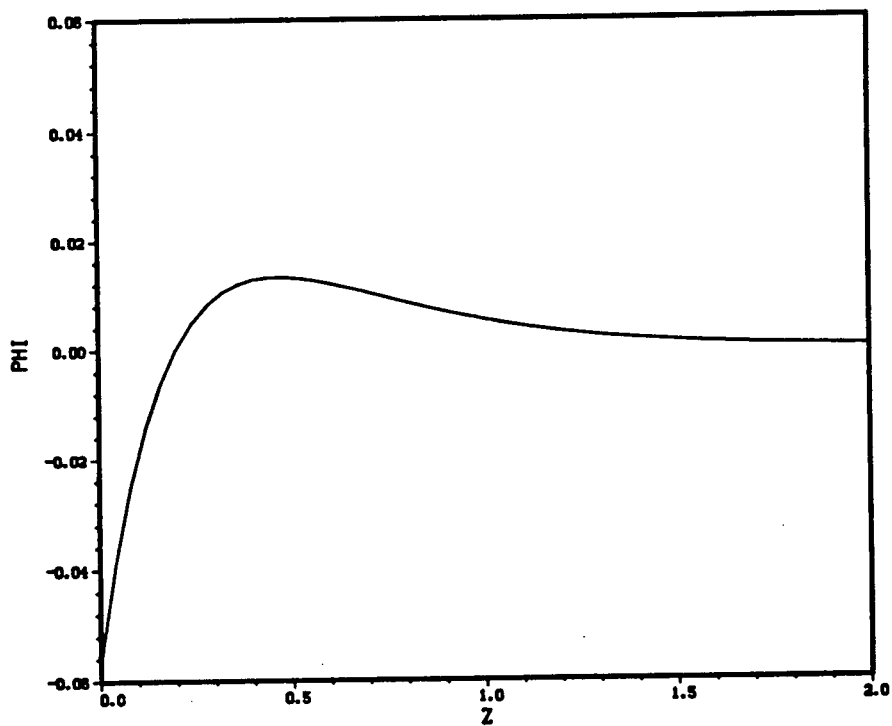


Figure 50 cont.

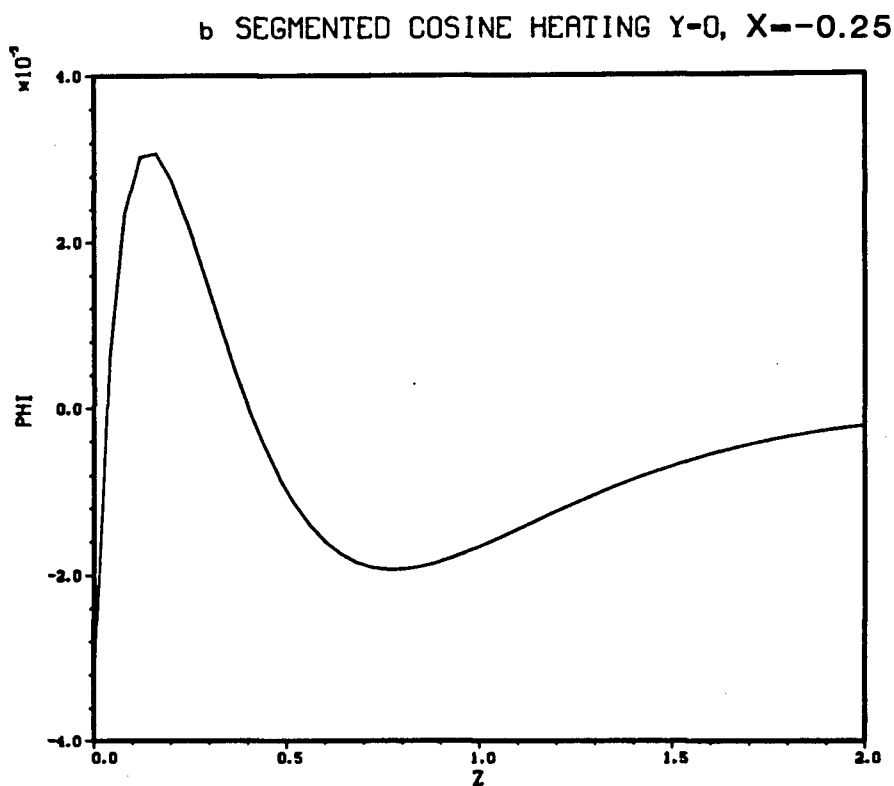
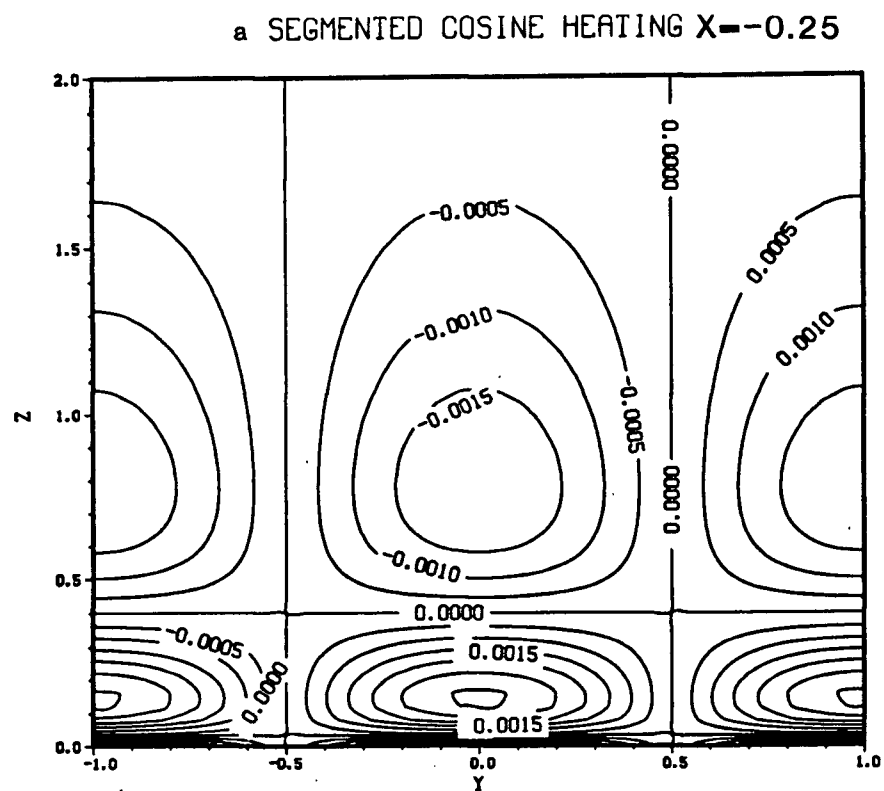


Figure 51 . Perturbation streamfunction ϕ for rectangular and segmented cosine heating structures with $x_0 = 0.5$ at $x = -0.25$. a) — $\phi(0, y, z)$ for segmented cosine heating; b) — $\phi(0, 0, z)$ for segmented cosine heating.

Fig. 45 and described in Section 6.5. The local response consists of a gradual transition from the region $x < -x_0$ to the far field region $x > x_0$. This negative response is certainly consistent with the observed large negative correlations (Fig. 42) downstream of the heating region, and hence is also consistent with the argument of Zhao and McBean (1987b).

In order to model the atmospheric response to heating with the structure of the first EOF of Zhao and McBean (1987a), we consider forcing of the form

$$Q = -Q_0 \cos ly \, e^{-\alpha z} \Pi \left(\frac{x}{2x_0} \right) \sin \left(\frac{\pi x}{x_0} \right), \quad (6.48)$$

with $x_0 = 4.55$. This corresponds to positive anomalous heating over the western half of the North Pacific and negative anomalous heating over the eastern half of the North Pacific. Following through an analysis similar to that of Section 6.4, we obtain

$$\begin{aligned} \phi(x, y, z) = & - \left(\frac{2}{\pi} \right)^{\frac{3}{2}} x_0 \eta \cos ly \, e^{cz} \int_b^{\infty} \frac{\{-c \sin(f(t)z) + f(t) \cos(f(t)z)\}}{t(t^2 + a^2)(1 + \frac{x_0^2 t^2}{\pi^2})} \\ & \times \begin{cases} e^{-|x|t} \sinh x_0 t \, \text{sgn} x, & \text{if } |x| \geq x_0; \\ e^{-x_0 t} \sinh xt + \frac{x_0 t}{\pi} \sin(\frac{\pi x}{x_0}), & \text{if } |x| \leq x_0; \end{cases} dt \\ & + \frac{\sqrt{\frac{2}{\pi}} x_0 \cos ly}{a^2} \left\{ \eta (S^{\frac{1}{2}} b + c) e^{(c - S^{\frac{1}{2}} b)z} - \chi e^{-\alpha z} \right\} \begin{cases} 0, & \text{if } |x| \geq x_0; \\ \{1 + \cos(\frac{\pi x}{x_0})\}, & \text{if } |x| \leq x_0; \end{cases} \end{aligned} \quad (6.49)$$

The functions $f(t)$ and $\text{sgn} x$ are defined by

$$f(t) = S^{\frac{1}{2}} (t^2 - b^2)^{\frac{1}{2}}, \quad \text{sgn}(x) = \begin{cases} 1, & \text{if } x > 0; \\ -1, & \text{if } x < 0. \end{cases} \quad (6.50)$$

Figure 52 shows the solution at $z=0.0$. This solution reveals a large negative response centered at $x = 0.0$, which when $x \rightarrow \pm\infty$ decays exponentially to zero. This result is in excellent agreement with the observed correlations of Fig. 42 (see also the discussion at the end of Section 7.6).

In the spatial correlation plots (Figs. 42a–c) the observed results are quasibarotropic (same sign with height), whereas the model results have opposite sign at $z = 0.0$ and $z = 0.5$. The most significant correlations however occur in the SLP plot (Fig. 42a), at

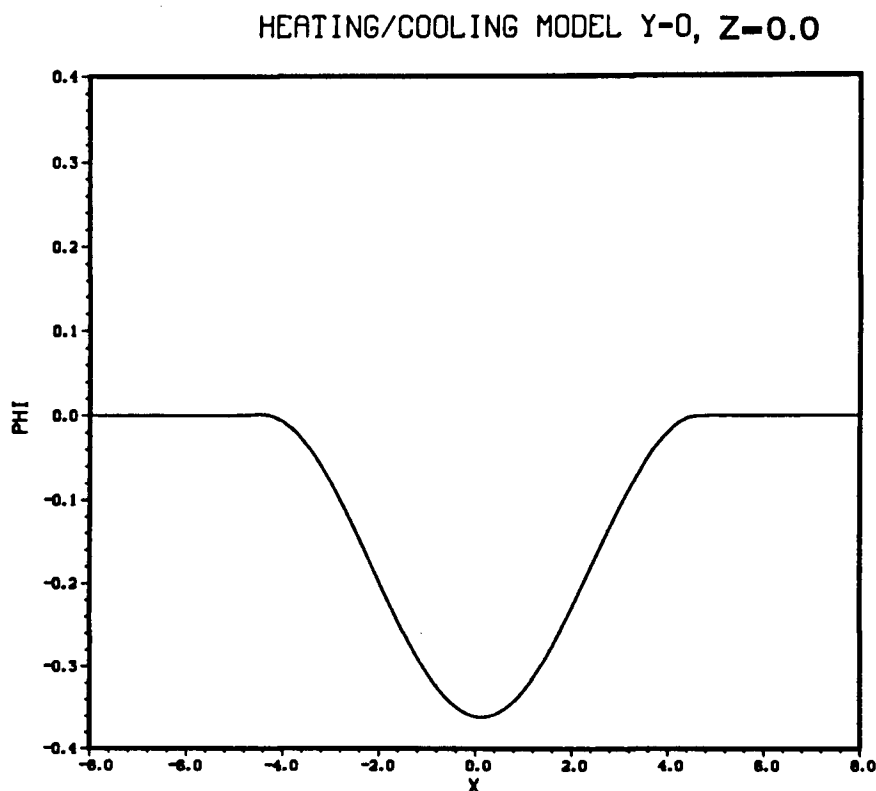


Figure 52 . Perturbation streamfunction ϕ along $y = 0.0$ at $z = 0.0$ for the western North Pacific heating and eastern North Pacific cooling model with $x_0 = 4.55$.

which level ($z = 0.0$) the response of the model is largest. At $z = 0.5$ the response of the model is small (see for example Fig. 50b) and hence would not be expected to contribute to the observed correlations. It appears therefore that the correlations in the upper level plots (Figs. 42b,c) simply arise from the spatial correlations of the geopotential field. This ridge/trough structure (described in Zhao and McBean 1987b, and often observed in teleconnection patterns associated with ENSO events, eg., Horel and Wallace, 1981; Emery and Hamilton, 1985; Mysak, 1986), in turn forces Kuroshio heating anomalies (and eastern Pacific cooling anomalies). The heating/cooling anomalies then “feedback” and intensify the low in the lower troposphere over the central North Pacific (Fig. 42a). This mechanism is in agreement with the argument of Zhao and McBean given in Section 5.6.

7. A Two Level Model of the Steady State Response of the Atmosphere to Midlatitude Heating with Various Zonal Structures

7.1 Introduction

As discussed in Chapter 6, Weaver, Mysak and Bennett (1987a,b) (WMB) examined the steady state atmospheric response to localized heating using a continuously stratified quasigeostrophic model. In this chapter the effects of vertical shear on the results of WMB are considered. To accomplish this a simple two level linear quasigeostrophic model is used. Also, a two level model is convenient for studying the transient response of the atmosphere to localized heating, which is the topic of Chapter 8.

The outline of this chapter is similar to that of Weaver (1987b) where this problem was first studied. In Section 7.2 the model and the assumed heating distributions are introduced. In Section 7.3 a line source zonal heating structure is examined. The solution obtained from this line source heating is used as a Green's function in Section 7.4 to obtain solutions for segmented cosine and segmented sine distributions. In Section 7.5 the solutions obtained in Sections 7.3 and 7.4 are analysed and compared with the results of WMB and other investigators. Finally, in Section 7.6 we examine the effect of sine forcing over one wavelength in order to model the atmospheric response to heating with the structure of the first EOF of Zhao and McBean (1987a), as in Chapter 6.

7.2 Description of the model

The two level quasigeostrophic model in the β -plane approximation is used. In pressure coordinates the linearized vorticity and thermodynamic equations for a small stationary disturbance are (Holton, 1979, Frankignoul, 1985a)

$$\bar{U} \frac{\partial}{\partial x} \nabla^2 \psi + \beta \frac{\partial}{\partial x} \psi - f_0 \frac{\partial}{\partial p} \omega = 0, \quad (7.1)$$

$$\bar{U} \frac{\partial}{\partial x} \frac{\partial \psi}{\partial p} - \frac{\partial \psi}{\partial x} \frac{\partial \bar{U}}{\partial p} + \frac{\bar{\sigma}}{f_0} \omega = -\frac{Rq'}{C_p f_0 p}, \quad (7.2)$$

where ψ is the geostrophic streamfunction, $\bar{U}(p)$ is the zonal wind, and ω is the vertical

motion field. The mean static stability parameter

$$\bar{\sigma} = \frac{R}{p} \left\{ \frac{R\bar{T}}{C_p p} - \frac{\partial \bar{T}}{\partial p} \right\} \quad (7.3)$$

is assumed to be constant and the diabatic heating q' is assumed to have the form (cf., 6.4)

$$q' = Q_0 \cos ly \delta(x - p). \quad (7.4)$$

The solution for the line source heating (7.4) will be used as a Green's function in Section 7.4 to obtain the atmospheric response to heating q' with other zonal structures.

In the two level approximation the vorticity is calculated at levels 1 and 3 (Fig. 53) and the thermodynamic equation (7.2) is applied at level 2. The boundary condition $\omega = 0$ is enforced at the surface, $p_4 = 1000$ mb and at the tropopause, $p_0 = 200$ mb. If U_1 and U_3 are the constant zonal flows at levels 1 and 3 respectively, the resulting system of equations is

$$U_1 \frac{\partial}{\partial x} \nabla^2 \psi_1 + \beta \frac{\partial}{\partial x} \psi_1 - \frac{f_0}{\Delta p_1} \omega_2 = 0, \quad (7.5)$$

$$U_3 \frac{\partial}{\partial x} \nabla^2 \psi_3 + \beta \frac{\partial}{\partial x} \psi_3 + \frac{f_0}{\Delta p_3} \omega_2 = 0, \quad (7.6)$$

$$U_3 \frac{\partial}{\partial x} \psi_1 - U_1 \frac{\partial}{\partial x} \psi_3 - \frac{\bar{\sigma} \Delta p_2}{f_0} \omega_2 = \frac{R \Delta p_2 q'}{C_p f_0 p_2}, \quad (7.7)$$

where $\Delta p_1 = p_2 - p_0$, $\Delta p_2 = p_3 - p_1$, $\Delta p_3 = p_4 - p_2$ and q' is given by (7.4). Here we have used the interpolated values $U_2 = \frac{p_2 - p_1}{\Delta p_2} U_3 + \frac{p_3 - p_2}{\Delta p_2} U_1$ and $\psi_2 = \frac{p_2 - p_1}{\Delta p_2} \psi_3 + \frac{p_3 - p_2}{\Delta p_2} \psi_1$ for U and ψ at level 2.

7.3 Solution of the Equations.

The β -plane is assumed to be of infinite extent in the zonal direction so that we may Fourier transform (7.5)–(7.7). Let

$$(\hat{\psi}_1, \hat{\psi}_3, \hat{\omega}_2) = \frac{1}{\sqrt{2\pi}} \int_{-\infty}^{\infty} e^{-i\xi x} (\bar{\psi}_1, \bar{\psi}_3, \bar{\omega}_2) dx \quad (7.8)$$

where

$$(\psi_1, \psi_3, \omega_2) = (\bar{\psi}_1, \bar{\psi}_3, \bar{\omega}_2) \cos ly. \quad (7.9)$$

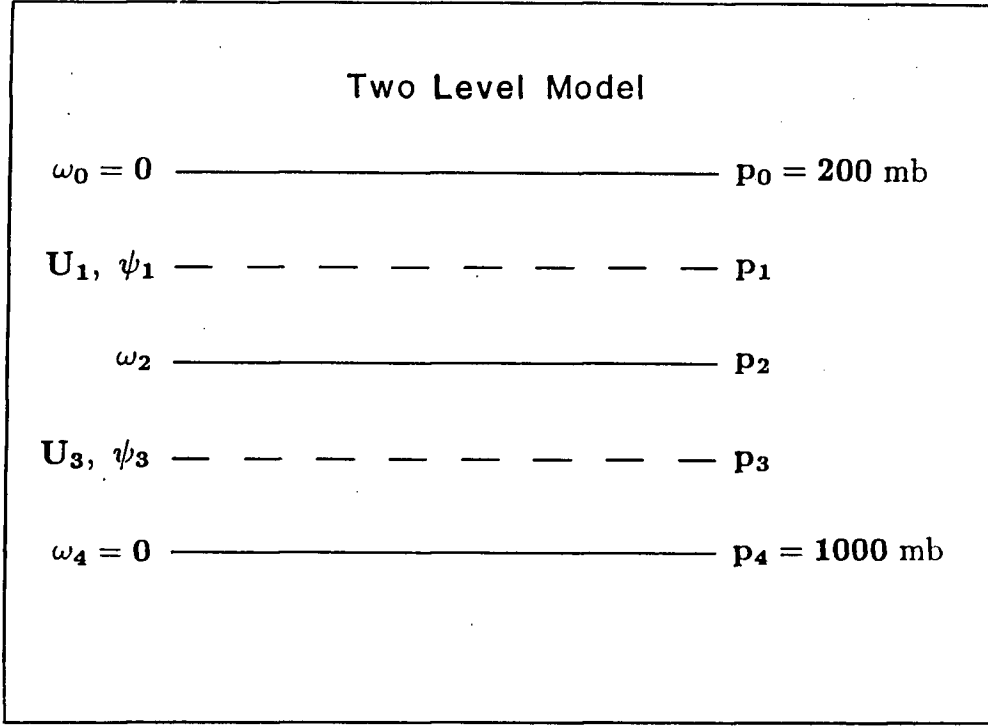


Figure 53 . Schematic diagram of the two level model indicating the five pressure levels. In Model 1 $p_1 = 400 \text{ mb}$, $p_2 = 600 \text{ mb}$, $p_3 = 800 \text{ mb}$; in Model 2 $p_1 = 500 \text{ mb}$, $p_2 = 800 \text{ mb}$, $p_3 = 900 \text{ mb}$.

The system of differential equations (7.5)–(7.7) is then transformed into a system of algebraic equations which yield

$$\hat{\omega}_2 = -\frac{Q_0 R f_1(\xi) f_3(\xi) e^{-ip\xi}}{\sqrt{2\pi} \bar{\sigma} C_p p_2 \{f_1(\xi) f_3(\xi) - \lambda^2 \{\alpha_1 f_1(\xi) + \alpha_3 f_3(\xi)\}\}}, \quad (7.10)$$

$$\hat{\psi}_1 = -\frac{Q_0 f_0 R f_3(\xi) e^{-ip\xi}}{\sqrt{2\pi} \Delta p_1 \bar{\sigma} C_p p_2 i \xi \{f_1(\xi) f_3(\xi) - \lambda^2 \{\alpha_1 f_1(\xi) + \alpha_3 f_3(\xi)\}\}}, \quad (7.11)$$

$$\hat{\psi}_3 = \frac{Q_0 f_0 R f_1(\xi) e^{-ip\xi}}{\sqrt{2\pi} \Delta p_3 \bar{\sigma} C_p p_2 i \xi \{f_1(\xi) f_3(\xi) - \lambda^2 \{\alpha_1 f_1(\xi) + \alpha_3 f_3(\xi)\}\}}, \quad (7.12)$$

where

$$\alpha_1 = \frac{2U_1 \Delta p_1}{\Delta p_1 + \Delta p_3}, \quad \alpha_3 = \frac{2U_3 \Delta p_3}{\Delta p_1 + \Delta p_3}, \quad f_1(\xi) = \beta - U_1(l^2 + \xi^2), \quad f_3(\xi) = \beta - U_3(l^2 + \xi^2). \quad (7.13)$$

The deformation radius λ^{-1} is defined such that

$$\lambda^2 = \frac{f_0^2(\Delta p_1 + \Delta p_3)}{2\bar{\sigma}\Delta p_1\Delta p_2\Delta p_3}. \quad (7.14)$$

The expression $f_1(\xi)f_3(\xi) - \lambda^2\{\alpha_1f_1(\xi) + \alpha_3f_3(\xi)\}$ in (7.10)–(7.12) has four zeros which occur at

$$\xi = \pm \left\{ -l^2 - \gamma \pm \left\{ \gamma^2 + \delta \right\}^{\frac{1}{2}} \right\}^{\frac{1}{2}}, \quad (7.15)$$

where

$$\gamma = \frac{\lambda^2(\alpha_1U_1 + \alpha_3U_3) - \beta(U_1 + U_3)}{2U_1U_3} \quad (7.16)$$

and

$$\delta = \frac{\beta}{U_1U_3} \left\{ \lambda^2(\alpha_1 + \alpha_3) - \beta \right\}, \quad (7.17)$$

are both independent of the meridional wavenumber l . Before taking the inverse Fourier transform of (7.10)–(7.12) we must find the location of the zeros defined by (7.15) and the pole at $\xi = 0$ in the complex ξ plane. To do this we include Rayleigh friction and Newtonian cooling in the problem (see Appendix II). For simplicity the Rayleigh friction and Newtonian cooling coefficients are assumed to be equal (τ_0).

We take the β -plane to be centered at 40° N, so that $f_0 = 9.4 \times 10^{-5} \text{s}^{-1}$ and $\beta = 1.8 \times 10^{-11} \text{m}^{-1} \text{s}^{-1}$. We also take $U_1 = 18 \text{ms}^{-1}$, $U_3 = 6 \text{ms}^{-1}$ and $\sigma = 3 \times 10^{-6} \text{m}^4 \text{s}^2 \text{kg}^{-2}$, typical of midlatitude wintertime conditions (Frankignoul, 1985a). There are two models which we consider. The first is for $p_1 = 400$ mb, $p_2 = 600$ mb, and $p_3 = 800$ mb, so that $\Delta p_1 = \Delta p_2 = \Delta p_3 = 400$ mb, $\alpha_1 = U_1$, $\alpha_3 = U_3$, and hence the levels are equally spaced. In this model the deformation radius is $\lambda^{-1} = 7.4 \times 10^5 \text{m}$, and from (7.16) and (7.17), $\gamma = 1.1 \times 10^{-12} > 0$ and $\delta = 4.4 \times 10^{-24} > 0$. To focus more on near surface heating we also consider a second model for which $p_1 = 500$ mb, $p_2 = 800$ mb, and $p_3 = 900$ mb, so that $\Delta p_1 = 600$ mb, $\Delta p_2 = 400$ mb, $\Delta p_3 = 200$ mb, $\alpha_1 = \frac{3}{2}U_1$ and $\alpha_3 = \frac{1}{2}U_3$. For this model the deformation radius is $\lambda^{-1} = 6.4 \times 10^5 \text{m}$, and from (7.16) and (7.17), $\gamma = 4.1 \times 10^{-12} > 0$ and $\delta = 1.2 \times 10^{-23} > 0$.

There are two cases which need to be considered for both models:

case 1 : $l^2 > \{\gamma^2 + \delta\}^{\frac{1}{2}} - \gamma$.

In this case there are two conjugate pairs of pure imaginary roots. Here we write

$$f_1(\xi)f_3(\xi) - \lambda^2\{U_1f_1(\xi) + U_3f_3(\xi)\} = U_1U_3\{\xi^2 - \xi_1^2\}\{\xi^2 - \xi_2^2\}, \quad (7.18)$$

with

$$\xi_1 = i \left\{ l^2 + \gamma - \{\gamma^2 + \delta\}^{\frac{1}{2}} \right\}^{\frac{1}{2}}, \quad (7.19)$$

and

$$\xi_2 = i \left\{ l^2 + \gamma + \{\gamma^2 + \delta\}^{\frac{1}{2}} \right\}^{\frac{1}{2}}. \quad (7.20)$$

Thus (7.10) can be written as

$$\hat{\omega}_2 = - \frac{Q_0 R f_1(\xi) f_3(\xi) e^{-ip\xi}}{\sqrt{2\pi} \bar{\sigma} C_p p_2 U_1 U_3 \{\xi^2 - \xi_1^2\} \{\xi^2 - \xi_2^2\}}. \quad (7.21)$$

In taking the inverse Fourier transform of (7.21) we close the contour of integration for $x > p$ in the upper half plane (UHP) and for $x < p$ in the lower half plane (LHP) (see Fig. 54). Thus

$$\bar{\omega}_2 = \frac{1}{\sqrt{2\pi}} \int_{-\infty}^{\infty} e^{i\xi x} \hat{\omega} d\xi = \begin{cases} \sqrt{2\pi} i \Sigma \text{Res at } \xi_1, \xi_2, & \text{if } x > p; \\ \sqrt{2\pi} i \Sigma \text{Res at } -\xi_1, -\xi_2, & \text{if } x < p. \end{cases}, \quad (7.22)$$

since by Jordan's Lemma $\int_{C_R} \rightarrow 0$ and $\int_{C'_R} \rightarrow 0$ as $R \rightarrow \infty$. Evaluating the residues at $\pm\xi_1, \pm\xi_2$, substituting the result into (7.22), and using (7.9) gives

$$\omega_2 = \frac{\chi \cos ly}{2(\eta_1^2 - \eta_2^2)} \left\{ \frac{f_1(i\eta_1)f_3(i\eta_1)}{\eta_1} e^{-\eta_1|x-p|} - \frac{f_1(i\eta_2)f_3(i\eta_2)}{\eta_2} e^{-\eta_2|x-p|} \right\} \text{sgn}(x-p), \quad (7.23)$$

where $i\eta_1 = \xi_1, i\eta_2 = \xi_2$ and

$$\chi = \frac{Q_0 R}{\bar{\sigma} C_p p_2 U_1 U_3}, \quad \text{sgn}(x-p) = \begin{cases} 1, & \text{if } x > p; \\ -1, & \text{if } x < p. \end{cases} \quad (7.24)$$

Thus the ω field consists of two components decaying exponentially away from the heating source. There is a discontinuity at $x = p$ which manifests itself as a sign change.

The geostrophic streamfunctions ψ_1 , and ψ_3 can be obtained in a similar way. When Rayleigh friction and Newtonian cooling are included in the problem (Appendix II), the

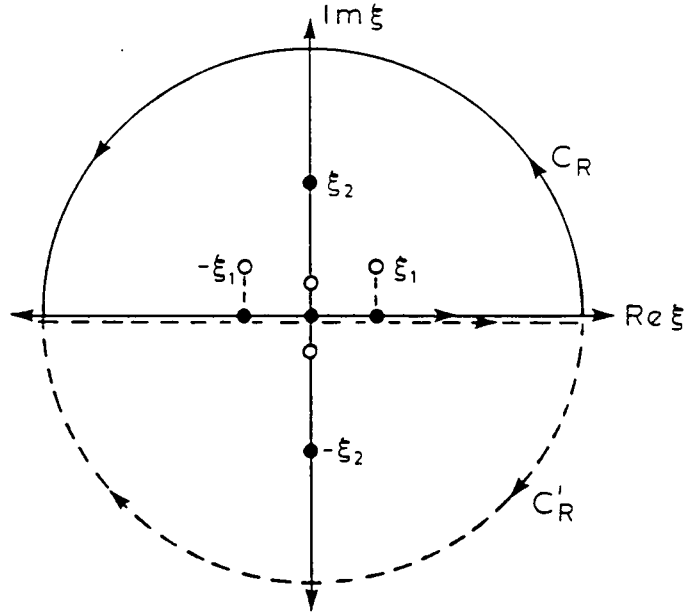


Figure 54 . Contour of integration for the evaluation of (7.22). The pole at $\xi = 0$ bifurcates and moves into the UHP when Rayleigh friction and Newtonian cooling are introduced into the problem. The solid line is for $x > p$, the dashed line is for $x < p$.

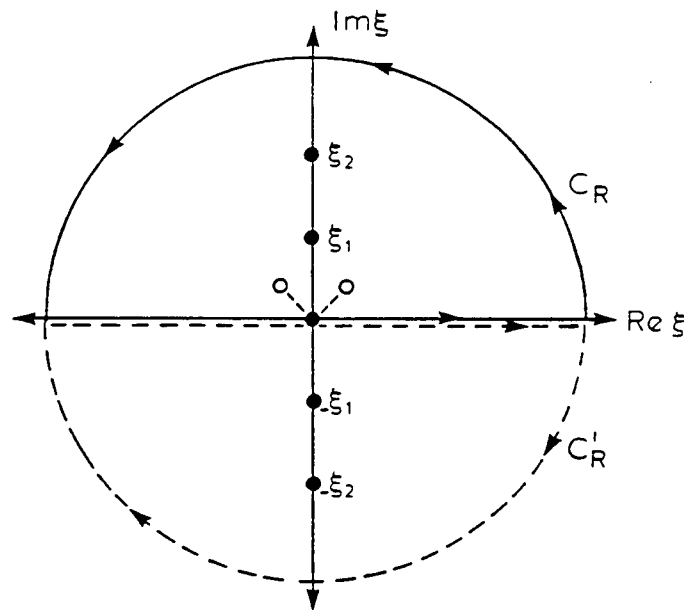


Figure 55 . Contour of integration for the evaluation of (7.28). The pole at $\xi = 0$ bifurcates and moves into both the UHP and the LHP and the poles at $\xi = \pm \xi_1$ move into the UHP, when Rayleigh friction and Newtonian cooling are introduced into the problem. The solid line is for $x > p$, the dashed line is for $x < p$.

pole at $\xi = 0$ bifurcates into two poles in the UHP (Fig. 54). We must therefore include the contribution from the residue at $\xi = 0$ for $x > p$. Applying Jordan's Lemma once more and letting the friction/cooling coefficient $\tau_0 \rightarrow 0$, gives

$$\psi_1 = -\frac{\chi f_0 \cos ly}{\Delta p_1} \left\{ \frac{f_3(0)}{\eta_1^2 \eta_2^2} H(x-p) + \frac{f_3(i\eta_1)}{2\eta_1^2(\eta_1^2 - \eta_2^2)} e^{-\eta_1|x-p|} - \frac{f_3(i\eta_2)}{2\eta_2^2(\eta_1^2 - \eta_2^2)} e^{-\eta_2|x-p|} \right\}, \quad (7.25)$$

and

$$\psi_3 = \frac{\chi f_0 \cos ly}{\Delta p_3} \left\{ \frac{f_1(0)}{\eta_1^2 \eta_2^2} H(x-p) + \frac{f_1(i\eta_1)}{2\eta_1^2(\eta_1^2 - \eta_2^2)} e^{-\eta_1|x-p|} - \frac{f_1(i\eta_2)}{2\eta_2^2(\eta_1^2 - \eta_2^2)} e^{-\eta_2|x-p|} \right\}, \quad (7.26)$$

where we have used (7.9) once more and $H(x-p)$ is the Heaviside step function defined by

$$H(x-p) = \begin{cases} 1, & \text{if } x > p; \\ 0, & \text{if } x < p. \end{cases} \quad (7.27)$$

The streamfunction at both the upper and lower levels consists of a component exponentially decaying away from the source and a component constant for all x . At $x = p$ both ψ_1 and ψ_3 have a step discontinuity.

case 2: $l^2 < \{\gamma^2 + \delta\}^{\frac{1}{2}} - \gamma$.

In this case (7.15) has two complex conjugate pure imaginary roots and two real roots of opposite sign. When Rayleigh friction and Newtonian cooling are included in the problem (Appendix II), the roots $\pm \xi_1 = \pm \{-l^2 - \gamma + \{\gamma^2 + \delta\}^{\frac{1}{2}}\}^{\frac{1}{2}}$ both move into the UHP (Fig. 55).

As in case 1, we close the contour of integration of the inverse Fourier transform in the UHP for $x > p$ and in the LHP for $x < p$, apply Jordan's Lemma to the integrals over the semicircular regions of Fig. 55, and obtain

$$\bar{\omega}_2 = \frac{1}{\sqrt{2\pi}} \int_{-\infty}^{\infty} e^{i\xi x} \hat{\omega} d\xi = \begin{cases} \sqrt{2\pi} i \Sigma \text{Res at } \pm \xi_1, \xi_2, & \text{if } x > p; \\ \sqrt{2\pi} i \Sigma \text{Res at } -\xi_2, & \text{if } x < p. \end{cases} \quad (7.28)$$

Evaluating the residues at $\pm \xi_1$ and $\pm \xi_2$ and substituting the result into (7.28) using (7.9) gives

$$\omega_2 = \frac{\chi \cos ly}{2(\xi_1^2 + \eta_2^2)} \left\{ \frac{2f_1(\xi_1)f_3(\xi_1)}{\xi_1} \sin \xi_1(x-p)H(x-p) + \frac{f_1(i\eta_2)f_3(i\eta_2)}{\eta_2} e^{-\eta_2|x-p|} \text{sgn}(x-p) \right\}. \quad (7.29)$$

The solution (7.29) consists of the exponentially decaying component which arises from the poles at $\xi = \pm \xi_2$ (cf., 7.23), and a sinusoidal component only for $x > p$. Once more a sign discontinuity is present at $x = p$.

To obtain ψ_1 and ψ_3 we notice that the pole at $\xi = 0$ bifurcates into two poles with the inclusion of Rayleigh friction and Newtonian cooling, one in the UHP and one in the LHP (Appendix II). After some residue calculus similar to the above, we obtain

$$\psi_1 = \frac{\chi f_0 \cos ly}{\Delta p_1} \left\{ \frac{f_3(0)}{\xi_1^2 \eta_2^2} - \frac{f_3(\xi_1)}{\xi_1^2(\xi_1^2 + \eta_2^2)} \cos \xi_1(x-p)H(x-p) - \frac{f_3(i\eta_2)}{2\eta_2^2(\xi_1^2 + \eta_2^2)} e^{-\eta_2|x-p|} \right\}, \quad (7.30)$$

and

$$\psi_3 = -\frac{\chi f_0 \cos ly}{\Delta p_3} \left\{ \frac{f_1(0)}{\xi_1^2 \eta_2^2} - \frac{f_1(\xi_1)}{\xi_1^2(\xi_1^2 + \eta_2^2)} \cos \xi_1(x-p)H(x-p) - \frac{f_1(i\eta_2)}{2\eta_2^2(\xi_1^2 + \eta_2^2)} e^{-\eta_2|x-p|} \right\}. \quad (7.31)$$

Both ψ_1 and ψ_3 retain the contributions from the poles at $\xi = \pm \xi_2$ which decays exponentially away from the heat source. The constant term is now found for both $x > p$ and $x < p$. For $x > p$ there is a sinusoidal term due to the contributions from the poles at $\xi = \pm \xi_1$. As in case 1 the streamfunction solutions are discontinuous at $x = p$.

7.4 Solutions for Other Heating Structures

In this section we consider the atmospheric response to the zonal heating distributions (cf., 6.6, 6.48)

$$q'_C = \frac{\pi Q_0}{4x_0} \cos ly \Pi\left(\frac{x}{2x_0}\right) \cos\left(\frac{\pi x}{2x_0}\right), \quad (7.32)$$

and

$$q'_S = -\frac{\pi Q_0}{4x_0} \cos ly \Pi\left(\frac{x}{2x_0}\right) \sin\left(\frac{\pi x}{x_0}\right), \quad (7.33)$$

where

$$\int_{-\infty}^{\infty} q'_C(x, y) dx = \int_{-\infty}^{\infty} q'(x, y) dx, \quad (7.34)$$

with q' defined by (7.4). Here $\Pi(\frac{x}{2x_0})$ is the rectangular function used in Chapter 6, viz.,

$$\Pi\left(\frac{x}{2x_0}\right) = \begin{cases} 0, & \text{if } x > x_0; \\ 1, & \text{if } -x_0 < x < x_0; \\ 0, & \text{if } x < -x_0. \end{cases} \quad (7.35)$$

The heating is thus confined to the positive part of one period of the cosine function in (7.32) and to one period of the inverted sine function in (7.33). Motivation for these zonal structures will be given in Section 7.6.

The solutions to (7.5)–(7.7) with diabatic heating of the form (7.32) and (7.33) are obtained by using the solutions (7.23), (7.25), (7.26) and (7.29), (7.30), (7.31) as Green's functions. Hence

$$(\psi_{1C,S}, \psi_{3C,S}, \omega_{2C,S})(x, y) = \int_{-\infty}^{\infty} f_{C,S}(p) G(x, y; p) dp, \quad (7.36)$$

where $f_C(p) = \frac{\pi}{4x_0} \Pi(\frac{p}{2x_0}) \cos(\frac{\pi p}{2x_0})$, $f_S(p) = -\frac{\pi}{4x_0} \Pi(\frac{p}{2x_0}) \sin(\frac{\pi p}{2x_0})$ and $G(x, y; p)$ is the solution to the system (7.5)–(7.7) with heating of the form (7.4). Upon substituting f_C and $G(x, y; p)$ into (7.36) and evaluating the integral, one obtains:

case 1 : $l^2 > \{\gamma^2 + \delta\}^{\frac{1}{2}} - \gamma$.

$$\omega_2 = \frac{\pi^2 \chi \cos ly}{2(\eta_1^2 - \eta_2^2)} \left\{ \frac{f_1(i\eta_1) f_3(i\eta_1)}{\eta_1(\pi^2 + 4\eta_1^2 x_0^2)} \begin{cases} e^{-\eta_1 |x|} \cosh \eta_1 x_0 \operatorname{sgn} x, & \text{if } |x| \geq x_0; \\ \sin \frac{\pi x}{2x_0} - e^{-\eta_1 x_0} \sinh \eta_1 x, & \text{if } |x| \leq x_0. \end{cases} \right. \\ \left. - \frac{f_1(i\eta_2) f_3(i\eta_2)}{\eta_2(\pi^2 + 4\eta_2^2 x_0^2)} \begin{cases} e^{-\eta_2 |x|} \cosh \eta_2 x_0 \operatorname{sgn} x, & \text{if } |x| \geq x_0; \\ \sin \frac{\pi x}{2x_0} - e^{-\eta_2 x_0} \sinh \eta_2 x, & \text{if } |x| \leq x_0. \end{cases} \right\}, \quad (7.37)$$

$$\begin{aligned}
\psi_1 = & -\frac{\chi f_0 \cos y}{\Delta p_1} \left\{ \frac{f_3(0)}{\eta_1^2 \eta_2^2} \begin{cases} 1, & \text{if } x \geq x_0; \\ \frac{1}{2} \{1 + \sin \frac{\pi x}{2x_0}\}, & \text{if } |x| \leq x_0; \\ 0, & \text{if } x \leq -x_0. \end{cases} \right. \\
& + \frac{\pi^2 f_3(i\eta_1)}{2\eta_1^2(\eta_1^2 - \eta_2^2)(\pi^2 + 4\eta_1^2 x_0^2)} \begin{cases} e^{-\eta_1 |x|} \cosh \eta_1 x_0, & \text{if } |x| \geq x_0; \\ e^{-\eta_1 x_0} \cosh \eta_1 x + \frac{2x_0 \eta_1}{\pi} \cos \frac{\pi x}{2x_0}, & \text{if } |x| \leq x_0. \end{cases} \\
& \left. - \frac{\pi^2 f_3(i\eta_2)}{2\eta_2^2(\eta_1^2 - \eta_2^2)(\pi^2 + 4\eta_2^2 x_0^2)} \begin{cases} e^{-\eta_2 |x|} \cosh \eta_2 x_0, & \text{if } |x| \geq x_0; \\ e^{-\eta_2 x_0} \cosh \eta_2 x + \frac{2x_0 \eta_2}{\pi} \cos \frac{\pi x}{2x_0}, & \text{if } |x| \leq x_0. \end{cases} \right\}, \quad (7.38)
\end{aligned}$$

and

$$\begin{aligned}
\psi_3 = & \frac{\chi f_0 \cos y}{\Delta p_3} \left\{ \frac{f_1(0)}{\eta_1^2 \eta_2^2} \begin{cases} 1, & \text{if } x \geq x_0; \\ \frac{1}{2} \{1 + \sin \frac{\pi x}{2x_0}\}, & \text{if } |x| \leq x_0; \\ 0, & \text{if } x \leq -x_0. \end{cases} \right. \\
& + \frac{\pi^2 f_1(i\eta_1)}{2\eta_1^2(\eta_1^2 - \eta_2^2)(\pi^2 + 4\eta_1^2 x_0^2)} \begin{cases} e^{-\eta_1 |x|} \cosh \eta_1 x_0, & \text{if } |x| \geq x_0; \\ e^{-\eta_1 x_0} \cosh \eta_1 x + \frac{2x_0 \eta_1}{\pi} \cos \frac{\pi x}{2x_0}, & \text{if } |x| \leq x_0. \end{cases} \\
& \left. - \frac{\pi^2 f_1(i\eta_2)}{2\eta_2^2(\eta_1^2 - \eta_2^2)(\pi^2 + 4\eta_2^2 x_0^2)} \begin{cases} e^{-\eta_2 |x|} \cosh \eta_2 x_0, & \text{if } |x| \geq x_0; \\ e^{-\eta_2 x_0} \cosh \eta_2 x + \frac{2x_0 \eta_2}{\pi} \cos \frac{\pi x}{2x_0}, & \text{if } |x| \leq x_0. \end{cases} \right\}. \quad (7.39)
\end{aligned}$$

case 2: $l^2 < \{\gamma^2 + \delta\}^{\frac{1}{2}} - \gamma$.

$$\begin{aligned}
\omega_2 = & \frac{\pi^2 \chi \cos y}{2(\xi_1^2 + \eta_2^2)} \left\{ \frac{2f_1(\xi_1)f_3(\xi_1)}{\xi_1(\pi^2 - 4\xi_1^2 x_0^2)} \begin{cases} \cos \xi_1 x_0 \sin \xi_1 x, & \text{if } x \geq x_0; \\ \frac{1}{2} \sin \xi_1(x + x_0) - \frac{x_0 \xi_1}{\pi} \cos \frac{\pi x}{2x_0}, & \text{if } |x| \leq x_0; \\ 0, & \text{if } x \leq -x_0. \end{cases} \right. \\
& \left. + \frac{f_1(i\eta_2)f_3(i\eta_2)}{\eta_2(\pi^2 + 4\eta_2^2 x_0^2)} \begin{cases} e^{-\eta_2 |x|} \cosh \eta_2 x_0 \operatorname{sgn} x, & \text{if } |x| > x_0; \\ \sin \frac{\pi x}{2x_0} - e^{-\eta_2 x_0} \sinh \eta_2 x, & \text{if } |x| < x_0. \end{cases} \right\}, \quad (7.40)
\end{aligned}$$

$$\begin{aligned}
\psi_1 = & \frac{\chi f_0 \cos y}{\Delta p_1} \left\{ \frac{f_3(0)}{\xi_1^2 \eta_2^2} \begin{cases} \cos \xi_1 x_0 \cos \xi_1 x, & \text{if } x \geq x_0; \\ \frac{1}{2} \{ \cos \xi_1(x + x_0) + \sin \frac{\pi x}{2x_0} \}, & \text{if } |x| \leq x_0; \\ 0, & \text{if } x \leq -x_0. \end{cases} \right. \\
& - \frac{\pi^2 f_3(\xi_1)}{\xi_1^2(\xi_1^2 + \eta_2^2)(\pi^2 - 4\xi_1^2 x_0^2)} \begin{cases} \cos \xi_1 x_0 \cos \xi_1 x, & \text{if } x \geq x_0; \\ \frac{1}{2} \{ \cos \xi_1(x + x_0) + \sin \frac{\pi x}{2x_0} \}, & \text{if } |x| \leq x_0; \\ 0, & \text{if } x \leq -x_0. \end{cases} \\
& \left. - \frac{\pi^2 f_3(i\eta_2)}{2\eta_2^2(\xi_1^2 + \eta_2^2)(\pi^2 + 4\eta_2^2 x_0^2)} \begin{cases} e^{-\eta_2 |x|} \cosh \eta_2 x_0, & \text{if } |x| \geq x_0; \\ e^{-\eta_2 x_0} \cosh \eta_2 x + \frac{2x_0 \eta_2}{\pi} \cos \frac{\pi x}{2x_0}, & \text{if } |x| \leq x_0. \end{cases} \right\}, \quad (7.41)
\end{aligned}$$

and

$$\begin{aligned} \psi_3 = & -\frac{\chi f_0 \cos ly}{\Delta p_3} \left\{ \frac{f_1(0)}{\xi_1^2 \eta_2^2} \right. \\ & - \frac{\pi^2 f_1(\xi_1)}{\xi_1^2 (\xi_1^2 + \eta_2^2) (\pi^2 - 4\xi_1^2 x_0^2)} \begin{cases} \cos \xi_1 x_0 \cos \xi_1 x, & \text{if } x \geq x_0; \\ \frac{1}{2} \{ \cos \xi_1 (x + x_0) + \sin \frac{\pi x}{2x_0} \}, & \text{if } |x| \leq x_0; \\ 0, & \text{if } x \leq -x_0. \end{cases} \\ & - \frac{\pi^2 f_1(i\eta_2)}{2\eta_2^2 (\xi_1^2 + \eta_2^2) (\pi^2 + 4\eta_2^2 x_0^2)} \begin{cases} e^{-\eta_2 |x|} \cosh \eta_2 x_0, & \text{if } |x| \geq x_0; \\ e^{-\eta_2 x_0} \cosh \eta_2 x + \frac{2x_0 \eta_2}{\pi} \cos \frac{\pi x}{2x_0}, & \text{if } |x| \leq x_0. \end{cases} \end{aligned} \quad (7.42) \end{aligned}$$

The solutions (7.37)–(7.42) approach the delta heating solutions (7.23), (7.25), (7.26), (7.29), (7.30), (7.31) in the limit as $x_0 \rightarrow 0$. It can be shown that that ω_2 , ψ_1 and ψ_3 are all continuous at $x = \pm x_0$.

The substitution of f_S and $G(x, y; p)$ into (7.36) yields:

case 1: $l^2 > \{\gamma^2 + \delta\}^{\frac{1}{2}} - \gamma$.

$$\begin{aligned} \omega_2 = & \frac{\pi^2 \chi \cos ly}{4(\eta_1^2 - \eta_2^2)} \left\{ \frac{f_1(i\eta_1) f_3(i\eta_1)}{\eta_1 (\pi^2 + \eta_1^2 x_0^2)} \begin{cases} -e^{-\eta_1 |x|} \sinh \eta_1 x_0, & \text{if } |x| \geq x_0; \\ \cos \frac{\pi x}{x_0} + e^{-\eta_1 x_0} \cosh \eta_1 x, & \text{if } |x| \leq x_0. \end{cases} \right. \\ & \left. - \frac{f_1(i\eta_2) f_3(i\eta_2)}{\eta_2 (\pi^2 + \eta_2^2 x_0^2)} \begin{cases} -e^{-\eta_2 |x|} \sinh \eta_2 x_0, & \text{if } |x| \geq x_0; \\ \cos \frac{\pi x}{x_0} + e^{-\eta_2 x_0} \cosh \eta_2 x, & \text{if } |x| \leq x_0. \end{cases} \right\}, \quad (7.43) \end{aligned}$$

$$\begin{aligned} \psi_1 = & -\frac{\chi f_0 \cos ly}{4\Delta p_1} \left\{ \frac{f_3(0)}{\eta_1^2 \eta_2^2} \begin{cases} 0, & \text{if } |x| \geq x_0; \\ 1 + \cos \frac{\pi x}{x_0}, & \text{if } |x| \leq x_0. \end{cases} \right. \\ & - \frac{\pi^2 f_3(i\eta_1)}{\eta_1^2 (\eta_1^2 - \eta_2^2) (\pi^2 + \eta_1^2 x_0^2)} \begin{cases} e^{-\eta_1 |x|} \sinh \eta_1 x_0 \operatorname{sgn} x, & \text{if } |x| \geq x_0; \\ e^{-\eta_1 x_0} \sinh \eta_1 x + \frac{x_0 \eta_1}{\pi} \sin \frac{\pi x}{x_0}, & \text{if } |x| \leq x_0. \end{cases} \\ & + \frac{\pi^2 f_3(i\eta_2)}{\eta_2^2 (\eta_1^2 - \eta_2^2) (\pi^2 + \eta_2^2 x_0^2)} \begin{cases} e^{-\eta_2 |x|} \sinh \eta_2 x_0 \operatorname{sgn} x, & \text{if } |x| \geq x_0; \\ e^{-\eta_2 x_0} \sinh \eta_2 x + \frac{x_0 \eta_2}{\pi} \sin \frac{\pi x}{x_0}, & \text{if } |x| \leq x_0. \end{cases} \end{aligned} \quad (7.44) \end{aligned}$$

and

$$\begin{aligned}
\psi_3 = & \frac{\chi f_0 \cos ly}{4\Delta p_3} \left\{ \frac{f_1(0)}{\eta_1^2 \eta_2^2} \begin{cases} 0, & \text{if } |x| \geq x_0; \\ 1 + \cos \frac{\pi x}{x_0}, & \text{if } |x| \leq x_0. \end{cases} \right. \\
& - \frac{\pi^2 f_1(i\eta_1)}{\eta_1^2(\eta_1^2 - \eta_2^2)(\pi^2 + \eta_1^2 x_0^2)} \begin{cases} e^{-\eta_1 |x|} \sinh \eta_1 x_0 \operatorname{sgn} x, & \text{if } |x| \geq x_0; \\ e^{-\eta_1 x_0} \sinh \eta_1 x + \frac{x_0 \eta_1}{\pi} \sin \frac{\pi x}{x_0}, & \text{if } |x| \leq x_0. \end{cases} \\
& \left. + \frac{\pi^2 f_1(i\eta_2)}{\eta_2^2(\eta_1^2 - \eta_2^2)(\pi^2 + \eta_2^2 x_0^2)} \begin{cases} e^{-\eta_2 |x|} \sinh \eta_2 x_0 \operatorname{sgn} x, & \text{if } |x| \geq x_0; \\ e^{-\eta_2 x_0} \sinh \eta_2 x + \frac{x_0 \eta_2}{\pi} \sin \frac{\pi x}{x_0}, & \text{if } |x| \leq x_0. \end{cases} \right\}. \quad (7.45)
\end{aligned}$$

case 2: $l^2 < \{\gamma^2 + \delta\}^{\frac{1}{2}} - \gamma$.

$$\begin{aligned}
\omega_2 = & \frac{\pi^2 \chi \cos ly}{4(\xi_1^2 + \eta_2^2)} \left\{ \frac{f_1(\xi_1) f_3(\xi_1)}{\xi_1(\pi^2 - \xi_1^2 x_0^2)} \begin{cases} 2 \sin \xi_1 x_0 \cos \xi_1 x, & \text{if } x \geq x_0; \\ \frac{x_0 \xi_1}{\pi} \sin \frac{\pi x}{x_0} + \sin \xi_1(x + x_0), & \text{if } |x| \leq x_0; \\ 0, & \text{if } x \leq -x_0. \end{cases} \right. \\
& \left. + \frac{f_1(i\eta_2) f_3(i\eta_2)}{\eta_2(\pi^2 + \eta_2^2 x_0^2)} \begin{cases} -e^{-\eta_2 |x|} \sinh \eta_2 x_0, & \text{if } |x| \geq x_0; \\ \cos \frac{\pi x}{x_0} + e^{-\eta_2 x_0} \cosh \eta_2 x, & \text{if } |x| \leq x_0. \end{cases} \right\}, \quad (7.46)
\end{aligned}$$

$$\begin{aligned}
\psi_1 = & -\frac{\pi^2 \chi f_0 \cos ly}{4\Delta p_1(\xi_1^2 + \eta_2^2)} \left\{ \frac{f_3(\xi_1)}{\xi_1^2(\pi^2 - \xi_1^2 x_0^2)} \begin{cases} -2 \sin \xi_1 x_0 \sin \xi_1 x, & \text{if } x \geq x_0; \\ \cos \xi_1(x + x_0) + \cos \frac{\pi x}{x_0}, & \text{if } |x| \leq x_0; \\ 0, & \text{if } x \leq -x_0. \end{cases} \right. \\
& \left. - \frac{f_3(i\eta_2)}{\eta_2^2(\pi^2 + \eta_2^2 x_0^2)} \begin{cases} e^{-\eta_2 |x|} \sinh \eta_2 x_0 \operatorname{sgn} x, & \text{if } |x| \geq x_0; \\ e^{-\eta_2 x_0} \sinh \eta_2 x + \frac{x_0 \eta_2}{\pi} \sin \frac{\pi x}{x_0}, & \text{if } |x| \leq x_0. \end{cases} \right\}, \quad (7.47)
\end{aligned}$$

and

$$\begin{aligned}
\psi_3 = & \frac{\pi^2 \chi f_0 \cos ly}{4\Delta p_3(\xi_1^2 + \eta_2^2)} \left\{ \frac{f_1(\xi_1)}{\xi_1^2(\pi^2 - \xi_1^2 x_0^2)} \begin{cases} -2 \sin \xi_1 x_0 \sin \xi_1 x, & \text{if } x \geq x_0; \\ \cos \xi_1(x + x_0) + \cos \frac{\pi x}{x_0}, & \text{if } |x| \leq x_0; \\ 0, & \text{if } x \leq -x_0. \end{cases} \right. \\
& \left. - \frac{f_1(i\eta_2)}{\eta_2^2(\pi^2 + \eta_2^2 x_0^2)} \begin{cases} e^{-\eta_2 |x|} \sinh \eta_2 x_0 \operatorname{sgn} x, & \text{if } |x| \geq x_0; \\ e^{-\eta_2 x_0} \sinh \eta_2 x + \frac{x_0 \eta_2}{\pi} \sin \frac{\pi x}{x_0}, & \text{if } |x| \leq x_0. \end{cases} \right\}, \quad (7.48)
\end{aligned}$$

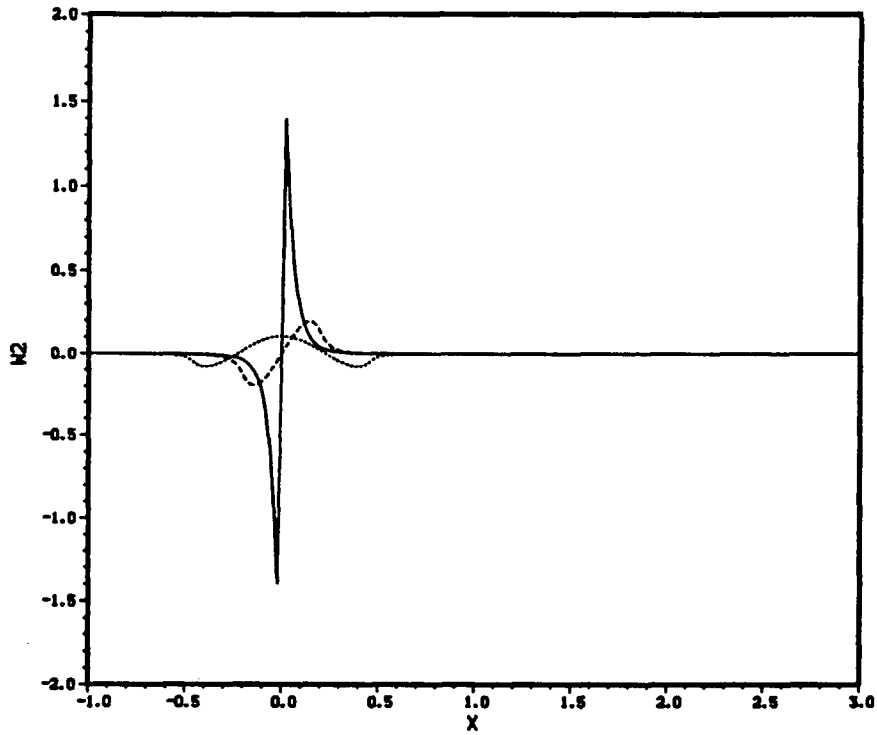
The solutions for the streamfunctions ψ_1 and ψ_3 and the vertical motion field ω_2 are all continuous at $x = \pm x_0$.

7.5 Discussion

The solutions for ω_2 , ψ_1 , and ψ_3 , presented in the previous two sections, have been plotted for the equally spaced level model (Model 1) in Figs. 56a,b,c along the line $y = 0$, for a wavenumber $l = 1.4 \times 10^{-6} \text{m}^{-1}$, typical of case 1. Here we use $Q_0 = 0.01 \text{ Wkg}^{-1}$, $C_p = 1005 \text{ Jkg}^{-1}\text{K}^{-1}$, $R = 290 \text{ Jkg}^{-1}\text{K}^{-1}$, and the parameters of Section 7.3. As we have normalized the heating structures (7.32) and (7.33) to satisfy (7.34), we must multiply the solutions given in Section 7.4 by a factor of 10^6 . For the line source heating solutions (solid line), there is a strong local response. In the streamfunction plots (Figs. 56b, 56c) this local response decays rapidly to a constant far field response. When heat forcing is spread over a broader region (dashed line; $x_0 = 2.0 \times 10^6 \text{m}$), the local response diminishes in magnitude. The solutions ω_2 , ψ_1 , ψ_3 for the unequally spaced level model (Model 2), where the thermodynamic equation is applied at the 800 mb (as opposed to the 600 mb level), are plotted in Figs. 57a,b,c. As expected the zonal structure of Figs. 57a–c is similar to that of Figs. 56a–c. The magnitude of the streamfunction at the upper level is significantly smaller in Fig. 57b than in Fig. 56b, while at the lower level the magnitude of ψ_3 is only slightly smaller in Fig. 57c. Similarly the magnitudes of ω_2 differ only slightly for the two models (Fig. 57a, cf., Fig. 56a). Since η_1 and η_2 are larger for Model 2 than Model 1 (see Tables 6 and 7 in Appendix II) the atmospheric response in Model 2 is more locally trapped.

Figures 56b,c and 57b,c are very similar to those obtained in Chapter 6 (see Figs. 45a and 46a) and indicate that the inclusion of wind shear has little effect on the results of the continuous model. Also we note that the results obtained above are very different from those that one would obtain if periodic heat forcing were used. If the system (7.5)–(7.7) were forced with periodic heating of wavenumber k , the solutions for ω_2 , ψ_1 , ψ_3 would also be periodic with wavenumber k .

a SOLUTION ALONG Y=0



b SOLUTION ALONG Y=0

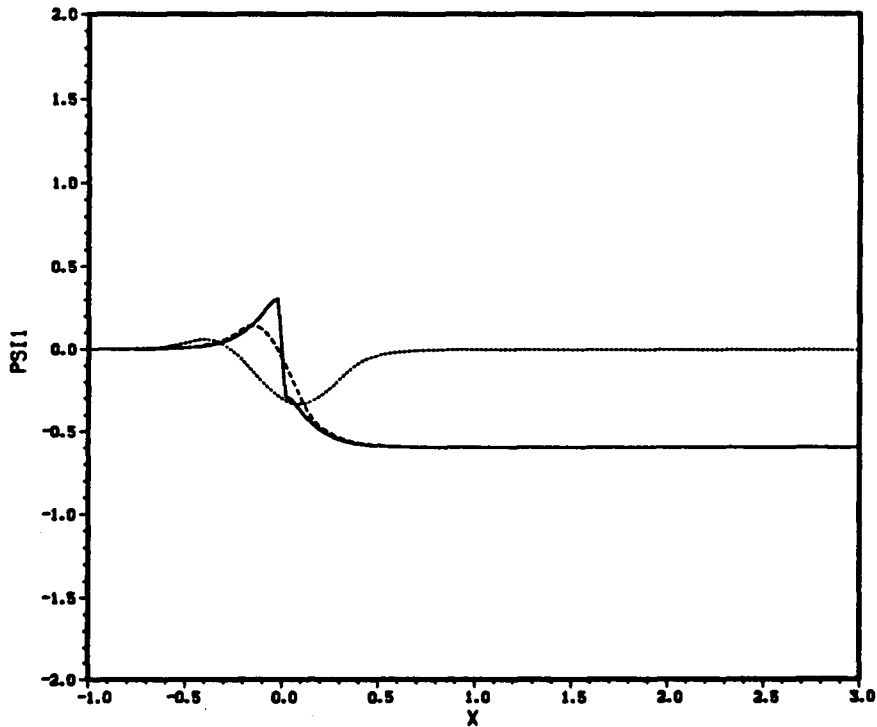


Figure 56 . Model 1 solutions for case 1 $l^2 > \{\gamma^2 + \delta\}^{\frac{1}{2}} - \gamma$, and the parameters of Section 7.3. The solid line is for line source heat forcing (7.4), the dashed line is for segmented cosine forcing (7.32), and the dotted line is for segmented sine forcing (7.33). a) — Vertical motion field ω_2 . b) — Streamfunction at the upper level, ψ_1 . c) — Streamfunction at the lower level, ψ_3 . The vertical axis in a) is in 10^{-4}mbs^{-1} , and in b) and c) is in $10^6 \text{m}^2 \text{s}^{-1}$. In all three plots the x -axis is in 10^7m .

c SOLUTION ALONG Y=0

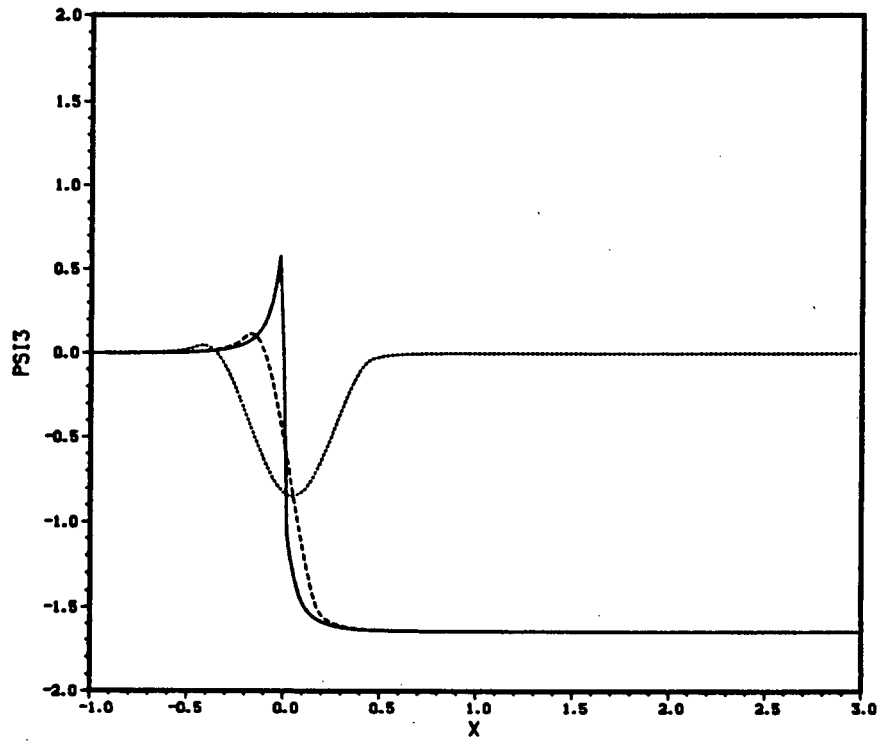
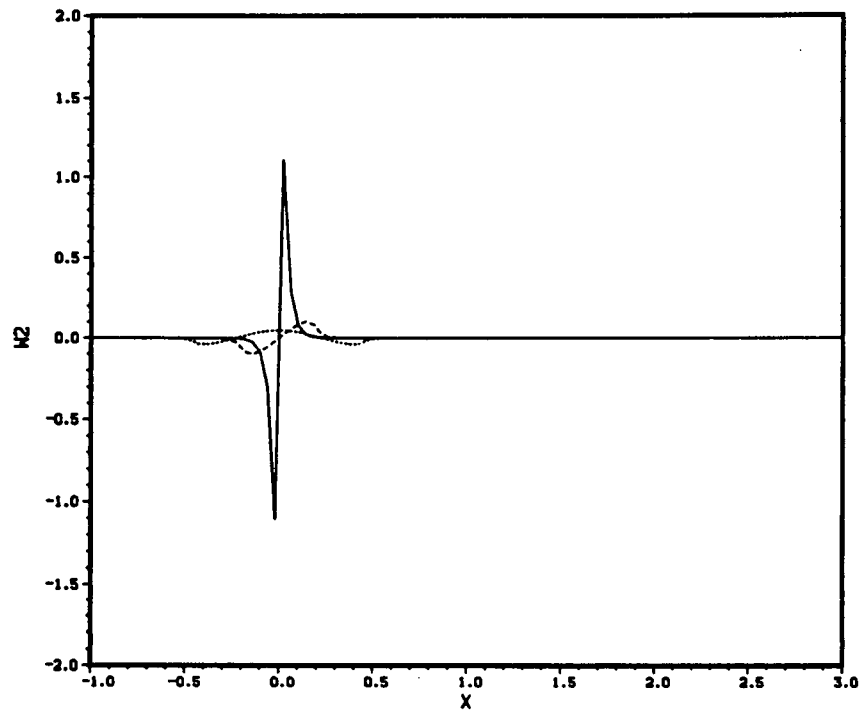


Figure 56 cont.

a SOLUTION ALONG Y=0



b SOLUTION ALONG Y=0

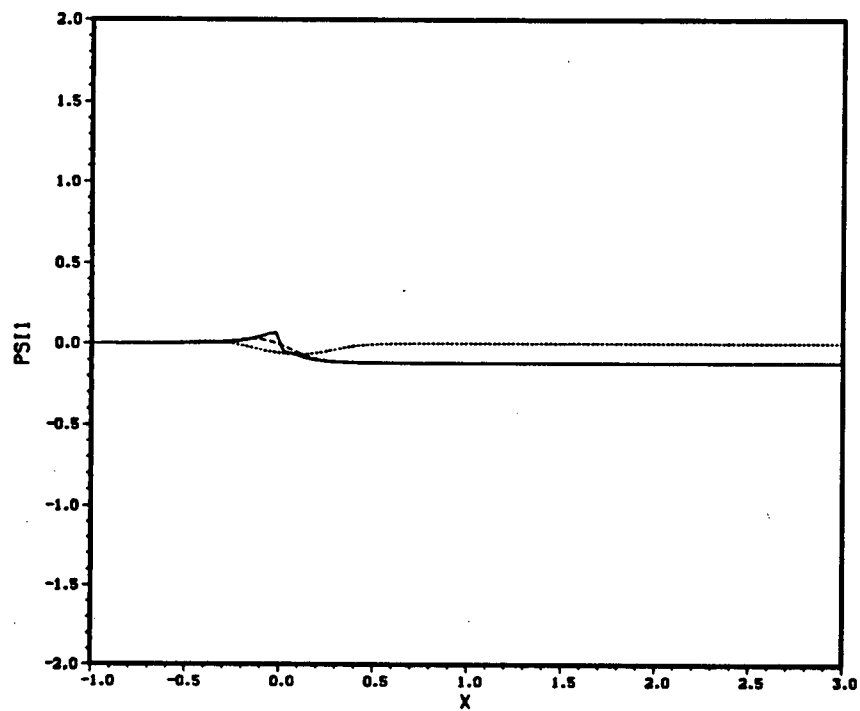


Figure 57 . As in Fig. 56 but for Model 2 for case 1 $l^2 > \{\gamma^2 + \delta\}^{\frac{1}{2}} - \gamma$.

c SOLUTION ALONG Y=0

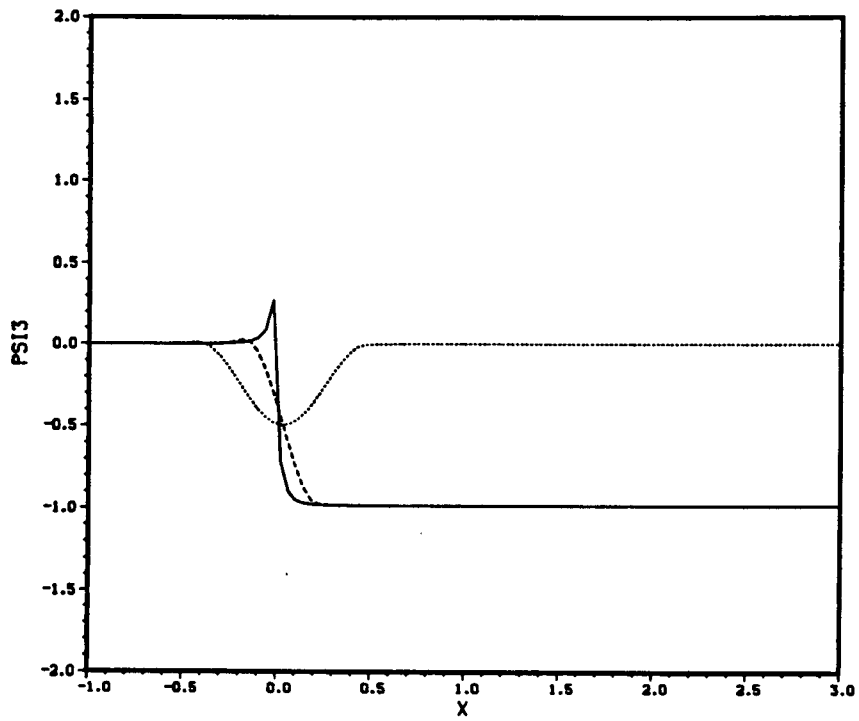


Figure 57 cont.

A discussion of the response for the segmented sine heating distribution will be delayed until the next section. It is interesting however to note that since, $\int_{-\infty}^{\infty} q'_s(x, y) dx = 0$ (see 7.33), the far field response is zero.

For small wavenumbers (case 2 —a case not examined in detail in Chapter 6) the far field solutions are very different from those described above. This is illustrated for Model 1 in Figs. 58a,b,c and for Model 2 in Figs. 59a,b,c. Here $l = 0.8 \times 10^{-6} \text{m}^{-1}$ while the other parameters remain the same. Once more a strong local response exists for the line source heating solutions (solid line in Figs. 58a–c). This diminishes in magnitude as the heating is spread over a broader region (dashed line in Figs. 58a–c). Unlike the solution one would obtain for forcing at a given wavenumber k , a natural wavenumber ξ_1 (given by 7.19) for the downstream disturbance, is forced. This corresponds to a wavelength of about 800 km if the parameters mentioned above are used. When the heating is distributed over a broader expanse, the magnitude of this far field stationary wave pattern decreases, although there is no effect on the wavelength or phase.

For Model 2 (Figs. 59a–c) the response once more has a similar zonal structure to that of Model 1, although the wavelength of the downstream stationary wave pattern has increased slightly due to a slightly smaller ξ_1 . The magnitudes of ω_2 , ψ_1 , ψ_3 are somewhat smaller especially for the upper level streamfunction ψ_3 .

The contribution from the first term in the RHS of (7.30) and (7.31) now forces the far field mean response of ψ_1 (Figs. 58b, and 59b) to be greater than zero and of ψ_3 to be less than zero (Figs. 58c, and 59c).

The segmented sine solutions (dotted line in Figs. 58a–c, 59a–c; $x_0 = 4.55 \times 10^6$) differ from those of case 1 in a similar manner to that described above.

In many of Figures 56–59 $\lim_{x \rightarrow \infty} (\omega_2, \psi_1, \psi_3) \neq \lim_{x \rightarrow -\infty} (\omega_2, \psi_1, \psi_3)$. When we try to apply these results to the sphere, which is periodic in x , this mismatching needs some interpretation. For simplicity we examine Model 1 for case 2 where the levels are equally spaced. The forced wavenumber for the downstream stationary wave pattern is $\xi_1 =$

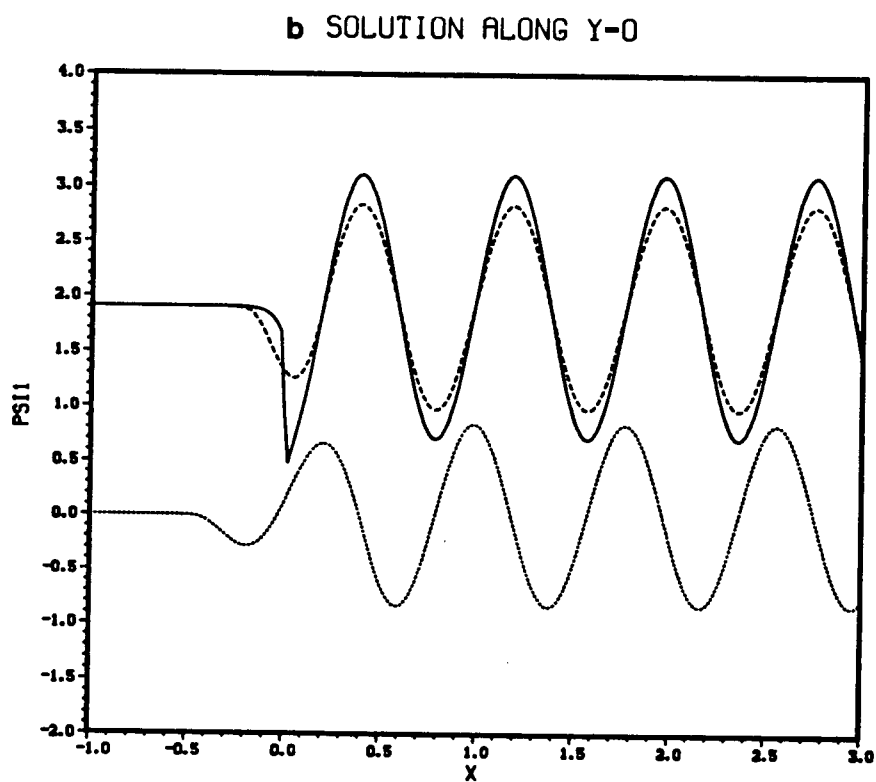
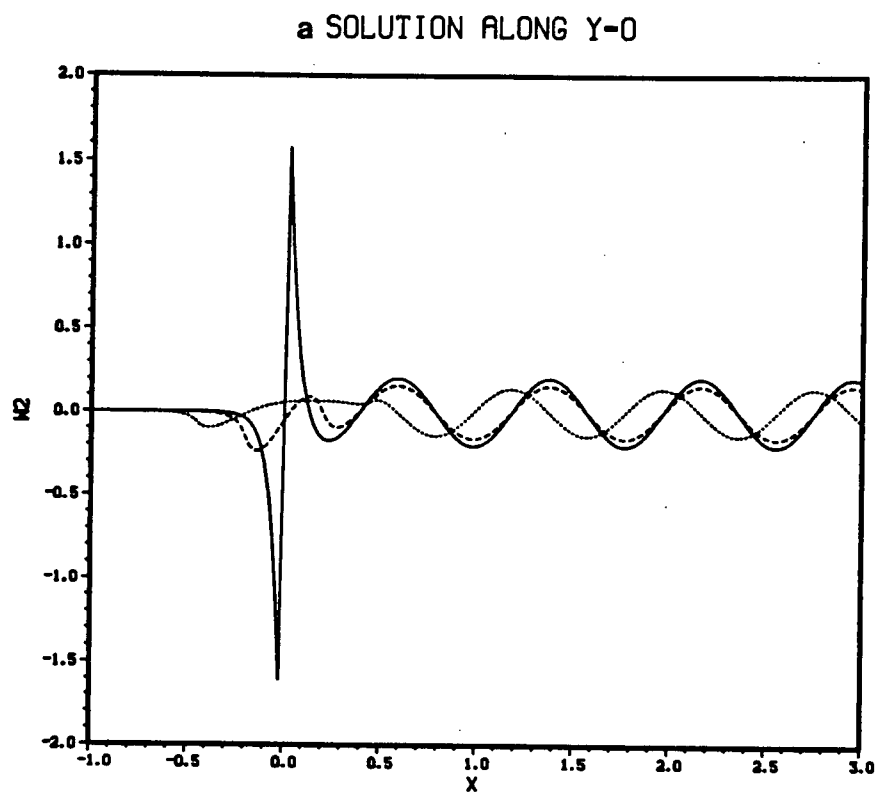


Figure 58 . As in Fig. 56 but for Model 1 for case 2 $l^2 < \{\gamma^2 + \delta\}^{\frac{1}{2}} - \gamma$.

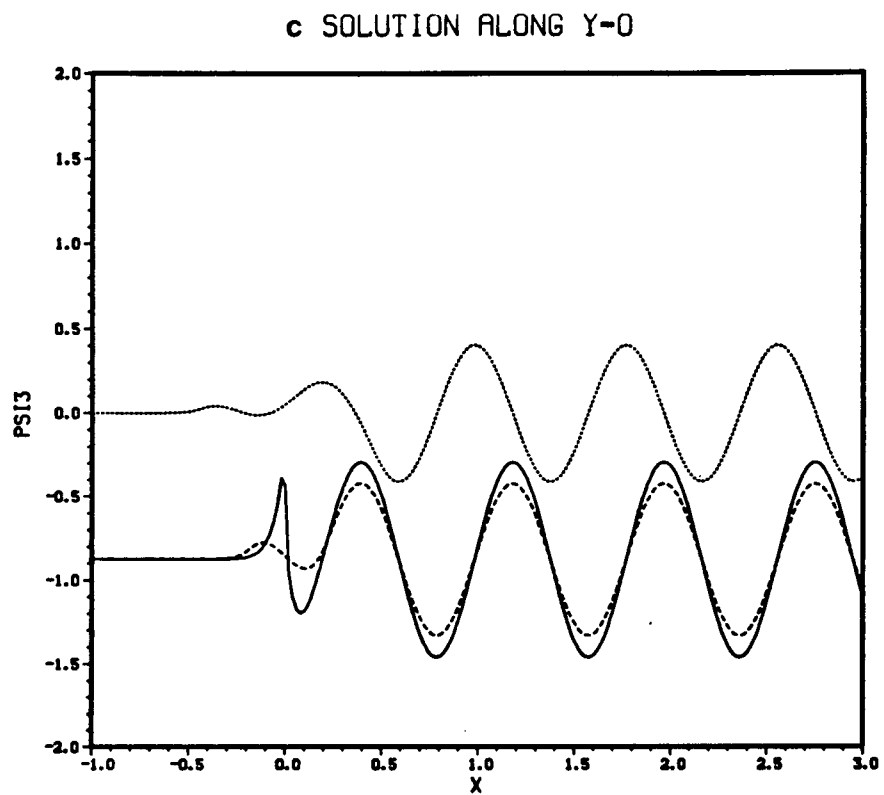
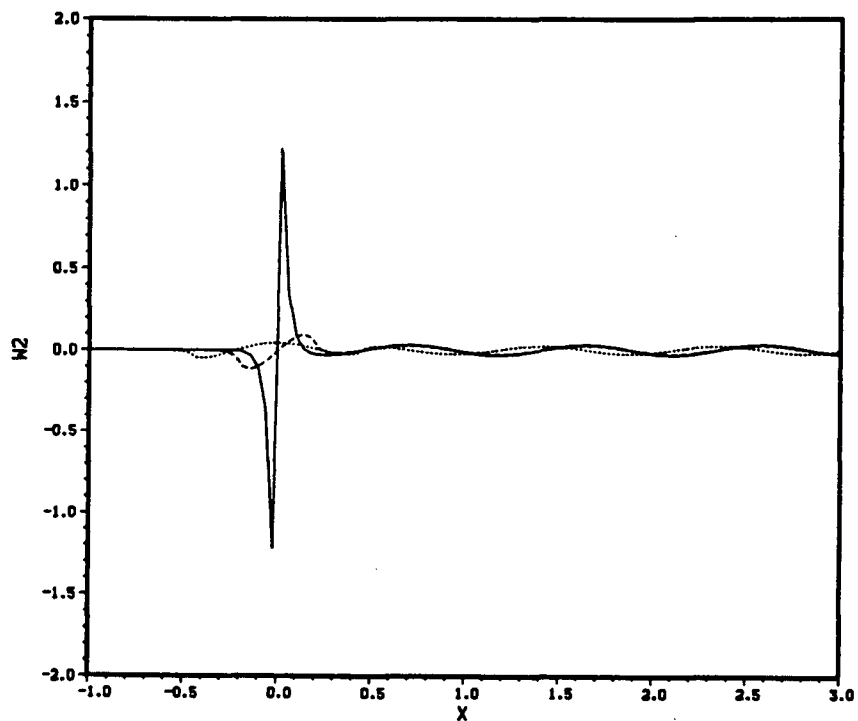


Figure 58 cont.

a SOLUTION ALONG Y=0



b SOLUTION ALONG Y=0

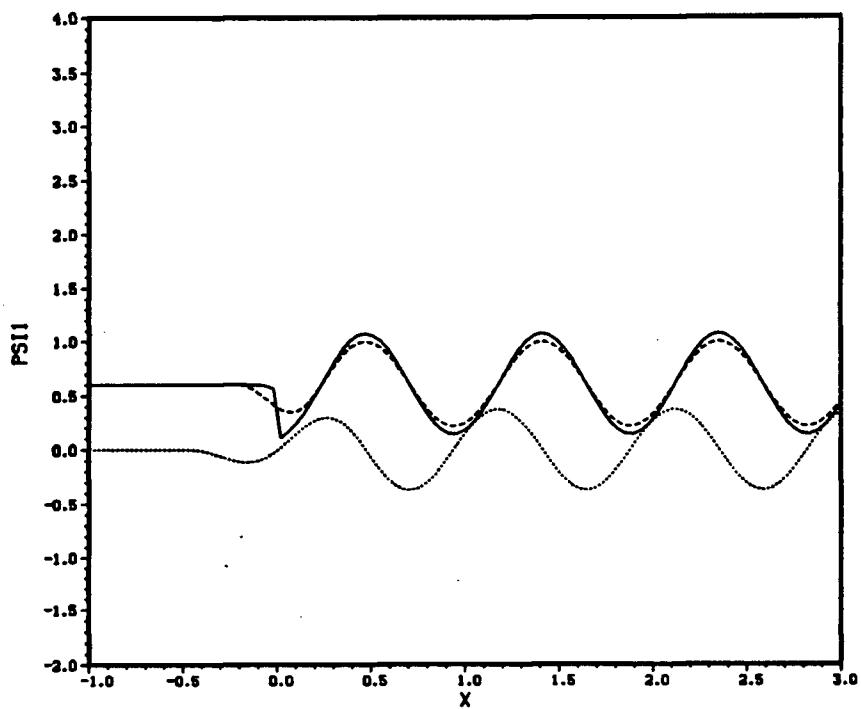


Figure 59 . As in Fig. 56 but for Model 2 for case 2 $l^2 < \{\gamma^2 + \delta\}^{\frac{1}{2}} - \gamma$.

c SOLUTION ALONG Y=0

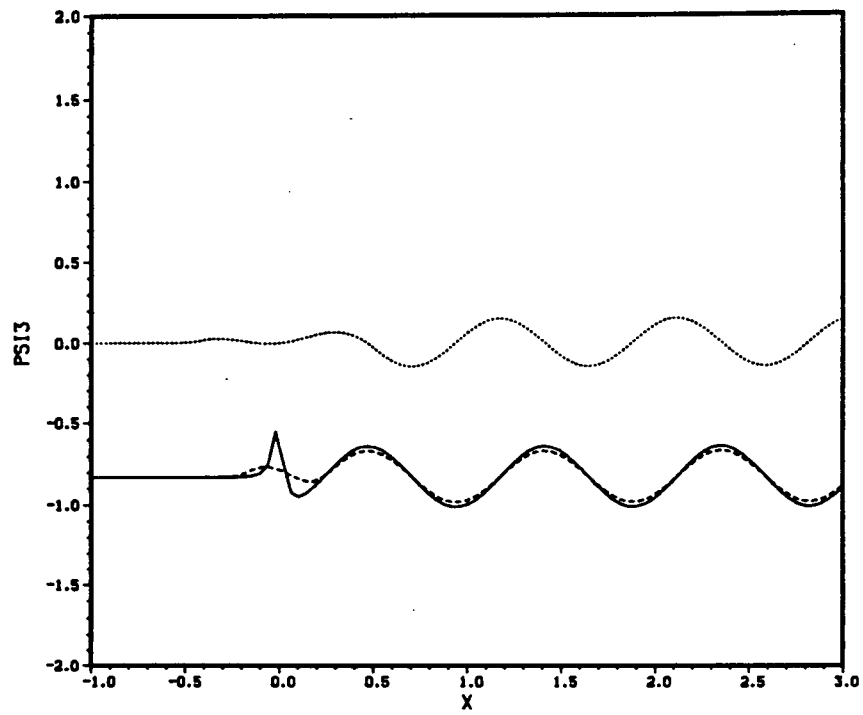


Figure 59 cont.

$8 \times 10^{-7} \text{m}^{-1}$ (see Table 6), which corresponds to wavenumber 4 on the sphere. Suppose now that we are on the sphere. The time dependent unforced versions of (7.5)–(7.7) allow free wave solutions $\propto e^{i(kx+ly-ct)}$ which have phase speed in the x -direction (Holton, 1979 p. 218)

$$c_x = U_m - \frac{\beta(K^2 + \lambda^2)}{K^2(K^2 + 2\lambda^2)} \pm \bar{\delta}^{1/2}, \quad (7.49)$$

where

$$\bar{\delta} = \frac{\beta^2 \lambda^4}{K^4(K^2 + 2\lambda^2)^2} - \frac{U_T^2(2\lambda^2 - K^2)}{(K^2 + 2\lambda^2)}, \quad (7.50)$$

and

$$U_m = \frac{U_1 + U_3}{2}, \quad U_T = \frac{U_1 - U_3}{2}, \quad K^2 = k^2 + l^2. \quad (7.51)$$

Now we let $k = \xi_1$ and we use the parameters of Section 7.3 to get two stable modes for which $c_{x1} = 6.3 \text{ ms}^{-1}$ and $c_{x2} = 0.015 \text{ ms}^{-1}$. These Rossby modes would propagate around the globe (at 40° N) in $t_1 = 57$ days and $t_2 = 66$ years(!), respectively. A typical time scale for dissipative damping is about $t_d = 6$ days (Frankignoul, 1985a). Since $t_d \ll t_1$ and t_2 , an eastward propagating wave would be damped rather quickly and would not likely propagate around the globe. Thus the assumption $-\infty < x < \infty$ is indeed justified. The response is mainly downstream of the heating with a small exponentially decaying response upstream.

In order to compare the model results with work by others we focus our attention on the segmented cosine heat forcing solutions (dashed line in Figs. 56–59). Egger (1977), using a two level, linear hemispheric model with friction, examined the stationary atmospheric response to a rectangular heat source. His heat source had a width of 1700 km, analogous to $l = 1.8 \times 10^{-6}$ (case 1) in this model, and was centered at 45° N with a 2000 km horizontal extent. The atmospheric response near the surface consisted of a strong low downstream of the heating region with a weak high upstream. The dashed lines of Figs. 56c and 57c are in excellent agreement with his results. If friction were included in our model, the response downstream would diminish as discussed above. The resulting solutions would be almost identical to Egger's Figs. 2 and 3.

Hoskins and Karoly (1981) also examined the steady state linear wave response of the atmosphere to midlatitude heating using a five level primitive equation model. They considered heating over a broad meridional extent and hence fall into case 2 in the model of this paper. In their model, Hoskins and Karoly observed weak ascending motion ahead of the heating and weak descending motion behind, with very small extrema. This is in excellent agreement with Fig. 59a (dashed line). Weak ascending motion is clearly visible ahead of the heating and weak descending motion behind. Similarly, they observed a strong lower level trough and an upper level high downstream of the heating region. These results are also apparent in Figs. 59b and 59c. If friction were included in the model the troughs and ridges still further downstream (Figs. 59b,c) would not be as prominent (see Chapter 8).

As mentioned above, the downstream stationary wave pattern for case 2 corresponds to wavenumber 4 for Model 1 and to wavenumber 3 for Model 2, on the sphere. It is interesting to note that in the GCM studies of Chervin *et al.* (1976, 1980), Kutzbach *et al.* (1977) and Frankignoul (1985b), the atmospheric response to SST anomaly heating was dominated by zonal wavenumber 3–4 perturbations, which are comparable to those observed in our model.

7.6 Application to the Kuroshio Region

In order to investigate the possible effect of the Kuroshio heating anomalies on the downstream atmospheric conditions, and hence to once more theoretically test the hypothesis of Zhao and McBean (1987b) given in Section 5.6, we use the segmented cosine heat forcing model with $x_0 = 2.0 \times 10^6$ m corresponding to heating over an area of 47° extent. Here we assume that the oceanic heat flux anomalies manifest themselves as diabatic heating anomalies at the 800 mb level (Model 2). The origin $(x, y) = (0, 0)$ is taken near the east coast of Asia at 120° E, 40° N. We have chosen Model 2 instead of Model 1 since over the Kuroshio the oceanic heat flux leads to shallow heating, especially in winter (Nitta and So, 1980; Hoskins and Karoly, 1981; Masuda, 1983).

Finally, in an attempt to model the atmospheric response to heating with the structure of the first EOF of Zhao and McBean (1987a) (see Chapter 5), we consider heating of the form (7.33) with $x_0 = 4.55 \times 10^6 \text{m}$. This corresponds to positive anomalous heating over the western half of the North Pacific and negative anomalous heating over the eastern half of the North Pacific.

A meridional wavenumber $l = 1.4 \times 10^{-6} \text{m}^{-1}$ (ie., a wavelength of $4.5 \times 10^6 \text{m}$), is chosen. This corresponds to positive heating over a region of 20° extent, centered at 40°N (see Fig. 38), and falls into case 1 as described earlier. The streamfunction at the upper and lower level has been plotted in Figs. 57b and 57c respectively, for both the segmented cosine model (dashed line) and the segmented sine model (dotted line).

When Kuroshio heating is included alone the local response at both levels consists of a gradual transition from the region $x < -x_0$, to the far field region $x > x_0$. The negative response is consistent with the observed large negative correlations (Figs. 42a–c) downstream of the heating region, and hence is consistent with the argument proposed by Zhao and McBean (1987b). In the region $x < -x_0$ there is a small positive response which is apparent in the correlation plots of Figs. 42a–c. As observed in WMB, the streamfunction at the upper level is of insignificant magnitude when compared to the response at the lower level. Thus the atmospheric response is trapped near to the surface.

Although the above results are consistent with the observations, a more satisfactory agreement is obtained when cooling in the eastern Pacific is included. Once more Figs. 57b,c portray the streamfunction at the upper and lower level, respectively. The positive response upstream of the Kuroshio region is once more barely visible in the lower level plot (Fig. 57c). Over the area corresponding to the central North Pacific there is a large negative response in Fig. 57c. This feature is in excellent agreement with the correlations of Figs. 42a–c. Once more the results are similar to those of WMB in that the upper level response is of insignificant magnitude when compared to the lower level.

In the spatial correlation plots (Figs. 42a–c) the observed results show significant cor-

relations at all heights, whereas the response of Model 2 is weak at the upper level. The most significant correlations however occur in the SLP plot (Fig. 42a), where the response of Model 2 is largest. At the upper level the response of the model is small (Fig. 57b) and hence would not be expected to contribute to the observed correlations. It appears therefore that the correlations in the upper level plots (Figs. 42b,c) simply arise from the spatial correlations of the geopotential field. This ridge/trough structure in turn forces Kuroshio heating anomalies (and eastern Pacific cooling anomalies). The heating/cooling anomalies then “feedback” and intensify the low in the lower troposphere over the central North Pacific (Fig. 42a). This mechanism is in agreement with the argument of Zhao and McBean given in Section 5.6 and is the same as the conclusion of Section 6.6.

8. A Time Dependent Model of the Atmosphere Response to Midlatitude Heating with Various Zonal Structures

8.1 Introduction

As mentioned in Chapter 6, in most linear wave theories of large-scale thermally-driven atmospheric motions the zonal structure of the heat forcing is assumed to have the form $q' \propto \cos kx$, in order to model the heating associated with the contrasting thermal properties of land and sea (e.g., Frankignoul 1985a, who uses a two level β -plane channel model; Pedlosky 1979, who employs a continuously stratified β -plane model). Moreover, these theories are steady state. As in Chapters 6 and 7, one purpose of this chapter is to introduce more realistic zonal structures of the oceanic diabatic heating anomalies and hence to determine the effects of these distributions on the transient atmospheric response. To accomplish this we use a simple linear, time dependent, two level quasigeostrophic model.

In Chapter 6 we examined the effects of localized heating on the steady state atmospheric response using a continuously stratified quasigeostrophic model, linearized about a constant zonal flow U_0 . We found that for parameters applicable to North Pacific wintertime conditions, there was a strong local response and a constant far field response. In order to examine the effects of vertical shear on these results we introduced a steady state two level quasigeostrophic model in Chapter 7, with diabatic heating with the same zonal structures as in Chapter 6. Two cases emerged in the analysis. For small scale meridional heating structures (large meridional wavenumbers, l) we found that the results were identical to those of Chapter 6, and hence concluded that the inclusion of vertical shear had little effect. On the other hand, for large scale meridional heating structures (small meridional wavenumbers, l), a case not examined in detail in Chapter 6, the response consisted of a wavelike perturbation corresponding to a zonal wavenumber 3–4 scale, superimposed on a constant downstream response. A major limitation of both the above chapters, however, is the assumption of an unbounded zonal domain needed to define the Fourier transform.

We argued in Section 7.5, that if friction were included in the model the response would decay rapidly away from the heating region, and hence the use of an unbounded domain was indeed justified. Another purpose of this chapter, therefore, is to examine in detail the validity of this assumption. We thus require that our model be zonally periodic and consider solutions for both frictional and frictionless cases.

Hoskins and Karoly (1981) pointed out that in midlatitudes the atmospheric response to diabatic heating was strongly dependent on the vertical structure of the heating. We also examine this dependence by considering two models. The first (Model 1) has the thermodynamic equation applied at the 600 mb level, while the second (Model 2) has the level of heat input at 800 mb in order to model *shallow heating* which occurs over the Kuroshio region in winter (Nitta and So, 1980; Masuda, 1983). We will use the exact same zonal heating structures as in Chapters 6 and 7 for simplicity (see Sections 6.2 and 6.6 for a detailed description of the motivation behind the choice of these structures).

The outline of this chapter is as in Weaver and Mysak (1987a,b). In Section 8.2 the model is introduced and in Section 8.3 the solution is obtained for zonally periodic heat forcing. The solution obtained in Section 8.3 is then used in Section 8.4 to obtain solutions for segmented cosine and segmented sine zonal heating distributions. In Section 8.5 we present a discussion of the results, compare our results with earlier work, and examine the stability of our solutions.

8.2 Description of the model

A two level, β -plane, quasigeostrophic model is used. In pressure coordinates the linearized vorticity and thermodynamic equations for small time dependent disturbances are (Holton, 1979, Frankignoul, 1985a)

$$\left(\frac{\partial}{\partial t} + \bar{U} \frac{\partial}{\partial x} \right) \nabla^2 \psi + \beta \frac{\partial}{\partial x} \psi - f_0 \frac{\partial}{\partial p} \omega = 0, \quad (8.1)$$

$$\left(\frac{\partial}{\partial t} + \bar{U} \frac{\partial}{\partial x} \right) \frac{\partial \psi}{\partial p} - \frac{\partial \psi}{\partial x} \frac{\partial \bar{U}}{\partial p} + \frac{\bar{\sigma}}{f_0} \omega = - \frac{Rq'}{C_p f_0 p}, \quad (8.2)$$

where ψ is the geostrophic streamfunction, $\bar{U}(p)$ is the zonal wind, and ω is the vertical motion field. The mean static stability parameter

$$\bar{\sigma} = \frac{R}{p} \left\{ \frac{R\bar{T}}{C_p p} - \frac{\partial \bar{T}}{\partial p} \right\} \quad (8.3)$$

is assumed to be constant. The diabatic heating q' is assumed to be zonally periodic with period c (where c is the circumference of the earth at 40°N) and is taken to have the form

$$q' = \begin{cases} Q_0 \cos ly \{1 - e^{-t/\tau}\} e^{ikx}, & \text{if } t \geq 0; \\ 0, & \text{if } t < 0. \end{cases}, \quad (8.4)$$

where $k = \frac{2\pi\bar{k}}{c}$, $\bar{k} = 0, \pm 1, \pm 2, \dots$. According to (8.4), we switch on the heating at time $t = 0$ and examine the time evolution of the atmospheric response. In Section 8.4 the Fourier series technique will be used (as in Lim and Chang, 1981, 1986) to obtain solutions for heating with different zonal structures.

In the two level approximation the vorticity is calculated at levels 1 and 3 (Fig. 53) and the thermodynamic equation (8.2) is applied at level 2. The boundary condition $\omega = 0$ is enforced at the surface, $p_4 = 1000$ mb and at the tropopause, $p_0 = 200$ mb. If lower level Ekman friction is included and U_1 and U_3 are the constant zonal flows at levels 1 and 3 respectively, the resulting system of equations is

$$\left(\frac{\partial}{\partial t} + U_1 \frac{\partial}{\partial x} \right) \nabla^2 \psi_1 + \beta \frac{\partial}{\partial x} \psi_1 - \frac{f_0}{\Delta p_1} \omega_2 = 0, \quad (8.5)$$

$$\left(\frac{\partial}{\partial t} + U_3 \frac{\partial}{\partial x} \right) \nabla^2 \psi_3 + \beta \frac{\partial}{\partial x} \psi_3 + \frac{f_0}{\Delta p_3} \omega_2 + \varepsilon \nabla^2 \psi_3 = 0, \quad (8.6)$$

$$\left(\frac{\partial}{\partial t} + U_3 \frac{\partial}{\partial x} \right) \psi_1 - \left(\frac{\partial}{\partial t} + U_1 \frac{\partial}{\partial x} \right) \psi_3 - \frac{\bar{\sigma} \Delta p_2}{f_0} \omega_2 = \frac{R \Delta p_2 q'}{C_p f_0 p_2}, \quad (8.7)$$

where $\Delta p_1 = p_2 - p_0$, $\Delta p_2 = p_3 - p_1$, $\Delta p_3 = p_4 - p_2$ and q' is given by (8.4). Here we have used the interpolated values $U_2 = \frac{p_2 - p_1}{\Delta p_2} U_3 + \frac{p_3 - p_2}{\Delta p_2} U_1$ and $\psi_2 = \frac{p_2 - p_1}{\Delta p_2} \psi_3 + \frac{p_3 - p_2}{\Delta p_2} \psi_1$ for U and ψ at level 2. The surface friction coefficient is given by ε . Equations (8.5)–(8.7) are the time dependent versions of equations (7.5)–(7.7) and include the effects of Ekman friction.

8.3 Solution of the Equations.

We define the Laplace transform of the perturbation variables by

$$\left(\hat{\psi}_1, \hat{\psi}_3, \hat{\omega}_2\right) = \int_0^{\infty} e^{-\nu t} (\bar{\psi}_1, \bar{\psi}_3, \bar{\omega}_2) dt, \quad (8.8)$$

where $\bar{\psi}_1(t)$, $\bar{\psi}_3(t)$ and $\bar{\omega}_2(t)$ are given by

$$(\psi_1, \psi_3, \omega_2) = (\bar{\psi}_1, \bar{\psi}_3, \bar{\omega}_2) \cos l y e^{i k x}. \quad (8.9)$$

We assume initially that the basic state is unperturbed (ie., $\psi_1 = \psi_3 = \omega_2 = 0$ at $t = 0$). The system of differential equations (8.5)–(8.7) is thus transformed into a system of algebraic equations which yield

$$\hat{\omega}_2 = -\frac{Q_0 R K^2 (\nu - i f_1)(\nu - i f_3)}{C_p \bar{\sigma} p_2 \tau \nu (\nu + \frac{1}{\tau}) g(\nu)}, \quad (8.10)$$

$$\hat{\psi}_1 = \frac{Q_0 R f_0 (\nu - i f_3)}{C_p \bar{\sigma} p_2 \tau \Delta p_1 \nu (\nu + \frac{1}{\tau}) g(\nu)}, \quad (8.11)$$

$$\hat{\psi}_3 = -\frac{Q_0 R f_0 (\nu - i f_1)}{C_p \bar{\sigma} p_2 \tau \Delta p_3 \nu (\nu + \frac{1}{\tau}) g(\nu)}, \quad (8.12)$$

where

$$K^2 = k^2 + l^2, \quad f_1 = k \left(\frac{\beta}{K^2} - U_1 \right), \quad f_3 = k \left(\frac{\beta}{K^2} - U_3 \right) + i \varepsilon. \quad (8.13)$$

The expression $g(\nu)$ is given by

$$g(\nu) = \lambda^2 \left\{ \left(\nu \frac{\alpha_3}{U_3} + i \alpha_3 k \right) (\nu - i f_3) + \left(\nu \frac{\alpha_1}{U_1} + i \alpha_1 k \right) (\nu - i f_1) \right\} + K^2 (\nu - i f_1) (\nu - i f_3), \quad (8.14)$$

where

$$\alpha_1 = \frac{2U_1 \Delta p_1}{\Delta p_1 + \Delta p_3}, \quad \alpha_3 = \frac{2U_3 \Delta p_3}{\Delta p_1 + \Delta p_3}, \quad (8.15)$$

and the deformation radius λ^{-1} is defined by

$$\lambda^2 = \frac{f_0^2 (\Delta p_1 + \Delta p_3)}{2 \bar{\sigma} \Delta p_1 \Delta p_2 \Delta p_3}. \quad (8.16)$$

The function $g(\nu)$ has two zeros ν_1 and ν_2 , so

$$g(\nu) = \left\{ K^2 + \lambda^2 \left(\frac{\alpha_1}{U_1} + \frac{\alpha_3}{U_3} \right) \right\} (\nu - \nu_1) (\nu - \nu_2), \quad (8.17)$$

with

$$\nu_1 = -\frac{B}{2} + \sqrt{\frac{B^2}{4} - B}, \quad \text{and} \quad \nu_2 = -\frac{B}{2} - \sqrt{\frac{B^2}{4} - C}, \quad (8.18)$$

where

$$B = i \frac{k\lambda^2(\alpha_1 + \alpha_3) - K^2(f_1 + f_3) - \lambda^2\left(\frac{f_1\alpha_1}{U_1} + \frac{f_3\alpha_3}{U_3}\right)}{K^2 + \lambda^2\left(\frac{\alpha_1}{U_1} + \frac{\alpha_3}{U_3}\right)}, \quad (8.19)$$

and

$$C = \frac{\lambda^2 k(\alpha_1 f_1 + \alpha_3 f_3) - K^2 f_1 f_3}{K^2 + \lambda^2\left(\frac{\alpha_1}{U_1} + \frac{\alpha_3}{U_3}\right)}. \quad (8.20)$$

If $\varepsilon = 0$ (ie., there is no surface friction) the discriminant in (8.18) is real, so that ν_1 and ν_2 are either purely imaginary or ν_1 may have a positive real part, in which case ν_2 has a negative real part. We now rewrite (8.10)–(8.12) in the form

$$\hat{\omega}_2 = -\frac{\eta(k)K^2(\nu - if_1)(\nu - if_3)}{f_0\nu(\nu + \frac{1}{\tau})(\nu - \nu_1)(\nu - \nu_2)}, \quad (8.21)$$

$$\hat{\psi}_1 = \frac{\eta(k)(\nu - if_3)}{\Delta p_1\nu(\nu + \frac{1}{\tau})(\nu - \nu_1)(\nu - \nu_2)}, \quad (8.22)$$

$$\hat{\psi}_3 = -\frac{\eta(k)(\nu - if_1)}{\Delta p_3\nu(\nu + \frac{1}{\tau})(\nu - \nu_1)(\nu - \nu_2)}, \quad (8.23)$$

with

$$\eta(k) = \frac{Q_0 R f_0}{C_p \bar{\sigma} p_2 \tau \left(K^2 + \lambda^2 \left(\frac{\alpha_1}{U_1} + \frac{\alpha_3}{U_3} \right) \right)}. \quad (8.24)$$

We take the inverse Laplace transform of (8.21)–(8.23) by closing the contour of integration as shown in Fig. 60 (for $\varepsilon = 0$). Since by Jordan's Lemma $\lim_{R \rightarrow \infty} \int_{C_R} = 0$ we obtain

$$(\bar{\psi}_1, \bar{\psi}_3, \bar{\omega}_2) = \frac{1}{2\pi i} \int_{d-i\infty}^{d+i\infty} e^{\nu t} (\hat{\psi}_1, \hat{\psi}_3, \hat{\omega}_2) d\nu = \sum \text{Res at } 0, \frac{-1}{\tau}, \nu_1, \nu_2. \quad (8.25)$$

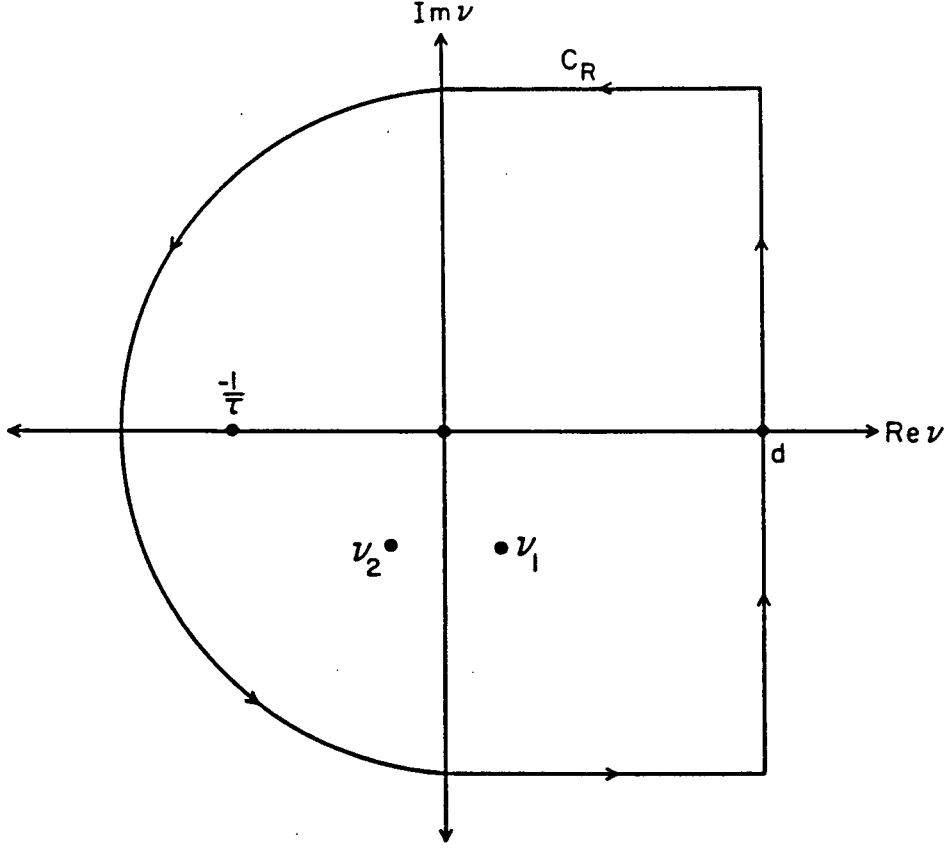


Figure 60 . Contour of integration for the evaluation of (8.25) in the case of no friction ($\varepsilon = 0$) and $\nu_{1,2}$ having a real part.

Evaluating the residues of (8.21)–(8.23) at $\nu = 0$, $-\frac{1}{\tau}$, ν_1 , ν_2 and substituting (8.25) back into (8.9) gives the solution

$$\omega_2 = \frac{-\eta(k)K^2}{f_0} \left\{ \frac{-\tau f_1 f_3}{\nu_1 \nu_2} - \frac{\tau(\frac{1}{\tau} + i f_1)(\frac{1}{\tau} + i f_3)e^{-t/\tau}}{(\frac{1}{\tau} + \nu_1)(\frac{1}{\tau} + \nu_2)} + \frac{1}{(\nu_1 - \nu_2)} \left\{ \frac{(\nu_1 - i f_1)(\nu_1 - i f_3)e^{\nu_1 t}}{\nu_1(\frac{1}{\tau} + \nu_1)} - \frac{(\nu_2 - i f_1)(\nu_2 - i f_3)e^{\nu_2 t}}{\nu_2(\frac{1}{\tau} + \nu_2)} \right\} \right\} \cos ly e^{ikx}, \quad (8.26)$$

$$\psi_1 = \frac{\eta(k)}{\Delta p_1} \left\{ \frac{-i\tau f_3}{\nu_1 \nu_2} + \frac{\tau(\frac{1}{\tau} + i f_3)e^{-t/\tau}}{(\frac{1}{\tau} + \nu_1)(\frac{1}{\tau} + \nu_2)} + \frac{1}{(\nu_1 - \nu_2)} \left\{ \frac{(\nu_1 - i f_3)e^{\nu_1 t}}{\nu_1(\frac{1}{\tau} + \nu_1)} - \frac{(\nu_2 - i f_3)e^{\nu_2 t}}{\nu_2(\frac{1}{\tau} + \nu_2)} \right\} \right\} \cos ly e^{ikx}, \quad (8.27)$$

$$\psi_3 = -\frac{\eta(k)}{\Delta p_3} \left\{ \frac{-i\tau f_1}{\nu_1 \nu_2} + \frac{\tau(\frac{1}{\tau} + i f_1)e^{-t/\tau}}{(\frac{1}{\tau} + \nu_1)(\frac{1}{\tau} + \nu_2)} + \frac{1}{(\nu_1 - \nu_2)} \left\{ \frac{(\nu_1 - i f_1)e^{\nu_1 t}}{\nu_1(\frac{1}{\tau} + \nu_1)} - \frac{(\nu_2 - i f_1)e^{\nu_2 t}}{\nu_2(\frac{1}{\tau} + \nu_2)} \right\} \right\} \cos ly e^{ikx}. \quad (8.28)$$

There are four contributions to the solutions for ω_2 , ψ_1 , ψ_3 given by (8.26)–(8.28) for $\varepsilon = 0$. A constant (with respect to time) component, an exponentially decaying time component (with decay rate, τ), and two propagating components. Since ν_1 may have a positive real part (see Section 8.5), and hence ν_2 would have a negative real part, the $e^{\nu_1 t}$ term may grow exponentially in time and the $e^{\nu_2 t}$ term would correspondingly decay exponentially with time. Further analysis of this baroclinic instability inherent in the problem and the effects of surface friction ($\varepsilon \neq 0$) will be delayed until Section 8.5. It should be noted that as $t \rightarrow 0$, $(\omega_2, \psi_1, \psi_3) \rightarrow 0$, a result demanded by our initial conditions.

In the special case $k = 0$ (ie., the case of constant zonal forcing), it is easy to solve the resulting system (8.5)–(8.7) with the aforementioned initial conditions. The result is

$$\omega_2 = -\frac{\eta(0)l^2\tau\cos ly}{f_0} \left\{ \frac{1}{\chi} - \frac{(1-\varepsilon\tau)e^{-t/\tau}}{(1-\varepsilon\tau\chi)} - \frac{(1-\chi)e^{-\varepsilon\chi t}}{\chi(1-\varepsilon\tau\chi)} \right\}, \quad (8.29)$$

$$\psi_1 = \frac{\eta(0)\tau^2\cos ly}{\Delta p_1} \begin{cases} \frac{t}{\tau} - 1 + e^{-t/\tau}, & \text{if } \varepsilon = 0; \\ \frac{1}{\chi} \left\{ \frac{1}{\varepsilon\tau} + \frac{t}{\tau} - 1 - \frac{1}{\varepsilon\tau\chi} \right\} + \frac{(1-\varepsilon\tau)e^{-t/\tau}}{(1-\varepsilon\tau\chi)} + \frac{(1-\chi)e^{-\varepsilon\chi t}}{\varepsilon\tau\chi^2(1-\varepsilon\tau\chi)}, & \text{if } \varepsilon \neq 0. \end{cases}, \quad (8.30)$$

$$\psi_3 = -\frac{\eta(0)\tau^2\cos ly}{\Delta p_3} \begin{cases} \frac{t}{\tau} - 1 + e^{-t/\tau}, & \text{if } \varepsilon = 0; \\ \frac{1}{\varepsilon\tau\chi} + \frac{e^{-t/\tau}}{(1-\varepsilon\tau\chi)} - \frac{e^{-\varepsilon\chi t}}{\varepsilon\tau\chi(1-\varepsilon\tau\chi)}, & \text{if } \varepsilon \neq 0. \end{cases}, \quad (8.31)$$

where

$$\chi = \frac{l^2 + \lambda^2 \frac{\alpha_2}{U_2}}{l^2 + \lambda^2 \left(\frac{\alpha_1}{U_1} + \frac{\alpha_3}{U_3} \right)}. \quad (8.32)$$

We will use this special solution in Section 8.4.

8.4 Solutions for Other Heating Structures

In this section we consider the atmospheric response to the zonal heating distributions (defined for $t \geq 0$)

$$q'_C = \frac{\pi Q_0}{4x_0} \cos ly \Pi\left(\frac{x}{2x_0}\right) \cos\left(\frac{\pi x}{2x_0}\right) \{1 - e^{-t/\tau}\}, \quad (8.33)$$

and

$$q'_S = -\frac{\pi Q_0}{4x_0} \cos ly \Pi\left(\frac{x}{2x_0}\right) \sin\left(\frac{\pi x}{x_0}\right) \{1 - e^{-t/\tau}\}, \quad (8.34)$$

where $\Pi(\frac{x}{2x_0})$ is the rectangular function, defined by

$$\Pi(\frac{x}{2x_0}) = \begin{cases} 0, & \text{if } x > x_0; \\ 1, & \text{if } -x_0 < x < x_0; \\ 0, & \text{if } x < -x_0. \end{cases} \quad (8.35)$$

The heating is thus confined to the positive part of one period of the cosine function in (8.33) and to one period of the inverted sine function in (8.34). The motivation for choosing these zonal structures was given in Sections 6.2 and 6.6.

Since our domain is zonally periodic we may write the x -dependent part of the heating distributions (8.33) and (8.34) as an infinite complex Fourier series,

$$\sum_{\bar{k}=-\infty}^{\infty} a_{\bar{k}} e^{i \frac{2\pi \bar{k}}{c} x}, \quad |x| \leq \frac{c}{2}.$$

This expansion procedure gives

$$q'_C = Q_0 \cos y \left\{ 1 - e^{-t/\tau} \right\} \left\{ \sum_{\bar{k}=1}^{\infty} \frac{2\pi^2 \cos k x_0 \cos k x}{c(\pi^2 - 4x_0^2 k^2)} + \frac{1}{c} \right\}, \quad (8.36)$$

$$q'_S = -Q_0 \cos y \left\{ 1 - e^{-t/\tau} \right\} \left\{ \sum_{\bar{k}=1}^{\infty} \frac{\pi^2 \sin k x_0 \sin k x}{c(\pi^2 - x_0^2 k^2)} \right\}, \quad (8.37)$$

where $k = \frac{2\pi \bar{k}}{c}$ and $c = 3.1 \times 10^7 \text{m}$ is the circumference of the earth at 40°N . It should be noted that as $k \rightarrow \frac{\pi}{2x_0}$ in (8.36) and as $k \rightarrow \frac{\pi}{x_0}$ in (8.37), both the numerator and the denominator vanish in (8.36) and (8.37), respectively, and hence the Fourier series are finite for these values of k .

The heating distributions (8.36) and (8.37) have been plotted in Fig. 61 in the limit as $t \rightarrow \infty$ by including the first 100 terms. Since the convergence of (8.36) and (8.37) is rapid (ie., like $\frac{1}{k^2}$), the inclusion of the first 100 terms is more than adequate to resolve the zonal heating distributions (8.33) and (8.34).

It is now relatively straightforward to obtain solutions to (8.5)–(8.7) using the heating structures (8.33) and (8.34). We write $\cos kx = \frac{e^{ikx} + e^{-ikx}}{2}$, $\sin kx = \frac{e^{ikx} - e^{-ikx}}{2i}$ and use the solutions (8.26)–(8.28) obtained in the last section. The term independent of k in the

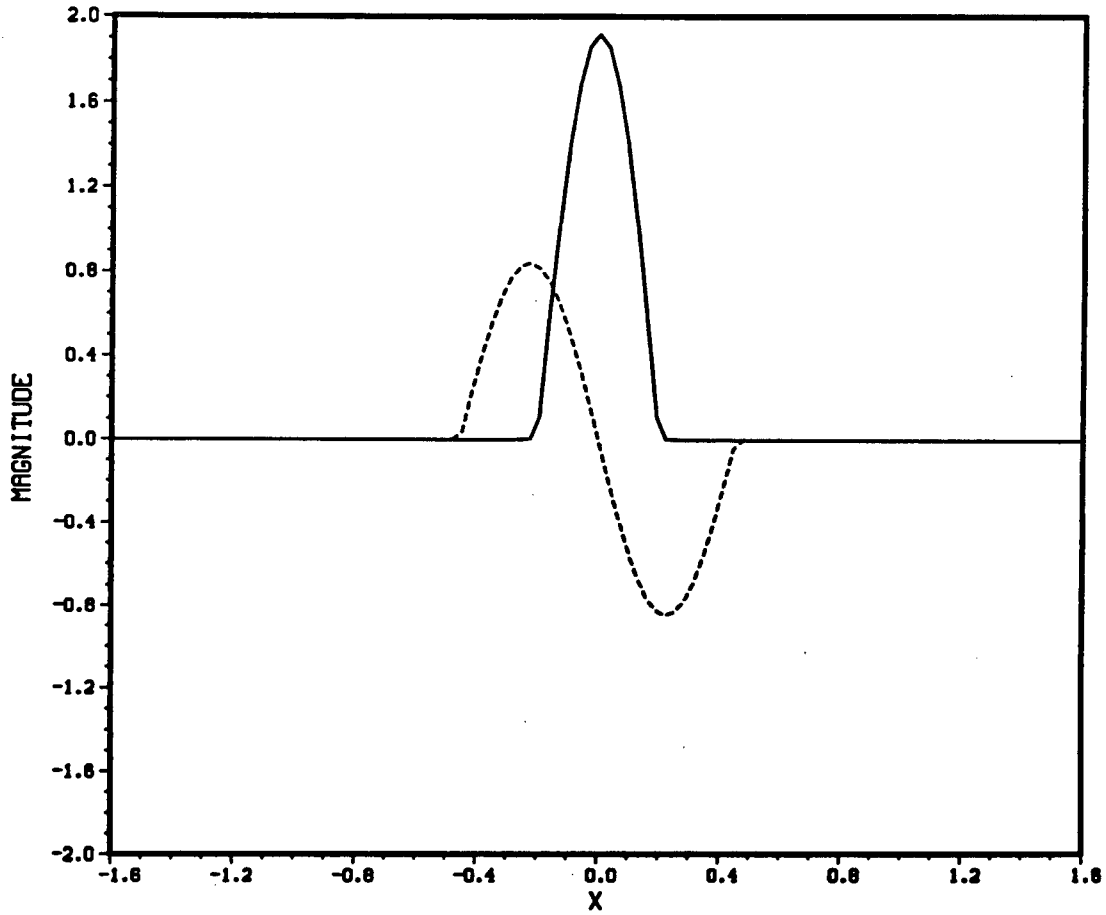


Figure 61 . Asymptotic ($t \rightarrow \infty$) zonal heating distributions for the segmented cosine (solid line; equation 8.36 in text) and segmented sine (dashed line; equation 8.37 in text) heating functions, along the line $y = 0$. The x -axis is in 10^7m and the y -axis is in $10^{-9} \text{Wkg}^{-1} \text{m}^{-1}$. For the purpose of illustration, x_0 has been chosen to be 2000 km and 4550 km for the segmented cosine and sine heating distributions, respectively.

expansion (8.36) yields a contribution which may be obtained from (8.29)–(8.31) at the end of Section 8.3. For the segmented cosine zonal distribution we therefore obtain

$$\omega_2 = -\frac{\cos y}{f_{0c}} \left\{ \eta(0) l^2 \tau \left\{ \frac{1}{\chi} - \frac{(1 - \epsilon \tau) e^{-t/\tau}}{(1 - \epsilon \tau \chi)} - \frac{(1 - \chi) e^{-\epsilon \chi t}}{\chi(1 - \epsilon \tau \chi)} \right\} + \right. \\ \left. \pi^2 \left\{ \sum_{\substack{\bar{k}=-\infty \\ \bar{k} \neq 0}}^{\infty} \frac{-\tau f_1 f_3}{\nu_1 \nu_2} - \frac{\tau (\frac{1}{\tau} + i f_1) (\frac{1}{\tau} + i f_3) e^{-t/\tau}}{(\frac{1}{\tau} + \nu_1) (\frac{1}{\tau} + \nu_2)} + \right. \right. \\ \left. \left. \frac{1}{(\nu_1 - \nu_2)} \left\{ \frac{(\nu_1 - i f_1)(\nu_1 - i f_3) e^{\nu_1 t}}{\nu_1 (\frac{1}{\tau} + \nu_1)} - \frac{(\nu_2 - i f_1)(\nu_2 - i f_3) e^{\nu_2 t}}{\nu_2 (\frac{1}{\tau} + \nu_2)} \right\} \frac{\eta(k) K^2 \cos k x_0 e^{i k z}}{(\pi^2 - 4 x_0^2 k^2)} \right\} \right\}, \quad (8.38)$$

$$\psi_1 = \frac{\cos y}{c\Delta p_1} \left\{ \eta(0)\tau^2 \begin{cases} \frac{t}{\tau} - 1 + e^{-t/\tau}, & \text{if } \varepsilon = 0; \\ \frac{1}{\chi} \left\{ \frac{1}{\varepsilon\tau} + \frac{t}{\tau} - 1 - \frac{1}{\varepsilon\tau\chi} \right\} + \frac{(1-\varepsilon\tau)e^{-t/\tau}}{(1-\varepsilon\tau\chi)} + \frac{(1-\chi)e^{-\varepsilon\chi t}}{\varepsilon\tau\chi^2(1-\varepsilon\tau\chi)}, & \text{if } \varepsilon \neq 0. \end{cases} + \right. \\ \left. \pi^2 \left\{ \sum_{\substack{\bar{k}=-\infty \\ \bar{k} \neq 0}}^{\infty} \frac{-i\tau f_3}{\nu_1\nu_2} + \frac{\tau(\frac{1}{\tau} + if_3)e^{-t/\tau}}{(\frac{1}{\tau} + \nu_1)(\frac{1}{\tau} + \nu_2)} + \right. \right. \\ \left. \left. \frac{1}{(\nu_1 - \nu_2)} \left\{ \frac{(\nu_1 - if_3)e^{\nu_1 t}}{\nu_1(\frac{1}{\tau} + \nu_1)} - \frac{(\nu_2 - if_3)e^{\nu_2 t}}{\nu_2(\frac{1}{\tau} + \nu_2)} \right\} \frac{\eta(k)\cos kx_0 e^{ikx}}{(\pi^2 - 4x_0^2 k^2)} \right\} \right\}, \quad (8.39)$$

$$\psi_3 = -\frac{\cos y}{c\Delta p_3} \left\{ \eta(0)\tau^2 \begin{cases} \frac{t}{\tau} - 1 + e^{-t/\tau}, & \text{if } \varepsilon = 0; \\ \frac{1}{\varepsilon\tau\chi} + \frac{e^{-t/\tau}}{(1-\varepsilon\tau\chi)} - \frac{e^{-\varepsilon\chi t}}{\varepsilon\tau\chi(1-\varepsilon\tau\chi)}, & \text{if } \varepsilon \neq 0. \end{cases} + \right. \\ \left. \pi^2 \left\{ \sum_{\substack{\bar{k}=-\infty \\ \bar{k} \neq 0}}^{\infty} \frac{-i\tau f_1}{\nu_1\nu_2} + \frac{\tau(\frac{1}{\tau} + if_1)e^{-t/\tau}}{(\frac{1}{\tau} + \nu_1)(\frac{1}{\tau} + \nu_2)} + \right. \right. \\ \left. \left. \frac{1}{(\nu_1 - \nu_2)} \left\{ \frac{(\nu_1 - if_1)e^{\nu_1 t}}{\nu_1(\frac{1}{\tau} + \nu_1)} - \frac{(\nu_2 - if_1)e^{\nu_2 t}}{\nu_2(\frac{1}{\tau} + \nu_2)} \right\} \frac{\eta(k)\cos kx_0 e^{ikx}}{(\pi^2 - 4x_0^2 k^2)} \right\} \right\}, \quad (8.40)$$

whereas for the segmented sine distribution we get

$$\omega_2 = -\frac{i\pi^2 \cos y}{2f_0 c} \left\{ \sum_{\bar{k}=-\infty}^{\infty} \frac{-\tau f_1 f_3}{\nu_1 \nu_2} - \frac{\tau(\frac{1}{\tau} + if_1)(\frac{1}{\tau} + if_3)e^{-t/\tau}}{(\frac{1}{\tau} + \nu_1)(\frac{1}{\tau} + \nu_2)} + \right. \\ \left. \frac{1}{(\nu_1 - \nu_2)} \left\{ \frac{(\nu_1 - if_1)(\nu_1 - if_3)e^{\nu_1 t}}{\nu_1(\frac{1}{\tau} + \nu_1)} - \frac{(\nu_2 - if_1)(\nu_2 - if_3)e^{\nu_2 t}}{\nu_2(\frac{1}{\tau} + \nu_2)} \right\} \frac{\eta(k)K^2 \sin kx_0 e^{ikx}}{(\pi^2 - x_0^2 k^2)} \right\}, \quad (8.41)$$

$$\psi_1 = \frac{i\pi^2 \cos y}{2c\Delta p_1} \left\{ \sum_{\bar{k}=-\infty}^{\infty} \frac{-i\tau f_3}{\nu_1 \nu_2} + \frac{\tau(\frac{1}{\tau} + if_3)e^{-t/\tau}}{(\frac{1}{\tau} + \nu_1)(\frac{1}{\tau} + \nu_2)} + \right. \\ \left. \frac{1}{(\nu_1 - \nu_2)} \left\{ \frac{(\nu_1 - if_3)e^{\nu_1 t}}{\nu_1(\frac{1}{\tau} + \nu_1)} - \frac{(\nu_2 - if_3)e^{\nu_2 t}}{\nu_2(\frac{1}{\tau} + \nu_2)} \right\} \frac{\eta(k)\sin kx_0 e^{ikx}}{(\pi^2 - x_0^2 k^2)} \right\}, \quad (8.42)$$

$$\psi_3 = -\frac{i\pi^2 \cos y}{2c\Delta p_3} \left\{ \sum_{\bar{k}=-\infty}^{\infty} \frac{-i\tau f_1}{\nu_1 \nu_2} + \frac{\tau(\frac{1}{\tau} + if_1)e^{-t/\tau}}{(\frac{1}{\tau} + \nu_1)(\frac{1}{\tau} + \nu_2)} + \right. \\ \left. \frac{1}{(\nu_1 - \nu_2)} \left\{ \frac{(\nu_1 - if_1)e^{\nu_1 t}}{\nu_1(\frac{1}{\tau} + \nu_1)} - \frac{(\nu_2 - if_1)e^{\nu_2 t}}{\nu_2(\frac{1}{\tau} + \nu_2)} \right\} \frac{\eta(k)\sin kx_0 e^{ikx}}{(\pi^2 - x_0^2 k^2)} \right\}, \quad (8.43)$$

where $k = \frac{2\pi\bar{k}}{c}$.

8.5 Discussion

8.5.1 Description of the Parameters Used

To illustrate the results of the last section we consider two models. In Model 1 we assume the levels of Fig. 53 are equally spaced so that $p_1 = 400$ mb, $p_2 = 600$ mb, $p_3 = 800$ mb and hence $\Delta p_1 = \Delta p_2 = \Delta p_3 = 400$ mb, $\alpha_1 = U_1$ and $\alpha_3 = U_3$. To examine the effects of shallow heating as observed, for example, over the Kuroshio region in winter (Nitta and So, 1980; Hoskins and Karoly, 1981; Masuda, 1983), we consider a second model (Model 2). In this model $p_1 = 500$ mb, $p_2 = 800$ mb, $p_3 = 900$ mb, so that $\Delta p_1 = 600$ mb, $\Delta p_2 = 400$ mb $\Delta p_3 = 200$ mb, $\alpha_1 = \frac{3}{2}U_1$ and $\alpha_3 = \frac{1}{2}U_3$. These two models correspond to Model 1 and Model 2 of Chapter 7.

We let the β -plane be centered at 40° N, so that $f_0 = 9.4 \times 10^{-5} \text{s}^{-1}$ and $\beta = 1.8 \times 10^{-11} \text{m}^{-1} \text{s}^{-1}$. We also take $U_1 = 18 \text{ ms}^{-1}$, $U_3 = 6 \text{ ms}^{-1}$ and $\sigma = 3 \times 10^{-6} \text{ m}^4 \text{s}^2 \text{kg}^{-2}$, typical of wintertime conditions (Frankignoul, 1985a). The deformation radius is then given by $\lambda^{-1} = 7.4 \times 10^5 \text{m}$ and $\lambda^{-1} = 6.4 \times 10^5 \text{m}$, for Model 1 and 2, respectively. These parameters are thus identical to those of Chapter 7.

Heating anomalies over the North Pacific have typical developmental times of 1–3 months (Frankignoul, 1985a). We therefore choose $\tau = 4.84 \times 10^6 \text{s}$, corresponding to an e-folding time of 8 weeks. The remaining parameters are chosen to be $Q_0 = 0.01 \text{ Wkg}^{-1}$, $C_p = 1005 \text{ Jkg}^{-1} \text{K}^{-1}$, $R = 290 \text{ Jkg}^{-1} \text{K}^{-1}$, as in Chapter 7.

In the last chapter we underlined the importance of the meridional scale of the heating in determining the structure of the stationary atmospheric response. In view of this we will consider the two cases discussed earlier. For small scale meridional heating we choose $l = 1.4 \times 10^{-6} \text{ m}^{-1}$ (case 1), while to model heating with larger meridional scale we choose $l = 0.8 \times 10^{-6} \text{ m}^{-1}$ (case 2). As in the earlier models we take $x_0 = 2.0 \times 10^6 \text{m}$ for the segmented cosine heating distribution (corresponding to heating over an area of 47° extent), and $x_0 = 4.55 \times 10^6 \text{m}$ for the segmented sine heating distribution (corresponding to heating over the western half of the North Pacific and cooling over the eastern half of

the North Pacific).

Finally, we will examine the effects of friction on the results by considering both $\varepsilon = 0$ and $\varepsilon = 2.0 \times 10^{-6} \text{s}^{-1}$, the latter corresponding to a 6 day damping time. In all the plots which follow we have included the first 100 Fourier components in the series (8.38)–(8.43). Since the convergence of (8.38)–(8.43) is rapid (ie., like $\frac{1}{k^2}$ for ω_2 and like $\frac{1}{k^5}$ for ψ_1 and ψ_3), the inclusion of the first 100 terms is more than adequate to resolve the solutions. It should be noted that since we have normalized the heating structures (8.33) and (8.34) as in Chapter 7, we must multiply the solutions given in Section 8.4 by a factor of 10^6 .

8.5.2 The Model Solutions for ψ_1 and ψ_3

The time evolution of the streamfunctions ψ_1 and ψ_3 is illustrated for the segmented cosine heat forcing using Model 1 (equally spaced levels) and small scale meridional heating (case 1) in the Hovmöller diagrams Figs. 62a,b ($\varepsilon = 0$) and Figs. 63a,b ($\varepsilon \neq 0$). At the upper level (Fig. 62a, Fig. 63a) an area of high pressure develops to the east of the heating region, propagating eastward with a speed of about 7.3 ms^{-1} . When friction is not present in the model the high pressure system becomes dominated by the most unstable wavenumber 4 mode (Fig. 62a—the wavelength scale is determined from the top right hand corner). With the inclusion of friction, however, this baroclinic instability is suppressed (Fig. 63a) and the model region is dominated by the high pressure response.

In the lower layer the inclusion of friction has a much more pronounced effect (as one would expect from the Ekman pumping mechanism). For the case $\varepsilon = 0$ (Fig. 62b), a strong low pressure develops over the heating region, propagating eastward and intensifying with time. Once more the most unstable mode $\bar{k} = 4$ dominates for large time. Friction ($\varepsilon \neq 0$), on the other hand, suppresses the instability and the results are remarkably different (Fig. 63b). The low pressure system is now weaker and confined nearer to the heating region. As time progresses this low intensifies in magnitude and propagates slowly eastward.

When the thermodynamic equation is applied at a level nearer to the surface the

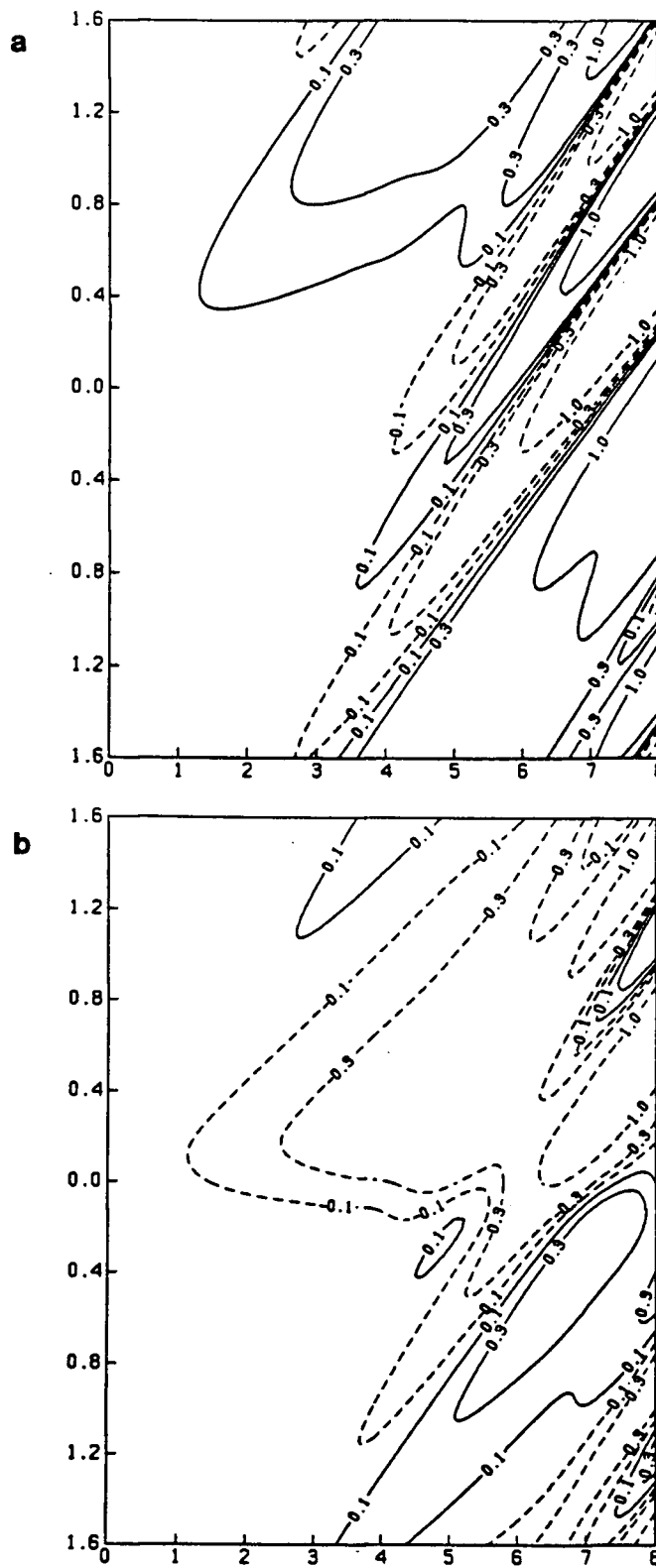


Figure 62 . Hovmöller diagram (longitude-time plot) of streamfunction contours in $10^6 \text{ m}^2\text{s}^{-1}$; a)— at the upper level (ψ_1); b)— at the lower level (ψ_3). Here we consider Model 1 (equally spaced levels) for the segmented cosine heating distribution with $\varepsilon = 0.0 \text{ s}^{-1}$ and $l = 1.4 \times 10^{-6} \text{ m}^{-1}$ (case 1—small meridional scale). The horizontal axis is in weeks and the vertical axis is in 10^7 m from the center of the heat source, with the eastward direction towards the top of the graph. Solid (dashed) contours denote high (low) pressure regions.

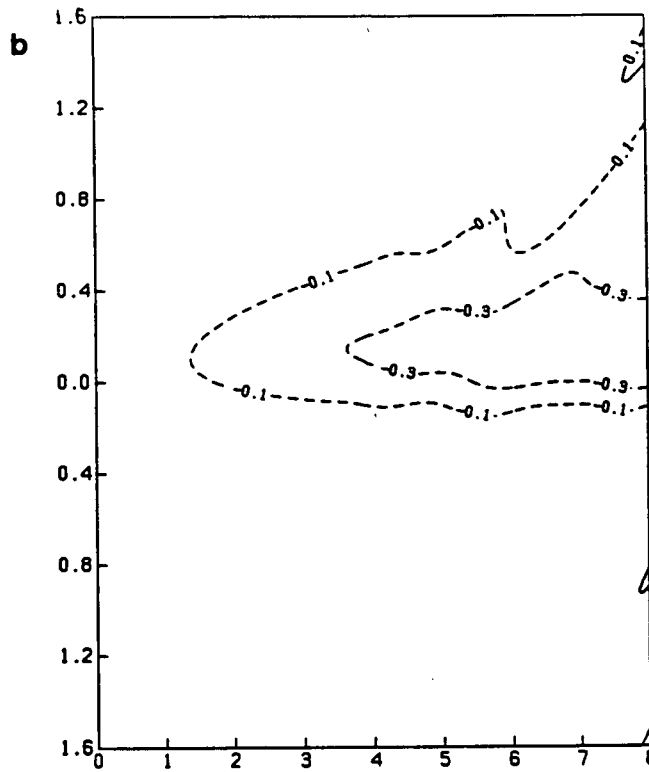
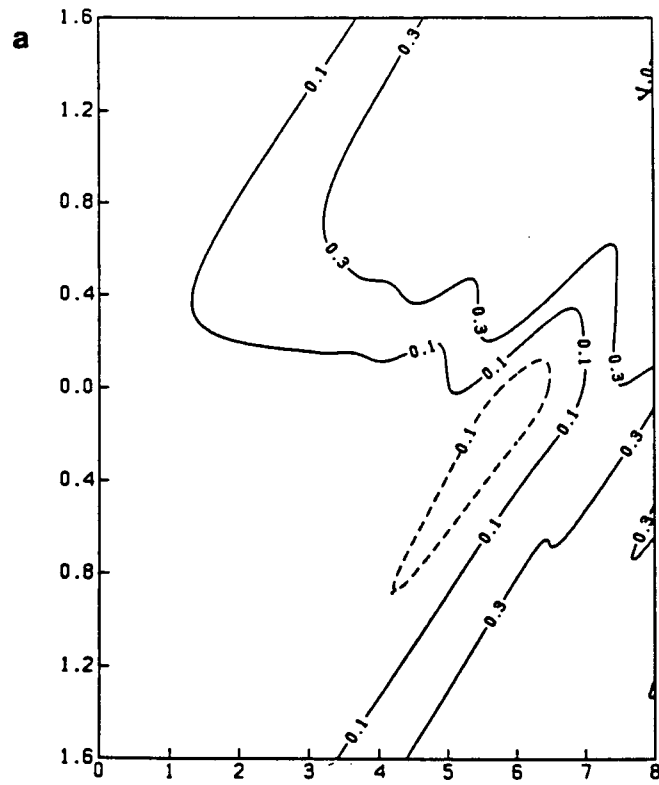


Figure 63 . As in Fig. 62 but for Model 1 for the segmented cosine heating distribution with $\varepsilon = 2.0 \times 10^{-6} \text{s}^{-1}$ and $l = 1.4 \times 10^{-6} \text{m}^{-1}$ (case 1).

instability mechanism plays a more important role in the governing dynamics. This is illustrated in Fig. 64 for the segmented cosine heating structure for Model 2, case 1 with $\varepsilon = 2.0 \times 10^{-6} \text{s}^{-1}$. The observed high and low responses in the upper and lower layers respectively, are once more observed in Figs. 64a,b, with the high developing further eastward from the heating region than the low. Again, in the lower troposphere, over and in the eastward vicinity of the heating region, the response is consistently negative. For large time the response is completely dominated by the unstable modes $\bar{k} = 5-6$.

For the segmented sine heat forcing, which corresponds to anomalous heating over the western half of the North Pacific and anomalous cooling over the eastern half of the North Pacific, there is very little response at the upper level. This is illustrated in Fig. 65a for Model 1, case 1 with $\varepsilon = 2.0 \times 10^{-6} \text{s}^{-1}$. In the lower layer (Fig. 65b) the response is also weak and mainly consists of a low pressure system centered about the zero crossing of the heating function (see Fig. 61). As time progresses this low intensifies slowly and broadens somewhat. At $t = 8$ weeks a quasi-steady state balance has been reached and the response is identical to the steady state results of Chapters 6 and 7 (see Figs. 52 and 56c). As time progresses further, unstable modes dominate the solution.

As mentioned above, the importance of the meridional scale of the heating was underlined in the last chapter. We can see this importance in Figs. 66–68, corresponding to case 2 ($l = 0.8 \times 10^{-6} \text{m}^{-1}$ —large meridional scale). In all these plots friction has been included. For the segmented cosine heating distribution and Model 1 the results are illustrated in Fig. 66a and Fig. 66b, for ψ_1 and ψ_3 , respectively. As observed in Figs. 63a,b (corresponding to case 1), the initial upper level response consists of a high which propagates eastward and the initial lower level response is negative. The main difference between these two figures is the sinusoidal nature of the eastward propagating disturbance as t increases (Figs. 66a,b, cf., Figs. 63a,b). This large-time behaviour is in excellent agreement with the steady state results of Chapter 7, where it was noticed that in the upper layer a wavenumber 3–4 perturbation was superimposed downstream on a positive constant re-

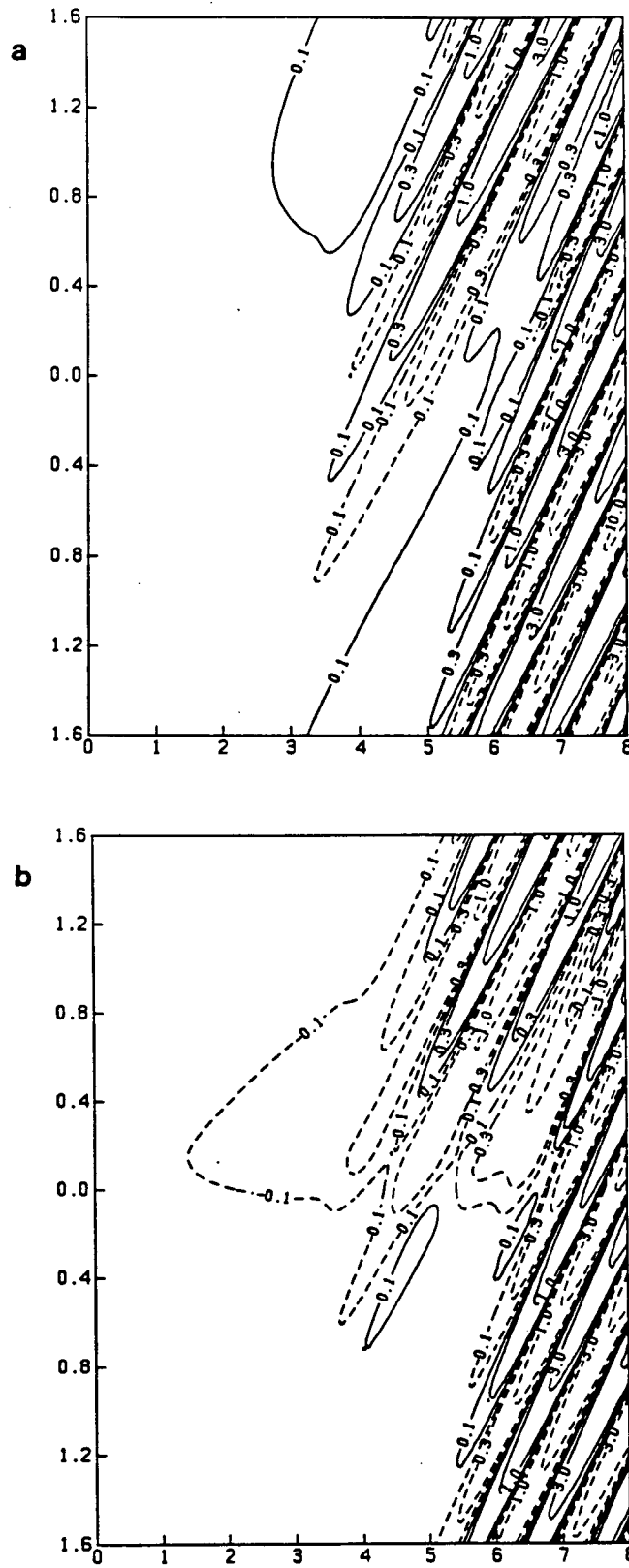


Figure 64 . As in Fig. 62 but for Model 2 (near surface heating) for the segmented cosine heating distribution with $\epsilon = 2.0 \times 10^{-6} \text{s}^{-1}$ and $l = 1.4 \times 10^{-6} \text{m}^{-1}$ (case 1).

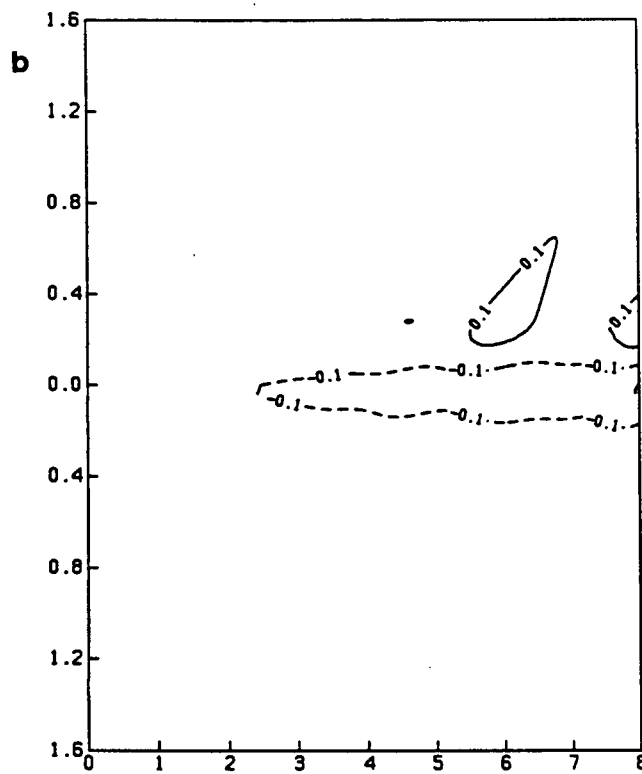
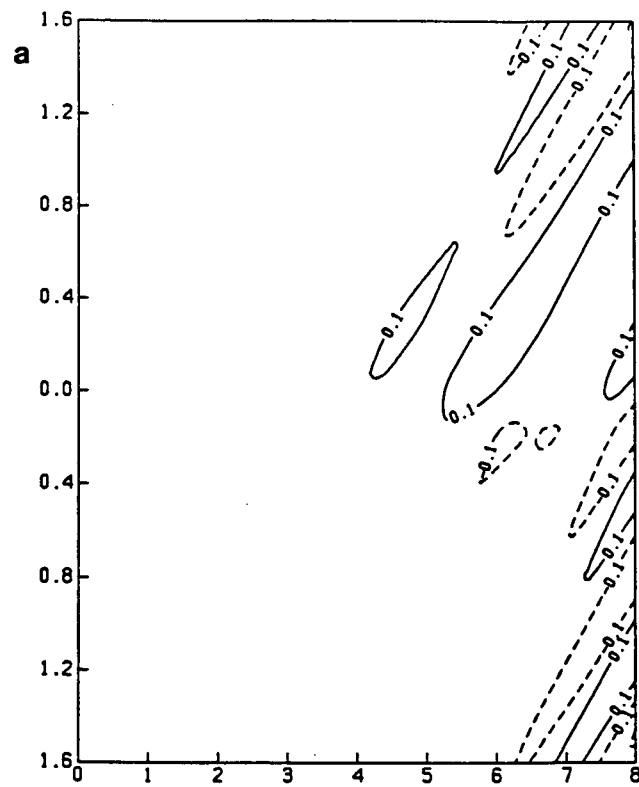


Figure 65 . As in Fig. 62 but for Model 1 for the segmented sine heating distribution with $\varepsilon = 2.0 \times 10^{-6} \text{s}^{-1}$ and $l = 1.4 \times 10^{-6} \text{m}^{-1}$ (case 1).

sponse (the net result being positive always but oscillating in magnitude—see Fig. 58b). Similarly, in the lower layer the net response was observed to be negative, oscillating with a wavenumber 3–4 downstream perturbation (see Fig. 58c). The lower level streamfunction was observed to lead the upper level streamfunction as is also the case in Figs. 66a,b. As time progresses, however, the most unstable modes $\bar{k} = 6$ and 7 dominate the response in the present time dependent calculation.

When the heating is now entered into the model nearer to the surface (Model 2), the picture becomes less clear. Although the discussion above seems to apply, the unstable mode $\bar{k} = 7$ dominates the entire response after a relatively short time (Figs. 67a,b). The reason for this will become clearer in the stability discussion below.

In Chapter 7 it was also observed that the steady state solution for the segmented sine heating distribution in case 2 consisted of a wavenumber 3–4 perturbation, but now superimposed on a zero mean since the integral over the entire x domain ($-\infty$ to ∞ in Chapter 7; $-\frac{\epsilon}{2}$ to $\frac{\epsilon}{2}$ herein) of the heating function (8.34) is zero (see Figs. 58b,c). This feature is clearly evident in Figs. 68a,b before the unstable modes $\bar{k} = 6, 7$ dominate.

The above discussion therefore suggests that the assumption of an unbounded x -domain used in Chapters 6 and 7 is indeed justified and underlines the importance of the meridional scale of the heating. For the segmented cosine heating distribution and small meridional scale heating, the response consists of an upper level high and a lower level low propagating eastwards. For large scale meridional heating the dominant forced response has a wavenumber 3–4 perturbation superimposed on a constant zonal response (as observed in Chapter 7). For large times (two months or more) unstable modes dominate the observed perturbation fields. The height at which the thermodynamic equation is applied (ie., the level of heat input) is also crucial in determining the response of the model (as pointed out by Hoskins and Karoly, 1981). When the heating is entered into the model near to the surface (Model 2), unstable modes are prevalent sooner than they would be when the heat forcing is applied at a higher level (Model 1).

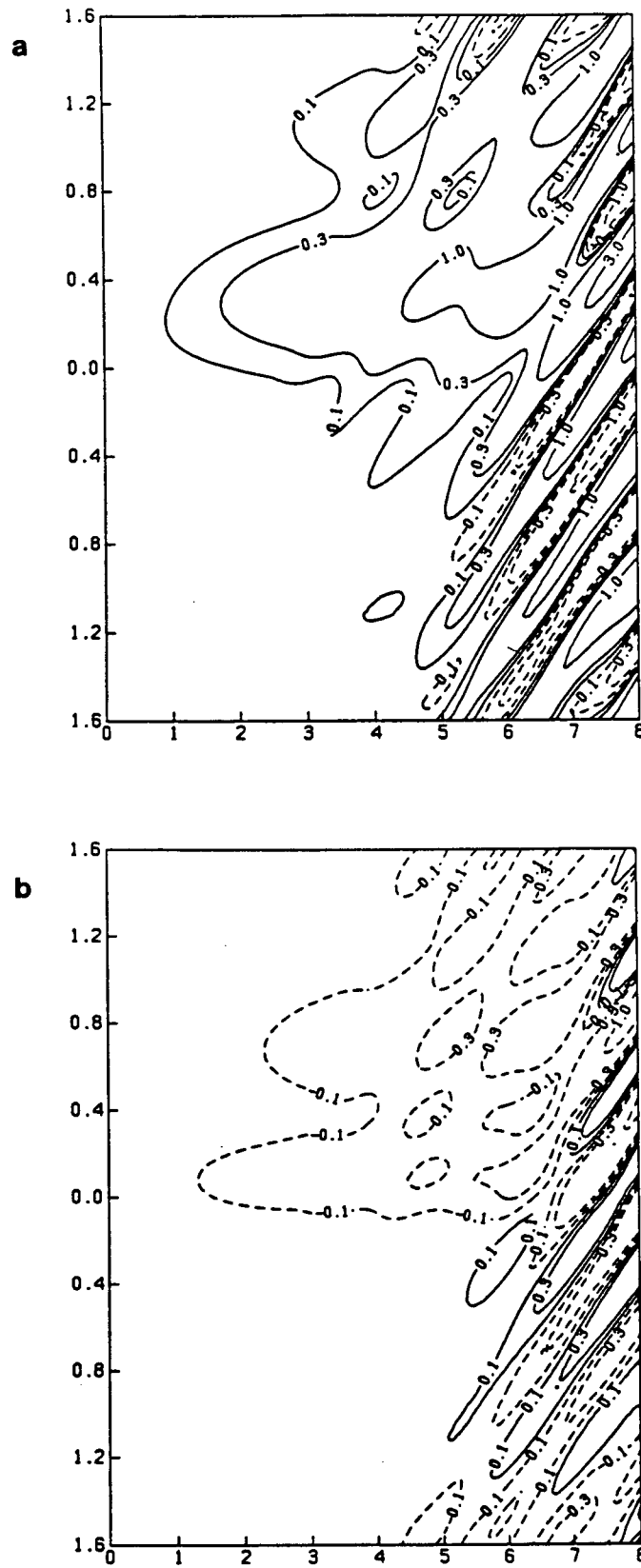


Figure 66 . As in Fig. 62 but for Model 1 for the segmented cosine heating distribution with $\varepsilon = 2.0 \times 10^{-6} \text{s}^{-1}$ and $l = 0.8 \times 10^{-6} \text{m}^{-1}$ (case 2—large meridional scale).

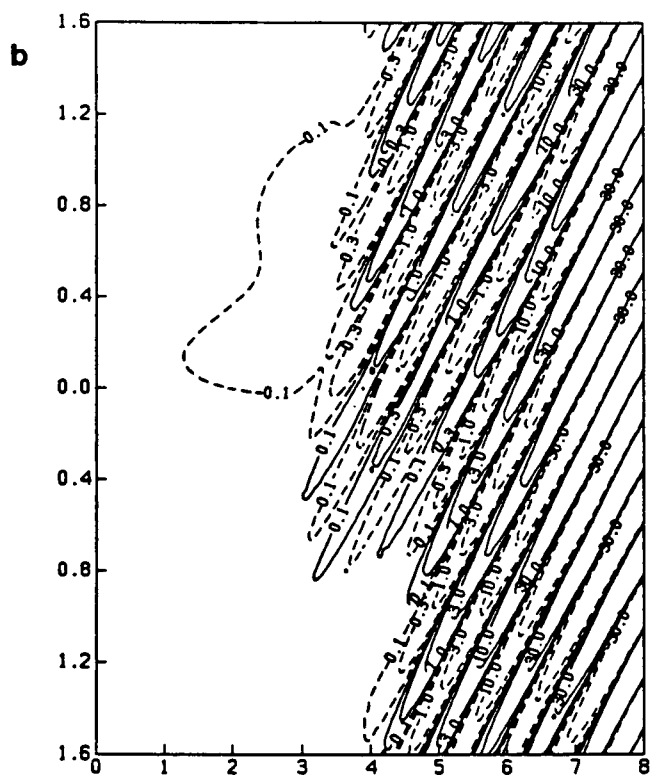
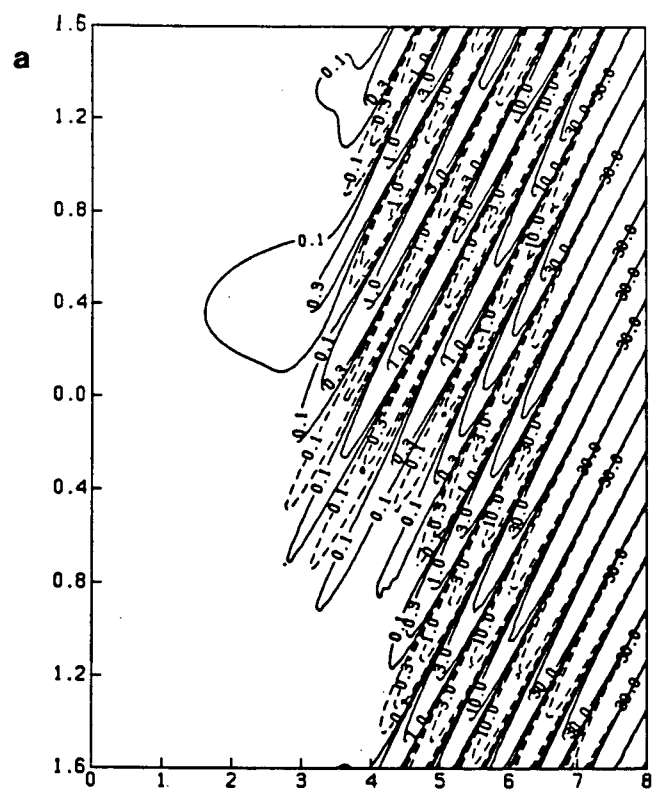


Figure 67 . As in Fig. 62 but for Model 2 for the segmented cosine heating distribution with $\varepsilon = 2.0 \times 10^{-6} \text{s}^{-1}$ and $l = 0.8 \times 10^{-6} \text{m}^{-1}$ (case 2).

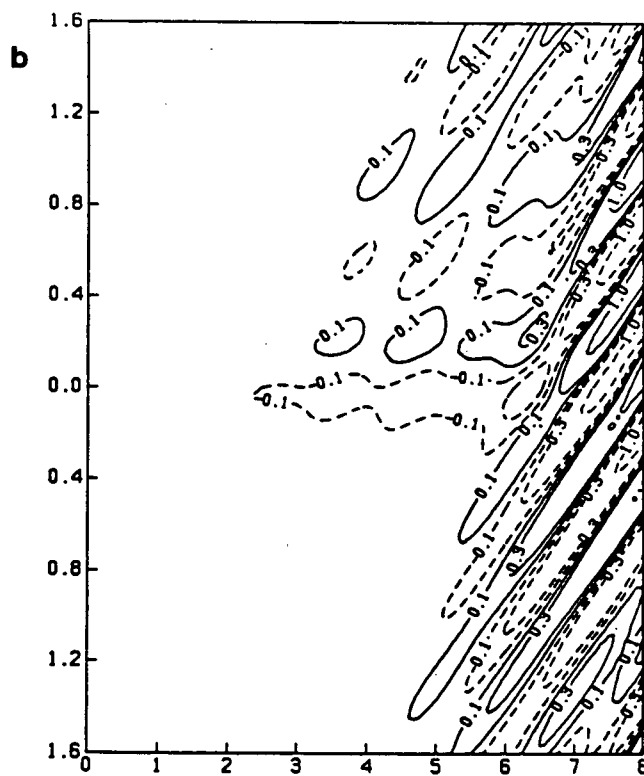
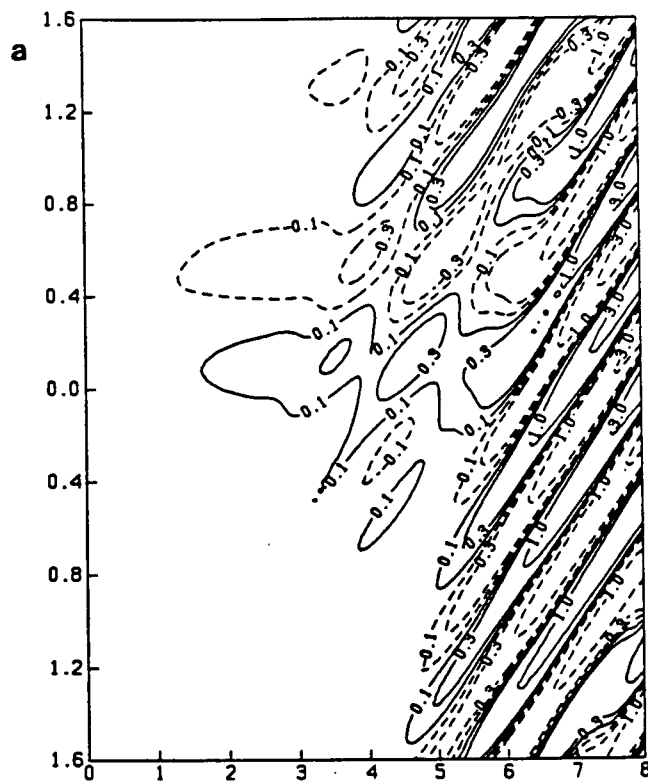


Figure 68 . As in Fig. 62 but for Model 1 for the segmented sine heating distribution with $\varepsilon = 2.0 \times 10^{-6} \text{s}^{-1}$ and $l = 0.8 \times 10^{-6} \text{m}^{-1}$ (case 2).

It was pointed out in Section 7.5 that the downstream forced response for case 2 corresponded to wavenumbers 3–4 oscillations, as observed in this chapter. As stated earlier, in the GCM studies of Chervin *et al.* (1976, 1980), Kutzbach *et al.* (1977) and Frankignoul (1985b), the atmospheric response to SST anomaly heating was dominated by zonal wavenumber 3–4 perturbations. This feature emerges in both the time dependent model of this chapter and the steady state model of the last chapter.

8.5.3 Stability Analysis

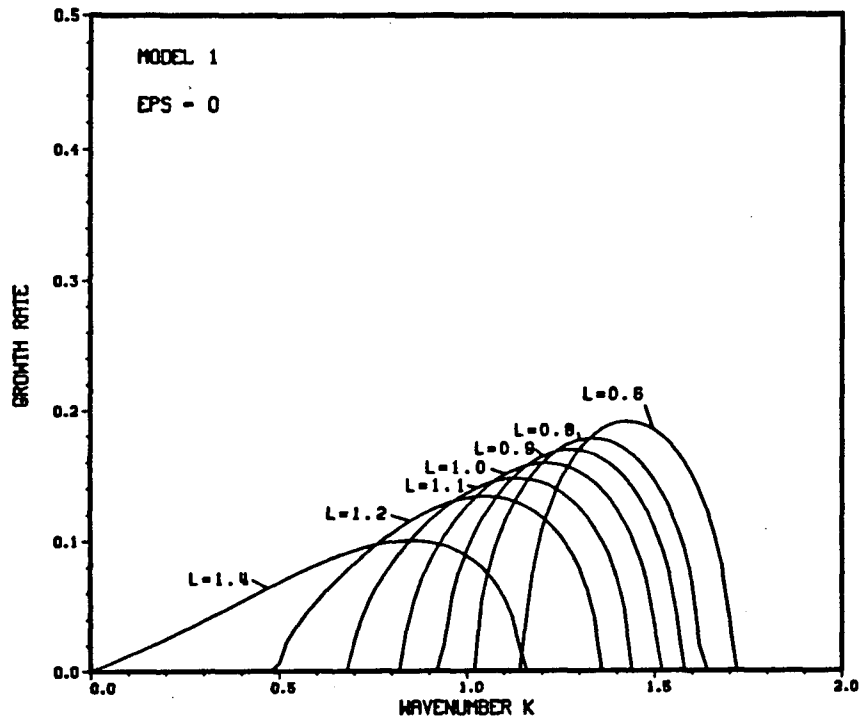
To further examine the instability inherent in the problem we must examine the real part of ν_1 (since $\text{Re}\{\nu_2\} \leq 0$). Figures 69a–d portray the growth rate (or $\text{Re}\{\nu_1\}$) in inverse days as a function of zonal wavenumber k for Models 1 and 2, with and without friction, and for varying meridional wavenumbers. The importance of the meridional wavenumber l on the growth rate of the unstable modes is evident in these figures. For the wavenumbers $l = 0.6\text{--}1.2 \times 10^{-6}\text{m}^{-1}$ there exists both a long and a short zonal wave cutoff for instability. As l increases, the maximum growth rate decreases and moves to smaller zonal wavenumbers k , and eventually the long wave cutoff vanishes ($l = 1.4 \times 10^{-6}\text{m}^{-1}$ in Figs. 69a–d).

The effect of including friction into the model (Figs. 69b,d, cf., Figs. 69a,c) is to diminish the magnitude of the growth rate, at the expense of removing the short wave instability cutoff. The curves in Fig. 69b,d are generally smoother than those of Figs. 69a,c and hence the maximum growth rates shift to slightly higher zonal wavenumbers.

As mentioned in the discussion of the results for Model 2, unstable modes tend to dominate the solutions more rapidly than for Model 1. This feature is also evident in Figs. 69a–d, where one also observes that the most unstable zonal wavenumbers have a growth rate that is larger for Model 2 than for Model 1.

To give a particular example of the effects of friction and the height of heat input, we consider the results for the meridional wavenumber $l = 0.8 \times 10^{-6}\text{m}^{-1}$. For Model 1 with $\varepsilon = 0$, the maximum instability has an e-folding time of about 5.6 days; when friction is included this rises to about 7.2 days. for Model 2 with $\varepsilon = 0$, the corresponding e-folding

a STABILITY CURVE



b STABILITY CURVE

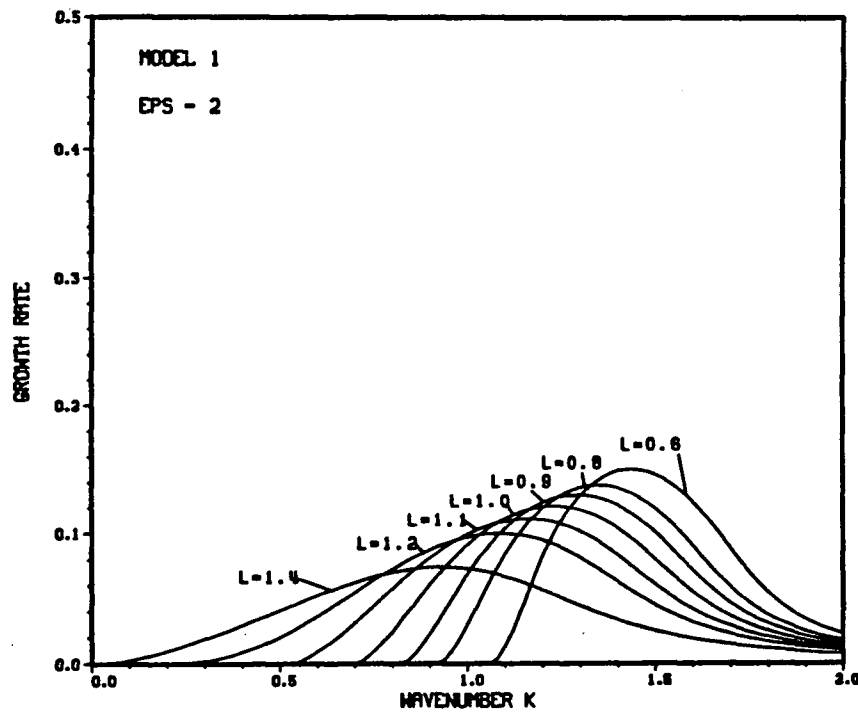
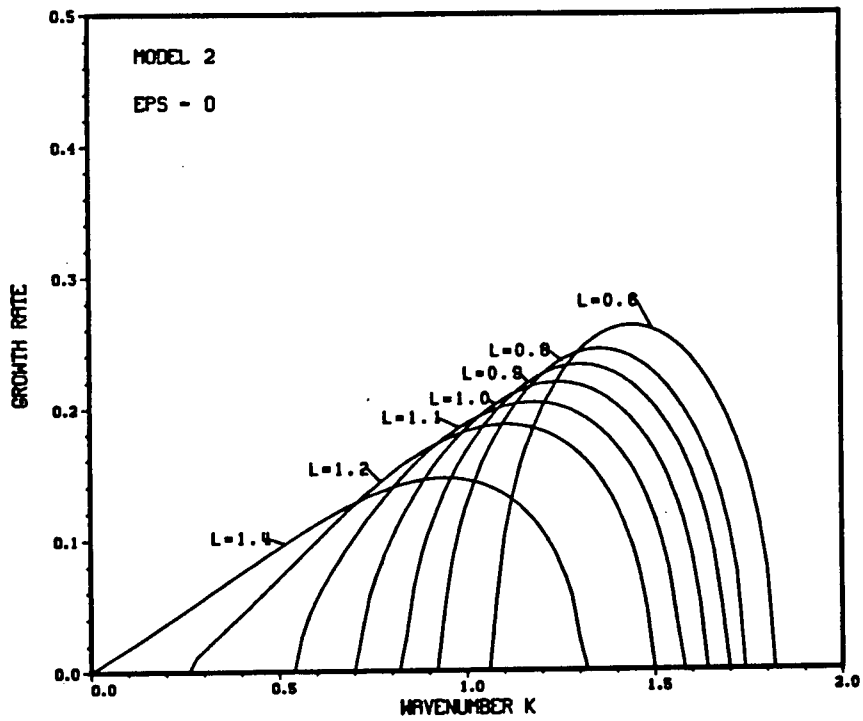


Figure 69 . Stability curves for a)– Model 1 with $\epsilon = 0.0 \text{ s}^{-1}$; b)– Model 1 with $\epsilon = 2.0 \times 10^{-6} \text{ s}^{-1}$; c)– Model 2 with $\epsilon = 0.0 \text{ s}^{-1}$; d)– Model 2 with $\epsilon = 2.0 \times 10^{-6} \text{ s}^{-1}$. The growth rate is given in inverse days and k ($= \frac{2\pi\bar{k}}{c}$) and l are in 10^{-6} m^{-1} .

c STABILITY CURVE



d STABILITY CURVE

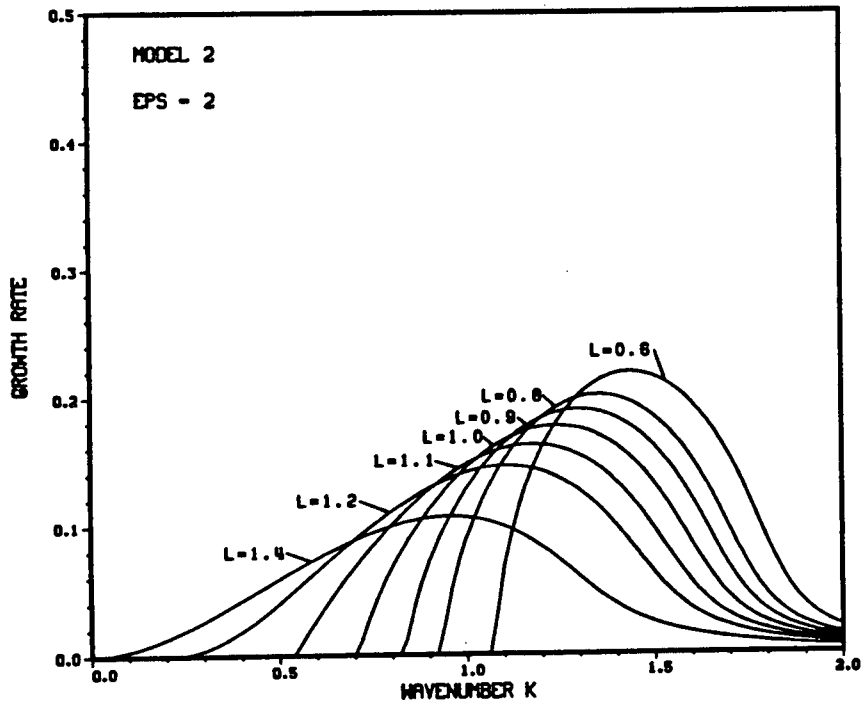


Figure 69 cont.

time for the most unstable $l = 0.8 \times 10^{-6} \text{m}^{-1}$ wave is 4.1 days, which rises to 5.0 days when friction is included. Even when friction is included in Model 2, the growth rate is still larger than for Model 1 with $\varepsilon = 0$.

In the discussion of Fig. 62 it was noted that the unstable mode with wavenumber $\bar{k} = 4$ (corresponding to $k = 0.8 \times 10^{-6} \text{m}^{-1}$; recall $k = \frac{2\pi\bar{k}}{c}$) appeared to dominate the solution for large time. This is what one would expect from Fig. 69a, since $\bar{k} = 4$ corresponds to the most unstable mode for $l = 1.4 \times 10^{-6} \text{m}^{-1}$. The other dominant unstable modes observed for large time in Figs. 62–68 also correspond to the most unstable modes of Figs. 69a–d.

9. Conclusions

Two topics in geophysical fluid dynamics were examined in this thesis: buoyancy driven coastal currents and large-scale air-sea interactions. In the second chapter we modelled the sudden release of a large amount of fresh water from an estuary to the continental shelf as a Rossby adjustment problem. As the initial salinity front was relaxed, a first mode baroclinic Kelvin wave front propagated into the estuary, while along the continental shelf, a disturbance propagated in the direction of coastally trapped waves. When the shelf was uniform in the alongshore direction, the propagation of the disturbance along the shelf was relatively slow and weak. In view of the nature of coastally trapped modes at mid-latitudes, where the first mode is often quasi-barotropic, while the higher modes are more baroclinic (Brink, 1982), it seems probable that a baroclinic process like frontal relaxation does not feed much energy directly into the quasi-barotropic first mode.

When a submarine canyon was placed at the mouth of the estuary, the joint effect of baroclinicity and relief provided a strong forcing term for barotropic flow. The disturbance now propagated along the shelf at the first mode phase speed, and the resulting circulation was significantly more energetic and barotropic than in the case without the canyon.

The surface outflow and the deeper inflow at the mouth of the estuary provided an interesting mechanism for eddy generation. As the deeper inflow encountered shallowing depth, the inflowing column of fluid was vertically compressed, thereby spinning up anticyclonically because of the constraint of potential vorticity conservation.

Comparing the *reverse estuary* with the normal estuary, we found that even when both estuaries had initial density fronts of equal magnitude, the *reverse estuary* had more available potential energy for conversion into kinetic energy, thereby producing a stronger continental shelf circulation.

The introduction of a wider shelf had little effect on the resulting baroclinic circulation and as in the narrower shelf model, little energy was transferred into barotropic motion. The wide estuary experiment, on the other hand, proved to be far more energetic than

the narrow estuary case due to the larger reservoir of fresh water available. The motion inside the wide estuary revealed the excitation of Poincaré modes in addition to the Kelvin mode. The coastally trapped waves appeared largely unaffected by width change of the estuary.

In Chapter 3 we focused on the application of the analysis of Chapter 2 to the Bass Strait region in Australia. The water in Bass Strait is often denser than the surrounding Tasman Sea water, especially in winter. We modelled this phenomenon numerically as a Rossby adjustment problem. Coastally trapped waves were generated when dense Bass Strait water flowed over deepening bottom topography, through the joint effect of baroclinicity and relief (JEBAR). A narrow northward flowing stream was also observed at the shelf edge. These results were found to agree well with field observations and the Australian Coastal Experiment (ACE).

Our study of air-sea interactions began with a demonstration in Chapter 4 of the strong control of the sea surface temperature (SST) along the coast of British Columbia by the regional atmospheric wind forcing. We showed that by constructing simple atmospheric pressure indices, it was possible to obtain high correlations between predicted and observed seasonal mean SSTAs at several coastal stations. These correlations were especially high in winter since the atmospheric winter circulation is dominated by the climatological Aleutian Low. The statistical analysis allowed us to obtain fairly credible estimates of seasonal mean SSTAs at Kains Island and Langara Island back to the turn of the century.

In Chapter 5 we examined the seasonal structure of the oceanic heat flux into the atmosphere and its anomalies over the North Pacific. In summer the marine heat flux exhibited a zonal structure, decreasing northward in magnitude whereas in winter, an intense heating over the Kuroshio region was observed. Spring and autumn appeared as transition seasons. The horizontal distribution of the oceanic heat flux anomalies over the Kuroshio region was found to vary greatly from year to year. This motivated the analysis of Chapters 6, 7 and 8, where atmospheric motions due to diabatic heat forcing

with varying zonal width was considered.

In Chapter 5 the persistence of oceanic heating anomalies was also studied. We found that summer heat flux anomalies in the Northwest Pacific could persist until winter, moving eastward with time, whereas winter anomalies persisted only in the area immediately south of the Kuroshio region. As in Zhao and McBean (1987a) an index was defined to represent the heating over the Kuroshio and its adjacent area. This index was correlated with the atmospheric surface pressure and 500 mb & 700 mb geopotential heights over the northern hemisphere. Three regions of significant correlations were found: a)—Over eastern Asia; b)—Over the central North Pacific; c)—Over northern Canada. Zhao and McBean (1987b) proposed the following argument to explain the regions of high correlation, a) and b) above: “The higher the pressure over eastern Asia, the colder and the dryer the air is over Siberia and the higher the wind velocities over the Kuroshio region. Hence the heat flux over the Kuroshio region would be larger and the resulting heating anomalies would cause the Aleutian Low to shift southwestward in winter”. This hypothesis was tested in the analysis of the later chapters.

Inspired by the motivation provided by Chapter 5, we examined in Chapter 6 the effect of the horizontal structure of midlatitude oceanic heating on the stationary atmospheric response by means of a simple continuously stratified quasigeostrophic model, linearized about a basic state with constant zonal flow U_0 on a beta plane. Solutions were obtained for three non-periodic zonal heating structures (line source, rectangular, and segmented cosine), and these were compared with the solution for the frequently used zonally periodic heating distribution. All four heating distributions assume an $e^{-\alpha z}$ vertical structure and a $\cos l y$ meridional structure.

The solutions for the rectangular and segmented cosine heating structures had a response in the neighbourhood of the forcing which increased in magnitude with decreasing horizontal heating extent. In the far field, the response in all three non-periodic models was constant. Decreasing the meridional wavenumber l had the effect of increasing the

magnitude of the local response. A second case of solutions was alluded to in Chapter 6 (ie., small meridional wavenumbers) but not examined in detail.

The model was applied to the Kuroshio heating problem as discussed above and in Chapter 5. The results were found to be consistent with the hypothesis of Zhao and McBean (1987b) that Kuroshio heating anomalies can force downstream low pressure anomalies, especially when they are associated with cooling over the eastern North Pacific (corresponding to heating with the structure of the first winter EOF of variability of the North Pacific ocean-to-atmosphere total heat transfer).

In order to examine the effects of vertical shear on the results for the continuous model, we used a two level model in Chapter 7 with the same heating structures as in Chapter 6. Little difference was observed between the solutions for these two different models. There were two cases which emerged in obtaining analytic solutions. In case 1, for large meridional wavenumbers, there existed a large local response and a constant downstream response. In case 2, for small meridional wavenumbers, the far field response was sinusoidal with wavenumber 3–4 perturbations superimposed on the solution for case 1. A critical wavenumber separating these two cases was also obtained. The effect of oceanic heating on the atmosphere over the Kuroshio region was also examined in an attempt to once more explain the regions of high correlations over eastern Asia and the central North Pacific. It was found that the model response was again consistent with the observed correlations and the hypothesis of Zhao and McBean (1987b). When western North Pacific heating and eastern North Pacific cooling was introduced into the model, a large low pressure response was observed over the central North Pacific. This feature was in excellent agreement with the observed correlations.

Finally, in Chapter 8 we examined the transient atmospheric response to oceanic heat forcing and removed the assumption of an unbounded zonal domain ($-\infty < x < \infty$) used in the previous two Chapters. This was accomplished by using a zonally periodic, time dependent version of the two level model in Chapter 7, with surface friction included in

the lower level vorticity equation. The solutions suggested that the assumption of the unbounded x -domain used in Chapters 6 and 7 was indeed justified and underlined the importance of the meridional scale of the heating and the height at which the thermodynamic equation was applied (ie., the level of heat input). When the heating was entered into the model near to the surface (Model 2), unstable modes were prevalent sooner than they would have been if the heat forcing were applied at a higher level (Model 1).

The same two cases as in Chapters 6 and 7 (dependent on the meridional wavenumber l) emerged in the analysis. For small scale meridional heating structures (case 1; large l), the response consisted of an upper level high and a lower level low which propagated eastward with time. For large scale meridional heating structures (case 2; small l) the response consisted of a wavenumber 3–4 perturbation superimposed on the solution for case 1. This wavenumber 3–4 perturbation is very similar to the dominant forced atmospheric response observed in the GCM studies of Chervin *et al.* (1976, 1980), Kutzbach *et al.* (1977) and Frankignoul (1985b).

To further examine the effects of the meridional scale of heating on the transient atmospheric response future work is being planned. It is hoped that simulations using numerical General Circulation Models will add further insight into the results obtained from the simple analytical models.

References

- Abramowitz, M. and I.A. Stegun, 1964: *Handbook of Mathematical Functions*, US Department of Commerce, National Bureau of Standards, Washington DC.
- Allen, J.S., 1980: Models of wind-driven currents on the continental shelf. *Annual Reviews of Fluid Mechanics*, 12, 389–433.
- Barnett, T.P., 1981: On the nature and causes of large-scale thermal variability in the central North Pacific. *Journal of Physical Oceanography*, 11, 887–904.
- Beardsley, R.C., and J. Hart, 1978: A simple theoretical model for the flow of an estuary onto a continental shelf. *Journal of Geophysical Research*, 83, 873–883.
- Beardsley, R.C., and C.D. Winant, 1979: On the mean circulation in the Mid-Atlantic Bight. *Journal of Physical Oceanography*, 9, 612–619.
- Boland, F.M., 1971: Temperature-salinity anomalies at depths between 200 m and 800 m in the Tasman Sea. *Australian Journal of Marine and Freshwater Research*, 22, 55–72.
- Brink, K.H., 1982: A comparison of long coastal trapped wave theory with observations off Peru. *Journal of Physical Oceanography*, 12, 897–913.
- Brink, K.H., 1987: Coastal ocean physical processes. *Reviews of Geophysics*, 25, 204–216.
- Bryan, K., 1969: A numerical method for the study of the circulation of the world ocean. *Journal of Computational Physics*, 4, 347–376.
- Buchwald, V.T., and B.J. Kachoyan, 1987: Shelf waves generated by a coastal flux. *Australian Journal of Marine and Freshwater Research*, in press.
- Budyko, M.I., 1963: *Atlas of the Heat Balance of the Earth* (in Russian). Academy of Sciences, Moscow, 69 pp. [Also, *Guide to the Atlas of the Heat Balance of the Earth*. Translated from Russian by I. A. Donchoo, U.S. Weather Bureau, WB/T-106, Washington, DC, 25pp.]
- Bunker, A.F., 1975: Energy exchange at the surface of the western North Atlantic Ocean. Woods Hole Oceanographic Institution, WHOI-75-3, 107pp.
- Chervin, R.M., W.M. Washington, and S.H. Schneider, 1976: Testing the statistical significance of the response of the NCAR general circulation model to North Pacific Ocean surface temperature anomalies. *Journal of the Atmospheric Sciences*, 33, 413–423.
- Chervin, R.M., J.E. Kutzbach, D.D. Houghton, and R.G. Gallimore, 1980: Response of the NCAR general circulation model to prescribed changes in ocean surface temperature, II, Midlatitude and subtropical changes. *Journal of Atmospheric Sciences*, 37, 308–322.

- Church, J.A., H.J. Freeland, and R.L. Smith, 1986a: Coastal-trapped waves on the East Australian continental shelf. Part I: Propagation of modes. *Journal of Physical Oceanography*, 16, 1929–1943.
- Church, J.A., H.J. White, A.J. Clarke, H.J. Freeland, and R.L. Smith, 1986b: Coastal-trapped waves on the East Australian continental shelf. Part II: Model Verification. *Journal of Physical Oceanography*, 16, 1945–1957.
- Clarke, A.J., and R.O.R.Y. Thompson, 1984: Large-scale wind-driven ocean response in the Australian Coastal Experiment region. *Journal of Physical Oceanography*, 14, 338–352.
- Cox, M.D., 1984: A primitive equation, 3-dimensional model of the ocean. *GFDL Ocean Group Technical Report No. 1*, August 30.
- Cox, M.D., 1985: An eddy resolving numerical model of the ventilated thermocline. *Journal of Physical Oceanography*, 15, 1312–1324.
- Cox, M.D., and K. Bryan, 1984: A numerical model of the ventilated thermocline. *Journal of Physical Oceanography*, 14, 674–687.
- Csanady, G.T., 1978: The arrested topographic wave. *Journal of Physical Oceanography*, 8, 47–62.
- Davis, R.E., 1976: Predictability of sea surface temperature and sea level pressure anomalies over the North Pacific Ocean. *Journal of Physical Oceanography*, 6, 249–266.
- Davis, R.E., 1978: Predictability of sea level pressure anomalies over the North Pacific Ocean. *Journal of Physical Oceanography*, 8, 233–246.
- Edwards, R.J., 1979: Tasman and Coral Sea ten year mean temperature and salinity fields, 1967–1976. CSIRO Australian Division of Fisheries and Oceanography, Report No. 88.
- Egger, J., 1977: On the linear theory of the atmospheric response to sea surface temperature anomalies. *Journal of the Atmospheric Sciences*, 34, 603–614.
- Emery, W.J., and J.S. Dewar, 1982: *Mean Temperature-Salinity, Salinity-Depth and Temperature-Depth Curves for the North Atlantic and the North Pacific*. Pergamon Press, 87 pp.
- Emery, W.J. and K. Hamilton, 1985: Atmospheric forcing of interannual variability in the northeast Pacific Ocean: Connections with El Niño. *Journal of Geophysical Research*, 90, 857–868.
- Frankignoul, C., 1985a: Sea surface temperature anomalies, planetary waves, and air-sea feedback in the middle latitudes. *Reviews of Geophysics*, 23, 357–390.

- Frankignoul, C., 1985b: Multivariate analysis of sensitivity studies with atmospheric GCM's, in *Coupled Atmosphere-Ocean Models*, Elsevier Oceanography Series, Vol. 40, edited by J.C.J. Nihoul, pp. 199–209, Elsevier, New York.
- Freeland, H.J., and K.L. Denman, 1982: A topographically controlled upwelling center off Southern Vancouver Island. *Journal of Marine Research*, 40, 1069–1093.
- Freeland, H.J., F.M. Boland, J.A. Church, A.J. Clarke, A.M.G. Forbes, A. Huyer, R.L. Smith, R.O.R.Y. Thompson, and N.J. White, 1986: The Australian coastal experiment: A search for coastal-trapped waves. *Journal of Physical Oceanography*, 16, 1230–1249.
- Gibbs, C.F., M. Tomczak Jr, and A.R. Longmore, 1986: The Nutrient Regime of Bass Strait. *Australian Journal of Marine and Freshwater Research*, 37, 451–466.
- Gill, A.E., 1976: Adjustment under gravity in a rotating channel. *Journal of Fluid Mechanics*, 77, 603–621.
- Gill, A.E., 1982: *Atmosphere-Ocean Dynamics*. Academic Press, 662 pp.
- Godfrey, J.S., I.S.F. Jones, J.G.H. Maxwell, and B.D. Scott, 1980: On the winter cascade from Bass Strait into the Tasman Sea. *Australian Journal of Marine and Freshwater Research*, 31, 275–286.
- Halpern, D., and J.R. Holbrook, 1972: STD measurements off the Oregon coast, July/August 1972. *Coastal Upwelling Ecosystems Analysis*, Data Report 4.
- Hamilton, K., 1984: Seasonal mean North Pacific sea level pressure charts, 1939–1982. *DOUBC*, Manuscript Report No. 41, University of British Columbia.
- Hamilton, K., 1985: A study of the variability of the return migration routes of Fraser River sockeye salmon (*Oncorhynchus nerka*) *Canadian Journal of Zoology*, 63, 1930–1943.
- Holbrook, J.R., and D. Halpern, 1974: STD measurements off the Oregon coast, July/August 1973. *Coastal Upwelling Ecosystems Analysis*, Data Report 12.
- Holton, J.R., 1979: *An Introduction to Dynamic Meteorology*, 319 pp., 2nd ed. Academic Press, New York.
- Horel, J.D. and J.M. Wallace, 1981: Planetary scale atmospheric phenomena associated with the southern oscillation. *Monthly Weather Review*, 109, 813–829.
- Hoskins, B.J., and D.J. Karoly, 1981: The steady linear response of a spherical atmosphere to thermal and orographic forcing. *Journal of the Atmospheric Sciences*, 38, 1179–1196.
- Hsieh, W.W., M.K. Davey, and R.C. Wajswicz, 1983: The free Kelvin wave in finite-difference numerical models. *Journal of Physical Oceanography*, 13, 1383–1397.

- Hsieh, W.W., and A.E. Gill, 1984: The Rossby adjustment problem in a rotating, stratified channel, with and without topography. *Journal of Physical Oceanography*, 14, 424–436.
- Huang, J.C.K., 1978: Response of the NCAR general circulation model to North Pacific sea surface temperature anomalies. *Journal of the Atmospheric Sciences*, 35, 1164–1179.
- Jenne, R.L., 1975: Data sets for meteorological research. NCAR Technical Note TN/IA-111, 194pp.
- Kutzbach, J.E., R.M. Chervin, and D.D. Houghton, 1977: Response of the NCAR general circulation model to prescribed changes in ocean surface temperature, I. *Journal of the Atmospheric Sciences*, 34, 1200–1213.
- LeBlond, P.H., and L.A. Mysak, 1978: *Waves in the Ocean*. Elsevier, 602 pp.
- Levitus, S., 1982: Climatological Atlas of the World. NOAA Professional Paper 13, 173 pp.
- Lim, H., and C.-P. Chang, 1981: A theory for midlatitude forcing of tropical motions during winter monsoons. *Journal of the Atmospheric Sciences*, 38, 2377–2392.
- Lim, H., and C.-P. Chang, 1986: Generation of internal- and external-mode motions from internal heating: Effects of vertical shear and damping. *Journal of the Atmospheric Sciences*, 43, 948–957.
- Masuda, K., 1983: Dynamical estimation of atmospheric diabatic heating over the northern hemisphere in winter. *Journal of the Meteorological Society of Japan*, 61, 449–454.
- Mysak, L.A., 1980: Recent advances in shelf wave dynamics. *Reviews of Geophysics and Space Physics*, 184, 211–241.
- Mysak, L.A., 1986: El Niño, interannual variability and fisheries in the northeast Pacific Ocean. *Canadian Journal of Fisheries and Aquatic Sciences*, 43, 464–497.
- Mysak, L.A., W.W. Hsieh, and T.R. Parsons, 1982: On the relationship between interannual baroclinic waves and fish populations in the northeast Pacific. *Biological Oceanography*, 2, 63–103.
- Mysak, L.A., C. Groot, and K. Hamilton, 1986: A study of climate and fisheries: Interannual variability of the Northeast Pacific Ocean and its influence on homing migration routes of sockeye salmon. *Climatological Bulletin*, 20, 26–35.
- Namias, J., 1959: Recent seasonal interactions between North Pacific waters and the overlying atmospheric circulation. *Journal of Geophysical Research*, 64, 631–646.
- Nitta, Ts., and S.S. So, 1980: Structure and heat, moisture and momentum budgets of a convective mixed layer during AMTEX'75. *Journal of the Meteorological Society of Japan*, 58, 378–393.

- Ou, H.W., 1984: Geostrophic adjustment: A mechanism for frontogenesis. *Journal of Physical Oceanography*, 14, 994-1000.
- Pedlosky, J., 1979: *Geophysical Fluid Dynamics*, 624 pp., Springer-Verlag, New York.
- Quinn, W.H., D.O. Zorf, K.S. Short, and R.T.W.K. Yang, 1978: Historical trends and statistics of the Southern Oscillation, El Niño, and Indonesian droughts. *Fisheries Bulletin*, 76, 663-678.
- Talley, L.D., 1984: Meridional heat transport in the Pacific Ocean. *Journal of Physical Oceanography*, 14, 231-241.
- Tomczak, M. Jr., 1985: The Bass Strait water cascade during winter 1981. *Continental Shelf Research*, 4, 255-278.
- Trenberth, K.E., and D.A. Paolino, 1980: Northern Hemisphere sea level pressure data set: trends, errors and discontinuities. *Monthly Weather Review*, 108, 855-872.
- Tully, J.P., 1942: Surface non-tidal currents in the approaches to Juan de Fuca strait. *Journal of the Fisheries Research Board of Canada*, 5, 398-409.
- Uda, M., 1962: Cyclic, correlated occurrence of world-wide anomalous oceanographic phenomena and fisheries conditions. *Journal of the Oceanographic Society of Japan*, 20th Anniversary Volume, 368-375.
- Van Heijst, K.H., 1985: A geostrophic model of a tidal mixing front. *Journal of Physical Oceanography*, 15, 1182-1190.
- Wang, D.P., 1984: Mutual intrusion of a gravity current and density front formation. *Journal of Physical Oceanography*, 14, 1191-1199.
- Ware, D.M., and R.E. Thomson, 1987: La Perouse Project: Second Annual Progress Report, 1986. 31pp. *Department of Fisheries and Oceans*, Pacific Biological Station, Nanaimo, British Columbia.
- Weaver, A.J., 1987a: Bass Strait as a reverse estuary source for coastally trapped waves. *Australian Journal of Marine and Freshwater Research*, to appear, 38, Number 6.
- Weaver, A.J., 1987b: A two level model of the steady state response of the atmosphere to midlatitude heating with various zonal structures. *Journal of the Meteorological Society of Japan*, to appear, 65, Number 4.
- Weaver, A.J., 1987c: Statistical relationships between Northeast Pacific atmospheric pressure and the sea surface temperature along the British Columbia coast. *Climatological Bulletin*, submitted.

- Weaver, A.J., and K. Hamilton, 1985: Statistical relationships between Northeast Pacific atmospheric pressure and the sea surface temperature along the British Columbia coast. *DOUBC*, Manuscript Report No. 44, University of British Columbia.
- Weaver, A.J., and L.A. Mysak, 1986a: Seasonal oceanic heat flux anomaly charts for the North Pacific 1950–1979. *DOUBC*, Manuscript Report No. 46, University of British Columbia.
- Weaver, A.J., and L.A. Mysak, 1986b: Statistical relationships between atmospheric surface pressure, 700mb geopotential height and oceanic heat flux anomalies over the Kuroshio region. *DOUBC*, Manuscript Report No. 47, University of British Columbia.
- Weaver, A.J., and L.A. Mysak, 1987a: A time dependent model of the atmospheric response to midlatitude heating with various zonal structures. *Journal of the Meteorological Society of Japan*, submitted.
- Weaver, A.J., and L.A. Mysak, 1987b: A time dependent model of the atmospheric response to midlatitude heating with various zonal structures. *CRG Report No. 87-7*, McGill University.
- Weaver, A.J., and W.W. Hsieh, 1987: The influence of buoyancy flux from estuaries on continental shelf circulation. *Journal of Physical Oceanography*, to appear, Adrian Gill Memorial Edition, 17, Number 11.
- Weaver, A.J., L.A. Mysak, and A.F. Bennett, 1987a: The steady state response of the atmosphere to midlatitude heating with various zonal structures. *Geophysical and Astrophysical Fluid Dynamics*, to appear, 38, Number 3.
- Weaver, A.J., L.A. Mysak, and A.F. Bennett, 1987b: The steady state response of the atmosphere to midlatitude heating with various zonal structures. *CRG Report No. 87-1*, McGill University.
- Webster P.J., 1981: Mechanisms determining the atmospheric response to sea surface temperature anomalies. *Journal of the Atmospheric Sciences*, 38, 554–571.
- Webster P.J., 1982: Seasonality in the local and remote atmospheric response to sea surface temperature anomalies. *Journal of the Atmospheric Sciences*, 39, 41–52.
- Zhao, Y.P., and G.A. McBean, 1986: Annual and interannual variability of the North Pacific ocean-to-atmosphere total heat transfer. *Atmosphere-Ocean*, 24, 265–282.
- Zhao, Y.P., and G.A. McBean, 1987a: Patterns of North Pacific ocean-to-atmosphere heat transfer. submitted to *Journal of Climatology*.
- Zhao, Y.P., and G.A. McBean, 1987b: The influence of heat transfer from the Kuroshio region on the atmospheric circulation, in preparation.

Appendix I

Inclusion of Rayleigh Friction in the Continuous Model

We include Rayleigh friction in the continuous model of Chapter 6 to examine the physical location in the complex plane of the poles at $\xi = 0, \pm a$ in equations (6.21), (6.25), (6.27) and (6.31). To accomplish this we replace $U_0 \frac{\partial}{\partial x}$ by $r_0 + U_0 \frac{\partial}{\partial x}$ in the governing equation (6.3) and the surface boundary condition (6.17), where $r_0 > 0$ is the Rayleigh friction coefficient. Proceeding with an analysis parallel to that of Section 6.3, yields (cf. equation 6.11),

$$\hat{\phi}_{zz} - \frac{1}{H} \hat{\phi}_z + S \left\{ \frac{\beta \xi}{(U_0 \xi - ir_0)} - l^2 - \xi^2 \right\} \hat{\phi} = - \frac{Q_0(1 + \alpha H) e^{-ip\xi} e^{-\alpha z}}{i\sqrt{2\pi}(U_0 \xi - ir_0)H}. \quad (I.1)$$

Assuming that $q^2 < 0$ again, so that the solution is exponentially decaying in z , we obtain an expression for $C(\xi)$ analogous to (6.13),

$$C(\xi) = \frac{-\alpha Q_0(1 + (\alpha H)^{-1}) e^{-ip\xi}}{i\sqrt{2\pi}(U_0 \xi - ir_0)(\alpha^2(1 + (\alpha H)^{-1}) + S(\frac{\beta \xi}{(U_0 \xi - ir_0)} - l^2 - \xi^2))}, \quad (I.2)$$

which in the limit as $r_0 \rightarrow 0$ is identical to (6.13). Thus, upon applying the boundary conditions at $z = 0$ and at $z \rightarrow \infty$, we simply replace the denominator of (6.21) and the denominators of the integrands of (6.25), (6.27), and (6.31) by,

$$(\xi - i\frac{r_0}{U_0}) \left\{ \left\{ \xi^2 + l^2 - \frac{\beta \xi}{(U_0 \xi - ir_0)} \right\} - \frac{\alpha^2}{S}(1 + (\alpha H)^{-1}) \right\}, \quad (I.3)$$

so that the poles occur at the roots of

$$\xi^3 - i\frac{r_0}{U_0} \xi^2 - a^2 \xi + i\frac{r_0}{U_0} (a^2 - \frac{\beta}{U_0}) = 0. \quad (I.4)$$

Let $\xi = i\mu$ so that (I.4) becomes,

$$\mu^3 - \frac{r_0}{U_0} \mu^2 + a^2 \mu - \frac{r_0}{U_0} (a^2 - \frac{\beta}{U_0}) = 0. \quad (I.5)$$

Since $a^2 > 0$, there exists one real root and one pair of complex conjugate roots of (I.5) (Abramowitz and Stegun 1964, p. 17). It is fairly straightforward to show that the real part of each root of (I.5) is positive. Hence the imaginary part of each root of (I.4) is positive, and so the poles at $\xi = 0, \pm a$ all move to the upper half plane when Rayleigh friction is included.

Appendix II

Inclusion of Rayleigh Friction and Newtonian Cooling in the Two Level Model

We include Rayleigh friction and Newtonian cooling in the two level model of Chapter 7 to examine the physical location in the complex plane of the poles at $\xi = 0, \pm\xi_1, \pm\xi_2$. To accomplish this we replace $U_1 \frac{\partial}{\partial x}$ by $r_0 + U_1 \frac{\partial}{\partial x}$ and $U_3 \frac{\partial}{\partial x}$ by $r_0 + U_3 \frac{\partial}{\partial x}$ in the governing equations (7.5)–(7.7), where $r_0 > 0$ is the Rayleigh friction and Newtonian cooling coefficient. If one carries through the analysis of Section 7.3, the resulting expression for $\hat{\omega}_2$ is (cf., 7.10).

$$\hat{\omega}_2 = - \frac{\chi U_1 U_3 e^{-ip\xi} R_1(\xi) R_3(\xi)}{\sqrt{2\pi} \{ R_1(\xi) R_3(\xi) - \lambda^2 \{ (\frac{r_0 \alpha_1}{U_1} + i\alpha_1 \xi) R_1(\xi) + (\frac{r_0 \alpha_3}{U_3} + i\alpha_3 \xi) R_3(\xi) \} \}}, \quad (II.1)$$

where

$$R_{1,3}(\xi) = i\xi f_{1,3}(\xi) - r_0(l^2 + \xi^2), \quad (II.2)$$

and $f_1(\xi)$ and $f_3(\xi)$ are given by (7.13). Similar expressions may be obtained for $\hat{\psi}_1$ and $\hat{\psi}_3$. We must therefore find the location of the zeroes of

$$R_1(\xi) R_3(\xi) - \lambda^2 \{ (\frac{r_0 \alpha_1}{U_1} + i\alpha_1 \xi) R_1(\xi) + (\frac{r_0 \alpha_3}{U_3} + i\alpha_3 \xi) R_3(\xi) \}, \quad (II.3)$$

which is sixth order in ξ .

The inclusion of Rayleigh friction and Newtonian cooling introduces two more zeros in the denominator of (II.1) near $\xi = 0$. As $r_0 \rightarrow 0$ the numerator and denominator of (II.1) both vanish at $\xi = 0$ and we retrieve (7.10).

The zeros of (II.3) were obtained numerically using the parameters of Section 7.3 for both $r_0 = 1.0 \times 10^{-14} \text{s}^{-1}$ and $r_0 = 1.0 \times 10^{-18} \text{s}^{-1}$, and have been compiled in Table 6 for Model 1 and in Table 7 for Model 2. Two wavenumbers, $l = 1.4 \times 10^{-6} \text{m}^{-1}$ and $l = 0.8 \times 10^{-6} \text{m}^{-1}$, corresponding to case 1 and case 2, were selected. The results indicate that for case 1 ($l^2 > \{\gamma^2 + \delta\}^{\frac{1}{2}} - \gamma$) the pole at $\xi = 0$ goes into the UHP (ξ_a, ξ_b in Tables 6, 7). The poles at $i\eta_1, i\eta_2$ are both located in the UHP (ξ_d, ξ_e in Tables 6, 7) and the poles at $-i\eta_1, -i\eta_2$ are both located in the LHP (ξ_c, ξ_f in Tables 6, 7).

For case 2 ($l^2 < \{\gamma^2 + \delta\}^{\frac{1}{2}} - \gamma$) the pole at $\xi = 0$ splits and goes into both the UHP and the LHP, whereas the real poles at $\pm\xi_1$ both move into the UHP (ξ_c, ξ_d in Tables 6, 7) and hence give the sinusoidal contribution of (7.29), (7.30), and (7.31) for $x > p$ only. Once more the poles at $i\eta_2$ and $-i\eta_2$ remain in the UHP and LHP respectively.

Table 6

Real and imaginary parts of the zeroes of (II.3) for Model 1 (equally spaced levels). Rayleigh friction and Newtonian cooling coefficients of $r_0 = 1.0 \times 10^{-14} s^{-1}$ and $r_0 = 1.0 \times 10^{-18} s^{-1}$ were used. Two wavenumbers, $l = 1.4 \times 10^{-6} m^{-1}$ and $l = 0.8 \times 10^{-6} m^{-1}$, corresponding to case 1 and case 2, were also selected.

wavenumber $\times 10^{-6}$	pole	$r_0 = 1.0 \times 10^{-14}$	$r_0 = 1.0 \times 10^{-18}$
$l = 0.8$	ξ_a	$5.97 \times 10^{-41}, -6.66 \times 10^{-16}$	$5.97 \times 10^{-45}, -6.66 \times 10^{-20}$
	ξ_b	$-9.86 \times 10^{-32}, 1.49 \times 10^{-15}$	$-1.20 \times 10^{-35}, 1.49 \times 10^{-19}$
	ξ_c	$-7.99 \times 10^{-7}, 6.16 \times 10^{-16}$	$-7.99 \times 10^{-7}, 6.16 \times 10^{-20}$
	ξ_d	$7.99 \times 10^{-7}, 6.16 \times 10^{-16}$	$7.99 \times 10^{-7}, 6.16 \times 10^{-20}$
	ξ_e	$1.32 \times 10^{-23}, 2.01 \times 10^{-6}$	$-6.62 \times 10^{-24}, 2.01 \times 10^{-6}$
	ξ_f	$1.32 \times 10^{-23}, -2.01 \times 10^{-6}$	$-6.62 \times 10^{-24}, -2.01 \times 10^{-6}$
$l = 1.4$	ξ_a	$3.96 \times 10^{-16}, 1.62 \times 10^{-15}$	$3.96 \times 10^{-20}, 1.62 \times 10^{-19}$
	ξ_b	$-3.96 \times 10^{-16}, 1.62 \times 10^{-15}$	$-3.96 \times 10^{-20}, 1.62 \times 10^{-19}$
	ξ_c	$-8.27 \times 10^{-22}, -8.26 \times 10^{-7}$	$-8.27 \times 10^{-22}, -8.26 \times 10^{-7}$
	ξ_d	$8.27 \times 10^{-22}, 8.26 \times 10^{-7}$	$8.27 \times 10^{-22}, 8.26 \times 10^{-7}$
	ξ_e	$-2.95 \times 10^{-22}, 2.32 \times 10^{-6}$	$-2.95 \times 10^{-22}, 2.32 \times 10^{-6}$
	ξ_f	$2.95 \times 10^{-22}, -2.32 \times 10^{-6}$	$2.95 \times 10^{-22}, -2.32 \times 10^{-6}$

Table 7

Real and imaginary parts of the zeroes of (II.3) for Model 2 (unequally spaced levels). Rayleigh friction and Newtonian cooling coefficients of $r_0 = 1.0 \times 10^{-14} s^{-1}$ and $r_0 = 1.0 \times 10^{-18} s^{-1}$ were used. Two wavenumbers, $l = 1.4 \times 10^{-6} m^{-1}$ and $l = 0.8 \times 10^{-6} m^{-1}$, corresponding to case 1 and case 2, were also selected.

wavenumber $\times 10^{-6}$	pole	$r_0 = 1.0 \times 10^{-14}$	$r_0 = 1.0 \times 10^{-18}$
$l = 0.8$	ξ_a	$-5.02 \times 10^{-42}, 9.83 \times 10^{-16}$	$-5.21 \times 10^{-41}, 9.83 \times 10^{-20}$
	ξ_b	$-4.93 \times 10^{-32}, -8.17 \times 10^{-16}$	$-1.20 \times 10^{-35}, -8.17 \times 10^{-20}$
	ξ_c	$-6.68 \times 10^{-7}, 6.55 \times 10^{-16}$	$-6.68 \times 10^{-7}, 6.55 \times 10^{-20}$
	ξ_d	$6.88 \times 10^{-7}, 6.55 \times 10^{-16}$	$6.68 \times 10^{-7}, 6.55 \times 10^{-20}$
	ξ_e	$-1.42 \times 10^{-23}, 3.03 \times 10^{-6}$	$-7.55 \times 10^{-24}, 3.03 \times 10^{-6}$
	ξ_f	$-1.23 \times 10^{-23}, -3.03 \times 10^{-6}$	$-5.69 \times 10^{-24}, -3.03 \times 10^{-6}$
$l = 1.4$	ξ_a	$3.25 \times 10^{-16}, 1.12 \times 10^{-15}$	$3.25 \times 10^{-20}, 1.12 \times 10^{-19}$
	ξ_b	$-3.25 \times 10^{-16}, 1.12 \times 10^{-15}$	$-3.25 \times 10^{-20}, 1.12 \times 10^{-19}$
	ξ_c	$8.49 \times 10^{-22}, -9.35 \times 10^{-7}$	$8.49 \times 10^{-22}, -9.35 \times 10^{-7}$
	ξ_d	$-8.49 \times 10^{-22}, 9.35 \times 10^{-7}$	$-8.49 \times 10^{-22}, 9.35 \times 10^{-7}$
	ξ_e	$2.45 \times 10^{-22}, 3.24 \times 10^{-6}$	$2.45 \times 10^{-22}, 3.24 \times 10^{-6}$
	ξ_f	$-2.45 \times 10^{-22}, -3.24 \times 10^{-6}$	$-2.45 \times 10^{-22}, -3.24 \times 10^{-6}$